Observation and Measurements of the Higgs Boson with the $H \rightarrow WW^{(*)} \rightarrow \ell\nu\ell\nu$ Decay

by

Jonathan David Long

A dissertation submitted in partial fulfillment
of the requirements for the degree of
Doctor of Philosophy
(Physics)
in The University of Michigan
2015

Doctoral Committee:

Professor Jianming Qian, Chair
Professor Dante E. Amidei
Professor Aaron T. Pierce
Professor Virginia R. Young
Assistant Professor Junjie Zhu

ACKNOWLEDGEMENTS

I am enormously grateful to have come across so many wonderful people over the course of my graduate career. It is impossible to name everyone who has been a mentor, supporter, and friend, but I think you all; it would not have been possible without you.

First, I would like to thank my advisor Jianming Qian who introduced me to high energy physics as an undergraduate and has been an invaluable source of knowledge and advice ever since. Thank you for positioning me to succeed in a large collaboration and then giving me the freedom to work autonomously.

Thanks to Dante Amidei, Aaron Pierce, Virgina Young, and Junjie Zhu for serving on my committee.

The Michigan ATLAS group supported me throughout my time at Michigan and at CERN. Being stationed at CERN for an extended period is really an incredible experience for which I am truly thankful for. We also have great computing resources, including the people who keep it running, which kept what could have been a hassle an effortless resource. I have enjoyed the intellectual and social company of several postdocs and fellow students. To Jonas Strandberg, Gemma Wooden, and Magda Chelstowska, Alan Wilson, Aaron Armbruster, Devin Harper, Tom Cheng, Lulu Liu, and the rest, thank you for making the transition to CERN easier and the long days well spent. Thanks to Homer Neal for showing me a different perspective my first year and Tiesheng Dai for his guidance on muon spectrometer service work.

Most of my time at CERN was spent with colleagues and friends from HSG3. You all shaped my experience over the past few years into a memorable one. Thanks to our conveners for organizing and dealing with our group, my fellow production and stats team members for churning out results and our endless technical discussion, and our core group battling through the conference gauntlet. To Olivier Arnaez, Valerio 'Marquis' Bortolotto, Johanna Bronner, Stefan Gadatsch, Joana Miguéns, Corrinne Mills, Richard Polifka, Pierre Savard, Doug Schaefer, Joe Taezner, the UPenn army, and the countless rest at CERN and by now beyond, thank you for being a colleague and friend; I look forward to the next time we meet. A special thanks to those who worked on the Higgs width analysis and $H \to WW^{(*)}$ prospects, without your help, this dissertation would have been a lot shorter.

Graduate school would not have been nearly as enjoyable if it were not for friends, new and old alike, sharing the ride. Fellow students, Skyler Degenkolb, Josh Gevirtz, Archis Joglekar, Jack Kearney, Dan Schafer, Scott Stephenson, Bob Zheng, and the rest, it has been a pleasure. We have a great community between students, staff, and faculty; I hope it continues to live up to what we have had. To Woodlawn and all of the fun times.

Finally, I would not be where I am today without the support and encouragement of my family. Mom, thank you for all that you have done, and still do, behind the scenes over the years and for all of the mail and packages. Dad, thanks for showing me your lab when I was little and for sharing your experience in academics. I have you two to thank for my original scientific inspiration and putting me on the right track (even if it is not chemistry). Thanks for all of the support, in all forms; it has made everything much more pleasant and much less complicated.

Thanks to everyone, mentioned here or not, for making the past several years an enjoyable journey.

For today, goodbye. For tomorrow,
good luck. And forever, Go Blue!

Mary Sue Coleman,
President Emerita,
University of Michigan

TABLE OF CONTENTS

LIST OF FIGURES

Figure

LIST OF TABLES

Table

LIST OF APPENDICES

Appendix

LIST OF ABBREVIATIONS

V–A Vector–Axial

LHC Higgs XS WG LHC

AFII Atlfast-II (ATLAS Fast Simulation)

ALICE A Large Ion Collider Experiment

ATLAS A Toroidal LHC Apparatus

BDT boosted decision tree

BSM Beyond the Standard Model

C/A Cambridge-Aachen

CaloTag Calorimeter-tagged

CB Combined

CERN the European Organization for Nuclear Research, formerly Conseil Européen pour la Recherche Nucléaire

CJV Central Jet Veto

CL Confidence Level

CMS Compact Muon Solenoid

CP Charge Parity

CR Control Region

CSC Cathode-Strip Chamber

CSM Chamber Service Module

DPI Double Parton Interaction

DY Drell–Yan

ECFA European Committee for Future Accelerators

$ee/\mu\mu$ Same-Flavor

EF Event Filter

EM Electromagnetic

$e\mu$ Different-Flavor

EMEC Electromagnetic End-cap

ES European Strategy

EW Electroweak

EWSB Electroweak Symmetry Breaking

FCal forward calorimeter

FPGA Field-Programmable Gate Array

FSR Final State Radiation

FTK Fast TracKer

ggF gluon Fusion

GRL Good Run List

GSF Gaussian Sum Filter

HEC Hadronic End-cap Module

HEP High Energy Physics

HL-LHC High Luminosity LHC

HLT High-Level Trigger

ID Inner Detector

IP Interaction Point

ISR Initial State Radiation

JBEE Jet b-tagging Efficiency Extrapolation

JER Jet Energy Resolution

JES Jet Energy Scale

JTAG Joint Test Action Group

JVE Jet Veto Efficiency

JVF Jet Vertex Fraction

JVSP Jet Veto Survival Probability

L1 Level-1

L2 Level-2

LAr liquid argon

LCW Local Cell Signal Weighting

LEP Large Electron–Positron Collider

LH likelihood

LHC Large Hadron Collider

LHCb Large Hadron Collider beauty

LHCf Large Hadron Collider forward

LO Leading Order

LS1 Long Shutdown 1

MC Monte Carlo

MDT Monitored Drift Tube

ME Matrix Element

MET Missing Transverse Momentum

MIP Minimally Ionizing Particle

MLE Maximum Likelihood Estimator

MoEDAL Monopole and Exotics Detector At the LHC

MS Muon Spectrometer

MVA Multivariate Analysis

NF Normalization Factor

NLL Next-to-Leading Log

NLO Next-to-Leading Order

NNLL Next-to-Next-Leading Log

NNLO Next-to-Next-Leading Order

NP Nuisance Parameter

OC Opposite-Charge

OLV Outside Lepton Veto

PDF Parton Distribution Function

PDG Particle Data Group

POI Parameter of Interest

pp proton-proton

PS Parton Shower

PSB Proton Synchrotron Booster

PV Primary Vertex

QCD Quantum Chromodynamics

QED Quantum Electrodynamics

QFT Quantum Field Theory

qqH Associated Heavy Quark Production

RMS Root Mean Square

RoI Regions of Interest

RPC Resistive Plate Chamber

s.d. Standard Deviation

SA Stand-Alone

SC Same-Charge

SCT Silicon Microstrip Tracker

SF Scale Factor

SLD SLAC Large Detector

SM Standard Model

SPS Super Proton Synchrotron

SR Signal Region

ST Segment-tagged

SUSY Supersymmetry

TGC Thin Gap Chamber

TOTEM TOTal Elastic and diffractive cross section Measurement

TRT Transition Radiation Tracker

UE Underlying Event

VBF Vector Boson Fusion

VBS Vector Boson Scattering

VEV Vacuum Expectation Value

VH Associated Production

VR Validation Region

VV Other Dibosons

ABSTRACT

Observation and Measurements of the Higgs Boson with the $H \to WW^{(*)} \to \ell\nu\ell\nu$ Decay
by
Jonathan David Long

Chair: Jianming Qian

A summary is presented of the observation of the Higgs boson decaying into a pair of W bosons and measurements of its properties using the $H \to WW^{(*)} \to \ell\nu\ell\nu$ channel with the ATLAS detector at the Large Hadron Collider. Up to $4.5\,\text{fb}^{-1}$ of data collected at center-of-mass energy $\sqrt{s} = 7\,\text{TeV}$ and $20.3\,\text{fb}^{-1}$ at $\sqrt{s} = 8\,\text{TeV}$ are used. An excess over the background only expectation is observed at 6.1 standard deviations with 5.8 expected. This corresponds to a measured signal strength, the ratio of the measured to expected cross section times branching ratio, for a Standard Model Higgs boson with $m_H = 125.36\,\text{GeV}$ of $\mu = 1.09^{+0.16}_{-0.15}(\text{stat.})\,^{+0.17}_{-0.14}(\text{syst.})$. The measured signal strengths for the gluon fusion and vector boson fusion production modes are $\mu_{\text{ggF}} = 1.02^{+0.19}_{-0.19}(\text{stat.})\,^{+0.22}_{-0.18}(\text{syst.})$ and $\mu_{\text{VBF}} = 1.27^{+0.44}_{-0.40}(\text{stat.})\,^{+0.30}_{-0.21}(\text{syst.})$ respectively. The presence of vector boson fusion production is tested using the ratio of these signal strengths resulting in evidence for vector boson fusion production at the level of 3.2 standard deviations. This analysis is projected to have an uncertainty on the signal strength of 14 % at the end of the Large Hadron Collider running with $300\,\text{fb}^{-1}$ and 10 % at the end of the High Luminosity LHC running with $3000\,\text{fb}^{-1}$, assuming no improvements on the current theoretical uncertainties on the signal. The WW final state is also used to determine the off-shell Higgs boson production signal strength in the mass range above $2m_W$. Using the CL_s method, a 95 % confidence level upper limit of 17.2 is placed on the off-shell signal strength, assuming a $gg \to WW$ background k-factor equal to that of the $gg \to H \to WW$ signal. The ratio of off-shell signal strength to on-shell strength can be interpreted as a measurement of the Higgs boson total decay width assuming the relevant Higgs boson couplings are independent of the production energy scale. Combining the $H \to WW$ and $H \to ZZ$ on- and off-shell analyses, the observed (expected) 95 % confidence level upper limit on the Higgs boson total width is 22.7 (33.0) MeV.

CHAPTER I

Introduction

The field of high energy physics (HEP) is rooted in the ambition to understand nature at its most fundamental level. It follows a long history of exploring the universe at smaller and smaller scales. Using high energies allows us to probe extremely small scales, smaller than the protons and neutrons which make up atomic nuclei. This is often equated with probing the physics of the universe shortly after the Big Bang, a time when the universe was very hot (energetic). In some sense, the birth of HEP came about in the late 1800s, which saw the advent of Maxwell's equations describing electromagnetism, discovery of electrons, and discovery of X-rays. Since then, descriptions of the weak and strong forces have emerged, cemented by the discovery of many particles in the latter-half of the 1900s.

A theory called the Standard Model (SM) of particle physics represents our current understanding of the fundamental building blocks of nature, particles, and their behavior through forces. It is a remarkably successful theory and a culmination of work over centuries, with its current form arising in the mid-1970s. Until the discovery of the Higgs boson in 2012 by the ATLAS (A Toroidal LHC Apparatus) [1] and CMS (Compact Muon Solenoid) [2] experiments at the Large Hadron Collider (LHC), the SM was missing one last piece of experimental evidence in order to be complete—complete in the sense of all predicted SM particles having been discovered, not as a description of nature. The Higgs boson is a consequence of the Higgs mechanism, which explains how the W and Z bosons can be massive while the photon is massless, and provides a method for including the masses of fundamental particles in the theory. Thus the discovery and measurements of the Higgs boson are a test of this important mechanism.

This dissertation describes two analyses using data collected by the ATLAS detector involving a particular decay mode of the Higgs boson into a pair of W bosons, which then decay leptonically: $H \to WW^{(*)} \to \ell\nu\ell\nu$. A brief overview of the underlying theory and motivation for the Higgs boson is found in Chapter II. Chapter III describes the LHC, the machine which produces proton-proton (pp) collisions, and the ATLAS detector, the instrument which records them. Chapter IV describes the performance of the ATLAS detector and objects used in the analyses in the latter chapters. The main analysis is described in Chapter V, serving as a baseline for the others. It contributed to the discovery of the Higgs boson and continues to play a role in the subsequent measurements of Higgs boson properties, such as how strongly the Higgs boson couples to other particles. The second analysis, presented in Chapter VI, probes the total decay width of the Higgs boson using a novel technique involving measurement the off-shell production rate of the Higgs boson. Direct measurement of the Higgs boson width at the LHC is difficult due to the detector resolution being much larger than the expected width. Finally, projected sensitivities of the $H \to WW^{(*)} \to \ell\nu\ell\nu$ analysis in the far future, including at the possible High Luminosity LHC (HL-LHC), are covered in Chapter VII.

CHAPTER II

The Standard Model and Higgs Boson

This chapter gives a brief overview of the background and formalism of the theory behind modern particle physics—the Standard Model (SM), plus the role of the Higgs mechanism and the expectations for the Higgs boson at the LHC. Many summaries of the SM and Higgs mechanism exist; in particular, Refs. [3–6] cover the quantum field theory (QFT) and setup of the SM discussed in this chapter. Natural units[1] are used for energy and momentum units in this and the remaining chapters. In brief, the SM does an excellent job at describing fundamental particles and forces and the Higgs mechanism completes it by allowing for a description of masses of fundamental particles. An extra particle, the Higgs boson, comes out of the Higgs mechanism.

2.1 The Standard Model

The SM [7–15] is a theory describing the fundamental building blocks of the universe, particles, and their interactions, forces. It is immensely successful at describing our experimental observations. For example, the prediction and measurement of the anomalous magnetic moment of an electron agree to nine significant digits [16]. The theory describes three of the four fundamental forces: the electromagnetic (EM), the weak, and the strong force. The EM force is responsible for the interaction of electrically charged particles, e.g., electrons in an atom. The weak force is responsible for radioactive decays and plays an important role in powering stars. The strong force governs the interactions within the nucleus and binds the constituents of protons and neutrons together. Each of these forces is mediated by the exchange of a particle, a force carrier. Including gravity, the fourth force, in a unified theory has long been a theoretical goal. However, gravity is much weaker than the other three forces and does not play a role in the processes relevant to this dissertation.

[1] Natural units are a redefinition of units with fundamental constants set to unity, e.g., $c = \hbar = 1$; thus, masses GeV/c^2 will be in terms of GeV.

The SM is built on the formalism of QFT, which describes fundamental particles with states of a quantized field. Forces are described by gauge theories, mediated by so-called gauge bosons. Much of the theory can be attributed to its $\mathrm{SU}(3)_C \times \mathrm{SU}(2)_L \times \mathrm{U}(1)_Y$ gauge invariance, meaning pieces of the theory are invariant under rotations in these spaces. Notably, the photon, the EM force carrier, is massless, while the W and Z bosons, force carries of the weak force, are massive. This difference is referred to as electroweak symmetry breaking (EWSB), and understanding the origins of EWSB is a fundamental goal of the LHC scientific program.

Basic properties of the fundamental particles and force carriers are listed in Table 2.1. Fermions are particles with half-integer spin and bosons are particles with integer spin. Quarks, shown in blue, are fermions with electric charge and carry a color charge of the strong force; they are the constituents of protons (uud) and neutrons (udd). Such composite particles with two quarks are called mesons and those with three, baryons; together, all composite particles made of quarks are called hadrons. Leptons, shown in green, are fermions with both massive, electrically charged leptons (e.g., the electron) and massless (in the SM) electric-charge zero neutrinos. Finally, bosons (or force carriers), shown in orange, mediate the electromagnetic force (photon γ), strong force (gluon g), and weak force (W and Z bosons). The force carriers are all spin-1, and henceforth also called vector bosons. Notably, the gluon carries color, and thus interacts with itself, unlike the photon. All of these particles have anti-particles, which have the same mass and spin, but opposite charge—the electrically neutral photon and Z boson are their own anti-particles. Anti-particles are generally denoted with a bar (e.g., $\bar{e}$ or $\bar{\nu}$) or in some cases by their charge when it is relevant, e.g., e^+.

Although the SM describes all of the particles and forces discovered so far (excluding gravity), it is an incomplete description of the universe. For example, we lack a description of the nature of dark matter and dark energy, which make up the majority of our universe. Supersymmetry (SUSY) is a theory which resolves some of the inadequacies of the SM, such as offering a dark matter candidate and providing corrections to the calculation of the Higgs boson mass. Thus, searching for SUSY is also a large part of the LHC physics program. Colloquially, such additional theories are referred to as beyond the Standard Model (BSM) theories. As mentioned, there is no satisfactory quantum theory of gravity, from which there is a hypothesized spin-2 graviton. The universe around us is dominated by matter; how this asymmetry between matter and anti-matter arose is an open question[2]. There is also no accounting for non-zero neutrino masses in the SM; though, they can easily be accounted for by adding a right-handed neutrino. Finally, before the LHC data taking, the origin of the masses of fundamental particles and EWSB were missing pieces to a complete SM. This last

[2]It is thought that the Big bang should have created matter and anti-matter in equal amounts.

2.3×10^{-6} Up (u) $\frac{1}{2}$ $\frac{2}{3}$	1.28 Charm (c) $\frac{1}{2}$ $\frac{2}{3}$	173.2 Top (t) $\frac{1}{2}$ $\frac{2}{3}$	0 Gluon (g) 1 0
4.8×10^{-6} Down (d) $\frac{1}{2}$ $-\frac{1}{3}$	9.5×10^{-5} Strange (s) $\frac{1}{2}$ -$\frac{1}{3}$	4.18 Bottom (b) $\frac{1}{2}$ $-\frac{1}{3}$	0 Photon (γ) 1 0
$< 2 \times 10^{-9}$ Electron Neutrino (ν_e) $\frac{1}{2}$ 0	$< 1.9 \times 10^{-4}$ Muon Neutrino (ν_μ) $\frac{1}{2}$ 0	$< 1.8 \times 10^{-2}$ Tau Neutrino (ν_τ) $\frac{1}{2}$ 0	91.19 Z^0 1 0
5.11×10^{-4} Electron (e) $\frac{1}{2}$ -1	1.06×10^{-1} Muon (μ) $\frac{1}{2}$ -1	1.78 Tau (τ) $\frac{1}{2}$ -1	80.39 $W^\pm$ 1 ± 1

Table 2.1: SM particles, excluding the Higgs boson, with their mass in GeV at the top of the cell, spin in the lower left of the cell, and electric charge in the lower right of the cell. Values are taken from the Particle Data Group (PDG) [17]. Fermions are in blue (quarks) and green (leptons). Bosons are in orange.

piece of the SM was the initial motivation for the analysis in Chapter V.

The dynamics of the SM are described by a Lagrangian formulation, with the action the integral over all space-time of the Lagrangian density $\mathcal{L}$ (henceforth the Lagrangian),

$$S = \int \mathcal{L}(x) d^4x \,. \tag{2.1}$$

Symmetries play an important role in the SM. There are both discrete symmetries, e.g., time reversal, and continuous symmetries, e.g., translation and rotation. These are transformations which leave the system, or Lagrangian, unchanged. Symmetries can be divided into two classes: global symmetries which do not depend on space-time coordinates and gauge (local) symmetries which do. Symmetries are particularly important because of the implications of Noether's theorem [18], which states that if a system has a continuous symmetry, then there is a corresponding conserved current, and thus a conserved charge. For example, translational invariance is associated with the conservation of momentum, and Lorentz invariance, physical laws are independent of their inertial reference frame, is associated with the conservation of the invariant mass, easily verified because the mass is a Lorentz scalar, i.e., it has no space-time indices. Give the SM contains spin-$\frac{1}{2}$ matter fields, we need to describe their dynamics, which will need to respect the symmetries of the theory.

The Dirac Lagrangian for a spinor field with mass m describes the kinematics of spin-$\frac{1}{2}$ particles:

$$\mathcal{L}_{\text{Dirac}} = \overline{\Psi}(x)\left(i\gamma^{\mu}\partial_{\mu} - m\right)\right)\Psi(x)\,, \tag{2.2}$$

where $\Psi(x)$ is a Dirac spinor (the fermion field) and $\overline{\Psi}(x) = \Psi^{\dagger}\gamma^{0}$ is its adjoint. The symbol γ^{μ} represents the Dirac matrices satisfying the anti-commutation relation

$$\{\gamma^{\mu}, \gamma^{\nu}\} = 2g^{\mu\nu}\,, \tag{2.3}$$

where $g^{\mu\nu}$ is the metric tensor. In four dimensions, they can be represented in terms of Pauli sigma matrices and the additional γ^{0} (in the Weyl basis):

$$\gamma^{i} = \begin{pmatrix} 0 & \sigma^{i} \\ -\sigma^{i} & 0 \end{pmatrix} \qquad \gamma^{0} = \begin{pmatrix} 0 & \mathbb{1} \\ \mathbb{1} & 0 \end{pmatrix} \tag{2.4}$$

This makes the term $\overline{\Psi}\Psi$ a Lorentz invariant, and such terms in a Lagrangian are associated with a particle's invariant mass. In this 2×2 representation, the Dirac spinor can be written as a left-handed (L) and right-handed (R) Weyl spinor:

$$\Psi = \begin{pmatrix} \psi_{L} \\ \psi_{R} \end{pmatrix}\,. \tag{2.5}$$

Putting the Dirac Lagrangian into the Euler-Lagrange equations yields the Dirac equation for fermions:

$$0 = (i\gamma^{\mu}\partial_{\mu} - m)\Psi(x)\,. \tag{2.6}$$

It will also be useful to introduce the projection operators

$$P_{L,R} = \frac{1 \mp \gamma^{5}}{2},\ \text{where } \gamma^{5} = \begin{pmatrix} -\mathbb{1} & 0 \\ 0 & \mathbb{1} \end{pmatrix}, \tag{2.7}$$

such that $P_{L,R}\Psi = \psi_{L,R}$ and the subscript L, R on $f_{L,R}$ implies $P_{L,R}f$.

2.1.1 Quantum electrodynamics

Quantum Electrodynamics (QED) describes the interactions of electrically charged particles and its force carrier, the photon. The dynamics associated with the electric field must be added to the Lagrangian. The Dirac Lagrangian (which is what we need for charged fermions) is invariant under a global U(1) transformation:

$$\Psi \to e^{-i\alpha}\Psi\,. \tag{2.8}$$

The associated current is $j^\mu = \overline{\Psi}\gamma^\mu\Psi$, which we will identify as the electric current by including the electric charge e, $j^\mu = e\overline{\Psi}\gamma^\mu\Psi$. The electric field term in the Lagrangian is built from the field strength tensor $F^{\mu\nu} = \partial^\mu A^\nu - \partial^\nu A^\mu$, where the gauge field A^μ is defined in terms of a scalar and vector potential $A^\mu = (\phi, \vec{A})$. In order to preserve the U(1) symmetry, the gauge field must also transform as

$$A^\mu \to A^\mu - \frac{1}{e}\partial^\mu\alpha(x)\,. \tag{2.9}$$

To make it a gauge symmetry, we replace the partial derivative with a covariant derivative $D_\mu = \partial_\mu - ieA_\mu$, where $\alpha(x)$ is now space-time dependent.

The QED Lagrangian is thus,

$$\mathcal{L}_{\text{QED}} = \overline{\Psi}\left(i\gamma^\mu D_\mu - m\right)\Psi - \frac{1}{4}F_{\mu\nu}F^{\mu\nu}\,. \tag{2.10}$$

Plugging in the covariant derivative, we get:

$$\mathcal{L}_{\text{QED}} = \overbrace{i\overline{\Psi}\gamma^\mu\partial_\mu\Psi - m\overline{\Psi}\Psi}^{\text{Dirac term}} - \overbrace{\frac{1}{4}F_{\mu\nu}F^{\mu\nu}}^{\text{Maxwell term}} - \overbrace{e\overline{\Psi}\gamma_\mu A^\mu\Psi}^{\text{Interaction term}}\ , \tag{2.11}$$

where the last term is the interaction of the charged particle (Ψ) with the field (A^μ), i.e., the $e\bar{e}\gamma$ vertex.

2.1.2 Unification with the weak force

The weak force and electromagnetic force can be described as one unified electroweak theory, which obeys $\text{SU}(2)_L \times \text{U}(1)_Y$. We will denote the gauge field associated with the $\text{U}(1)_Y$ symmetry as B_μ. The non-abelian SU(2) gauge invariance requires three gauge fields, $W_i^\mu (i = 1, 2, 3)$, one for each SU(2) generator, in order to preserve the symmetry, similar to what was done in the previous section. The transformation is written as

$$\Psi \to e^{i\vec{\theta}\cdot\vec{T}}\Psi\,, \tag{2.12}$$

where the three components of $T^i = \tau^i/2$ are related to the Pauli matrices $\tau^i = \sigma^i$ in this representation. The W_i fields represent three spin-1 bosons, which can be written in a mass basis:

$$W^{\pm} = \frac{W^1 \mp iW^2}{\sqrt{2}}$$
$$W^0 = W^3\,.$$

With all of this we can write the associated covariant derivative needed for gauge invariance for left-handed and right-handed fields:

$$D^L_\mu = \partial_\mu - ig_1\frac{Y}{2}B_\mu - ig_2\frac{1}{2}\vec{\tau}\cdot\vec{W}_\mu \qquad (2.13)$$
$$D^R_\mu = \partial_\mu - ig_1\frac{Y}{2}B_\mu\,,$$

where g_1 and g_2 are couplings that determine the strength of the interactions. $Y = 2(Q - T_3)$ is the weak hypercharge, computed from the electric charge Q and third component of the weak isospin for each particle. The value of T_3 for components of SU(2) multiplets is analogous to that of spin: spin-0 corresponding to a singlet, spin-$\frac{1}{2}$ to a doublet, and spin-1 to a triplet. Charged leptons and down-type quarks have $T_3 = -1/2$, neutrinos and up-type quarks have $T_3 = +1/2$, and right-handed particles $T_3 = 0$. The fields transform as

$$W^i_\mu \to W^i_\mu + \frac{1}{g_2}\partial_\mu\theta^i - \epsilon_{ijk}\theta^j W^k_\mu\ . \qquad (2.14)$$

Fermions are represented by left-handed SU(2) doublets, which are charged under $\mathrm{U}(1)_Y$, and right-handed SU(2) singlets. Using electrons as an example, we would write them as

$$L = \begin{pmatrix}\nu_e \\ e^-\end{pmatrix}_L \quad \text{and} \quad e^-_R\,, \qquad (2.15)$$

or with quarks,

$$Q_L = \begin{pmatrix}u \\ d\end{pmatrix}_L \quad \text{and} \quad u_R, d_R\,. \qquad (2.16)$$

Putting this all together, we can write down the terms in the Lagrangian with a sum over the three families:

$$\mathcal{L}_{\mathrm{EW}} = \sum_f^{\text{family}=1,2,3} \Big[\overline{L}^f i\gamma^\mu D^L_\mu L^f + \bar{e}^f_R i\gamma^\mu D^R_\mu e^f_R + \overline{Q}^f_L i\gamma^\mu D^L_\mu Q^f_L \qquad (2.17)$$
$$+ \bar{u}^f_R i\gamma^\mu D^R_\mu u^f_R + \bar{d}^f_R i\gamma^\mu D^R_\mu d^f_R\Big] - \frac{1}{4}W^i_{\mu\nu}W^{\mu\nu}_i - \frac{1}{4}B_{\mu\nu}B^{\mu\nu}\,,$$

where the field strength tensor $B_{\mu\nu}$ has the same form as $F_{\mu\nu}$, and $W^i_{\mu\nu} = \partial_\mu W^i_\nu - \partial_\nu W^i_\mu + g_2 \epsilon^{abc} W^b_\mu W^c_\nu$ is the field strength tensor of W^i_μ, with the extra term arising because the SU(2) generators do not commute, $[T^a, T^b] = i\epsilon^{abc} T^c$. The Levi-Civita symbol, ϵ^{abc}, is an antisymmetric tensor.

The charged W bosons are linear combinations of the W^i_μ gauge fields, seen in Equation 2.13. The neutral fields, observed as the photon and Z boson, are combinations of the W^3_μ and B_μ fields:

$$\begin{aligned} A_\mu =& \frac{g_2 B_\mu + g_1 W^3_\mu}{\sqrt{g_2^2 + g_1^2}} \\ Z_\mu =& \frac{-g_1 B_\mu + g_2 W^3_\mu}{\sqrt{g_2^2 + g_1^2}} \,. \end{aligned} \tag{2.18}$$

These can be parametrized in terms of the Weinberg, or weak mixing, angle θ_W, where $\sin\theta_W = {g_1}/{\sqrt{g_1^2 + g_2^2}}$ and $\cos\theta_W = {g_2}/{\sqrt{g_1^2 + g_2^2}}$, such that:

$$\begin{pmatrix} A_\mu \\ Z_\mu \end{pmatrix} = \begin{pmatrix} \cos\theta_W & \sin\theta_W \\ -\sin\theta_W & \cos\theta_W \end{pmatrix} \begin{pmatrix} B_\mu \\ W^3_\mu \end{pmatrix} \,. \tag{2.19}$$

Notably, the relation $e = g_1 \cos\theta_W = g_2 \sin\theta_W$ arises when matching A_μ terms to those from QED.

Plugging in the covariant derivatives gives rise to a charged-current (CC), neutral-current (NC) (including the QED interaction), and self interactions among the gauge bosons $(VVV, VVVV)$ [6, 19]:

$$\begin{aligned} \mathcal{L}_{CC} =& \sum_i^{\text{family}=1,2,3} \frac{e}{\sin\theta_W \sqrt{2}} \left[(\bar{u}^i_L \gamma^\mu d^i_L + \bar{\nu}^i_{e,L} \gamma^\mu e^i_L) W^+_\mu + \text{h.c.} \right] \\ \mathcal{L}_{NC} =& \sum_i^{\text{family}=1,2,3} \sum_{f^i}^{\nu_e, e, u, d} e Q_{f^i} (\bar{f^i} \gamma^\mu f^i) A_\mu \\ &+ \frac{e}{\sin\theta_W \cos\theta_W} \left[\bar{f}^i_L \gamma^\mu f^i_L (T_{3,f^i} - Q_{f^i} \sin^2\theta_W) + \bar{f}^i_R \gamma^\mu f^i_R (-Q_{f^i} \sin^2\theta_W) \right] Z_\mu \\ \mathcal{L}_{VVV} =& ie \cot\theta_W \left[(\partial^\mu W^{\nu -} - \partial^\nu W^{\mu -}) W^+_\mu Z_\nu + \text{h.c.} + W^-_\mu W^+_\nu (\partial^\mu Z^\nu - \partial^\nu Z^\mu) \right] \\ &+ ie \left[(\partial^\mu W^{\nu -} - \partial^\nu W^{\mu -}) W^+_\mu A_\nu + \text{h.c.} + W^-_\mu W^+_\nu (\partial^\mu A^\nu - \partial^\nu A^\mu) \right] \end{aligned} \tag{2.20}$$

$$
\begin{aligned}
\mathcal{L}_{VVVV} = & \frac{e^2}{2\sin^2\theta_W}\left[(W^+_\mu W^{\mu-})^2 - W^+_\mu W^{\mu+} W^-_\nu W^{\nu-}\right] - \\
& + e\cot^2\theta_W\left[W^+_\mu W^{\mu-} Z_\nu Z^\nu - W^+_\mu Z^\mu W^-_\nu Z^\nu\right] \\
& - e^2\cot\theta_W\left[2W^+_\mu W^{\mu-} Z_\nu A^\nu - W^+_\mu Z^\mu W^-_\nu A^\nu - W^+_\mu A^\mu W^-_\nu Z^\nu\right] \\
& - e^2\left[W^+_\mu W^{\mu-} A_\nu A^\nu - W^+_\mu A^\mu W^-_\nu A^\nu\right] .
\end{aligned}
$$

Now consider a mass term in the Lagrangian, which will have the form $m\overline{\Psi}\Psi$. We can expand this in terms of its left- and right-handed components using the projection operators:

$$
\begin{aligned}
m\overline{\Psi}\Psi = & m\overline{\Psi}(P_L + P_R)\Psi \\
= & m(\overline{\Psi}_R\Psi_L + \overline{\Psi}_L\Psi_R) .
\end{aligned}
\tag{2.21}
$$

The terms have one SU(2) doublet and one singlet; thus, these terms do not obey an SU(2) symmetry. Similarly, the boson mass terms, $\sim \frac{1}{2}m^2 W_\mu W^\mu$, transform as in Equation 2.14, and are not invariant under an SU(2) transformation. Thus, they are also not gauge invariant. However, we have observed the bosons to have mass experimentally! This is the crucial point in electroweak theory that is addressed by the Higgs mechanism—how does this EWSB occur? We have observed massive W and Z bosons, but a massless photon, which the theory thus far cannot account for.

2.2 The Higgs mechanism

The 'Brout-Englert-Guralnik-Hagen-Higgs-Kibble' mechanism [20–25] is an attempt to address EWSB. A scalar field, the Higgs field, with a particular potential is introduced. The Higgs field is a complex doublet in SU(2) space, carries $Y = 1$ under $\mathrm{U}(1)_Y$, and is colorless. The special potential has a non-zero ground state, and it is this vacuum expectation value (VEV) which spontaneously breaks the $\mathrm{SU}(2)_L \times \mathrm{U}(1)_Y$ electroweak symmetry, leaving only the electromagnetic $U(1)_{EM}$. The spontaneous breaking of the symmetry results in massless Goldstone bosons, which are absorbed by the W and Z bosons as their longitudinal polarizations as they become massive, and the remaining degree of freedom results in a massive scalar boson, the Higgs boson. A comprehensive review of EWSB can be found in Ref. [26] by Djouadi.

The Higgs field has the form of

$$
\Phi = \begin{pmatrix} \phi^+ \\ \phi^0 \end{pmatrix} ,
\tag{2.22}
$$

where $\phi^+ = (\phi_1 + i\phi_2)/\sqrt{2}$ and $\phi^0 = (\phi_3 + i\phi_4)/\sqrt{2}$ are complex fields. We will consider a

Lagrangian with a mass term and four-point vertex:

$$\mathcal{L} = (D_\mu \Phi)^\dagger D_\mu \Phi - \mu^2 \Phi^\dagger \Phi - \lambda(\Phi^\dagger \Phi)^2 \,. \tag{2.23}$$

The potential, $\mu^2\Phi^\dagger\Phi + \lambda(\Phi^\dagger\Phi)^2$, is invariant under a local gauge transformation $\Phi \rightarrow e^{i\vec{\theta}(x)\cdot\vec{T}}\Phi$. The quartic coupling λ should be positive so that the potential is bounded. Then, we have two cases for μ^2. If $\mu^2 > 0$, then the potential has a minimum at zero, i.e., the ground state is at zero and the VEV of Φ is zero. However, if we consider a potential where $\mu^2 < 0$, then the ground state is no longer at zero, but rather at a finite value of $\Phi^\dagger\Phi = \frac{-\mu^2}{2\lambda} = \frac{v^2}{2}$, where v is substituted as the VEV of the Higgs field. See Fig. 2.1 for an example with a real scalar field.

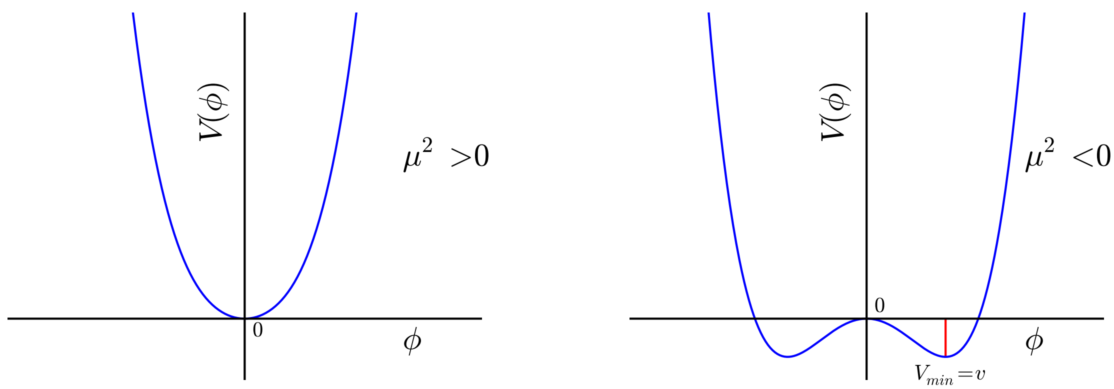

Figure 2.1: Example of symmetry breaking for the potential with a real scalar $V(\phi) = \mu^2\phi^2 + \lambda\phi^4$, where the ground state for $\mu^2 < 0$ no longer respects the symmetry $\phi \rightarrow -\phi$.

Since we need to preserve the U(1) symmetry of electromagnetism, the neutral component of Φ picks up the non-zero expectation value:

$$\langle\Phi\rangle_0 = \frac{1}{\sqrt{2}}\begin{pmatrix} 0 \\ v \end{pmatrix} \,. \tag{2.24}$$

We have chosen $\phi_3 = v$ and $\phi_1 = \phi_2 = \phi_4 = 0$, a direction in SU(2) space, and the symmetry of the potential is now broken. Then we expand around the minimum for small perturbations $v + h(x)$ in order to investigate the excitations of the field. The kinetic term of the Lagrangian is now

$$
\begin{aligned}
|D_\mu \Phi|^2 &= \left| \left(\partial_\mu - i g_1 \frac{Y}{2} B_\mu - i g_2 \frac{1}{2} \vec{\tau} \cdot \vec{W}_\mu \right) \Phi \right|^2 \\
&= \frac{1}{2} \left| \begin{pmatrix} \partial_\mu - i g_1 \frac{1}{2} B_\mu - i g_2 \frac{1}{2} W_\mu^3 & -i g_2 \frac{1}{2} (W_\mu^1 - i W_\mu^2) \\ -i g_2 \frac{1}{2} (W_\mu^1 + i W_\mu^2) & \partial_\mu - i g_1 \frac{1}{2} B_\mu + i g_2 \frac{1}{2} W_\mu^3 \end{pmatrix} \begin{pmatrix} 0 \\ v + h(x) \end{pmatrix} \right|^2 \\
&= \frac{1}{2} (\partial_\mu h)^2 + \frac{1}{8} g_2^2 (v+h)^2 |W_\mu^1 + i W_\mu^2|^2 + \frac{1}{8} (v+h)^2 |g_2 W^3 - g_1 B_\mu|^2 \\
&= \frac{1}{2} (\partial_\mu h)^2 + \frac{1}{4} g_2^2 (v+h)^2 (W_\mu^+ W^{\mu -}) + \frac{1}{8} (g_2^2 + g_1^2)(v+h)^2 Z_\mu Z^\mu \,,
\end{aligned}
\tag{2.25}
$$

where we've used the relations in Equations 2.13 and 2.18. Finally, we have terms corresponding to masses of the W and Z bosons! Due to foresight, the hypercharge of the scalar was chosen as $Y = 1$ and no mass term for the photon arises. The Higgs mechanism successfully breaks the symmetry, generating the mass terms we require while leaving the photon massless. The boson masses are $m_{W^\pm} = v g_2/2$ and $m_Z = v\sqrt{g_1 + g_2}/2$, where we have the relation $m_W/m_Z = \cos\theta_W$. Interaction terms arise between the W and Z bosons and h, which we call the Higgs boson.

Plugging in the expansion around the VEV into the potential in Equation 2.23,

$$
\mathcal{L}_h = -\lambda v^2 h^2 - \lambda v h^3 - \frac{\lambda}{4} h^4 \tag{2.26}
$$

gives rise to a three-point, four-point Higgs boson vertex, and mass term where $m_H = \sqrt{2\lambda v^2}$.

Fermion mass terms are accounted for by adding interactions between the fermions and Φ scaled by Yukawa couplings :

$$
\begin{aligned}
\mathcal{L}_{\text{Yukawa}} = &\sum_f^{\text{family}=1,2,3} \left[-\lambda_f \overline{L} \Phi e_R - \lambda_d \overline{Q} \Phi d_R + \text{h.c.} \right] \\
+ &\sum_f^{\text{family}=1,2,3} \left[-\lambda_u \overline{Q} (-i\tau_2) \Phi^* u_R + \text{h.c.} \right] \,,
\end{aligned}
\tag{2.27}
$$

where $(-i\tau_2)\Phi^*$ is needed to get the VEV aligned with the up-type quarks; it is still invariant under SU(2) [6]. Expanding in the same way as for the bosons produces mass terms, as well as interactions with the Higgs boson, e.g., $-\frac{1}{\sqrt{2}} \lambda_e (v+h) \bar{e}_L e_R$, where we can denote the mass $m_e = \lambda_e v/\sqrt{2}$. Thus the Higgs mechanism also accommodates fermion masses. It is important to note that the coupling of particles with the Higgs boson scales with the particles mass—the Higgs boson couples more strongly to heavier particles.

2.2.1 The Higgs boson

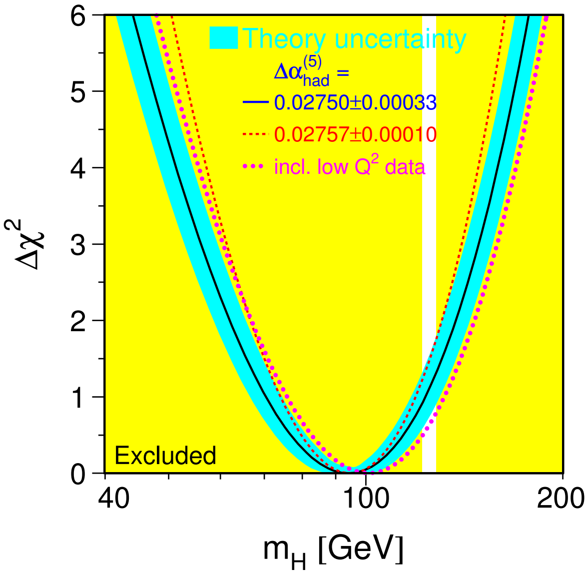

Figure 2.2: Constraint on the Higgs boson mass from precision electroweak measurements. The preferred mass is 94^{+29}_{-24} GeV and LEP excluded masses below 114.4 GeV at 95 % CL [27]. The excluded area in yellow includes recent Tevatron and LHC data.

As discussed in the previous section, a new scalar boson comes with the Higgs mechanism. Its mass is not predicted in terms of other SM parameters. Before the LHC data, the Large Electron–Positron Collider (LEP) electroweak (EW) Working Group used a global fit of the rest of SM EW parameters; for which we have measurements from LEP, SLD (SLAC Large Detector), and the Tevatron; to constrain the Higgs boson mass. Precise predictions of EW parameters rely on loop corrections involving the Higgs boson. A preferred mass of 94^{+29}_{-24} GeV was obtained, see Fig. 2.2, and a lower 95 % confidence level (CL) limit on the Higgs boson mass from the LEP experiments was set at 114.4 GeV [27]. This motivated the search for a light Higgs boson. Searches were also performed at the Tevatron, resulting in an exclusion of possible Higgs boson masses in the range 147–180 GeV [28] and later 3 standard deviation (s.d.) evidence in 120–135 GeV region [29]. The Higgs boson was initially observed by both the ATLAS [1] and CMS [2] experiments in 2012. It has since been measured by both experiments [30] to be close to $m_H = 125$ GeV.

Higgs bosons at the LHC are produced in pp collisions. There are several production modes. The dominant mode is gluon fusion (ggF) ($gg \to H$), where gluons from the protons fuse through a loop of mostly top- and bottom-quarks into a Higgs boson, see Fig. 2.3(a).

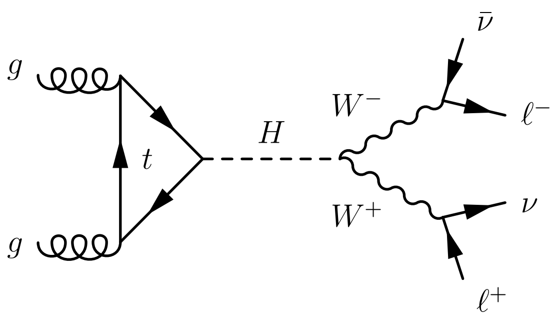

(a) Gluon fusion (ggF)

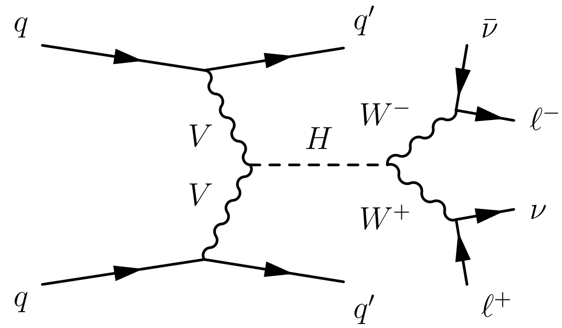

(b) Vector boson fusion (VBF)

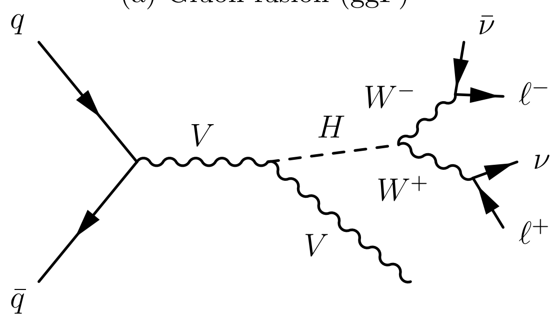

(c) Associated production (VH) "Higgs-Strahlung"

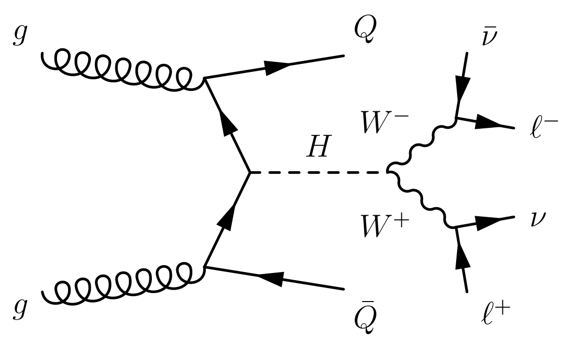

(d) Associated heavy quark production (qqH)

Figure 2.3: Feynman diagrams of the leading Higgs boson production modes at the LHC with the $WW^* \to \ell\nu\ell\nu$ decay, where $V = (W, Z)$, $\ell = (e, \mu, \tau)$, and $Q = (t, b)$.

Next largest is vector boson fusion (VBF) production ($qq \to q'q'H$), which is about 8 % of the ggF rate at $m_H = 125\,\text{GeV}$. Quarks from the protons scatter off of each other via vector bosons ($V = W, Z$) which produce a Higgs boson, with two additional quarks in the final state, see Fig. 2.3(b). A Higgs boson can also be produced in association with a vector boson ($q\bar{q} \to V^* \to VH$), associated production (VH), as radiation, see Fig. 2.3(c). The smallest of the four production modes listed here, associated heavy quark production (qqH), is similar in diagram to VBF, but is initiated via gluons which radiate (mostly heavy) quarks that produce a Higgs boson, with heavy quarks in the final state. These are commonly referred to as $t\bar{t}H$ and $b\bar{b}H$, for associated production with top- and bottom-quarks respectively. Figure 2.4 shows the various production cross sections of the Higgs boson at 8 TeV center-of-mass energy at the LHC as a function of m_H. The ggF and VBF cross sections at 7 TeV are about 22 % smaller.

The Higgs boson can decay directly into a fermion-anti-fermion pair, a W^+W^- pair, or two Z bosons. It can also decay via a charged loop to two photons, or through a colored loop to two gluons. Figure 2.5(a) shows the branching ratios of the Higgs boson as a function of m_H. At $m_H = 125\,\text{GeV}$, the decay to $b\bar{b}$ dominates at 58 % of all decays. Second behind it is the decay to W^+W^-, the relevant process for this dissertation, with a branching fraction

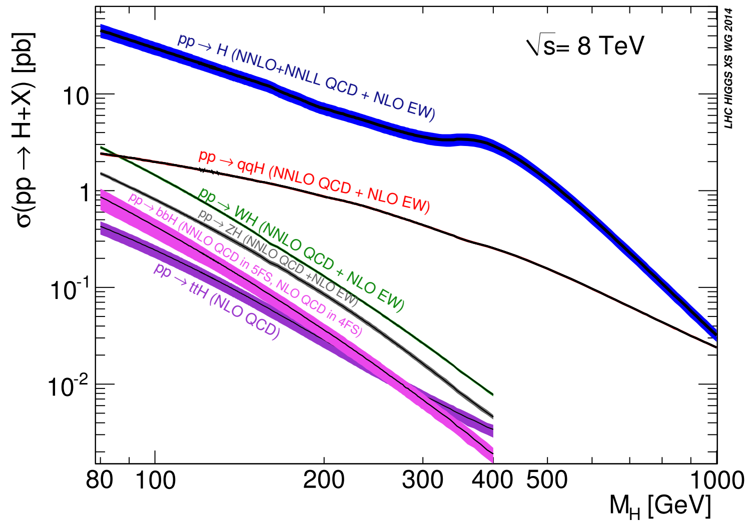

Figure 2.4: Higgs boson production cross sections at 8 TeV. For $m_H = 125\,\text{GeV}$ the production cross section is 19.3 pb for ggF, 1.58 pb for VBF, 0.705 pb for WH, 0.415 pb for ZH, 0.129 pb for $t\bar{t}H$, and 0.204 pb for $b\bar{b}H$ [31].

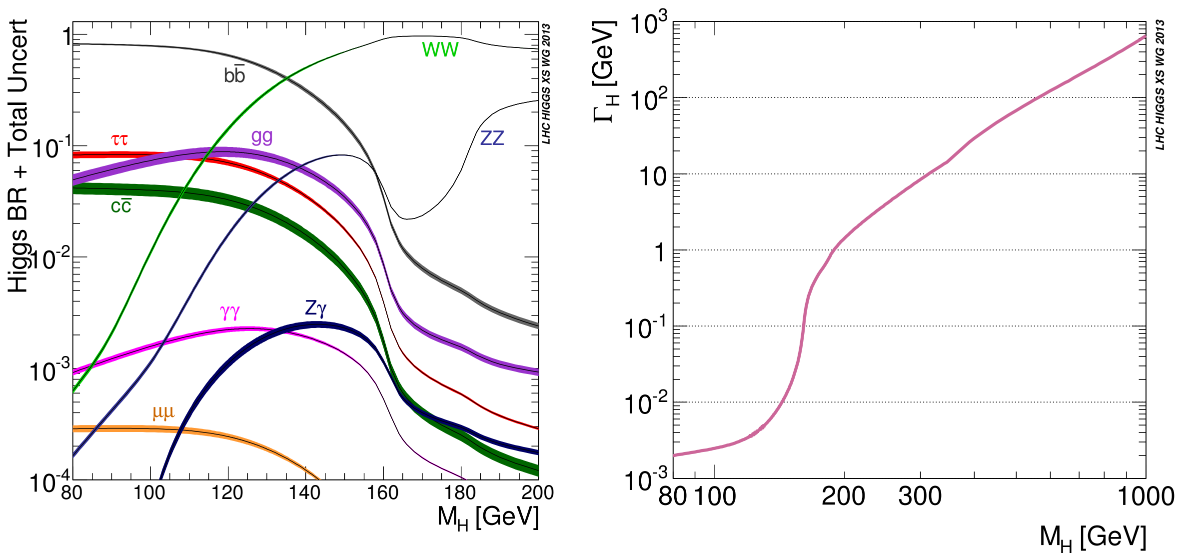

(a) (b)

Figure 2.5: (a), Higgs boson branching ratios as a function of m_H. The WW branching ratio at $m_H = 125\,\text{GeV}$ is 22 % [31]. (b) Higgs boson total width as a function of m_H [31]. The expected Higgs boson width at $m_H = 125\,\text{GeV}$ is 4.07 MeV [32].

of 22 %. The decay to two photons is 0.2 % and to two Z bosons is 3 % of the total decays. The total decay width of the Higgs boson is expected to be small, $\Gamma_H = 4\,\text{MeV}$, well below experimental energy resolution. Figure 2.5(b) shows the total width of the Higgs boson as a function of m_H. The width grows with mass, crossing $\mathcal{O}(1)$ GeV around $m_H = 200\,\text{GeV}$.

2.3 Quantum chromodynamics

Quantum Chromodynamics (QCD) is the theory describing the strong force, which acts on color-charged particles, mediated by gluons. Though it does not play a role in EWSB, it plays a large role in interactions at the LHC. The SM has a third symmetry, following the non-Abelian SU(3) group. For SU(3), there are eight generators and thus eight fields G^a_μ ($a = 1 \ldots 8$) needed, representing eight spin-1 massless gluons. QCD describes the behavior of gluons and their interaction with quarks, which are triplets under SU(3). Quarks do not exist by themselves; when produced, they quickly hadronize into colorless mesons and baryons due to so-called color confinement.

An additional piece is added to the covariant derivative, acting on quark fields, to preserve gauge symmetry:

$$D_\mu = \partial_\mu - ig_3 \frac{1}{2}\vec{\lambda} \cdot \vec{G}_\mu \,. \tag{2.28}$$

With this we can write a Lagrangian for quarks and gluons,

$$\mathcal{L}_{\text{QCD}} = \sum_q^{u,d,s,c,t,b} \overline{\Psi}_q (i\gamma^\mu D_\mu - m)\Psi_q - \frac{1}{4} G^a_{\mu\nu} G^{\mu\nu}_a \,, \tag{2.29}$$

where the field strength tensor $G^a_{\mu\nu} = \partial_\mu G^a_\nu - \partial_\nu G^a_\mu + g_3 f^{abc} G^b_\mu G^c_\nu$, g_3 is the strong coupling, and f^{abc} is the structure constant for SU(3) in $[\lambda^a, \lambda^b] = i f^{abc} \lambda^c$. Plugging in the covariant derivative, the interaction term with quarks is [6]:

$$\mathcal{L} = \frac{g_3}{2} \sum_q^{u,d,s,c,t,b} \bar{q}_\alpha \gamma^\mu \lambda^a_{\alpha\beta} q_\beta G^a_\mu \,, \tag{2.30}$$

where α and β are the color indices $1, 2, 3$. Similar to the case of the electroweak bosons, the non-commuting of the SU(3) algebra generates self interaction terms for gluons (three- and four-point interactions) [5].

The interactions of protons are modeled in terms of partons, the gluons and quarks of which they are comprised. Cross sections of processes depend on the parton distribution functions (PDFs), which give the probability to find a parton of a particular flavor with x

fraction of the proton's momentum at some energy scale Q of the hard interaction. Figure 2.6 shows example PDFs at two energy scales. The valence quarks, up and down, carry most of the momentum, with the up-quark fraction roughly twice that of the down-quark since there are two up-quarks and one down-quark in a proton. At higher energy scales, the sea quarks and gluons carry more of the proton's momentum; thus, for higher energy collisions, processes initiated with gluons or sea quarks become more prominent.

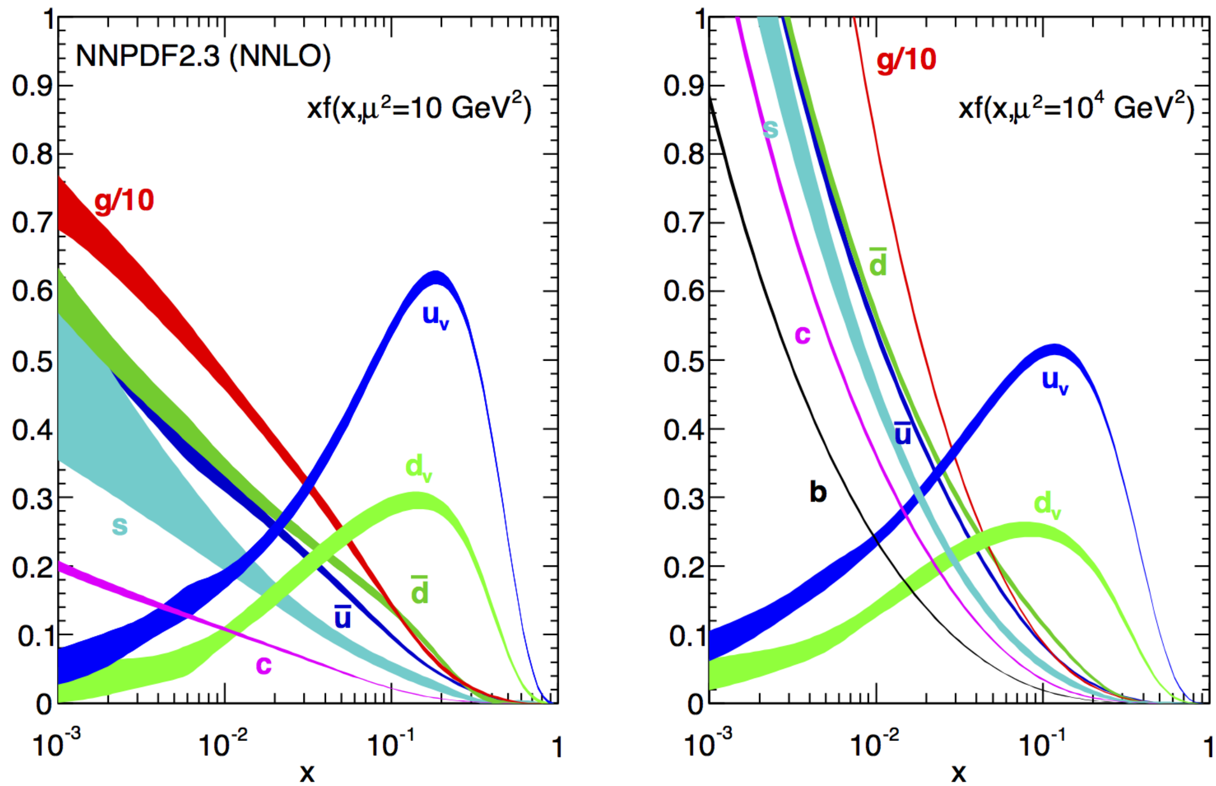

Figure 2.6: Fraction of energy x carried by the parton times the parton distribution function $f(x, \mu^2)$ for protons at scales $\mu^2 = 10\,\text{GeV}^2$ and $10^4\,\text{GeV}^2$ [33].

CHAPTER III

The Large Hadron Collider and ATLAS Experiment

This chapter gives a brief overview of the LHC and CERN (the European Organization for Nuclear Research, formerly Conseil Européen pour la Recherche Nucléaire) complex in Section 3.1 and ATLAS detector in Section 3.2. More detailed information on the LHC can be found in the conceptual design, an overview, and the initial commissioning [34–36] and in an overview and technical design reports [37–39] for the ATLAS detector. In brief, the LHC collides protons which can produce a Higgs boson and these events are recorded by the ATLAS detector.

3.1 The Large Hadron Collider

The LHC is a 26.7 km superconducting, circular particle accelerator and collider hosted by CERN, the European Organization for Nuclear Research, sitting approximately 100 m under the Franco-Swiss border near Geneva, Switzerland. It resides in the tunnel originally built for the Large Electron–Positron Collider (LEP) [40] in the mid 1980s. The LHC is a machine which first accelerates bunches of protons and then steers them to collide head on; the results of which are recorded by large purpose-built detectors. Four main experiments lie at the LHC's interaction points (IPs): ALICE (A Large Ion Collider Experiment) [41], ATLAS [37], CMS [42], and LHCb (Large Hadron Collider beauty) [43]. ATLAS and CMS are two general purpose detectors intended to search for the Higgs boson and SUSY, ALICE focuses on lead-ion collisions and quark-gluon plasma, and LHCb specializes in measurements involving b-hadrons. Three additional experiments have been added since the initial conception: TOTEM (TOTal Elastic and diffractive cross section Measurement) a forward detector near the CMS detector measuring the total pp cross section [44], MoEDAL (Monopole and Exotics Detector At the LHC) in the LHCb cavern [45], and LHCf (Large Hadron Collider forward) sitting 140 m down the beamline on either side of ATLAS intended to measure very forward photons and neutral pions [46].

The possibility of a hadron collider in the LEP tunnel was first officially recognized in a workshop held by CERN and organized by the European Committee for Future Accelerators (ECFA) in 1984 [47]. The project was approved by the CERN Council in December, 1994 and construction was approved two years later [48]. ATLAS and CMS were formally approved in January, 1997. Many years later, proton beams first circulated the LHC on September 10th, 2008. Nine days later, a faulty electrical interconnect between two magnets caused the magnets to quench, become non-superconducting, and release a large amount of helium into the tunnel; the force of which damaged several magnets, with about 50 segments needing to be moved from the tunnel for repairs or cleaning [49]. After repairs, proton beams again circulated the LHC in late 2009. Data taking started in earnest in 2011 with a 7 TeV center-of-mass energy, quickly surpassing the 45 pb^{-1} of pp collision data collected in 2010 at the same energy. It continued in 2012 at 8 TeV, reaching a peak instantaneous luminosity of $0.7 \times 10^{34}\,\mathrm{cm}^{-2}\,\mathrm{s}^{-1}$, approaching the design goal of of $10^{34}\,\mathrm{cm}^{-2}\,\mathrm{s}^{-1}$, see Table 3.1. Interspersed were runs with lead-ions. A two year shutdown, long shutdown 1 (LS1), beginning in 2013 allowed for repairs and upgrades to the LHC and detectors around its ring. In particular, many interconnects were redone such that the center-of-mass energy could be raised closer to the designed energy of 14 TeV. Data taking is planned to resume in the summer of 2015 at 13 TeV.

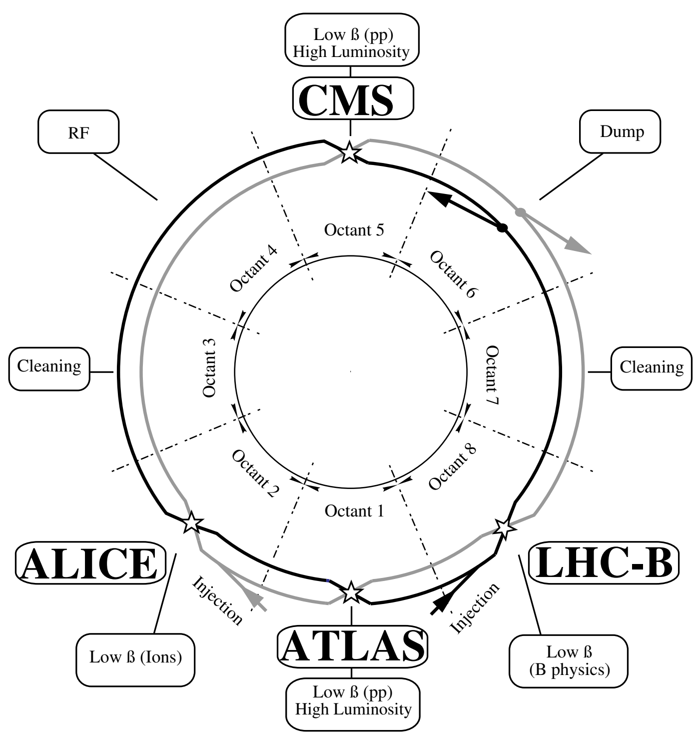

Figure 3.1: The octants and interaction points (stars) of the LHC ring [34].

The LHC is primarily a proton-proton (pp) collider, thus needing two magnetic field directions to guide the two proton beams in opposite directions. It uses two beam pipes to contain the counter-rotating beams. Particle-anti-particle colliders, such as the Tevatron can use one beam pipe. The LHC is not a perfect circle; it has eight straight sections approximately 528 m long, four of which have beam crossings to provide collisions for the main experiments, see Fig. 3.1. A total of 1232 dipole magnets are used to guide the beams around the arc, reaching a peak magnetic field of 8.33 T required for running at 7 TeV per beam. In order to reach such a high field, as compared to the roughly 5 T at the Tevatron with magnets cooled to 4.2 K, the LHC magnet's NbTi cables need to be cooled to 2 K, made possible with superfluid helium. At 8.33 T, the LHC's dipole magnets have a bending radius of 2804 m, which can be obtained from a simple calculation using the Lorentz force law,

$$F = q(v \times B) = \frac{mv^2}{r} \to r = \frac{p}{qB} = \frac{7\,[\mathrm{TeV/c}]}{1.6 \times 10^{-19}\,[\mathrm{C}] \cdot 8.33\,[\mathrm{T}]} = 2803\,\mathrm{m}\,. \tag{3.1}$$

The dipole magnets are 16.5 m long and 0.57 m in diameter, weighing 27.5 t. In order to accommodate the bending path of the particles, the dipole magnet cold mass is curved with an apical angle of 5.1 µrad, which corresponds to a bending radius of 2812 m at room temperature. About 858 quadrupole magnets are used to focus the beams, keeping them within the apertures of the LHC and squeezing the beams for collisions.

A long chain of accelerators, see Fig. 3.2, prepares protons for injection into the LHC. Protons are obtained by stripping hydrogen atoms of electrons and then accelerated to 50 MeV by the Linac2. The Proton Synchrotron Booster (PSB) then accelerates the protons to 1.4 GeV for the Proton Synchrotron which accelerates the protons to 25 GeV, injecting them into the Super Proton Synchrotron (SPS). Finally, the SPS accelerates the protons to 450 GeV for injection into the LHC.

The LHC uses a 400 MHz RF system to accelerate the protons to their final TeV scale energy. Eight cavities per beam accelerate the protons with a 5.5 MV m^{-1} field. In order to constantly accelerate the protons, the RF frequency must be a multiple of the revolution frequency of the protons. The LHC is designed to operate up to a harmonic number of $h = f_{\mathrm{RF}}/f_r = 35640$. The intended design has a total of 2808 proton bunches in 'buckets' around the ring. A small gap in the proton beam is left such that the beam dump magnets have time to ramp up to full field strength, a couple beam revolutions, so that a partial field strength does not guide the beam across sensitive equipment.

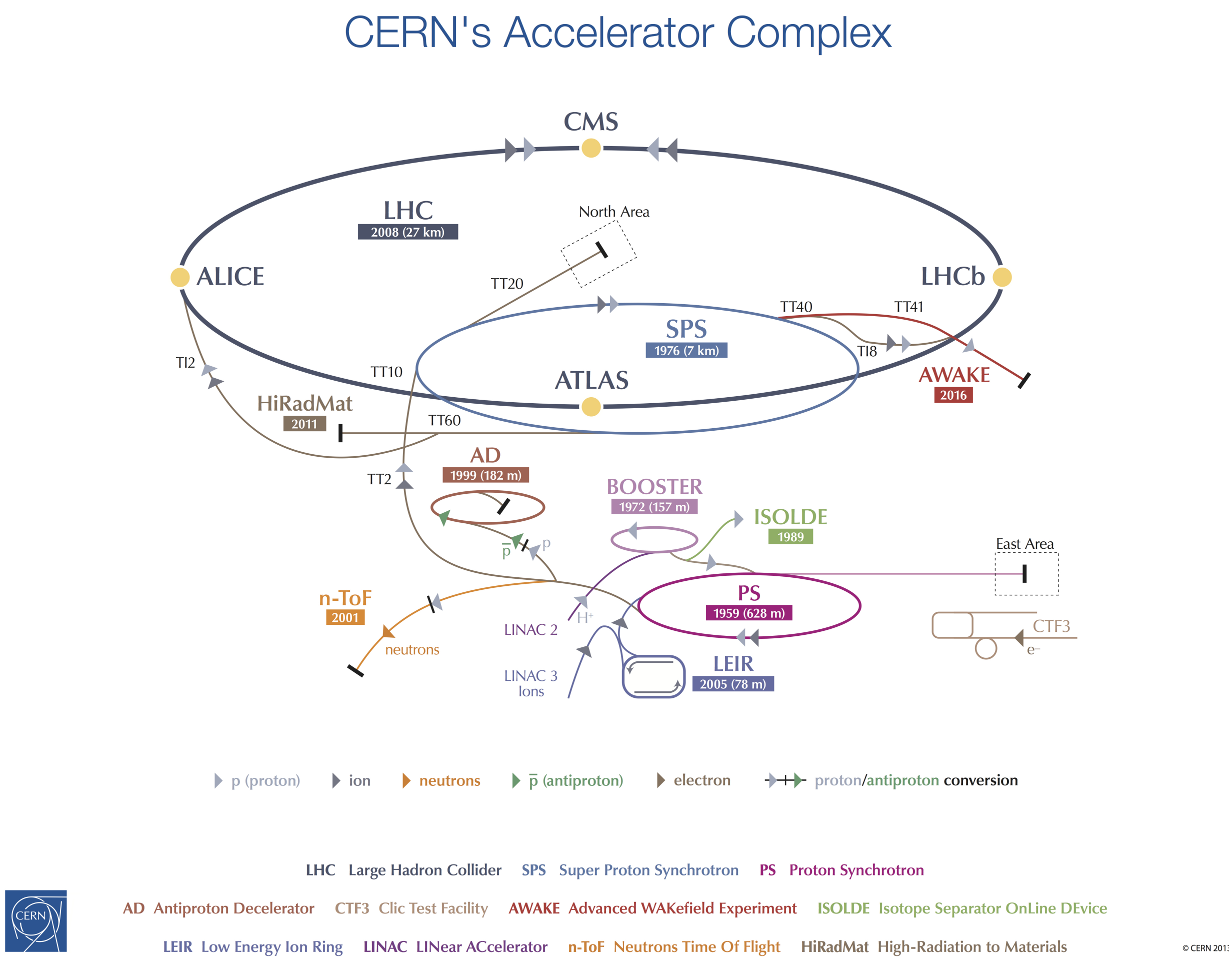

Figure 3.2: The CERN accelerator complex as of 2013 [50].

3.2 The ATLAS detector

The ATLAS detector [37, 56] is a general purpose particle detector with a nearly 4π coverage in solid angle around the beam IP. It stands 25 m in diameter and 44 m in length, weighing approximately 7000 t—if sealed, ATLAS would float in water. The detector is composed of several subsystems in layers around the beam line. The inner detector (ID) [57, 58], described in Section 3.2.1, is made up of a silicon tracker and transition radiation tracker (TRT) and is immersed in 2 T magnetic field produced by a superconducting solenoid, which is needed to measure the momentum of charged particles. Surrounding the ID are the electromagnetic and hadronic calorimeters, see Section 3.2.2. The outermost, and most visible, detector sub-system is the muon spectrometer (MS), see Section 3.2.3, interspersed with superconducting air-core toroid magnets, see Section 3.2.4. Table 3.2 lists general ATLAS

Parameter	2011	2012	Design	HL-LHC
Beam Energy [TeV]	3.5	4	7	7
Max Number of Bunches colliding	1854	1380	2808	2736
Bunch Intensity [10^{11}]	1.5	1.48	1.15	2.2
Bunch Spacing [ns]	50	50	25	25
Peak Inst. Lumi. [$10^{33}\,\mathrm{cm}^{-2}\,\mathrm{s}^{-1}$]	3.65	7.73	10	50 (72†)
Avg. Inelastic Interactions per crossing $\langle\mu\rangle$	9.1	20.7	19	138 (198†)
Peak Inelastic Interactions per crossing	34	72		
Trans. Norm. Emittance [µm]	1.9-2.3	2.6	3.75	2.5
Longitudinal Emittance [eV s]			2.5	2.5
β^* [m]	1	0.60	0.55	0.15
IP Beam Spot [µm]	~ 25	19	16.7	
Beam Current [A]	0.38	0.41	0.582	1.09
RMS Bunch Length [cm]		≥ 9	7.55	7.55
Crossing Angle [µrad]	240	290	285	590

Table 3.1: LHC parameters for the 2011 [51] and 2012 data taking runs (also taken from the ATLAS data summary [52]). The machine parameters quoted are generally at their peak; the conditions, especially in 2011, ramped up over the year [53, 54]. These are compared with the designed parameters [35] and those of the proposed High Luminosity LHC (HL-LHC) [55]. The parameters of the HL-LHC are not final; those quoted here are considered for the 25 ns bunch spacing using crab-cavities and luminosity leveling († w/o the aforementioned).

detector resolution performance goals. Test beam, cosmic ray, and LHC collision data show that the detector is performing close to its goals [59–66].

ATLAS uses a right-handed coordinate system centered on the nominal IP with the z-axis along the beamline, y-axis vertical, and x-axis pointing toward the center of the LHC, see Fig. 3.4 for an illustration. The half of the detector on the positive z-axis is referred to as the "A-side", the other the "C-side". Polar coordinates are often used to describe events. The azimuthal angle ϕ is measured from the x-axis around the beamline. The polar angle θ is defined from the positive z-axis toward the y-axis. Instead of using θ, rapidity is used, defined as

$$y = \ln \sqrt{\frac{E + p_z}{E - p_z}}\,. \tag{3.2}$$

It is preferred over θ as differences in rapidity are invariant under boosts along the beamline. However, for highly relativistic particles, the difference between $E \sim p$ is hard to measure. Pseudorapidity, which is equivalent to rapidity in the highly relativistic limit, uses the polar angle and is defined as

$$\eta = -\ln\tan(\theta/2)\,, \tag{3.3}$$

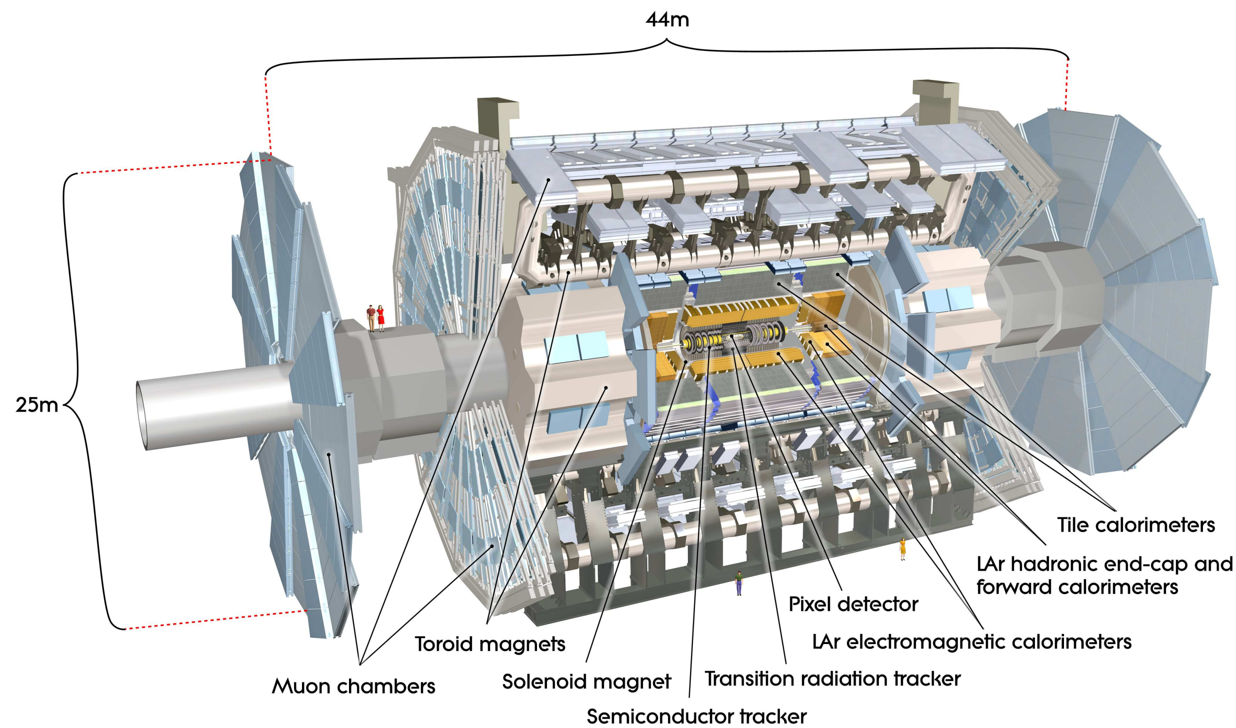

Figure 3.3: The ATLAS Detector [37].

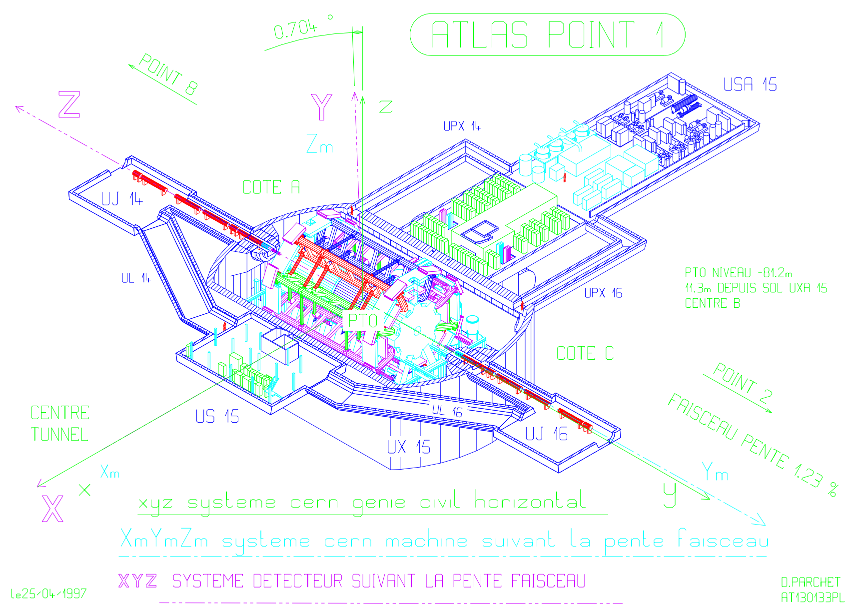

Figure 3.4: Technical drawing with the ATLAS cavern and coordinate system [67]. The coordinate system in purple corresponds to that used by the detector. Also written is "FAISCEUR PENTE" (beam slope).

which goes from zero at the x–y plane to plus or minus infinity along the beamline. Distances ΔR in η–ϕ space are defined as $\Delta R = \sqrt{\Delta\eta^2 + \Delta\phi^2}$.

Quantities, such as momentum, are often measured in the transverse x–y plane and denoted with a subscript 'T'. A common example is the transverse momentum, p_{T}, of a particle since we can make use of conservation of momentum, knowing that the initial total transverse momentum is zero.

Detector component	**Required resolution**	**$\lvert\eta\rvert$ coverage** Measurement	Trigger
Tracking	$\sigma_{p_{\mathrm{T}}}/p_{\mathrm{T}} = 0.05\,\%\ p_{\mathrm{T}} \oplus 1\,\%$	2.5	†
EM calorimetry	$\sigma_E/E = 10\,\%/\sqrt{E} \oplus 0.7\,\%$	3.2	2.5
Hadronic calorimetry (jets)			
barrel and end-cap	$\sigma_E/E = 50\,\%/\sqrt{E} \oplus 3\,\%$	3.2	3.2
forward	$\sigma_E/E = 100\,\%/\sqrt{E} \oplus 10\,\%$	3.1-4.9	3.1-4.9
Muon spectrometer	$\sigma_{p_{\mathrm{T}}}/p_{\mathrm{T}} = 10\,\%$ at $p_{\mathrm{T}} = 1\,\mathrm{TeV}$	2.7	2.4

Table 3.2: ATLAS detector general performance goals [37]. †The Fast TracKer (FTK) upgrade [68] provides hardware based tracking, expected to be operational in 2015, allowing track based triggering. Energy and momentum units are in GeV.

3.2.1 The inner detector

The ATLAS tracking volume, or ID, is composed of three sub-detectors: the pixel detector [70, 71], silicon microstrip tracker (SCT) [72–74], and TRT [75, 76], layered as shown in Fig. 3.5, arranged in a cylinder of radius 1.15 m and 7 m long around the z-axis, centered on the IP. The ID provides high-resolution tracking and vertexing of charged particles emerging from the IP out to $|\eta| < 2.5$, as well as enhanced electron identification for $|\eta| < 2$ from the TRT. It is immersed in a 2 T solenoidal field along the z-axis. These capabilities allow for heavy-flavor quark and τ-lepton tagging (e.g., via displaced vertices) and impact parameter measurements. The ID has a nominal lower p_{T} reconstruction threshold of of 0.5 GeV.

The pixel detector provides the highest spatial resolution, close to the beam-line. The main goal of the pixel detector is the accurate reconstruction of the primary vertex (PV) and any displaced vertices. Three layers in cylinders (disks in the forward region) have a resolution of 10 µm in $(R - \phi)$, the transverse direction, and 115 µm along z or R. The barrel layers lie at a radius of 50.5, 88.5, and 122.5 mm and the end-cap disks lie at a z of 495, 580, and 650 mm. Each pixel measures $50 \times 400\,\mu\mathrm{m}^2$ resulting in roughly 80 million readout channels.

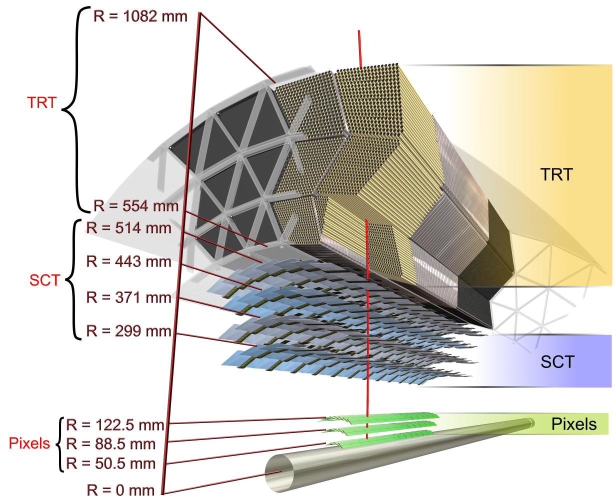

Figure 3.5: ATLAS barrel tracking volume, part of the inner detector (ID), with a 10 GeV charged particle track in red [69].

The second shell of ATLAS is the SCT, made up of silicon strips with a 40 µrad stereo angle. This arrangement provides a lower priced solution than pixels for a high resolution in the transverse plane, 17 µm in $(R - \phi)$, at the cost of a worse resolution along z (R), 580 µm, in the barrel (end-cap disks). The barrel portion is arranged in a cylindrical geometry with four double-layers at a radius of 299, 371, 443, and 514 mm using roughly 6×6 cm sensors with an 80 µm pitch. The SCT disks are placed along the z-axis in nine double-layers from ± 853.8 to ± 2720.2 mm. Both the pixel and SCT are operated between -5 and $-10\,^{\circ}$C in order to reduce noise

The TRT is a straw tube tracker sitting outside of the SCT from $R = 563$ to 1066 mm in the barrel. The detector provides an average of 36 hits per track at a large radius and measures transition radiation of energetic charged particles to help discriminate between electrons and charged pions. The straws are 144 cm long in the barrel and 37 cm long in the end-caps with a 32 µm gold plated tungsten wire. They are filled with a gas mixture composed of 70 % Xe, 27 % CO_2, and 3 % O_2. With this mixture, transition radiation yields larger signal amplitudes than minimally ionizing particles (MIPs), allowing for discrimination. The straws have an $R - \phi$ resolution of 130 µm.

3.2.2 Calorimeters

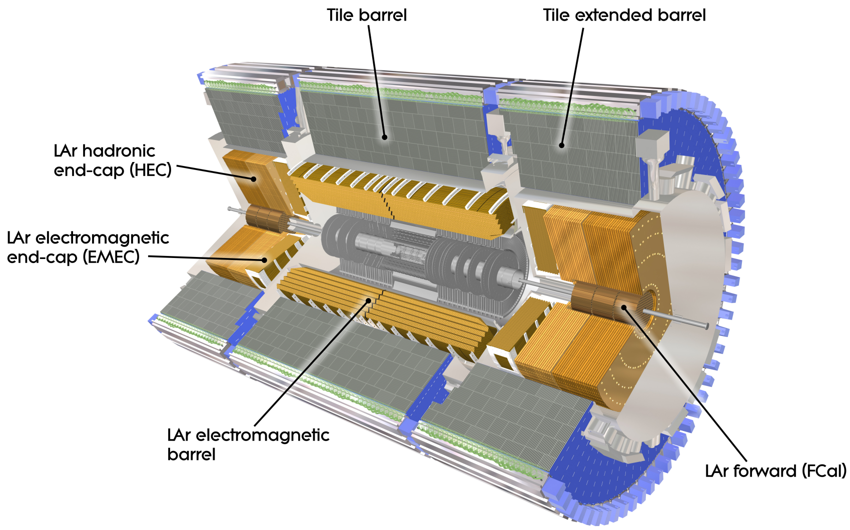

Figure 3.6: ATLAS calorimeters [77].

The ATLAS detector makes use of sampling calorimeters (alternating layers of dead and active material) [78] to measure the energy of particles produced in collisions out to $|\eta| < 4.9$. They play an important role in the measurement of jets and missing transverse momentum (MET). The inner layer, around the ID, is the liquid argon (LAr) EM calorimeter [79, 80] designed to measure the energy of charged particles and photons. Around this, the hadronic tile calorimeter [81] measures the energy of hadrons which tend to pass through the EM calorimeter.

The EM calorimeter uses steel-clad lead plates as absorbers and LAr as a measurement medium in an accordion geometry to provide ϕ symmetry and full azimuthal coverage. Liquid argon was chosen for its radiation hardness and fast response. The LAr EM calorimeter has 3 active layers in the barrel ($0 < |\eta| < 2.5$) and two in the more forward region ($2.5 < |\eta| < 3.2$), the electromagnetic end-cap (EMEC) calorimeter. Fine segmentation of the first layer in the η direction allows for position measurement and photon pointing, when combined with the second layer. The central region ($0 < |\eta| < 1.8$) is augmented by an active LAr presampler which measures energy lost by particles before reaching the calorimeters. The very forward region is covered by the forward calorimeter (FCal) from ($3.1 < |\eta| < 4.9$), sitting approximately ± 4.7 m from the IP, which uses LAr as the active medium and copper as the absorbing medium for the EM module, FCal1.

The hadronic tile calorimeter surrounds the EM calorimeter and is designed to measure the energy of hadrons which make it through the ID and EM calorimeter. Steel plates are

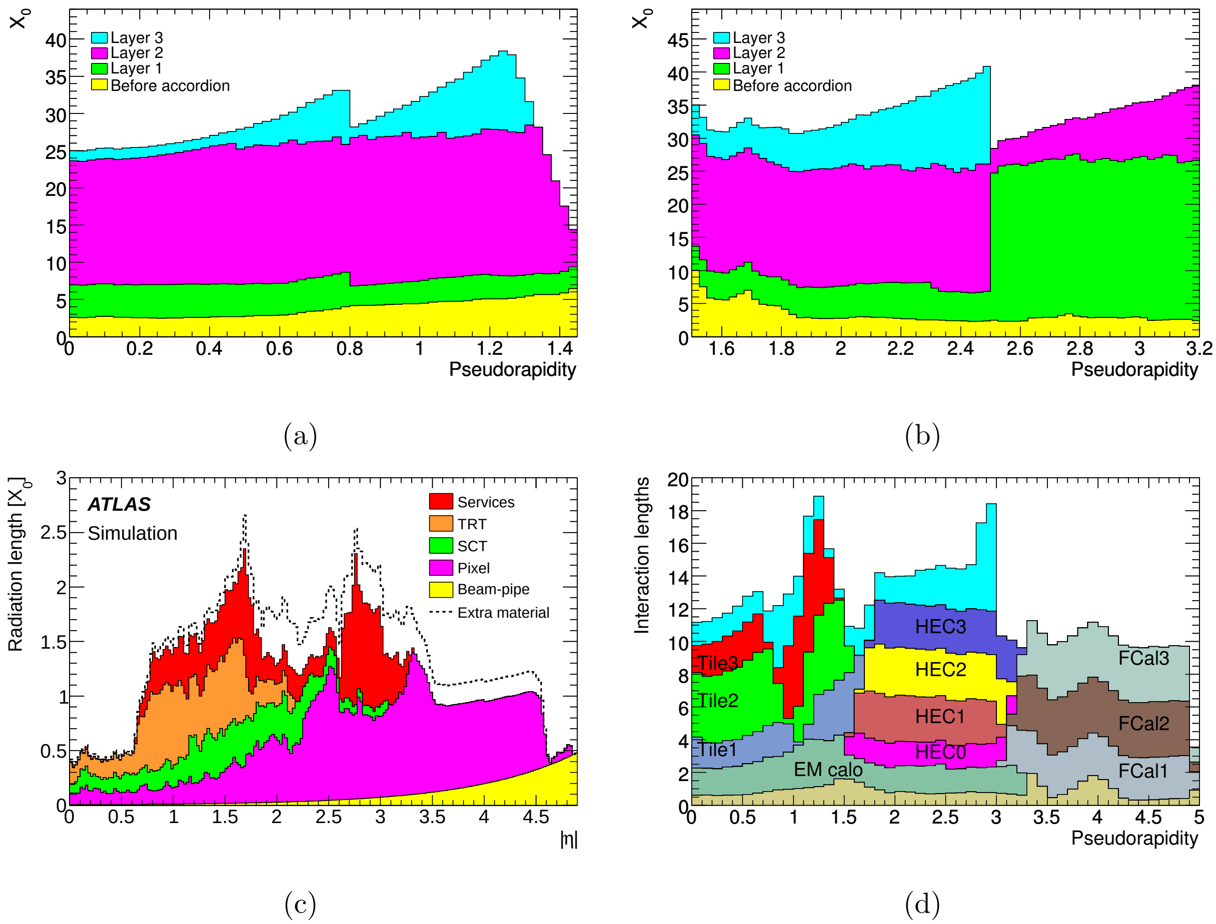

Figure 3.7: (a) and (b), radiation length (X_0) of material before the electromagnetic calorimeter (yellow) and for the three layers [37]. (c), radiation length of material in the ID [82]. (d), interaction length (λ) of material in front of the electromagnetic calorimeters (tan), the various calorimeters, and first active layer of the MS (cyan) [37].

used as the absorber material and scintillating plates with wavelength shifting fibers as the active sampling material. Three radial layers allow for three dimensional segmentation. The tile calorimeter extends from 2280 to 4230 mm radially and is composed of a 5640 mm long central barrel and two 2910 mm barrel extensions on either side. This corresponds to a coverage of $|\eta| < 1.7$. The hadronic end-cap calorimeter (HEC) is a LAr–copper sampling calorimeter and covers the region $1.5 < |\eta| < 3.2$. It consists of two wheels on either end-cap with outer radius 2030 mm. The very forward region is covered by the two hadronic modules of the FCal, FCal2 and FCal3, which use LAr as the active medium and tungsten as the absorbing medium.

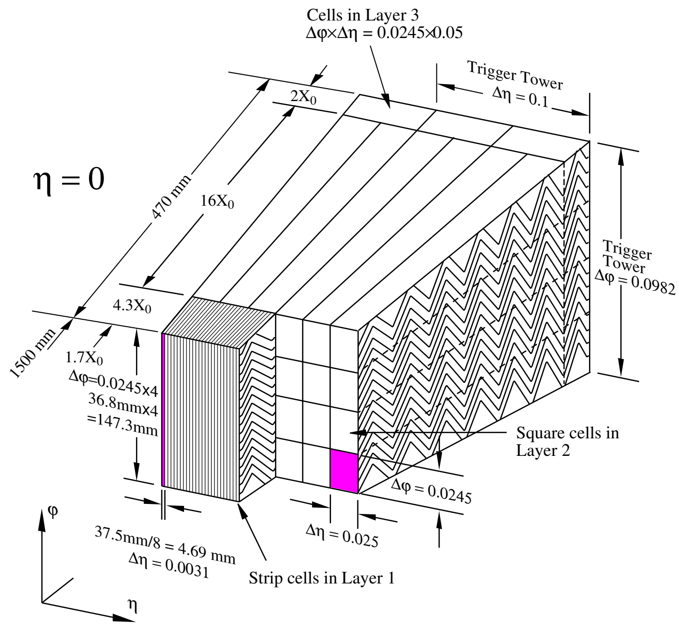

Figure 3.8: Electromagnetic calorimeter barrel module showing the three radial layers and granularity in η and ϕ [37].

3.2.3 The muon spectrometer

The MS [83] is ATLAS's outermost detector, surrounding the calorimeters. Information on its performance from commissioning with cosmic rays can be found in [84]. The MS makes use of several technologies to track high momentum muons. It has three cylindrical layers at approximate radii of 5, 7.5, and 10 m in the barrel and three main disks plus an extension at $|z| \approx 7.4$, 10.8, 14, and 21.5 m in the end-caps, shown in Fig. 3.9. This corresponds to a coverage of $|\eta| < 2.7$ with triggering within $|\eta| < 2.4$. In the barrel region, $|\eta| < 1$, muon tracks are bent by the large, eight coil, toroidal magnet. For $1.4 < |\eta| < 2.7$, the magnetic field is produced by smaller end-cap magnets inserted into both ends of the barrel toroid. Muon tracks in the transition region, $1 < |\eta| < 1.4$, are bent by a combination of both magnets. Figure 3.10 displays the bending power of the magnetic field around the muon chambers.

The very central region, $\eta \sim 0$, has poor acceptance due to partial coverage to allow for ID services. In the positive η end-cap, for $1.1 < \eta < 1.3$, there are regions in ϕ where muons will pass only one layer due to missing chambers. These chambers were installed during the LS1 [85].

Most of the range in pseudorapidity is covered by monitored drift tubes (MDTs), which provide precision position measurements at an average resolution of 80 µm per tube. In the forward regions, cathode-strip chambers (CSCs) are used to handle the high flux. A

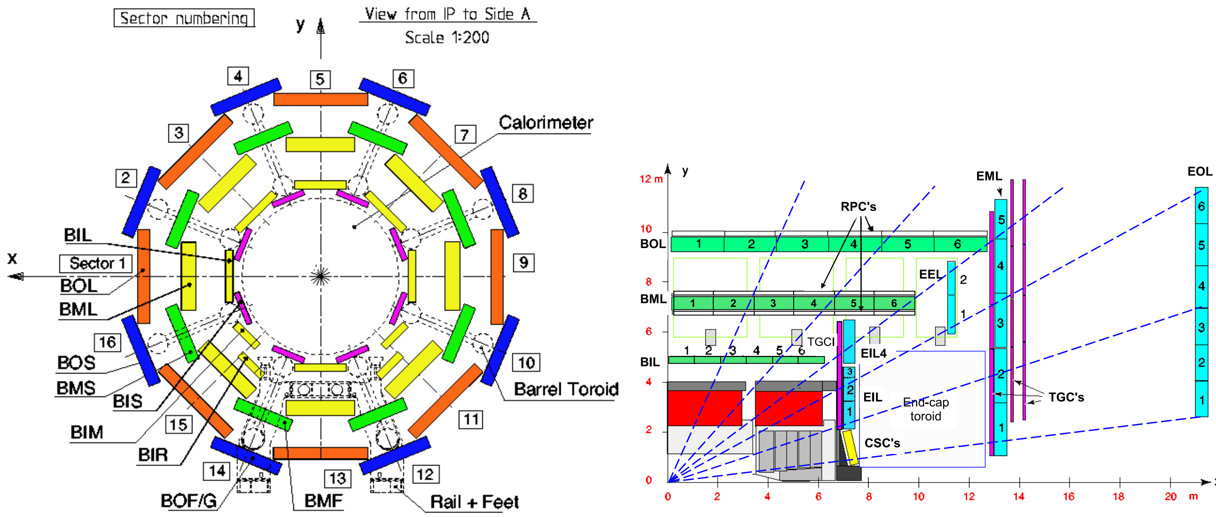

(a)

(b)

Figure 3.9: The ATLAS muon spectrometer. (a), cross section of the barrel. (b), a cross section in the y–z plane including the end-cap [37].

chamber provides a resolution in the bending plane of 40 µm and measurement of an additional coordinate with 5 mm resolution in the transverse plane. Faster responding resistive plate chambers (RPCs), in the barrel, and thin gap chambers (TGCs), in the end-caps, are used for triggering.

The MDT tubes are 3 cm in diameter and 0.7 to 6.3 m in length. A 50 µm tungsten-rhenium wire runs down the center of the tubes, which are filled with a 93 % Ar and 7 % CH_4 gas mixture. The CSCs are multiwire proportional chambers using 30 µm W-Re wires with a 80 % Ar and 20 % CO_2 gas mixture. RPCs are made with a 2 mm gap filled with 94.7 % $C_2H_2F_4$, 5 % C_4H_{10}, and 0.3 % SF_6 gas between resistive Bakelite plates, with read out via capacitive strips. The other trigger chambers, TGCs, are similar to multiwire proportional chambers, except that the anode wire pitch is larger than the cathode-to-anode separation. The TGCs are filled with a 55 % CO_2 and 45 % n-C_5H_{12} gas mixture. Gas mixtures were chosen based on performance needs and aging properties; more details can be found in Ref. [37].

3.2.4 The magnet system

A magnetic field is needed to measure the momentum of charged particles, which is done by measuring how much the path of the particle changes in a known magnetic field. Usually it is assumed that the particle has charge $\pm|e|$, with the sign determined from the direction of the bending. The ATLAS magnetic system is made up of four superconducting magnets: the barrel solenoid [86], barrel toroid [87], and two end-cap toroids [88] seen in Fig. 3.3. The solenoid, sitting inside of the EM calorimeter, provides a 2 T field along the z-axis for for the inner detector. It contributes about 0.66 radiation lengths of material at $\eta = 0$ before the calorimeters and is cooled to 4.5 K for operation. The toroid magnets produce approximately 0.5 and 1 T fields in the barrel and end-caps respectively. The eight loops for the barrel toroid span from 9.4 to 20.1 m radially and 25.3 m along the axis. The two end-cap toroids span from 1.65 to 10.7 m radially and 5 m along the axis. The bending power of the toroidal magnets in the MS is shown in Fig. 3.10.

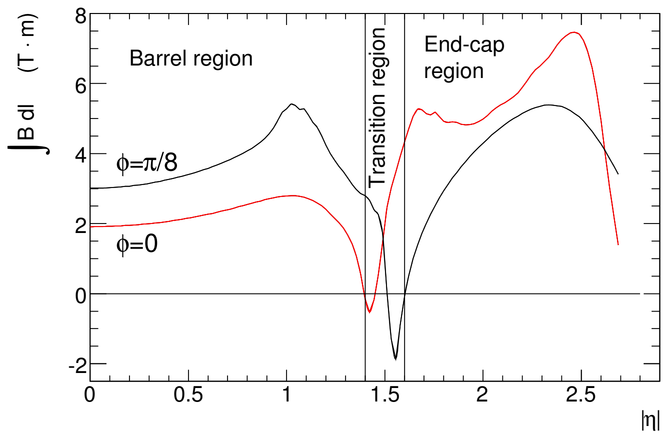

Figure 3.10: Toroidal magnet bending power of the azimuthal field component, integrated between the innermost and outermost muon chambers [56].

3.3 The dataset

The analyses in Chapters V and VI make use of data collected during the 2011 and 2012 LHC runs, collectively referred to as Run I. ATLAS recorded a total integrated luminosity of 5.2 fb^{-1} at 7 TeV in 2011 and 21.7 fb^{-1} at 8 TeV in 2012, see Fig. 3.11(a).

In terms of accelerator parameters, the instantaneous luminosity can be written as ([53, 89] for more details)

$$\mathcal{L} = \frac{\gamma \beta_{\text{rel}} f_r n_1 n_2 N_1 N_2 S}{4\pi \sqrt{\epsilon_x^N \beta_x^* \epsilon_y^N \beta_y^*}}\,, \tag{3.4}$$

where f_r is the revolution frequency, $n_{1/2}$ are the number of bunches in beam 1 and 2 respectively, $N_{1/2}$ are the number of protons per bunch, S is a reduction factor from the geometry of the crossing (e.g. non-zero angle), $\epsilon_{x/y}^N$ the transverse normalized emittance in the x and y direction (defined by the beam preparation), and $\beta_{x/y}^*$ are the value of the β-amplitude function at the interaction point (defined by the accelerator magnet setup and smaller the more squeezed the beam is). The β parameter is related to the emittance by

$\beta = \pi\sigma^2\gamma\beta_{\rm rel}/\epsilon^N$ where σ is the width of the beam, e.g. Gaussian width, and $\beta_{\rm rel}$ is the relativistic factor.

ATLAS monitors the luminosity by measuring the observed number of interactions per crossing, $\mu_{\rm vis}$, with a variety of detectors [90]. The instantaneous luminosity can be expressed as

$$\mathcal{L} = \frac{R_{\rm inel}}{\sigma_{\rm inel}} = \frac{\mu n_b f_r}{\sigma_{\rm inel}}\,, \tag{3.5}$$

where $R_{\rm inel}$ is the rate of inelastic collisions, $\sigma_{\rm inel}$ is the pp inelastic cross-section, μ is the average number of inelastic interactions per bunch crossing, n_b is the number of bunches colliding per revolution, and f_r is the revolution frequency. The luminosity can then be written with $\mu_{\rm vis}/\sigma_{\rm vis}$ replacing $\mu_{\rm inel}/\sigma_{\rm inel}$, where the visible quantities are related to the inelastic ones by an efficiency ϵ of the detector. The luminosity measurement is calibrated by dedicated van der Meer scans, where the two beams are set to cross with various known separations.

The integrated luminosity is simply the time integrated sum of the instantaneous luminosity,

$$L = \int \mathcal{L} dt\,, \tag{3.6}$$

and is a measurement of how much data is collected.

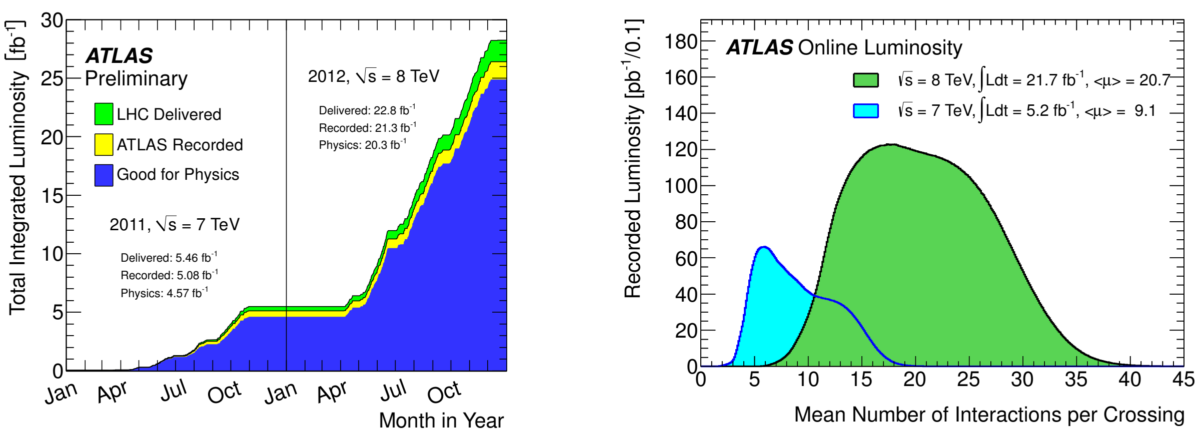

(a) (b)

Figure 3.11: Left, integrated luminosity of pp collisions as a function of time for the 2011 and 2012 data taking periods. The flat period in the middle corresponds to the winter shutdown and lead-ion runs [91]. Right, pile-up for the 2011 and 2012 data taking periods [92].

3.3.1 Pile-up

In order to achieve a sufficient luminosity, the LHC runs with successive bunches of protons. When proton bunches cross, multiple interactions may occur resulting in "in-time" event pile-up. While the rapid succession of bunches can result in remnants of previous interactions existing in the detector for the next crossings, "out-of-time" event pile-up. Seen in Fig. 3.11(b), the 7 TeV dataset has an average of 9 interactions per crossing and the 8 TeV dataset has an average of 21 interactions per crossing. Event pile-up can pose a challenge, effectively introducing noise, and must be taken into consideration when designing object reconstruction and event selection.

3.3.2 Trigger

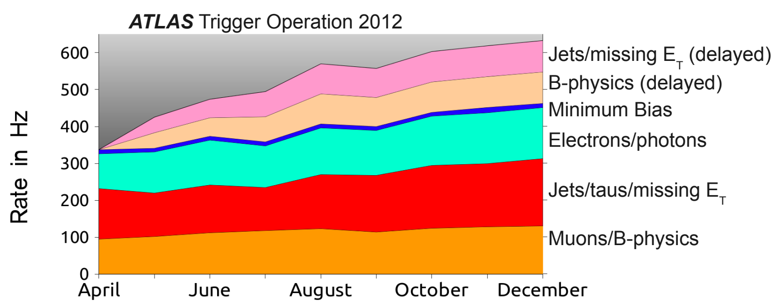

(a)

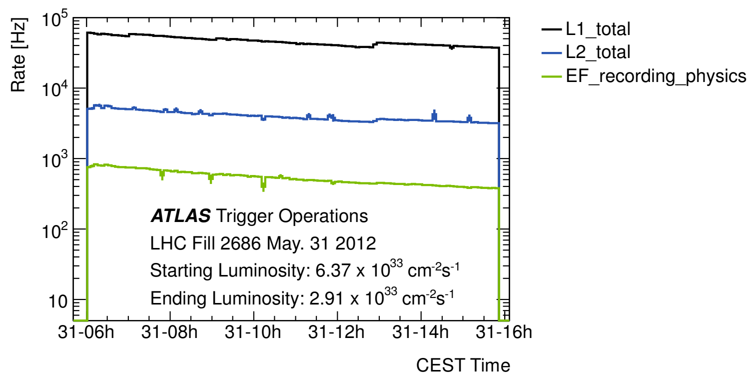

(b)

Figure 3.12: (a), event filter (EF) stream average rates for the 2012 data taking period. (b), example Level-1 (L1), Level-2 (L2), and event filter (EF) rates for an LHC fill from 2012. The EF rate includes the delayed streams [93].

Storing all of the collisions provided by the LHC at approximately 20 MHz for the 7 and 8 TeV data taking is impossible. A three level trigger system, L1 [94], L2, and EF [95], is used to successively reduce the data rate to a manageable level. The trigger is the first step of event selection and performs the crucial task of selecting interesting events out of many millions per second. Events rejected are lost forever. The L1 trigger is hardware based, searching for high transverse-momentum particles, events with large total transverse energy, and events with large MET. It makes decisions in less than 2.5 μs, reducing the rate to about 75 kHz. To do this, it makes use of the MS trigger chambers and the calorimeters, whose cells are grouped into larger trigger towers, as seen in Fig. 3.8. The L2 trigger uses the full granularity in regions of interest (RoI) defined by the L1 trigger. The L2 selection, using a computing farm, is designed to bring the triggered data rate down to about 3.5 kHz by making use of fast reconstructed objects, taking 40 ms per event on average. Finally, the EF implements further refined selections, similar to the offline event reconstruction, reducing the rate to about 200 Hz, at design, taking about 4 s per event. The L2 trigger and EF are collectively referred to as the high-level trigger (HLT). The output of the EF is categorized by the type of trigger into streams. The analyses described in this dissertation make use the Egamma and Muons streams. The EF trigger stream rates in 2012 are shown in Fig. 3.12, along with rates during an example LHC fill. Improvements in computing since the initial design allow for more bandwidth in triggered rates, roughly 6 kHz for the L2 trigger and 400 Hz for the EF, the final data-stream rate written to disk. An additional approximate 200 Hz is written as a delayed stream (reconstructed later) [96].

The triggers used for the analyses in this dissertation, described in Section 5.2.1, are found to be about 90 % efficient for electrons and 70 (90) % efficient for muons in the barrel (end-cap) for leptons satisfying the selection in Section 5.3.1. More details on the performance of the trigger system can be found in [97] for electrons in 2011, and in [98] for muons in 2012.

CHAPTER IV

Object and Event Reconstruction

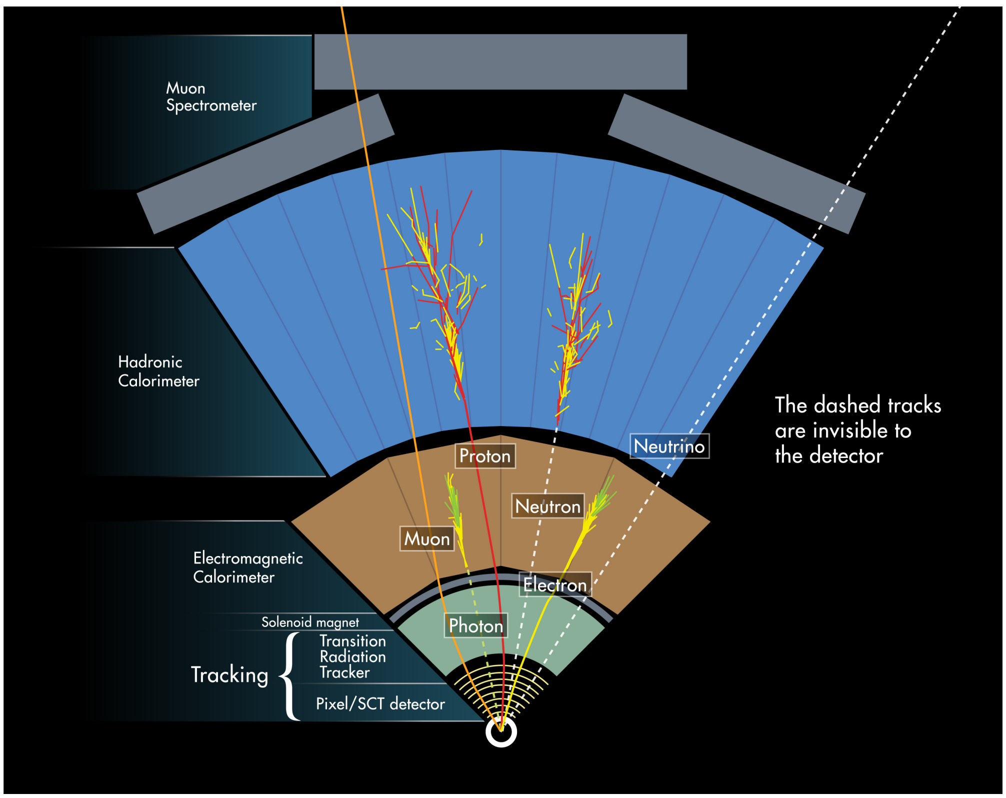

Figure 4.1: Schematics of how various particles are detected (or not in the case of neutrinos) in the ATLAS detector [99].

This chapter summarizes object reconstruction, identification, and performance in the ATLAS detector. The objects and quantities described are used in the analyses in the later chapters. Objects entering the detector, e.g., the electron shown in in Fig. 4.1, must be identified and their properties reconstructed starting with low-level electrical signals from the detector sub-systems. First, tracks from the ID and MS and clusters from the calorimeters are built, which can then be used to construct electron, muon, and jet candidates. Even after rigorous identification requirements, we can never truly say a particular object is what it is identified to be. There is always the possibility that it was misidentified. Only after summing over many objects or events, can we say that some fraction of the objects are real or fake within the uncertainties of the identification procedure. Details on the expected performance of the ATLAS detector can be found in Ref. [56].

An 'event' refers to a triggered bunch crossing and everything recorded about it by the detector. It makes up a basic discrete counting unit for referring to how many times a particular process is expected to occur. All of this, from the initial physics process, to detector response, and reconstruction, is simulated using Monte Carlo (MC), see Section 4.6. We use these simulated events to compare our predictions to the data.

4.1 Tracks and vertices

ATLAS measures charged particle tracks with $|\eta| < 2.5$ using the ID, see Section 3.2.1. The lower limit for tracks to pass through the entire ID is roughly 0.5 GeV. Tracks are defined by five parameters: q/p the charge-momentum ratio, d_0 and z_0 transverse and longitudinal impact parameters (distance to origin at closest approach in the R–ϕ and R–z planes respectively), and η and ϕ the angular coordinates for the direction emanating from the vertex. More details on ATLAS tracking can be found in Refs. [100–102].

Hits in the detector are first transformed into spacial coordinates (a barrel track typically has 3 pixel, 8 SCT, and 30 TRT hits). The 'inside-out' algorithm is designed for tracks emanating from the IP. Three hits from the silicon detectors are used to form a track seed. Seeds are used to search with a Kalman filter for further hits to complete the track. Many track candidates are formed and ambiguities are resolved by taking into account holes (missing expected hits) and the χ^2 of the fits. Tracks are then extended into the TRT. Final tracks come from a fit using all three ID sub-systems. The efficiency of track reconstruction as a function of p_{T} and η in 8 TeV minimum bias simulation is showing in Fig. 4.2.

An 'outside-in' algorithm starts with TRT segments and works inward adding silicon hits. This strategy is used to reconstruct tracks from secondary interactions coming from conversions or long-lived particles.

Tracks are used to find vertices, the IPs, by following the tracks back to a convergence. Pile-up and secondary interactions can result in multiple vertices. An iterative algorithm [104] is used to reconstruct vertices by first considering tracks close to the luminous region, as well as tracks close to the global maximum of the z_0 distribution, to form a vertex seed. Tracks not associated to a vertex are used to seed new vertices until no unassociated tracks

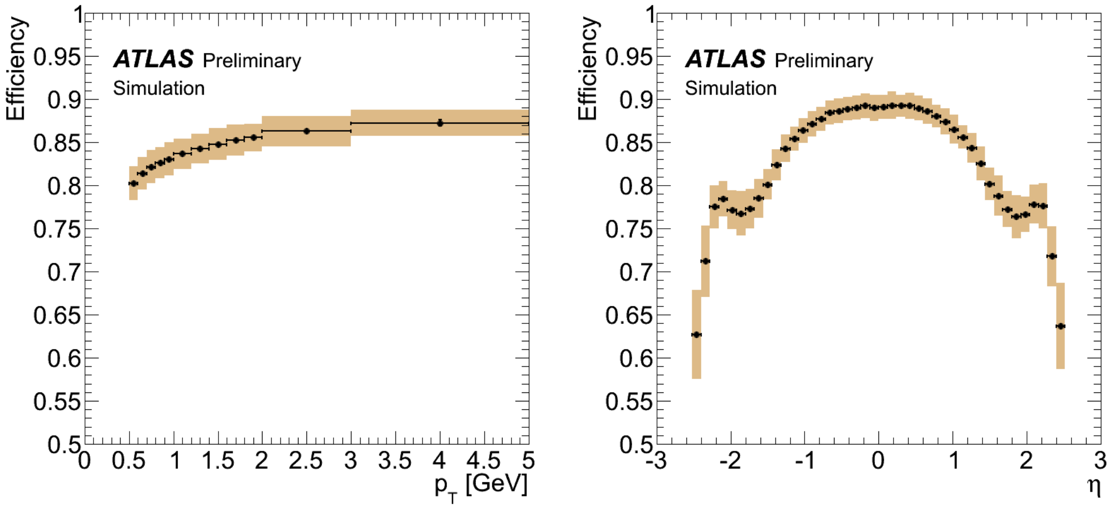

(a) (b)

Figure 4.2: Track reconstruction efficiency as a function of (a) p_{T} and (b) η in no pile-up, minimum bias, 8 TeV simulation [103].

remain. Once vertices are found, a second fitting-algorithm reconstructs the position of the vertices, included adjusting the origin of associated tracks. If multiple vertices are found, the one with the largest $\sum p_{\mathrm{T}}^2$ of associated tracks is considered as the primary vertex (PV), the most interesting interaction. Beam-spot information is used for both finding and fitting vertices. The number of reconstructed vertices as a function of the pile-up and the vertex position resolution are shown in Fig. 4.3.

4.2 Electrons

Electrons are one of the fundamental final-state objects used in physics analyses. An electron candidate is composed of an ID track matched to an EM calorimeter cluster (energy deposit).

ATLAS can identify electrons out to $|\eta| < 4.9$; however, the analyses in this dissertation use central electrons ($|\eta| < 2.47$), which are more robust. Unless otherwise mentioned, the electron reconstruction and identification below is within the tracking acceptance ($|\eta| < 2.5$). Clusters are reconstructed [106] from seeds found by using a sliding-window algorithm, searching for longitudinal towers with $E_{\mathrm{T}} > 2.5\,\mathrm{GeV}$. The window is 3×5 in units of 0.025×0.025 in $\eta \times \phi$ space, corresponding to the middle EM calorimeter layer granularity, which contains about 80 % of an EM shower. Cluster reconstruction is found to be 95 % efficient for electrons with $E_{\mathrm{T}} = 7\,\mathrm{GeV}$ using simulation, and 99 % efficient for those with

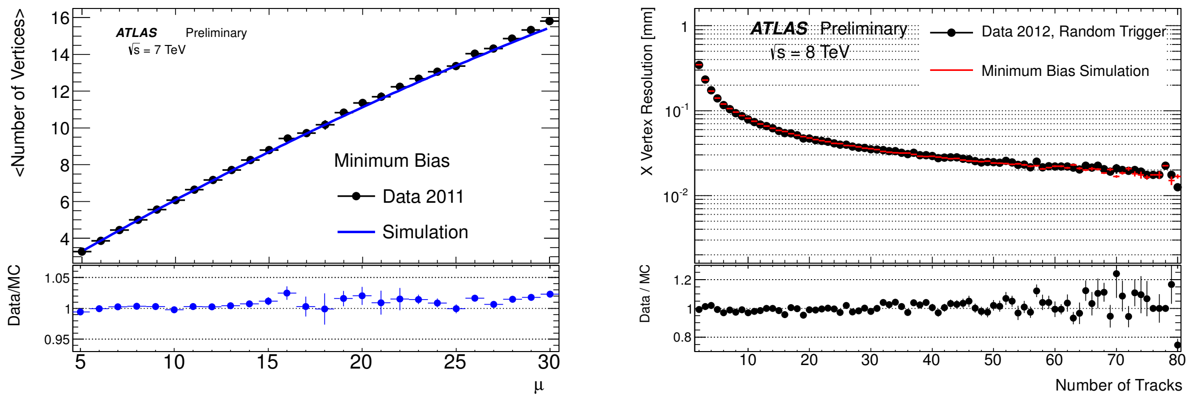

(a)

(b)

Figure 4.3: (a), average number of reconstructed vertices as a function of μ_{pu} (average number of pile-up interactions per bunch crossing) for data collected in 2011 using the minimum bias trigger. (b), vertex position resolution as a function of the number of tracks in the vertex fit [105].

$E_{\text{T}} > 15\,\text{GeV}$ from W and Z decays [107]. Tracks are then extrapolated out to the seeds with a loose matching in the track impact point and cluster η, to account for Bremstrahlung losses. If a single seed has multiple tracks, tracks with silicon hits are preferred and the track closest in ΔR space is chosen. The final electron cluster is then rebuilt using a 3×7 (5×5) area in the barrel (end-cap). The cluster energy is determined by summing four contributions: estimated energy deposit before the EM calorimeter, EM calorimeter energy deposit, estimated energy deposited around the cluster (lateral leakage), and the estimated energy deposited beyond the EM calorimeter (longitudinal leakage). The electron candidate's energy is taken from the cluster and direction from the associated track [82]. The electron energy scale is calibrated via a combination of test beam data, MC derived corrections, and *in situ* $Z \to ee$ data [108]

The 2011 dataset uses the same track fitting for all charged particles. Since electrons may lose considerable energy, and thus change direction, via Bremstrahlung while traversing the detector, this leads to losses in efficiency. Data taking in 2012 used a new approach to re-fit electron tracks called the Gaussian sum filter (GSF) algorithm [109]. The GSF algorithm is used to account for energy losses due to Bremstrahlung. Electron candidates with tracks of $p_{\text{T}} > 400\,\text{MeV}$ can be re-fit and put into the cluster matching again, recovering reconstruction efficiency. This algorithm also improves the electron direction and impact parameter resolutions.

The efficiency of electron reconstruction, see Fig. 4.4, and identification, see Fig. 4.5, described below, are measured using the tag-and-probe method making use of the well known $Z \to ee$ and $J/\psi \to ee$ decays. Strict selection requirements are used to "tag" one of the electrons, then the second electron is used as a "probe" for efficiency measurements. Event selections are used to reject background contamination along with a requirement on the dielectron invariant mass [107].

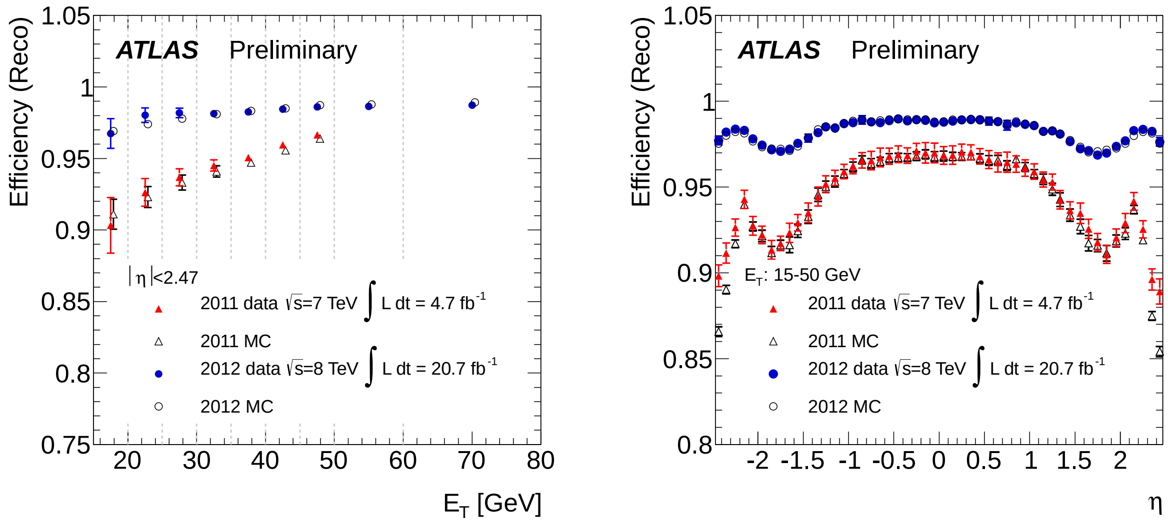

(a) (b)

Figure 4.4: Measured electron reconstruction efficiency over (a) E_{T} and (b) η comparing data to MC for both 7 TeV and 8 TeV runs. The dashed lines represent the binning in E_{T} used. The η distribution is for electrons with $15 < E_{\mathrm{T}} < 50\,\mathrm{GeV}$ [107].

At this stage, electron candidates are dominated by hadrons, photon conversions from π^0 decays, and heavy-flavor decays [110]. The former are referred to as fake electrons and the latter two non-prompt electrons (for our purposes both are 'fakes'). Although non-prompt electrons exist in the final state, they are not what we are looking for. Rather we usually want prompt electroweak decays of Ws, Zs, or some new particle. To select the desired electrons, i.e., perform electron identification, various requirements are made based on the candidate's calorimeter and track qualities, as well as the matching of cluster to track. Electron identification is performed in the range $|\eta| < 2.47$, excluding the transition region (crack) between the barrel and end-cap EM calorimeter at $1.37 < |\eta| < 1.52$.

Two identification methods are used, a cut-based[1] selection [82, 110, 111] and multivariate analysis (MVA) likelihood (LH) selection [107]. Three sets of requirements, optimized in η and p_{T}, define the *loose*, *medium*, and *tight* cut-based electron identification. The *loose* selection uses shower-shape variables, hadronic leakage information, track quality, and track-cluster matching quality. The *medium* selection adds on a B-layer[2] hit requirement to reject

[1] A cut is a requirement or selection, e.g., $p_{\mathrm{T}} > 10\,\mathrm{GeV}$.
[2] The B-layer is the inner most pixel layer.

photon conversions, a loose $|d_0|$ requirement, and makes use of the TRT to identify transition radiation. The *tight* selection further adds E/p (calorimeter versus ID measurement), photon conversion vertex rejection, and stricter selections on previous variables.

Three levels of the LH based identification *loose*, *medium*, and *very tight* make use of the mostly same set of variables plus d_0 significance, additional shower shape variables, and additional track-cluster matching variables. They are designed to have similar electron efficiencies as the cut-based selection, with better rejection of light-flavor jets and conversions.

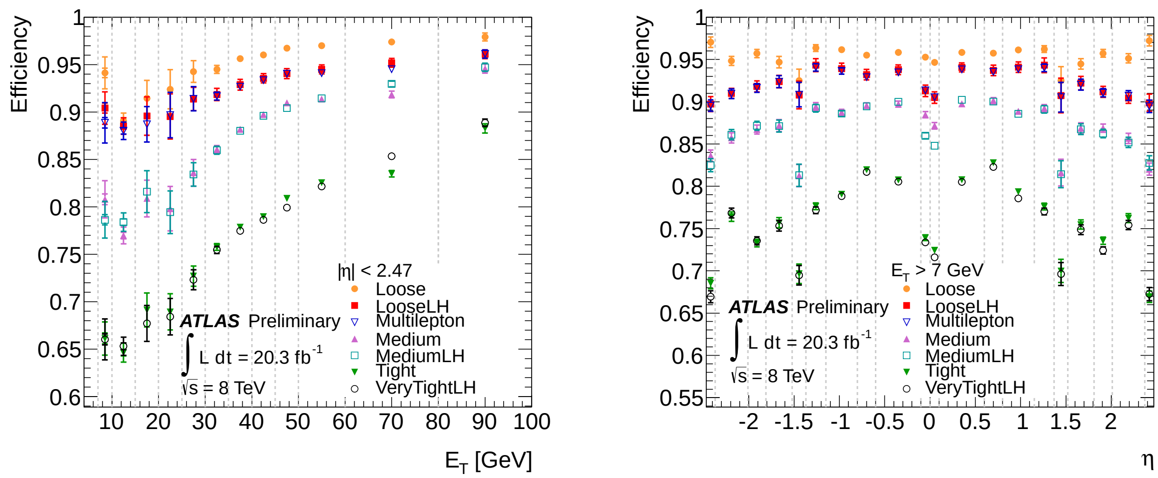

(a) (b)

Figure 4.5: Measured electron identification efficiency for various cut-based and likelihood (LH) selections over (b) E_{T} and (b) η for the 8 TeV run. The efficiency is calculated from data-to-MC efficiency ratios and the efficiency measured with $Z \to ee$ MC. The dashed lines represent the binning used [107].

Prompt electrons from decays of heavy particles such as the W or Z bosons are expected to be isolated, that is without other particles producing tracks or depositing energy in the calorimeter nearby. To further reject background contributions, isolation requirements are imposed on electrons. A requirement is made on the calorimeter energy and tracks summed in a ΔR cone around the electron [107], $p_{\mathrm{T}}^{\mathrm{cone}}$ and $E_{\mathrm{T}}^{\mathrm{cone}}$ respectively. In the 2012 data analysis, the calorimeter energy is computed using the topological cluster algorithm [106], which starts with cluster seeds and adds neighboring cells if they are above a noise threshold. Calorimeter cells within 0.125×0.175 in $\eta \times \phi$ around the electron are excluded. Pile-up contributions are estimated and subtracted event-by-event [112]. For the analyses in this dissertation, the isolation requirements are optimized in E_{T} bins based on signal to background ratios. Table 4.1 contains the total efficiency of the electron reconstruction, identification, and isolation requirements for a $m_H = 125\,\text{GeV}$ $H \to WW^{(*)} \to \ell\nu\ell\nu$ signal sample with the selection in Chapter V. The table also contains the uncertainties on the efficiency. Differences in measured efficiencies of the reconstruction, identification, and isolation between data and MC are corrected for with scale factors applied to the MC.

E_T	Total eff.	Iso. unc. (relative)	ID+Rec. unc. (relative)	Total enc. (relative)
10-15	0.412	0.016	0.016	0.022
15-20	0.619	0.009	0.024	0.025
20-25	0.668	0.008	0.027	0.028
25-30	0.755	0.007	0.014	0.016
30-35	0.770	0.007	0.005	0.009
35-40	0.796	0.006	0.003	0.007
40-45	0.798	0.006	0.002	0.006
45-50	0.813	0.006	0.002	0.006

Table 4.1: Total electron selection efficiencies and uncertainties from isolation (iso.) and identification plus reconstruction (ID+Rec.) for an $m_H = 125\,\text{GeV}$ $H \to WW^{(*)} \to \ell\nu\ell\nu$ ggF signal sample. All uncertainties are added in quadrature for the total. Energy scale and resolution uncertainties are not included.

4.3 Muons

Muons are the other final-state lepton used in the analyses in this dissertation. They are are reconstructed by an ID track matched to an MS track and less likely to be misidentified from a jet since they only deposit a relatively small amount of energy in the calorimeters.

The MS is designed to identify particles out to $|\eta| < 2.7$. However, muon candidates for the analyses in this dissertation are built from MS tracks matched to ID tracks, which form Combined (CB) muons. The use of the ID limits coverage to $|\eta| < 2.5$.

There are four categories of identified muons [85]: stand-alone (SA), CB, segment-tagged (ST), and calorimeter-tagged (CaloTag). SA muons are reconstructed with the MS only and mainly used to extend coverage out to $|\eta| < 2.7$. Tracks are extrapolated back to the IP taking into account the estimated effects of the calorimeters. CB muons are the main analysis muons. They are formed by combining tracks formed independently in the ID and MS. ST muons are ID tracks tagged as a muon if it extrapolates to at least one track-segment in the MS; these are generally used for low p_T muons or in regions of poor MDT acceptance. Finally, CaloTag muons are ID tracks tagged as a muon if it is associated with a calorimeter energy deposit compatible with a minimally ionizing particle (MIP). These have the lowest purity, but can be used to recover acceptance in the $|\eta| < 0.1$ region.

Muons are reconstructed with two independent strategies: Staco (chain 1) [113] and Muid (chain 2) [114]. A third chain combining the best parts of the first two is planned to be used for Run II. The Staco method, used by the analyses in this dissertation, performs a statistical combination (hence 'Staco') of the SA and ID track parameters using the corresponding covariance matrices. Muid re-fits the track using hits from the ID and MS.

Quality cuts are imposed on the muon candidates. The ID track is required to have at least 1 Pixel hit, at least 5 SCT hits, at most 2 silicon holes, and at least 9 TRT hits if in $0.1 < |\eta| < 1.9$. If the track passes a silicon sensor known to be inefficient, the first two hit requirements are reduced by one.

The performance of muon reconstruction and identification is also measured using the tag-and-probe method with samples of Z, J/ψ, and Υ decays to $\mu\mu$. The efficiency as a function of p_{T} and η is shown in Fig. 4.6. The drop in CB muon efficiency around $\eta = 0$ and the dips in efficiency in the transition region are due to partial detector coverage, described in Section 3.2.3. As with electrons, differences between the efficiency in data and MC is corrected for with scale factors. The correction factors are generally consistent with 1, except around the transition region where the simulation of the magnetic field is difficult. As seen in Fig. 4.6, ST muons recover these inefficiencies by requiring only one segment, not the ≥ 2 segments needed for an MS track. Figure 4.7 shows the dimuon invariant mass resolution, which varies between $\sim 1 - 3\,\%$ depending on the p_{T} and η of the muons. The resolution from J/ψ and Υ decays is plotted as a function of the average of the two muon p_{T}s, while the resolution calculated with Z-boson decays is plotted as a function of

$$p_{\mathrm{T}}^{*} = m_Z \sqrt{\frac{\sin\theta_1 \sin\theta_2}{2\,(1-\cos\alpha_{12})}}\,, \tag{4.1}$$

where $\theta_{1,2}$ are the polar angles of the muons and α_{12} is the opening angle of the muon pair. This definition removes the correlation between the measurement of the dimuon mass and average p_{T} [85].

Muons are also required to be isolated, using both calorimeter energy and track isolation. A similar procedure as for electrons is carried out, optimizing the isolation requirements for the $H \to WW^{(*)} \to \ell\nu\ell\nu$ analysis. Table 4.2 contains the total efficiency for the muon reconstruction, identification, and isolation for a $m_H = 125\,\mathrm{GeV}$ signal sample. The calorimeter isolation energy in a cone of $\Delta R < 0.05$ is excluded, and the remaining isolation energy is corrected for the number of PVs (N_{PV}) in the event.

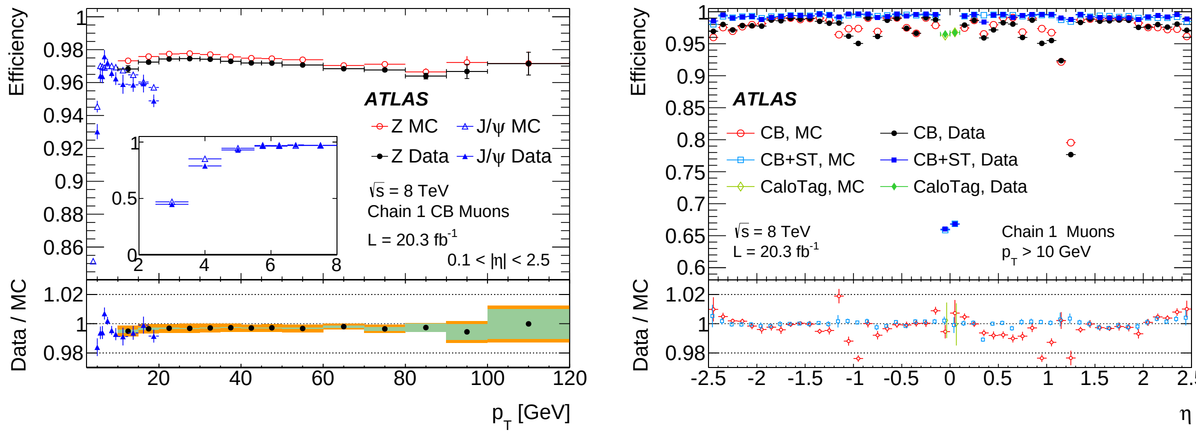

(a) (b)

Figure 4.6: (a), reconstruction efficiency for CB muons as a function of p_{T}. The insert shows the low p_{T} region. The error bars on the efficiencies are statistical for $Z \to \mu\mu$ and statistical plus modeling uncertainties for $J/\psi \to \mu\mu$. The green band represents the statistical uncertainty and the orange additional systematic uncertainty. (b), reconstruction efficiency for various muon types as a function of η measured with $Z \to \mu\mu$ events. The error bars in the ratios combine statistical and systematic uncertainties [85].

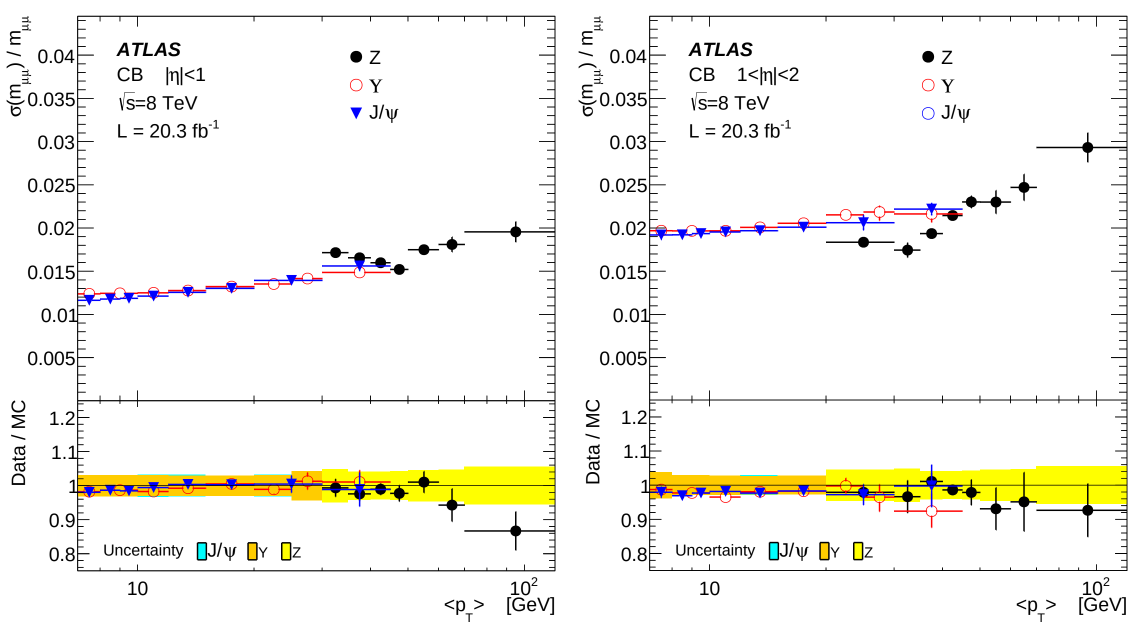

(a) (b)

Figure 4.7: Dimuon invariant mass resolution in 8 TeV data for CB muons in two η regions as a function of the average of the two muon p_{T}'s ($\langle p_{\mathrm{T}} \rangle$) for J/ψ and Υ events and as a function of p_{T}^{*}, defined in Equation 4.1, for Z events [85].

E_{T}	Total eff.	Iso. unc. (relative)	ID+Rec. unc. (relative)	Total unc. (relative)
10-15	0.574	0.027	< 0.005	0.027
15-20	0.808	0.012	< 0.005	0.013
20-25	0.904	0.007	< 0.005	0.009
25-30	0.924	0.006	< 0.005	0.008
30-35	0.932	0.006	< 0.005	0.008
35-40	0.942	0.005	< 0.005	0.007
40-45	0.943	0.005	< 0.005	0.007
45-50	0.944	0.005	< 0.005	0.007

Table 4.2: Total muon selection efficiencies and uncertainties from isolation (iso.) and identification plus reconstruction (ID+Rec.) for an $m_H = 125\,\mathrm{GeV}$ $H \to WW^{(*)} \to \ell\nu\ell\nu$ ggF signal sample. All uncertainties are added in quadrature for the total. The momentum scale and resolution uncertainties are not included.

4.4 Jets

A jet is a collection of objects in a cone emanating from the IP, defined by an algorithm. They are usually formed by the hadronization of quarks or gluons and thus in analyses represent a quark or gluon in the decay process. Jets can be defined with tracks, calorimeter clusters, or particles. For the analyses in this dissertation, they are measured as splashes of energy in the calorimeters using topological calorimeter clusters [106].

The topological clusters are used as inputs to a jet finding algorithm. Algorithms for jet finding are chosen based on several theoretical and experimental considerations [56]. The method should be infrared safe, meaning soft particles should not interfere with the reconstruction of a jet, e.g., number of jets found. It should also have collinear safety, jet reconstruction which is independent of how the momentum is distributed among particles. Experimentally, the resolution of the detector and detector environment play a role in the selection of the algorithm.

Several very similar methods implement a sequential cluster combination to form jets. They make use of a measure of separation of objects d_{ij}, defined in Equation 4.2, which is computed over all pairs ij of input objects, where $k_{t,i}$ is the transverse momentum of the ith object and R is an input distance parameter. Additionally, d_i, defined in Equation 4.3, is computed. If $d_{ij} < d_i$ then the four-momenta of objects i and j are combined and added to the list of objects (removing objects i and j). Once $d_i < d_{ij}$, the object i is set aside (removed from the list) and considered a jet. This continues until all input objects have been combined into a jet or are considered one itself.

$$d_{ij} = \min\left(k_{t,i}^{2p}, k_{t,j}^{2p}\right) \frac{\Delta R_{ij}^2}{R^2} \tag{4.2}$$

$$d_i = k_{t,i}^{2p} \tag{4.3}$$

The k_t algorithm [115, 116] is defined with $p = 1$ and first merges the soft objects with low k_t. The Cambridge-Aachen (C/A) algorithm [117, 118] uses $p = 0$, which means it does not use the transverse momenta and combines the closest objects first. It can provide a better resolution of jet substructure. This differs from cone algorithms in that it iteratively combines objects, rather than combining everything within a fixed cone.

The anti-k_t algorithm [119] uses $p = -1$ and merges objects with nearby hard objects first. If the hard object has no other hard neighbors within $2R$, it will accumulate all of the soft particles in a cone of R around it. If two hard objects are within R to $2R$ of each other, there will be a boundary between the cones of the jets determined by the relative momenta of the hard objects. In general, for separated hard objects, anti-k_t results in conical jets. The analyses in this dissertation use anti-k_t jets with distance parameter $R = 0.4$.

The topological clusters used for jet finding are initially reconstructed with a local cell signal weighting (LCW) method [120]. This is meant to better reconstruct jets from hadronic deposits than using the EM scale which was determined from electron test-beam data [121]—EM scale jets were used in the 7 TeV analyses. Based on the shower shape, the LCW method classifies topological clusters as either electromagnetic or hadronic, which allows the use of energy corrections from MC simulation of charged and neutral pions.

Jets are corrected for both in-time and out-of-time pile-up [122], which contribute extra energy to the calorimeter. The energy contributed from pile-up is calculated with MC simulation and subtracted off from the reconstructed jet. The average number of interactions per bunch crossing μ_pu is used for the out-of-time correction and N_PV is used for the in-time correction. For 2012 data, this correction was further refined [123] to take into account the jet area, defined by associated tracks, and event pile-up activity, measured with the median p_T density. Jets are also corrected to point to the PV.

Jet p_T and η are first calibrated to the jet energy scale (JES) using p_T and η dependent corrections from MC simulation comparing reconstructed and truth jets [121]. The correction is the inverse of the jet response, see Fig. 4.8(a). These jets are referred to as LCW+JES calibrated jets. Finally, jets are corrected with an *in situ* derived correction to account for differences between data and MC, see Fig. 4.8(b).

Systematic uncertainties on the JES [120] are evaluated as a function of p_T and η and provided by the JetEtmiss combined performance group. The uncertainties are broken down into several experimental sources, for a total of thirteen used by the 8 TeV analyses in this

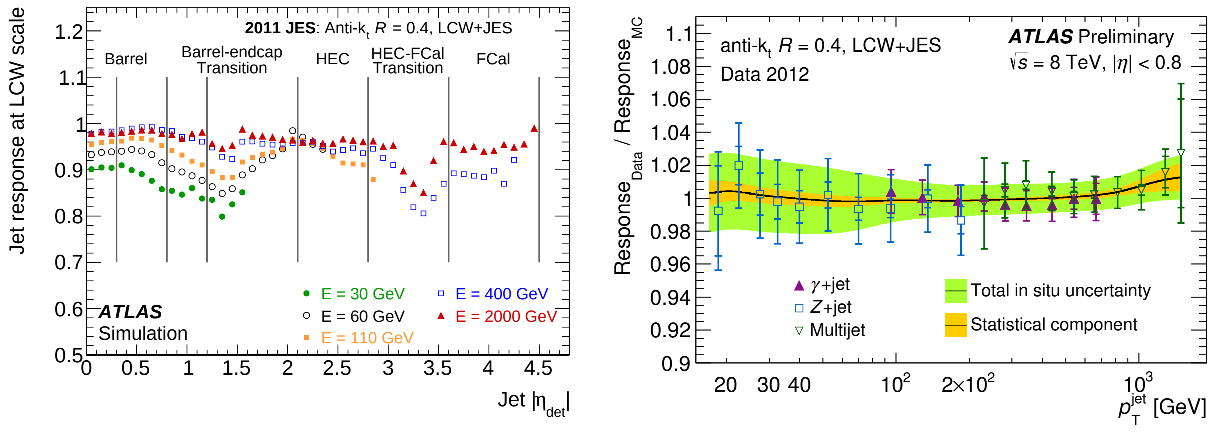

(a) (b)

Figure 4.8: (a), average response ($E_{\text{jet}}^{\text{LCW}}/E_{\text{jet}}^{\text{truth}}$) of simulated jets in 2011 conditions for the LCW scale as a function of uncorrected η [120]. (b), jet response data-to-MC ratio for 2012 conditions with the dark line being the *in situ* correction [124].

dissertation:

- detector1 and modelling1: *in situ* calibration uncertainties
- modelling and stat+method η intercalibration: calibration of forward regions using central jets
- high p_{T} jets: propagation of single hadron uncertainties to jets
- in- and out-of-time pile-up: uncertainties as a function of N_{PV} and μ_{pu}
- pile-up ρ topology and p_{T}: uncertainties for pile-up effects on jet area and p_{T}
- flavor composition and response: differences in quark-initiated and gluon-initiated jet response
- b-JES: b-jet versus light-jet energy scale
- AFII[3] non-closure: extra uncertainty for using different simulation than was used for the evaluation of the JES uncertainties

The size of the JES uncertainties as a function of jet p_{T} and η are shown in Fig. 4.9. They are at most 7 %.

Extra interactions per bunch crossing generally result in more jets. Compared to the ID, the slower responding calorimeters are particularly sensitive to out-of-time pile-up. The jet area pile-up subtraction removes the majority of pile-up jets by reducing their energy to be

[3]Atlfast-II (AFII) simulation is a fast calorimeter simulation, see Section 4.6.

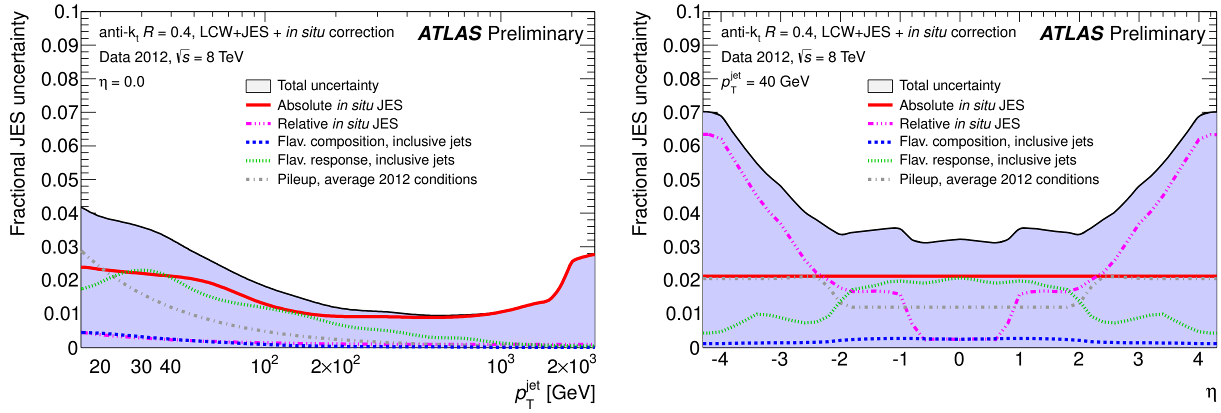

(a) (b)

Figure 4.9: Fractional JES systematic uncertainty for LCW+JES anti-k_t jets with $R = 0.4$ from inclusive dijet samples with average 2012 pile-up conditions, (a), as a function of p_T at $\eta = 0$, (b), as a function of η at $p_T = 40$ GeV. The uncertainty on the scale of b-jets is not included [124].

below threshold. However, the increase in μ_{pu} in 2012, lead to the development of a new technique to suppress pile-up jets. The jet vertex fraction (JVF) [123], defined as

$$\text{JVF} = \frac{\sum_k p_T\left(\text{track}_k^{\text{PV}}\right)}{\sum_j p_T\left(\text{track}_j\right)}\,, \tag{4.4}$$

is the fraction of tracks k p_T associated to the jet from the PV relative to all tracks j p_T associated with the jet. It is used to estimate the vertex of a jet, by selecting those with the most tracks associated to the jet. Therefore, it can be used to remove jets which are not associated with the PV, and thus likely from pile-up collisions.

Only tracks with $p_T > 0.5$ GeV are used for the computation. The use of tracks limits the method to $|\eta| < 2.5$; though, to reduce signal loss where jets fall partly outside of the ID, the JVF is only used out to $|\eta| < 2.4$. Further, jet multiplicity for $p_T^{\text{jet}} > 50$ GeV is found to be independent of μ_{pu}, and this p_T is set as an upper bound for using JVF.

The JVF distribution for hard-scatter (from the primary vertex) and pile-up jets is shown in Fig. 4.10. It also shows the efficiency in data and MC for selecting hard-scatter jets as a function of μ_{pu}. Figure 7.3 shows the number of pile-up jets as a function of μ_{pu}.

4.4.1 *b*-tagging

Events with b-quarks are a signature of $t\bar{t}$ and single-top processes—the top quark decays to a W boson and b-quark with a branching ratio near 100 %. Thus, the ability to tag jets

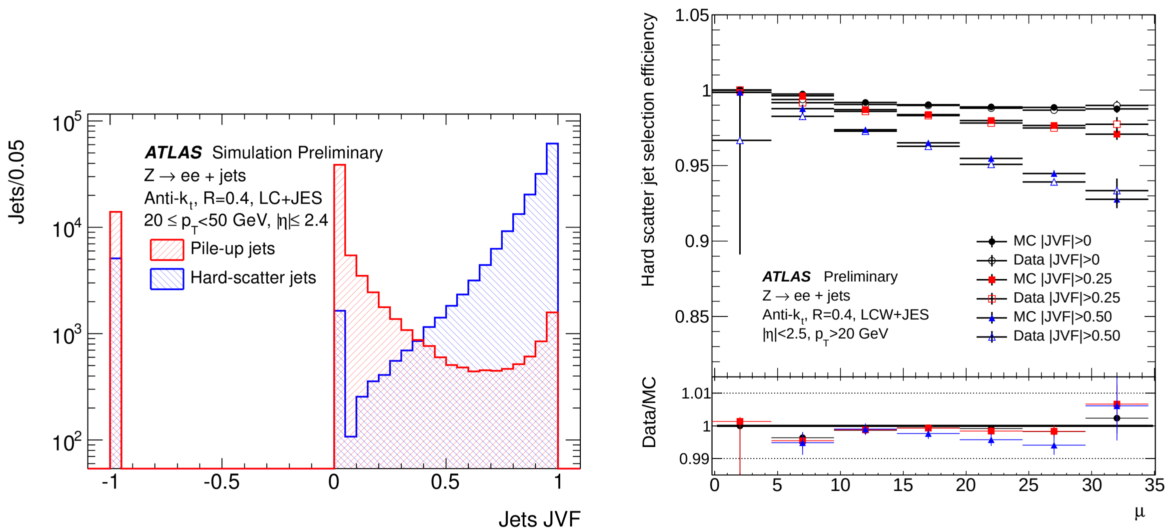

(a) (b)

Figure 4.10: (a), JVF distribution for hard-scatter and pile-up jets in 8 TeV simulation. Jets with no associated tracks are assigned a value of -1. (b), JVF hard-scatter jet selection efficiency as a function of average number of inelastic interactions per bunch crossing μ_{pu} in 8 TeV data and MC [123].

originating from b-quarks is a powerful tool to preferentially select top-quark processes, which are backgrounds for the analyses in this dissertation. This is made possible by the relatively longer lifetime of B-hadrons, resulting in a displaced decay vertex. Algorithms for b-tagging exploit the topology of b-quark decays. The need for vertexing limits the identification of b-quarks to the tracking volume ($|\eta| < 2.5$).

The MV1 [125] algorithm is used by the analyses in this dissertation to tag b-quarks. It makes use of a neural network with three algorithms as inputs: IP3D based on the impact parameter, SV1 secondary vertexing, and JetFitter which exploits the topology of decays with a Kalman filter [126]. IP3D uses the transverse (d_0/σ_{d_0}) and longitudinal (z_0/σ_{z_0}) impact parameter significances. SV1 looks for the secondary vertex from the b-quark decay products. JetFitter exploits the topology of b- and c-quark decays using a Kalman filter to find the line between the PV and secondary vertex. All three use a likelihood ratio technique. The output of the MV1 algorithm is a weight which is cut on to determine if a jet is tagged as a b-quark or not. The value of this cut is selected based on the desired b-tagging efficiency, or operating point. Figure 4.11(a) shows the b-tagging efficiency versus light-jet rejection for a simulated $t\bar{t}$ sample with the MV1 algorithm.

The algorithm is calibrated as a function of p_{T} using leptonically decaying $t\bar{t}$ events with a likelihood based method [127]. A sample of $N_{\text{jets}} = 2$ and $N_{\text{jets}} = 3$, with all combinations of $N_{b\text{-jets}}$, is fed into the likelihood. The difference between data and MC is corrected for with a scale factor (SF), for example in Fig. 4.11. The SFs are computed for jets with p_T between 20 and 300 GeV with an uncertainty of about 2 % for jets with $p_T = 100$ GeV.

The mistag rate, fraction of light flavored jets tagged as b-jets, shown in Fig. 4.11(b), is also measured in data [125] using the so-called 'negative tag' method. This method reverses impact parameter and decay length selections. The negative and normal tagging are expected to be symmetric for light-flavor jets, while not for heavy-flavor jets, because the light-flavor jets are uncorrelated with the apparent displaced vertex.

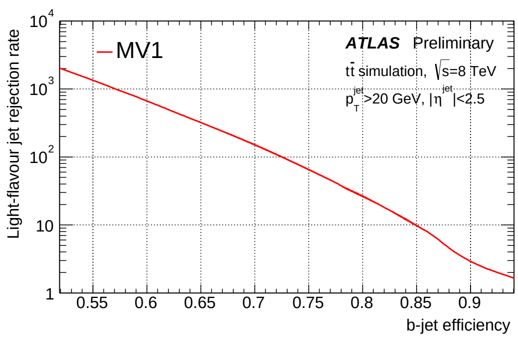

(a)

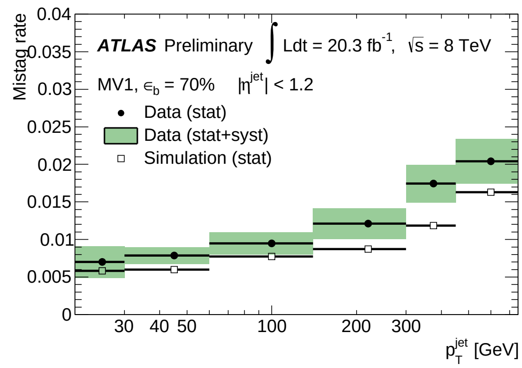

(b)

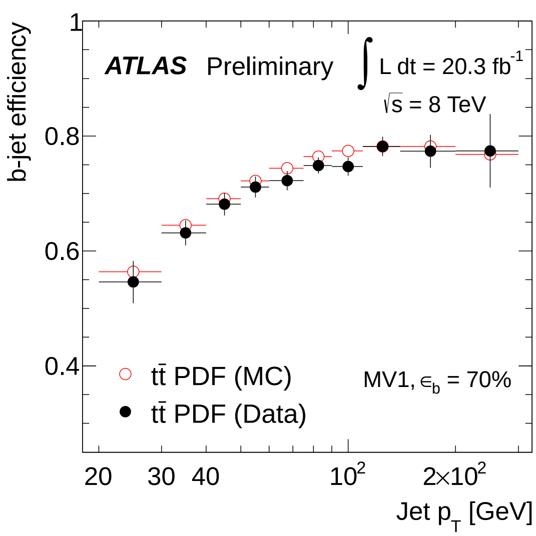

(c)

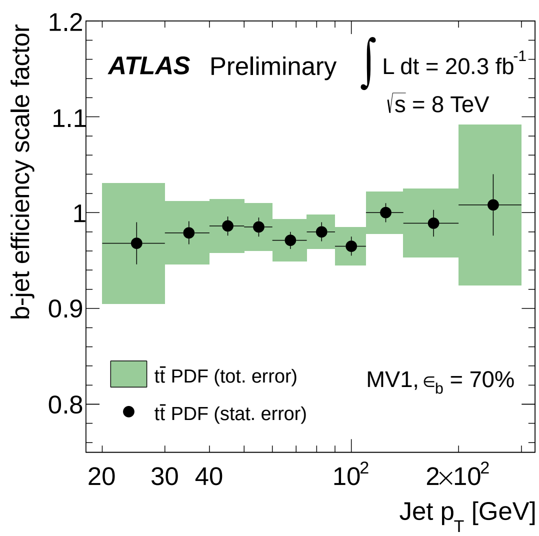

(d)

Figure 4.11: (a) MV1 b-tagging algorithm efficiency versus light-jet rejection and (b) light-jet (u, d, s, or g) mistag rate versus jet p_T [125]. (c), b-jet tagging efficiency in data and MC and (d) the resulting scale factor as a function of jet p_T [127].

4.5 Missing transverse momentum

Missing transverse momentum (MET) is defined as the momentum imbalance in the transverse plane, making use of momentum conservation as an extra constraint since the proton beams are along the z-axis. It is a useful quantity in collider physics because it encapsulates all of the knowledge we have about particles which are not detected by the detector, e.g., neutrinos, and thus leave an imbalance in observed momenta. Thus, MET plays an important role in the analysis of $H \to WW^{(*)} \to \ell\nu\ell\nu$ events.

MET is calculated as the negative vector sum of all of the objects in the detector, usually divided into the identified hard-objects; photons, leptons, and jets; and the remaining soft-objects, i.e., everything else:

$$\boldsymbol{E}_{\mathrm{T}}^{\mathrm{miss}} = -\left(\sum_{\substack{\text{hard}\\\text{objects}}} \boldsymbol{p}_{\mathrm{T}} + \sum_{\substack{\text{soft}\\\text{objects}}} \boldsymbol{p}_{\mathrm{T}} \right) . \tag{4.5}$$

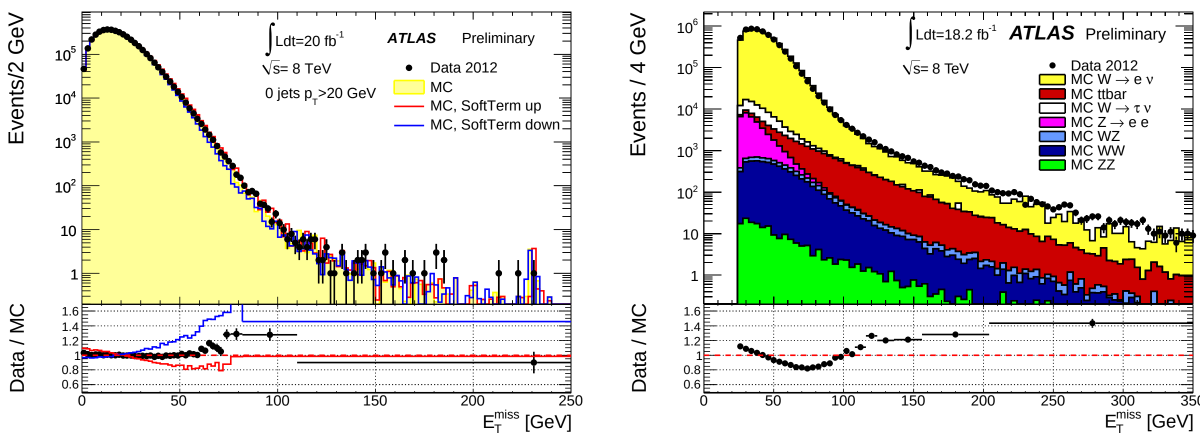

(a) (b)

Figure 4.12: $E_{\mathrm{T}}^{\mathrm{miss}}$ as measured in a sample of (a) $Z \to \mu\mu$ events with no jets of $p_{\mathrm{T}} > 20\,\mathrm{GeV}$ and (b) in a sample of $W \to e\nu$ events [128]. The bottom of each figure shows the ratio of data over MC. Additionally in (a), the bottom includes the ratio to a scaled and smeared soft-term, representing a systematic uncertainty.

Three versions of MET are used by the analyses in this dissertation. The first, $E_{\mathrm{T}}^{\mathrm{miss}}$, uses calorimeter deposits for the soft-term, and the other two, $p_{\mathrm{T}}^{\mathrm{miss}}$ and $p_{\mathrm{T}}^{\mathrm{miss,trk}}$, use tracks for the soft-term. The calorimeter based MET assigns energy deposits, in order, to electrons, photons, hadronically decaying τ-leptons, jets, and muons. Jets and photons with $p_{\mathrm{T}} > 20\,\mathrm{GeV}$ are considered hard-objects. Remaining topological clusters and tracks are lumped into the soft-term. The use of the topological clusters reduces the impact of noise in the calorimeter. All of the hard-objects are corrected with their respective calibrations. The soft topological-clusters are also calibrated using the LCW technique and overlaps with tracks are removed [128, 129].

The track-based MET is motivated by the pile-up induced degradation of $E_{\mathrm{T}}^{\mathrm{miss}}$, see Fig. 4.13. An $\mathcal{O}(20\,\%)$ improvement in resolution is obtained by using tracks, with $p_{\mathrm{T}} > 0.5\,\mathrm{GeV}$ originating from the PV, for the soft-term, see Fig. 4.14. Tracks associated with identified leptons, described in Section 5.3.1, are not included to avoid double counting. In order to account for neutral particles in events with jets, tracks within a cone of $\Delta R < 0.4$ are removed and the calorimeter energy of the jet is used instead, resulting in a 'jet-corrected track-MET' [112]. A simpler track-based ($p_{\mathrm{T}}^{\mathrm{miss,trk}}$) without the track-jet substitution is also used in some categories of the $H \to WW^{(*)} \to \ell\nu\ell\nu$ analysis.

Since we rely on the measurement of everything else in order to reconstruct the MET, mismeasurement of objects, as well as detector inefficiencies and resolution lead to fake MET. Systematic uncertainties on all of the objects which enter the MET calculation are propagated to it accordingly. The only MET-specific uncertainties are on the soft-term itself, seen in the left of Fig. 4.12 for the calorimeter-based soft-term. Both a scale and resolution uncertainty are evaluated, with $Z \to \mu\mu$ events without jets for the calorimeter-based soft-term [128] and similarly for $p_{\mathrm{T}}^{\mathrm{miss}}$, except also using the balance between the soft-term and jets.

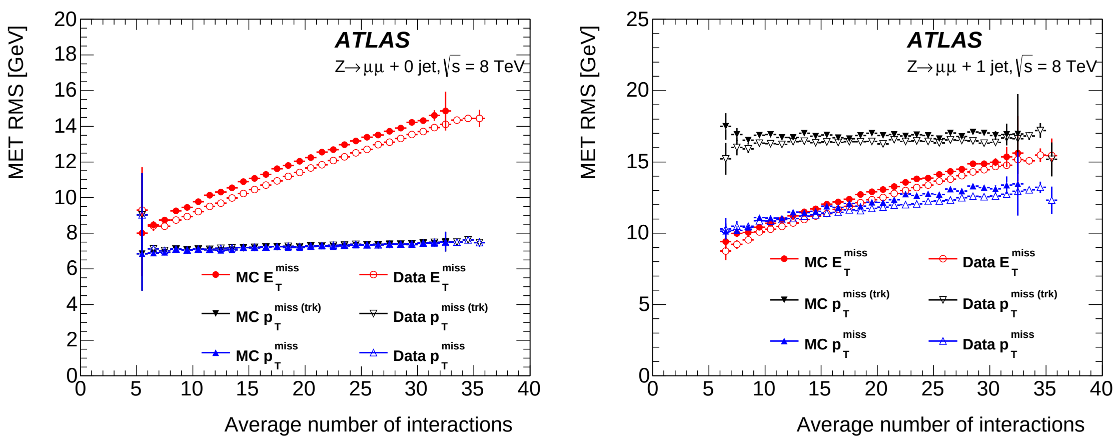

(a) (b)

Figure 4.13: Root mean square (RMS) of the MET for $Z \to \mu\mu$ events in data and MC for the calorimeter based $E_{\mathrm{T}}^{\mathrm{miss}}$, track-based $p_{\mathrm{T}}^{\mathrm{miss}}$, and non-jet-corrected $p_{\mathrm{T}}^{\mathrm{miss,trk}}$ [112] (a) for $N_{\mathrm{jets}} = 0$ and (b) for $N_{\mathrm{jets}} = 1$. In the case of $N_{\mathrm{jets}} = 0$, $p_{\mathrm{T}}^{\mathrm{miss}} = p_{\mathrm{T}}^{\mathrm{miss,trk}}$ by definition.

4.6 Simulation

Predictions of physics processes, such as $H \to WW^{(*)} \to \ell\nu\ell\nu$, are simulated in several stages to replicate how the process will appear in the detector to the best of our knowledge.

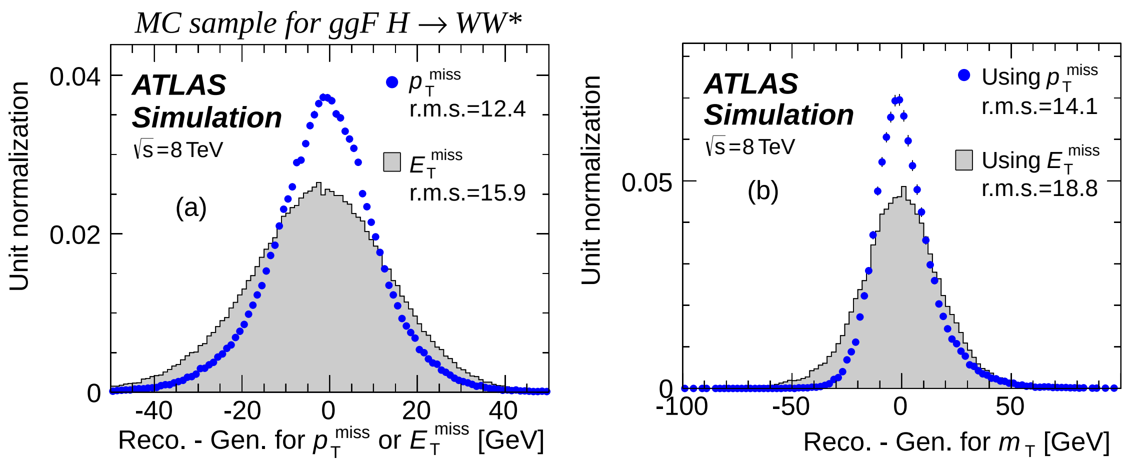

(a) (b)

Figure 4.14: (a), resolution of calorimeter-based ($E_{\mathrm{T}}^{\mathrm{miss}}$) and track-based ($p_{\mathrm{T}}^{\mathrm{miss}}$) MET. (b), resolution of m_{T}, see Equation 5.1 for definition, built with calorimeter- or track-based MET for the ggF signal MC in the $N_{\mathrm{jets}} = 0$ category [112]. The resolution is computed by subtracted the reconstructed quantity from that derived with the generated leptons and neutrinos.

The Monte Carlo (MC) method is used to generate events based on calculated differential distributions for the process from the matrix element (ME). PDFs are used as inputs for the distribution of energies of the constituents of the protons. The hard-scatter event is input into a parton shower (PS) simulation to include initial state radiation (ISR) and final state radiation (FSR), radiation of gluons, not included in the ME. All of these particles are then run through a hadronization simulation to combine the resulting partons into the final observable hadrons. Finally, a model of the underlying event (UE) is used to overlay what happened to the rest of the protons. The PYTHIA8 [130] event generator is used to simulate pile-up interactions.

If only the total cross-section is known to higher order, i.e., not the shape, the ratio of higher to lower-order cross section (k-factor) is used to account for the difference. Many of the MEs used in event generators are known only to the leading order (LO), but the inclusive total cross section is generally easier to calculate to higher order.

For event simulation in ATLAS [131], the first step is handled by event generators. These simulate the initial hard process, including prompt decays, which happen before the need to consider interaction with the detector. This includes the PS, hadronization, and UE. A cutoff of $c\tau > 10\,\mathrm{mm}$ is used to consider the particle 'stable' in terms of the event generator. The resulting particles from the event generation are handed to GEANT4 [132], which propagates each particle through the full ATLAS detector. Energy deposits in the detector are noted and recorded as ‘hits’. Digitization translates these hits into detector signals, including overlays for pile-up and other non-hard scatter processes. Simulation of the triggers is also performed; though, no events are rejected, merely the trigger decision is recorded. The simulated detector output is finally fed into the same reconstruction software as data. Along the way, information about the generated particles is kept, referred to as ‘truth’ information. The truth record can be used during analysis to compute signal acceptance and object resolutions, among other things.

A fast simulation of the calorimeter for photons, electrons, and charged pions, referred to as Atlfast-II (AFII) [133], can be used to decrease the time needed for detector simulation. AFII uses a parametrized response for the EM and hadronic calorimeters, which can be quite slow to fully simulate, still using GEANT4 for the remaining simulation.

CHAPTER V

The $H \rightarrow WW^{(*)} \rightarrow \ell\nu\ell\nu$ Analysis

This chapter covers the strategy, implementation, and results of the $H \rightarrow WW^{(*)} \rightarrow \ell\nu\ell\nu$ analysis. These results include the statistical significance of the excess in data over the background only model, measurement of $H \rightarrow WW^{(*)} \rightarrow \ell\nu\ell\nu$ process rate at the LHC, and interpretation of this as evidence of VBF production and a measurement of Higgs boson coupling strengths to fermions and vector bosons. It serves as a reference for the analyses in VI and Chapters VII. The analysis is described in a recent publication [112]. In brief, $H \rightarrow WW^{(*)} \rightarrow \ell\nu\ell\nu$-like events are selected and we observe an excess over the background only expectation compatible with the presence of $H \rightarrow WW^{(*)} \rightarrow \ell\nu\ell\nu$ decays.

5.1 Introduction

The $H \rightarrow WW^{(*)} \rightarrow \ell\nu\ell\nu$ decay is one of the three main channels used to discover the Higgs boson; the others being $H \rightarrow ZZ^{(*)}$ and $H \rightarrow \gamma\gamma$. The decay to two W bosons is the second largest branching ratio in the SM for $m_H \sim 125\,\text{GeV}$, behind decays to $b\bar{b}$, making up for the inability to fully reconstruct the Higgs boson mass from the final state due to the presence of two neutrinos. The final state with two leptons, $\ell = e$ or μ, is the most sensitive $H \rightarrow WW^{(*)}$ decay channel for a light Higgs boson. Another search takes advantage of the larger W branching ratio into quarks, $\ell\nu qq$, but it is only sensitive in the high m_H regime. Both ggF and VBF production modes are considered in this analysis, with ggF the dominant mode. In the SM around $m_H \sim 125\,\text{GeV}$, VBF production is about 8 % of the ggF rate and VH production is smaller still, about 6 % of the ggF rate, and is included as signal, but another analysis [134] is optimized for this production mode. Observation of the Higgs boson coupling to W bosons is an important test of EWSB in the SM.

A well measured mass is important as the Higgs boson branching ratio has a strong dependence on its mass. Since the $\ell\nu\ell\nu$ final state has a poor mass resolution, the mass used for this analysis is based on a combined measurement by ATLAS using the two high resolution channels, ZZ and $\gamma\gamma$, resulting in $m_H = 125.36 \pm 0.37(\text{stat.}) \pm 0.18(\text{syst.})\,\text{GeV}$ [135]. A newer measurement combining ATLAS and CMS analyses [30] has since been released, $m_H = 125.09 \pm 0.21(\text{stat.}) \pm 0.11(\text{syst.})\,\text{GeV}$, which is consistent with the ATLAS measurement.

The results of this analysis include evidence for VBF production, measurements of the production rate[1] relative to the SM expectation (signal strength μ), their interpretation as ggF and VBF cross section times branching ratios, and their interpretation in terms of couplings to vector bosons and fermions. A separate analysis [136] is dedicated to measuring the spin and parity of the Higgs boson using the $H \to WW^{(*)} \to \ell\nu\ell\nu$ channel.

The $H \to WW^{(*)}$ analysis started with the early LHC data, and has improved ever since. A brief history of the analysis follows. The first public results with data [137] used $35\,\text{pb}^{-1}$ 7 TeV of the 2010 data set; no evidence was seen, and an upper limit on the signal strength of $\mu = 1.2$ at $m_H = 160\,\text{GeV}$ was set. This was quickly surpassed by the 2011 data taking. About half of the dataset, $2.05\,\text{fb}^{-1}$ at 7 TeV, was used to exclude an SM Higgs boson with mass $145 < m_H < 206\,\text{GeV}$ [138]. The rest of the data, $4.7\,\text{fb}^{-1}$ in total, was included in a second publication [139] which excluded a SM Higgs boson with $133 < m_H < 261\,\text{GeV}$. No significant excess was observed (even with hindsight, there is only a one standard deviation (s.d.) excess in the low mass region). The ATLAS Higgs boson discovery paper [1] used the $H \to WW^{(*)}$ ICHEP 2012 results, which claimed, "Observation of an Excess..." [140] based on $5.8\,\text{fb}^{-1}$ at 8 TeV plus $4.7\,\text{fb}^{-1}$ at 7 TeV. At this point, the $H \to WW^{(*)} \to \ell\nu\ell\nu$ analysis alone observed a 2.8 s.d. excess at $m_H = 125\,\text{GeV}$ and the combination of search channels resulted in a 5.9 s.d. observed significance. The discovery paper was followed by an updated analysis with more data for HCP 2012 [141] using only the different-flavor ($e\mu$) channel with $13\,\text{fb}^{-1}$ at 8 TeV, resulting in a 2.8 s.d. excess at $m_H = 125\,\text{GeV}$. Finally, the complete data set, $25\,\text{fb}^{-1}$ at 7 and 8 TeV, was presented at the Moriond 2013 conference [142]. A 3.8 s.d. excess was observed at $m_H = 125\,\text{GeV}$, with a signal strength of $\mu = 1.01 \pm 0.31$. The final Run I publication [112], described in this dissertation, uses the same dataset with a much improved analysis.

5.1.1 Analysis strategy

The $H \to WW^{(*)} \to \ell\nu\ell\nu$ analysis was originally designed for sensitivity across a broad mass range. The final Run I analysis is improved by increasing the signal acceptance and reducing systematic uncertainties, focusing on the low m_H region.

The $H \to WW^{(*)} \to \ell\nu\ell\nu$ analysis mainly considers ggF and VBF production and searches for a final state with two oppositely charged leptons and two neutrinos (plus two

[1] cross section times branching ratio ($\sigma \cdot \text{BR}$)

forward jets in the case of VBF). The initial selection is thus fairly simple, requiring exactly two oppositely charged leptons and MET due to the neutrinos. For this analysis a lepton ℓ refers to electrons (e) or muons (μ), unless otherwise noted. Only these two are considered in the final state; leptonic τ decays are included.

There are many background processes which contribute to this final state, so understanding and reducing these backgrounds is the motivation for many pieces of the analysis. We divide the data in order to isolate various backgrounds, separate the production modes, and take advantage of varying signal to background ratios. Events are binned by the number of jets; this allows us to define a VBF rich category and consider the WW background separately from the top-quark background, which dominates at higher jet multiplicities. Since there are two neutrinos in the final state, it is impossible to fully reconstruct the Higgs boson mass from the final state. Instead, a transverse mass m_{T} is constructed and used as a discriminant,

$$m_{\mathrm{T}} = \sqrt{\left(E_{\mathrm{T}}^{\ell\ell} + p_{\mathrm{T}}^{\nu\nu}\right)^2 - \left|\boldsymbol{p}_{\mathrm{T}}^{\ell\ell} + \boldsymbol{p}_{\mathrm{T}}^{\nu\nu}\right|^2}\,, \tag{5.1}$$

where $E_{\mathrm{T}}^{\ell\ell} = \sqrt{\left(p_{\mathrm{T}}^{\ell\ell}\right)^2 + m_{\ell\ell}^2}$. Here $\boldsymbol{p}_{\mathrm{T}}^{\ell\ell}$ is the vector sum of lepton transverse momenta and $\boldsymbol{p}_{\mathrm{T}}^{\nu\nu}$ the same for the neutrinos, measured as MET. In order to further isolate the signal and separate backgrounds, events are divided by the lepton flavor (different-flavor ($e\mu$) and same-flavor ($ee/\mu\mu$)), the dilepton invariant mass ($m_{\ell\ell}$), subleading lepton transverse momentum ($p_{\mathrm{T}}^{\mathrm{sub}}$), and in bins of transverse mass (m_{T}).

Control regions (CRs), which are additional background-rich regions (ideally defined similarly to the signal regions), are used to normalize many of the background processes. These trade theoretical uncertainties on the normalization for the statistical uncertainty from the CR sample size and modeling of the extrapolation from the CR to signal region (SR). Nearly all of the backgrounds in the $N_{\mathrm{jets}} \leq 1$ categories, and the major backgrounds in the $N_{\mathrm{jets}} \geq 2$ categories, are normalized to data in this way. Several more complicated background estimation techniques are used, e.g., for Drell–Yan (DY) in the same-flavor ($ee/\mu\mu$) channel, with details later.

Results quantifying the agreement of the signal and background models with data are obtained with a profile likelihood fit, performed with all of the SRs, binned m_{T} histograms (or binned boosted decision tree (BDT) output in the case of the VBF channel), and CRs, single bin regions. This is in effect a three dimensional fit in $m_{\ell\ell}$, $p_{\mathrm{T}}^{\mathrm{sub}}$, and m_{T} in the most sensitive regions.

5.2 Data and Monte Carlo

5.2.1 Dataset and triggers

The full Run I dataset is used, described in Section 3.3. We enforce data quality, that the detector sub-systems were operating properly during data acquisition, by referencing a so-called good run list (GRL) containing the periods of optimal conditions. After this requirement, a total integrated luminosity of $4.5\,\text{fb}^{-1}$ at $7\,\text{TeV}$ and $20.3\,\text{fb}^{-1}$ at $8\,\text{TeV}$ of data are used for the analysis.

A three level trigger system is used to select events, see Section 3.3.2. We include dilepton triggers in addition to single lepton triggers because the acceptance of lower p_{T} leptons is improved. The requirement of a second lepton lowers the triggered rate so that the required p_{T} can be lowered for the same bandwidth. This allowed for the leading lepton p_{T} requirement to be lowered from $25\,\text{GeV}$ to $22\,\text{GeV}$, important due to the relatively soft signal leptons. Table 5.1 lists the hardware and software p_{T} thresholds for the electron and muon triggers used.

Name	Level-1 trigger	High-level trigger
Single lepton		
e	18 or 30	24i or 60
μ	15	24i or 36
Dilepton		
e, e	10 and 10	12 and 12
μ, μ	15	18 and 8
e, μ	10 and 6	12 and 8

Table 5.1: Lower lepton-trigger p_{T} thresholds, in GeV, during the $8\,\text{TeV}$ data taking. For the single-electron triggers, the hardware and software thresholds are either 18 and 24i or 30 and 60, respectively. The "i" denotes an isolation requirement that is less restrictive than the isolation requirement imposed in the offline selection. For the dilepton triggers, the pair of thresholds corresponds to the leading and subleading lepton, respectively; the dimuon trigger requires only a single muon at L1 [112].

5.2.2 Monte Carlo samples

The $H \to WW^{(*)} \to \ell\nu\ell\nu$ analysis has many backgrounds and an almost equal number of MC samples to model them. Dedicated samples are generated for the signal processes considered (ggF, VBF, and VH) and all of the background processes except $W+\text{jets}$ and multijet production, which use a data-driven method described in Section 5.5.4. Table 5.2

summarizes the processes considered and the MC generators used.

5.2.2.1 Signal treatment

The POWHEG generator [143] matched to PYTHIA8 is used for event simulation of the ggF and VBF signal processes. The branching fraction as a function of m_H is calculated with PROPHECY4F [144], and HDECAY [145] is used to compute the total width. The central values along with their uncertainties are taken from the LHC Higgs cross section working group (LHC Higgs XS WG) [32]. The $H \to WW^{(*)}$ branching fraction at $m_H = 125.36\,\text{GeV}$ is 22 % with a relative uncertainty of 4.2 %.

The ggF total cross section is calculated with the infinite top-quark mass approximation to next-to-next-leading order (NNLO) in QCD corrections [146] and next-to-leading order (NLO) in electroweak corrections. An NLO correction for the finite top-quark mass of a few percent is included [147]. Resummation of the soft QCD radiation is carried out to next-to-next-leading log (NNLL) [148], again in the infinite top-quark mass limit, and to next-to-leading log (NLL) for finite top- and bottom-quark masses. Electroweak corrections to NLO [149] are included using the complete factorization approximation [150]. This results in a total cross section of 19.15 pb for $m_H = 125.36\,\text{GeV}$ at 8 TeV [151]. The total cross section has an uncertainty of 10 %, with 7.5 % from QCD scale variations and 7.2 % from PDF+α_s uncertainties [32].

The interference with direct $gg \to WW$ production [152] has a negligible impact for the on-shell analysis in this chapter; however, plays an important role in the off-shell analysis described in Chapter VI.

For ggF production, POWHEG, which uses a fixed scale, is tuned with the resummation scale to reproduce the NNLO+NLL Higgs boson p_{T} spectrum from HQT2.0 [153, 154], see Fig. 5.1. POWHEG includes the effects of finite quark masses. To improve the modeling of the spectrum, a reweighting is applied to reproduce the NNLO+NNLL dynamic-scale calculation from HRES2.1 [155, 156]. Since events with $N_{\text{jets}} \geq 2$ are relying on the PS, PYTHIA8, they are reweighted separately to the p_{T} spectrum of Higgs boson production in associated with two jets from POWHEG+MINLO [157].

Since the analysis is divided into categories by the number of jets, uncertainties are calculated on the predicted division into jet bins. The jet veto efficiency (JVE) method [158, 159] is used for the ggF channels and the Stewart-Tackmann method [160] is used for the VBF channel, because of the central jet veto (CJV), see Section 5.4.4. The JVE method separates the total cross section calculation ($\sigma_{\text{tot.}}$) from the efficiency of the jet vetoes (ϵ)

Process		MC generator	PDF Set	Simulation	$\sigma \cdot \mathcal{B}$ (pb)
Signal					
ggF	$H \to WW^{(*)}$	POWHEG+PYTHIA8	CT10	Fullsim	0.435
VBF	$H \to WW^{(*)}$	POWHEG+PYTHIA8	CT10	Fullsim	0.0356
VH	$H \to WW^{(*)}$	PYTHIA8	CTEQ6L1	Fullsim	0.0253
ggF	$H \to \tau\tau$	POWHEG+PYTHIA8	CT10	Fullsim	0.151
VBF	$H \to \tau\tau$	POWHEG+PYTHIA8	CT10	Fullsim	0.0124
WW					
$q\bar{q} \to WW$ and $qg \to WW$		POWHEG+PYTHIA6	CT10	Fullsim	5.68
$gg \to WW$		GG2VV+HERWIG	CT10	Fullsim	0.196
$(q\bar{q} \to W) + (q\bar{q} \to W)$ (DPI)		PYTHIA8	CTEQ6L1	Fullsim	0.480
VBS $WW + 2\,\text{jets}$		SHERPA	CT10	Fullsim	0.0397
Top quarks					
$t\bar{t}$		POWHEG+PYTHIA6	CT10	AFII	26.6
Wt		POWHEG+PYTHIA6	CT10	AFII	2.35
$tq\bar{b}$ (t-channel)		ACERMC+PYTHIA6	CTEQ6L1	AFII	28.4
$t\bar{b}$ (s-channel)		POWHEG+PYTHIA6	CT10	AFII	1.82
Other dibosons (VV)					
$W\gamma$	($p_{\mathrm{T}}^{\gamma} > 8\,\text{GeV}$)	ALPGEN+HERWIG	CTEQ6L1	Fullsim	369
$W\gamma^*$	($m_{\ell\ell} \leq 7\,\text{GeV}$)	SHERPA	CT10	Fullsim	12.2
WZ	($m_{\ell\ell} > 7\,\text{GeV}$)	POWHEG+PYTHIA8	CT10	Fullsim	12.7
VBS $WZ + 2\,\text{jets}$ ($m_{\ell\ell} > 7\,\text{GeV}$)		SHERPA	CT10	Fullsim	0.0126
$Z\gamma$	($p_{\mathrm{T}}^{\gamma} > 8\,\text{GeV}$)	SHERPA	CT10	Fullsim/AFII	163
$Z\gamma^*$	(min. $m_{\ell\ell} \leq 4\,\text{GeV}$)	SHERPA	CT10	Fullsim	7.31
ZZ	($m_{\ell\ell} > 4\,\text{GeV}$)	POWHEG+PYTHIA8	CT10	Fullsim	0.733
$ZZ \to \ell\ell\,\nu\nu$ ($m_{\ell\ell} > 4\,\text{GeV}$)		POWHEG+PYTHIA8	CT10	Fullsim	0.504
VBS $ZZ \to \ell\ell\,\nu\nu$		SHERPA	CT10	Fullsim	1.23×10^{-3}
Drell–Yan (DY)					
Z	($m_{\ell\ell} > 10\,\text{GeV}$)	ALPGEN+HERWIG	CTEQ6L1†	Fullsim	16500
VBF $Z + 2\,\text{jets}$ ($m_{\ell\ell} > 7\,\text{GeV}$)		SHERPA	CT10	Fullsim	5.36

Table 5.2: Monte Carlo samples used to model the signal and background processes. The corresponding cross sections times branching fractions, $\sigma{\cdot}\mathcal{B}$, are quoted at $\sqrt{s} = 8\,\text{TeV}$ and $m_H = 125\,\text{GeV}$ for the signal. Here ℓ refers to e, μ, or τ. The branching fractions include the decays $t \to Wb$, $W \to \ell\nu$, $Z \to \ell\ell$ ($ZZ \to \ell\ell\,\nu\nu$ includes the $\ell\ell$ and $\nu\nu$ branching fraction), and $\tau \to \ell$ for $H \to \tau\tau$. The neutral current $Z/\gamma^* \to \ell\ell$ process is denoted Z or γ^*, depending on the mass of the produced lepton pair. Vector-boson scattering (VBS) and vector-boson fusion (VBF) background processes include all leading-order diagrams with zero QCD vertices for the given final state (except for diagrams with Higgs bosons, which only appear in the signal processes) [112]. Atlfast-II (AFII) refers to fast calorimeter simulation and Fullsim refers to the full GEANT4 simulation, described in Section 4.6. †The DY background is reweighted to the MRSTmcal PDF.

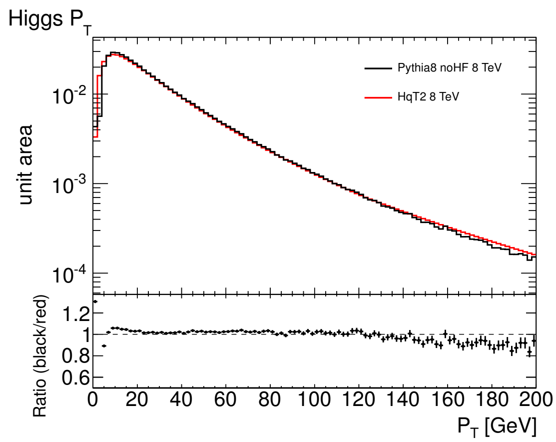

Figure 5.1: Higgs boson p_{T} spectrum of ggF production for $m_H = 125\,\mathrm{GeV}$ at $8\,\mathrm{TeV}$ from HQT2.0 and POWHEG+PYTHIA8 without underlying event (UE), hadronization, or heavy-quark effects, which are not included in the HQT2.0 calculation. The two agree within approximately 5 %.

and treats the uncertainties as uncorrelated:

$$\sigma_0 = \epsilon_0 \sigma_{\mathrm{tot.}}, \quad \sigma_1 = \epsilon_1 (1 - \epsilon_0) \sigma_{\mathrm{tot.}}, \quad \sigma_{\geq 2} = (1 - \epsilon_1)(1 - \epsilon_0) \sigma_{\mathrm{tot.}}\,, \tag{5.2}$$

where the σ_i's are the cross sections for i jets, ϵ_0 is the efficiency of rejecting a jet (defining the $N_{\mathrm{jets}} = 0$ cross section), and ϵ_1 is the efficiency to to reject an additional jet. This allows us to use the highest-order calculation available for each component. We include a resummation calculation for ϵ_0 and the NLO calculation of $H + 2$jets in ϵ_1.

The efficiency ϵ_0 is calculated with JETVHETO [161] as $\epsilon_0 = 0.613 \pm 0.072$ for a jet $p_{\mathrm{T}} > 25\,\mathrm{GeV}$ threshold. Given an event has a jet, the efficiency of rejecting a second jet ϵ_1 is used to define the $N_{\mathrm{jets}} = 1$ and $N_{\mathrm{jets}} \geq 2$ cross sections. It is calculated the same way as ϵ_0 to be $\epsilon_1 = 0.615 \pm 0.086$.

The Stewart-Tackmann method uses inclusive cross section calculations with progressively more jets required:

$$\sigma_0 = \sigma_{\mathrm{tot.}} - \sigma_{\geq 1}, \quad \sigma_1 = \sigma_{\geq 1} - \sigma_{\geq 2}, \quad \sigma_{\geq 2}\,. \tag{5.3}$$

This method does not allow mixing of the order, in order to preserve the total cross section, and is thus limited to the highest common-order calculation available. The fraction of events expected per jet bin, as calculated for the Stewart-Tackmann method are 0.614, 0.267, and 0.119 for the $N_{\mathrm{jets}} = 0, = 1,$ and ≥ 2 categories. The exclusive jet binned uncertainties from the Stewart-Tackmann (JVE) method are 18 %(15 %), 43 %(27 %), and 70 %(34 %) for the $N_{\mathrm{jets}} = 0, = 1,$ and ≥ 2 categories. The uncertainty on the ggF contribution to the VBF channel includes the CJV, i.e., a third jet veto. The Stewart-Tackmann method is used to evaluate this extra 29 % uncertainty.

Additional sources of acceptance uncertainty on ggF Higgs boson production, beyond the jet binning, are evaluated. The QCD scale and PDF uncertainties are a few percent. The PDF uncertainty is taken from the larger of the difference between the nominal PDF compared to the MSTW [162] PDF set or the eigenvector variations of the CT10 set [163]. The generator, and matching of the ME to the PS, uncertainty comes from comparing POWHEG+HERWIG to aMC@NLO[164]+HERWIG. The UE/PS uncertainties are estimated by comparing POWHEG+HERWIG to POWHEG+PYTHIA8. The ggF acceptance uncertainties split by signal region are shown in Table 5.4. The effects of the QCD scale, UE/PS, and generator uncertainties on the m_{T} shape are applied as a systematic uncertainty, correlated with the normalization uncertainty, using a linear parametrization between 40 and 140 GeV. This results in a relative change of roughly 10 % at the bounds.

The VBF total cross section is evaluated with VBF@NNLO [165] for an approximately NNLO in QCD computation. NLO electroweak corrections are evaluated with HAWK [166]. QCD scale variations are negligible and the uncertainty from the PDFs is 2.7 %. The same sources of acceptance uncertainties as for ggF are evaluated for the VBF process and shown for the most sensitive BDT output bin, bin 3, in Table 5.3. The other two bins have similar uncertainties, except for UE/PS, which is 5.2 % in bin 2 and < 1 % in bin 1.

5.2.2.2 Backgrounds

In this section, decays to leptons ℓ include leptonically decaying τs. Most processes are simulated using POWHEG, which is at NLO in QCD. SHERPA [167] and ALPGEN [168] provide merged calculations to include higher parton multiplicities. ALPGEN is used for the $Z/\gamma^* \to \ell\ell$ sample, which is calculated with up to five additional partons. For $gg \to WW$ and single-top-quark t-channel production ($tq\bar{b}$), the LO generators GG2VV [169] and ACERMC [170] are used, respectively. Table 5.2 summarizes the generators and cross sections used for each signal and background process.

The ME from the event generators is matched to a model of the PS, hadronization, and UE. PYTHIA6 [171], PYTHIA8 [130], HERWIG[172] (with JIMMY[173] for the UE), or SHERPA are used for this. The CT10 PDF is used for POWHEG, SHERPA, and GG2VV; and CTEQ6L1 [174] is used for ALPGEN and ACERMC. The ALPGEN $Z \to \ell\ell$ sample is reweighted to the MRSTmcal [175] PDF set.

The programs used to model and normalize the backgrounds follow. The WW inclusive cross section is calculated to NLO in QCD with MCFM [176]. The $q\bar{q}/qg$ (later referred to as $q\bar{q}$) initiated production is modeled with POWHEG+PYTHIA6 for $N_{\mathrm{jets}} \leq 1$ and SHERPA for $N_{\mathrm{jets}} \geq 2$. Non-resonant ggF WW production is calculated to LO in QCD with GG2VV, which

Uncertainty source	N_{jets}=0	N_{jets}=1	$N_{\text{jets}} \geq 2$ ggF	$N_{\text{jets}} \geq 2$ VBF
Gluon-gluon fusion				
Total cross section	10	10	10	7.2
Jet binning or veto	11	25	33	29
Acceptance				
Scale	See Table 5.4			48
PDF				-
Generator				-
UE/PS				15
Vector-boson fusion				
Total cross section	2.7	2.7	2.7	2.7
Acceptance				
Scale	-	-	-	3.0
PDF	-	-	-	3.0
Generator	-	-	-	4.2
UE/PS	-	-	-	14

Table 5.3: Jet binned signal uncertainties (%) for ggF and VBF production. The VBF uncertainties are shown for bin 3, the most sensitive O_{BDT} bin [112]. See Table 5.4 for the ggF acceptance uncertainties.

also includes ZZ to the same final state, and interference between the two. Non-resonant ggF $ZZ \to 4\ell$ is small and not listed in the summary table, but included for completeness, simulated with GG2ZZ [177].

The $t\bar{t}$ cross section is calculated to NNLO+NNLL with TOP++2.0 [178] and modeled with POWHEG+PYTHIA6. Single top-quark production is calculated to NNLL for the s-channel [179], t-channel [180], and associated W channel [181] and modeled with POWHEG/ACERMC+PYTHIA6.

The $W\gamma^*$ process is defined as the associated production of a W boson with a virtual photon and separated from the simulation of WZ by $m_{\ell\ell} < 7\,\text{GeV}$ when there is an opposite-charge (OC) same-flavor lepton pair. It is modeled with SHERPA with up to one extra parton. The jet multiplicity is corrected with a SHERPA sample with up to two additional partons—this sample could not be used outright because the range $2m_e < m_{\gamma^*} < 0.5\,\text{GeV}$ could not be simulated. The cross section is corrected with an NLO MCFM calculation in the same mass region. $W\gamma^*$ with $m_{\ell\ell} > 7\,\text{GeV}$ is simulated with POWHEG+PYTHIA8, which can't model down to the dielectron production threshold. $W\gamma$(defined as the photon originating from ISR, FSR, or radiating off of the Wboson) is modeled using ALPGEN+HERWIG with up to five additional partons and normalized to an NLO MCFM calculation. The sample is

N_{jets}	$m_{\ell\ell}$	$p_{\text{T}}^{\text{lead}}$	Scale	PDF MSTW	PDF 68 % CL	PS/Had./UE PYTHIA	PS/Had./UE HERWIG	NLO-PS Matching (Gen.)
				$ee/\mu\mu$ channel				
0	12–55	> 10	1.4	+1.9	3.2	+1.6	+6.4	-2.5
1			1.9	+1.8	2.8	(-)1.5	+2.1	(-)1.4
				$e\mu$ channel				
0	10–30	10–15	2.6	+1.8	3.2	-1.7	+5.7	-3.5
		15–20	1.3	+1.9	3.2	(+)2.4	+4.9	-2.9
		> 20	1.0	+1.9	3.2	-2.2	(-)1.6	(-)1.4
	30–55	10–15	1.5	+1.8	3.3	(+)2.0	+5.5	-3.8
		15–20	1.5	+1.9	3.3	(-)2.5	(+)2.4	-2.5
		> 20	3.5	+1.9	3.3	-1.9	-2.4	(-)1.3
1	10–30	10–15	3.7	+1.7	2.9	+2.9	+10.8	-3.8
		15–20	9.0	+1.7	2.9	(+)3.8	(+)3.9	(+)3.6
		> 20	3.5	+1.8	2.7	(+)2.1	(+)2.0	(-)1.9
	30–55	10–15	5.7	+1.7	3.0	(+)3.2	+11.4	-6.8
		15–20	3.4	+1.9	3.3	(+)2.6	+13.5	+6.7
		> 20	1.4	+1.8	2.8	(-)1.9	(-)1.8	(+)1.7
≥2	10–55	> 10	18	+2.0	2.2	(-)1.7	(+)1.7	-4.5

Table 5.4: Percent theoretical acceptance uncertainties on the ggF signal process divided into the ggF signal regions. The sign is included to indicate the correlation; when parenthesized, the sign is not statistically significant and the statistical error, rather than central value, of the computation is reported. Mass and momentum units are in GeV.

generated with requirements $p_{\text{T}}^{\gamma} > 8\,\text{GeV}$ and $\Delta R(\gamma, \ell) > 0.25$.

The DY (Z/γ^*) background is also modeled with ALPGEN+HERWIG with up to five additional partons, and is normalized to the NNLO DYNNLO [182, 183] calculation. An additional SHERPA sample, normalized to NLO with MCFM, is used to improve the modeling of $Z\gamma$. The photon is required to have $p_{\text{T}}^{\gamma} > 8\,\text{GeV}$ and $\Delta R(\gamma, \ell) > 0.1$. Overlapping events are removed from the ALPGEN sample.

Non-resonant $WW/WZ/ZZ$ from vector boson scattering (VBS) is included at LO with SHERPA, including the small $ZZ \to 4\ell$ contribution, not included in the summary table. Double parton interaction (DPI) production of two W bosons $(q\bar{q} \to W) + (q\bar{q} \to W)$ is included with PYTHIA8. The DPI cross section is computed using the NNLO $W^{\pm}$ cross section and an effective multiparton cross section, $\sigma_{\text{eff}} = 15\,\text{mb}$, measured by ATLAS using Wjj production [184]. Using an estimate of σ_{eff} for WW production [185], an uncertainty of 60 % is assigned to $\sigma_{\rm eff}$ and the DPI cross section. The contribution of this process is so small, that even a factor of ten increase in the cross section has a 1 % effect on the measured signal strength.

5.3 Object selection

We consider electrons, muons, MET, and jets in the $H \to WW^{(*)} \to \ell\nu\ell\nu$ analysis. The electrons and muons tend to be rather soft, low in $p_{\rm T}$, and so keeping a low $p_{\rm T}$ threshold is important for signal acceptance. Requiring them to be isolated rejects fake-lepton producing backgrounds, such as $W+$jets. MET is used to select events with neutrinos, mostly rejecting DY production. Finally, jets are mostly used for counting to separate backgrounds and signal production modes; however, their topology does play an important role in selecting VBF-like events.

Leptons and jet candidates may lie close to each other in $\eta - \phi$ space and even come from the same particle passing through the detector. Thus an overlap removal procedure is implemented in order to remove such cases. If a muon and electron overlap within $\Delta R < 0.1$, the muon is kept and electron removed. If two electrons overlap within $\Delta R < 0.1$, then the one with the highest $p_{\rm T}$ is kept. If an electron and jet are close, within $\Delta R < 0.3$, the jet is removed because electrons are also reconstructed as jets. However, if a muon and jet overlap within $\Delta R < 0.3$, the muon is removed, in order to reject more non-prompt muons from heavy-flavor decays. Electrons with tracks extending to the MS are removed.

5.3.1 Leptons

Leptons are selected with $p_{\rm T} > 10\,{\rm GeV}$ and $|\eta| < 2.5$ for muons and $|\eta| < 2.47$, excluding the barrel-endcap transition region between $1.37 < |\eta| < 1.52$, for electrons.

The very-tight likelihood (LH) electron identification is used for electrons with $p_{\rm T} < 25\,{\rm GeV}$ because it rejects fake leptons better for the same signal efficiency compared to its cut-based equivalent. Above 25 GeV, fake leptons are less of a problem, and the looser cut-based medium identification, with additional requirements to reject electron candidates with tracks coming from conversion vertices and candidates without a hit in the inner-most pixel lager, is used to increase the signal acceptance. Both relative calorimeter- and track-based isolation requirements are used, loosening with increasing $p_{\rm T}$. Finally, to further reduce fake leptons, the transverse impact parameter significance is required to satisfy $d_0/\sigma_{d_0} < 3.0$, where σ_{d_0} is the estimated uncertainty. The longitudinal impact parameter is required to be $|z_0 \sin\theta| < 0.4\,{\rm mm}$. The electron selection as a function of $p_{\rm T}$ is summarized in Table 5.5.

<table>
<tr><th>E_{T} (GeV)</th><th>Electron ID</th><th>Calo. Isolation Cone Size ΔR</th><th>Track Isolation Cone Size ΔR</th><th>Impact Parameters</th></tr>
<tr><td>10-15</td><td rowspan="3">Very Tight LH</td><td>$\Delta R(0.3)/E_{\mathrm{T}} < 0.20$</td><td>$\Delta R(0.4)/E_{\mathrm{T}} < 0.06$</td><td rowspan="4">$d_0/\sigma_{d_0} < 3.0$, $|z_0 \sin\theta| <$ 0.4 mm</td></tr>
<tr><td>15-20</td><td>$\Delta R(0.3)/E_{\mathrm{T}} < 0.24$</td><td>$\Delta R(0.3)/E_{\mathrm{T}} < 0.08$</td></tr>
<tr><td>20-25</td><td rowspan="2">$\Delta R(0.3)/E_{\mathrm{T}} < 0.28$</td><td rowspan="2">$\Delta R(0.3)/E_{\mathrm{T}} < 0.10$</td></tr>
<tr><td>> 25</td><td>Medium with "CBL"</td></tr>
</table>

Table 5.5: Electron selection as a function of E_{T}. "CBL" refers to the photon conversion flag and B-layer hit, rejecting candidates that have an ID track from a conversion vertex and without a B-layer hit respectively. The energy in the ΔR cone listed is used for the relative isolation calculation as described in Section 4.2.

Muons[2] are required to have segments in at least two MS layers and meet minimum hit requirements for the matched ID track. Requirements similar to electrons on the isolation and impact parameters are imposed, except with a looser longitudinal impact parameter requirement of $|z_0 \sin\theta| < 1.0$ mm and separately optimized isolation requirements, summarized in Table 5.6.

<table>
<tr><th>p_T (GeV)</th><th>Calo. Isolation Cone Size ΔR</th><th>Track Isolation Cone Size ΔR</th><th>Impact Parameters</th></tr>
<tr><td>10-15</td><td>$\Delta R(0.3)/p_{\mathrm{T}} < 0.06$</td><td>$\Delta R(0.4)/p_{\mathrm{T}} < 0.06$</td><td rowspan="4">$d_0/\sigma_{d_0} < 3.0$, $|z_0 \sin\theta| <$ 1.0 mm</td></tr>
<tr><td>15-20</td><td>$\Delta R(0.3)/p_{\mathrm{T}} < 0.12$</td><td>$\Delta R(0.3)/p_{\mathrm{T}} < 0.08$</td></tr>
<tr><td>20-25</td><td>$\Delta R(0.3)/p_{\mathrm{T}} < 0.18$</td><td rowspan="2">$\Delta R(0.3)/p_{\mathrm{T}} < 0.12$</td></tr>
<tr><td>> 25</td><td>$\Delta R(0.3)/p_{\mathrm{T}} < 0.30$</td></tr>
</table>

Table 5.6: Muon selection as a function of p_{T}. The energy in the ΔR cone listed is used for the relative isolation calculation as described in Section 4.3.

5.3.2 Jets

Jets are reconstructed using the anti-k_{t} method with a distance parameter of $R = 0.4$. A requirement of $|\mathrm{JVF}| > 0.5$ for jets with $p_{\mathrm{T}} \leq 50$ GeV and $|\eta| \leq 2.4$ reduces the number of selected pile-up jets. For determining the jet multiplicity, N_{jets}, jets with $p_{\mathrm{T}} > 25$ GeV for

[2] In ATLAS terminology, they are staco combined muons.

$|\eta| \leq 2.4$ and $p_{\mathrm{T}} > 30\,\mathrm{GeV}$ for $2.4 < |\eta| < 4.5$ are used. For events with $N_{\mathrm{jets}} \geq 2$, the two highest p_{T} jets are used as the VBF jets for the calculation of topological variables such as the dijet invariant mass.

Three other sets of jets are used. First, those with $p_{\mathrm{T}} > 20\,\mathrm{GeV}$ are considered when rejecting events with jets in the rapidity gap between the two VBF jets (CJV). Second, jets with $p_{\mathrm{T}} > 20\,\mathrm{GeV}$ and $|\eta| \leq 2.4$ are used for b-tagging. Finally, the jets used for the soft-hadronic recoil calculation, f_{recoil}, are considered if they have $p_{\mathrm{T}} > 10\,\mathrm{GeV}$ with no JVF requirement. The jet calibration is applied to jets with $p_{\mathrm{T}} > 20\,\mathrm{GeV}$; since the DY estimate using f_{recoil} uses data, see Section 5.5.3.2, the MC modeling of jet response below $p_{\mathrm{T}} < 20\,\mathrm{GeV}$ does not need to be corrected.

Identifying jets from b-quarks is done with the MV1 b-tagger using an 85 % efficient operating point. The corresponding probability to mistag a light-jet as a b-jet is 10.3 % [112].

5.3.3 Missing transverse momentum

Three definitions of MET are used, described in more detail in Section 4.5. A track-based MET, $p_{\mathrm{T}}^{\mathrm{miss}}$, is used in the $e\mu$ channel and for the construction of m_{T}. The soft-term is measured with tracks, except in the case where they are replaced by the energy of a selected jet. The $ee/\mu\mu$ channel uses the simpler (no jet correction) $p_{\mathrm{T}}^{\mathrm{miss,trk}}$, which has a better rejection of DY. Calorimeter-based MET, denoted $E_{\mathrm{T}}^{\mathrm{miss}}$, is also used by the $ee/\mu\mu$ channel. The MET distributions of $e\mu$ events, before requirements, are shown in Fig. 5.2 for the three difference definitions.

A relative MET is defined to help separate cases with fake MET from mismeasured objects, leading to the MET aligning with the object, and to separate DY, in particular to $\tau\tau$ where the MET tends to align with the final-state leptons. For the calorimeter based MET, this is defined as

$$E_{\mathrm{T,rel}}^{\mathrm{miss}} = \begin{cases} E_{\mathrm{T}}^{\mathrm{miss}} \cdot \sin\Delta\phi & \text{if } \Delta\phi < \pi/2 \\ E_{\mathrm{T}}^{\mathrm{miss}} & \text{else} \end{cases} , \tag{5.4}$$

where $\Delta\phi$ is the separation between $\boldsymbol{E}_{\mathrm{T}}^{\mathrm{miss}}$ and any selected lepton or jet. Similarly as for $E_{\mathrm{T,rel}}^{\mathrm{miss}}$ in Equation 5.4, we define a $p_{\mathrm{T,rel}}^{\mathrm{miss}}$.

5.4 Event selection

The event selection is divided into a general preselection and per-channel optimized requirements. The preselection picks out the final state. From a technical stand point, its a general selection as a starting point, which reduces the selected number of events to a more manageable level. Table 5.8 lists the complete event selection.

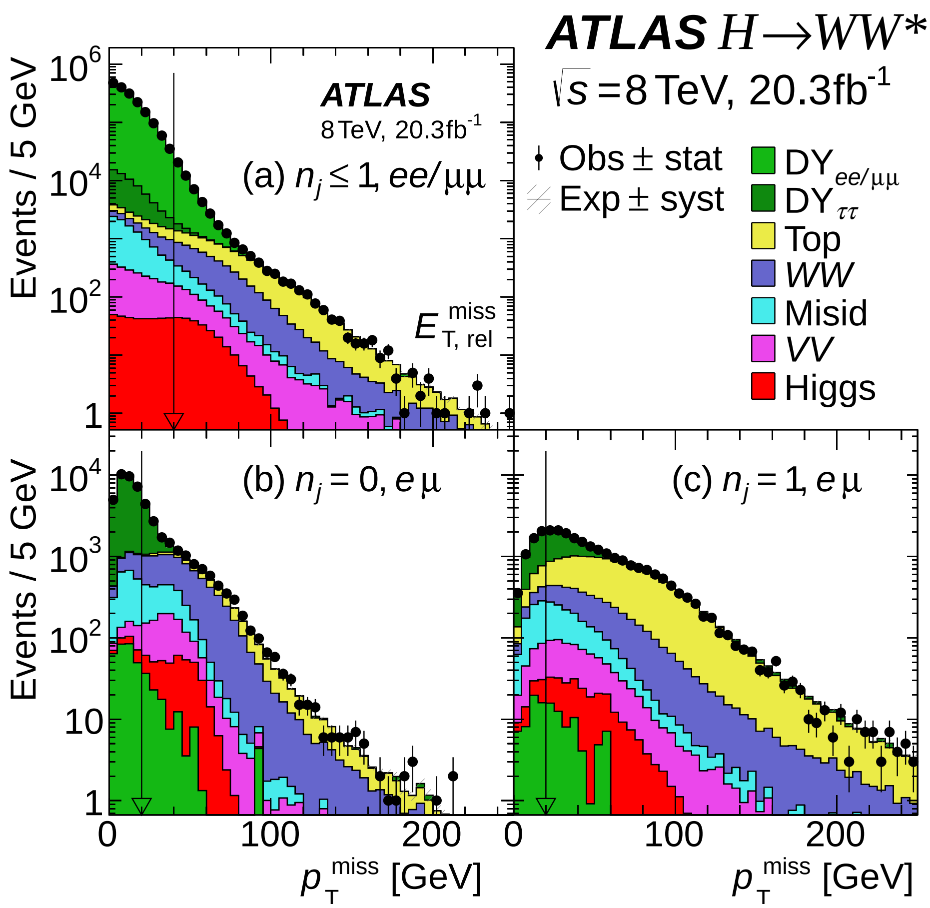

Figure 5.2: MET distributions after the preselection requirements, but before the cuts on MET shown with the black arrow [112]. The observed data, black points, include their statistical uncertainty. The filled histograms (MC) represent the SM signal for $m_H = 125$ GeV and background prediction. Included is a hashed band representing the systematic uncertainty on the prediction, which includes experimental sources and theoretical uncertainties related to the acceptance of signal and backgrounds—it is only visible in the tails of the distributions. The band does not include shape uncertainties on individual processes; the uncertainty on the shape is in any case dominated by the relative normalizations of the backgrounds.

5.4.1 Preselection

Events with two oppositely charged leptons, electrons or muons, with leading $p_{\mathrm{T}}^{\mathrm{lead}} >$ 22 GeV and subleading $p_{\mathrm{T}}^{\mathrm{sub}} > 10$ GeV are selected. Events are required to have a primary vertex (PV) with at least three tracks with $p_{\mathrm{T}} \geq 400$ MeV. A requirement of $m_{\ell\ell} > 10(12)$ GeV for different(same)-flavor events removes low mass resonances. The Z boson resonance is removed by requiring $|m_{\ell\ell} - m_Z| > 15\,\text{GeV}$ for $ee/\mu\mu$ events. Finally, MET requirements are imposed. Except for the VBF channel, the $e\mu$ channels require $p_{\text{T}}^{\text{miss}} > 20\,\text{GeV}$. The $N_{\text{jets}} = 0$ and $N_{\text{jets}} = 1$ $ee/\mu\mu$ categories require $E_{\text{T,rel}}^{\text{miss}} > 40\,\text{GeV}$, and the $ee/\mu\mu$ VBF channel requires $E_{\text{T}}^{\text{miss}} > 45\,\text{GeV}$. The stronger MET requirements for the $ee/\mu\mu$ channels are needed to reduce the large DY background.

The MET distributions are shown in Fig. 5.2 before they are cut on. Good agreement between data and MC over many orders of magnitude is observed. Table 5.7 shows the expected and observed yields after each requirement. After the preselection, the events are binned by N_{jets}, seen in Fig. 5.3, to separate the ggF and VBF production modes as well as backgrounds. WW and DY dominate at low jet multiplicities, while top-quark production quickly dominates with one or more jets.

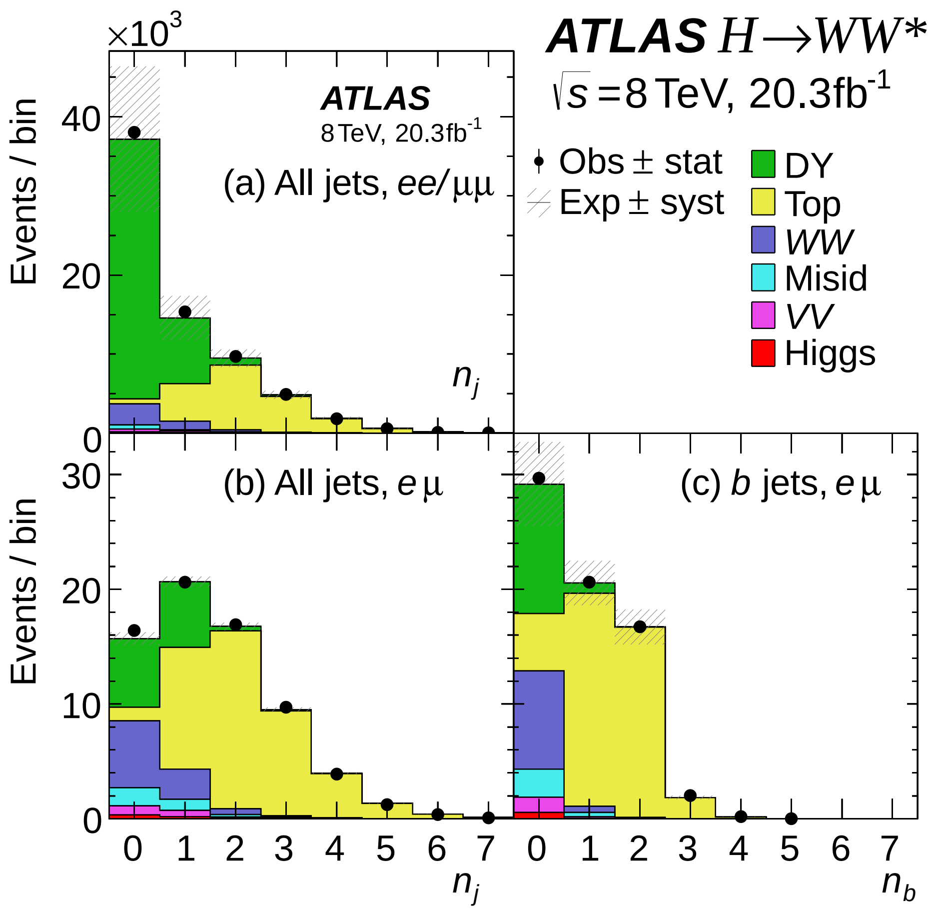

Figure 5.3: Jet multiplicity (n_j) distributions for all jets and b-tagged jets (n_b). The plots are made after the preselection requirements and divided by final state lepton flavor [112].

Cut	Signal	WW	Other VV	$t\bar{t}$	Single Top	$Z \to \ell\ell + \gamma$/jets	$Z \to \tau\tau + \gamma$/jets	$W +$ jets	Multijet	Total Bkg.	Observed	Data/MC
						$e\mu$ Channel						
Sum Weights	847 ± 2	11524 ± 15	4754 ± 22	59897 ± 29	5749 ± 7	2540 ± 90	52130 ± 100	3550 ± 50	7857 ± 11	148000 ± 150	157631	1.07 ± 0.0
$p_{\mathrm{T}}^{\ell} > 22(10)$	811 ± 2	11379 ± 15	4239 ± 20	59387 ± 29	5704 ± 7	910 ± 40	44760 ± 90	6240 ± 40	3447 ± 8	136070 ± 110	142993	1.05 ± 0.0
Opp. Charge	786 ± 2	11341 ± 15	2126 ± 14	62087 ± 30	5917 ± 7	581 ± 35	44640 ± 90	3716 ± 31	2228 ± 6	132630 ± 110	136073	1.03 ± 0.0
$m_{\ell\ell} > 12, 10$ GeV	778 ± 2	11323 ± 15	2017 ± 14	62011 ± 30	5911 ± 7	573 ± 35	44610 ± 90	3726 ± 30	2176 ± 6	132340 ± 110	135734	1.03 ± 0.0
$p_{\mathrm{T}}^{\mathrm{miss}} > 20$	591 ± 2	9122 ± 13	1471 ± 12	37803 ± 23	4351 ± 6	185 ± 21	12020 ± 50	2332 ± 19	600 ± 4	67880 ± 60	69280	1.02 ± 0.0
						$ee/\mu\mu$ Channel						
Sum Weights	910 ± 3	11970 ± 15	10238 ± 24	60872 ± 29	5847 ± 7	16500000 ± 8000	55570 ± 100	21990 ± 160	11914 ± 11	16678000 ± 8000	17084938	1.02 ± 0.0
$p_{\mathrm{T}}^{\ell} > 22(10)$	877 ± 3	11830 ± 15	9728 ± 23	60385 ± 29	5805 ± 7	16160000 ± 8000	49080 ± 90	18530 ± 150	7998 ± 9	16323000 ± 8000	16570089	1.02 ± 0.0
Opp. Charge	848 ± 2	11801 ± 15	7726 ± 18	63153 ± 30	6027 ± 7	16127000 ± 8000	49000 ± 90	18830 ± 150	6902 ± 8	16290000 ± 8000	16535346	1.02 ± 0.0
$m_{\ell\ell} > 12$	825 ± 2	11743 ± 15	7542 ± 18	62900 ± 30	6007 ± 7	16097000 ± 8000	48940 ± 90	22170 ± 140	2429 ± 5	16259000 ± 8000	16394493	1.01 ± 0.0
Z veto	768 ± 2	9217 ± 13	2647 ± 12	49740 ± 27	4745 ± 6	1783800 ± 2000	47130 ± 90	7870 ± 70	2194 ± 5	1907400 ± 2000	2014469	1.06 ± 0.0
$E_{\mathrm{T,rel}}^{\mathrm{miss}} > 40$	288 ± 1	4076 ± 9	631 ± 7	18590 ± 16	2040 ± 4	40190 ± 260	1059 ± 13	836 ± 14	45.0 ± 0.7	67470 ± 260	70655	1.05 ± 0.01

Table 5.7: Expected and observed event yields for the 8 TeV $e\mu$ and $ee/\mu\mu$ channels for the preselection, described in Section 5.4.1. For aesthetics, a normalization factor (NF) of 1.049 ± 0.005 from a jet-inclusive b-tagged region after the MET requirement is applied at "Opp. Charge" to the top-quark backgrounds and the $N_{\mathrm{jets}} = 1$ $Z/\gamma^* \to \tau\tau$ NF of 1.05 ± 0.04 is applied at the MET cut. The errors are statistical only, i.e., from the MC sample size. The signal column includes ggF, VBF, and VH processes at $m_H = 125$ GeV. The last column is the ratio of the observed to total background column. The "Sum Weights" row is a technical reference, two leptons are already required there. Momentum, mass, and MET quantities are in GeV.

Objective	ggF-enriched			VBF-enriched
	$N_{\text{jets}} = 0$	$N_{\text{jets}} = 1$	$N_{\text{jets}} \geq 2$ ggF	$N_{\text{jets}} \geq 2$ VBF
Preselection All N_{jets}	$p_{\text{T}}^{\text{lead}} > 22$ for the leading lepton ℓ_1 $p_{\text{T}}^{\text{sub}} > 10$ for the subleading lepton ℓ_2 Opposite-charge leptons $m_{\ell\ell} > 10$ for the $e\mu$ sample $m_{\ell\ell} > 12$ for the $ee/\mu\mu$ sample $\lvert m_{\ell\ell} - m_Z \rvert > 15$ for the $ee/\mu\mu$ sample			
	$p_{\text{T}}^{\text{miss}} > 20$ for $e\mu$ $E_{\text{T,rel}}^{\text{miss}} > 40$ for $ee/\mu\mu$	$p_{\text{T}}^{\text{miss}} > 20$ for $e\mu$ $E_{\text{T,rel}}^{\text{miss}} > 40$ for $ee/\mu\mu$	$p_{\text{T}}^{\text{miss}} > 20$ for $e\mu$ -	$E_{\text{T}}^{\text{miss}} > 45$ for $ee/\mu\mu$
Reject backgrounds Top	-	$N_{b\text{-jets}} = 0$	$N_{b\text{-jets}} = 0$	$N_{b\text{-jets}} = 0$
	-	-	-	$p_{\text{T}}^{\text{tot}}$ BDT input
	-	-	-	$\Sigma m_{\ell j}$ BDT input
Misid.	-	$m_{\text{T}}^{\ell} > 50$ for $e\mu$	-	-
DY	$\Delta\phi(\boldsymbol{p}_{\text{T}}^{\ell\ell}, \boldsymbol{p}_{\text{T}}^{\text{miss}}) > \pi/2$	-	-	-
	$p_{\text{T}}^{\ell\ell} > 30$	$m_{\tau\tau} < m_Z - 25$ for $e\mu$	$m_{\tau\tau} < m_Z - 25$ for $e\mu$	$m_{\tau\tau} < m_Z - 25$ for $e\mu$
	$p_{\text{T,rel}}^{\text{miss,trk}} > 40$ for $ee/\mu\mu$	$p_{\text{T,rel}}^{\text{miss,trk}} > 35$ for $ee/\mu\mu$	-	$p_{\text{T}}^{\text{miss}} > 40$ for $ee/\mu\mu$
	$f_{\text{recoil}} < 0.1$ for $ee/\mu\mu$	$f_{\text{recoil}}^{j} < 0.1$ for $ee/\mu\mu$	-	
VBF topology	-	-	See Section 5.4.5 for rejection of VBF & VH ($W, Z \to jj$), where $H \to WW^{(*)}$	m_{jj} BDT input Δy_{jj} BDT input ΣC_{ℓ} BDT input $C_{\ell 1} < 1$ & $C_{\ell 2} < 1$ $C_{j3} > 1$ for j_3 with $p_{\text{T}}^{j_3} > 20$ $O_{\text{BDT}} \geq -0.48$
$H \to WW^{(*)} \to \ell\nu\ell\nu$ decay topology	$m_{\ell\ell} < 55$	$m_{\ell\ell} < 55$	$m_{\ell\ell} < 55$	$m_{\ell\ell}$ BDT input
	$\Delta\phi_{\ell\ell} < 1.8$	$\Delta\phi_{\ell\ell} < 1.8$	$\Delta\phi_{\ell\ell} < 1.8$	$\Delta\phi_{\ell\ell}$ BDT input
	-	-	-	m_{T} BDT input

Table 5.8: Summary of event selection divided by N_{jets}. Selections are noted with $e\mu$ and $ee/\mu\mu$ is they are specific to the lepton-flavors in the final state. A dash (-) indicates no selection. The requirements listed are those for the 8 TeV analysis for $m_H = 125$ GeV. Differences with the 7 TeV analysis are given in Section 5.4.6. Momentum, mass, and MET quantities are in GeV [112].

5.4.2 0-Jet category

The MET is expected to balance the dilepton system in events without a jet. We reject events where the MET significantly deviates from this expectation by requiring the MET to be in the other hemisphere with $\Delta\phi(\boldsymbol{p}_{\text{T}}^{\ell\ell}, \boldsymbol{p}_{\text{T}}^{\text{miss}}) > 1.57$. Without a jet to boost the system, DY is expected to have low $p_{\text{T}}^{\ell\ell}$, thus a requirement of $p_{\text{T}}^{\ell\ell} > 30$ GeV is imposed. DY in the $ee/\mu\mu$ channel is further suppressed by requiring $p_{\text{T,rel}}^{\text{miss,trk}} > 40$ GeV.

The next set of requirements are based on the topology of the spin-0 Higgs boson decay and vector–axial (V–A) nature of the W boson decay. The spin correlation of the final state leptons leads to a smaller opening angle. This is particularly useful for separating the Higgs boson signal from the WW continuum background. To take advantage of this, the dilepton invariant mass is required to be low, $m_{\ell\ell} < 55\,\text{GeV}$, and the opening angle between the charged leptons is required to be small, $\Delta\phi_{\ell\ell} < 1.8$.

The $ee/\mu\mu$ channel makes use of an additional discriminant, f_{recoil}, against DY. The variable is based on soft-hadronic recoil against the $p_{\text{T}}^{\ell\ell}$ system. The DY passing the selection up to this point, generally has a mismeasurement of the p_{T} balance. The variable is built by looking for jets with $10 < p_{\text{T}} < 20\,\text{GeV}$ within a $\pi/2$ wedge in ϕ, centered on $-\boldsymbol{p}_{\text{T}}^{\ell\ell}$:

$$f_{\text{recoil}} = \frac{\left|\sum_{\text{jets } j} \text{JVF}_j \cdot \boldsymbol{p}_{\text{T}}^{j}\right|}{p_{\text{T}}^{\ell\ell}}\,. \tag{5.5}$$

The jet momenta are weighted by the jet JVF value to reduce contamination from pile-up jets. A requirement of $f_{\text{recoil}} < 0.1$ is used to further suppress the DY background.

Figure 5.4 shows $\Delta\phi(\boldsymbol{p}_{\text{T}}^{\ell\ell}, \boldsymbol{p}_{\text{T}}^{\text{miss}})$, $p_{\text{T}}^{\ell\ell}$, $m_{\ell\ell}$, $\Delta\phi_{\ell\ell}$, and f_{recoil} in the $N_{\text{jets}} = 0$ category before they are cut on. Table 5.9 shows the expected and observed event yields after each requirement. Generally good agreement between data and MC is observed, with an excess over the background where we expect the signal to appear.

5.4.3 1-Jet category

The $N_{\text{jets}} = 1$ category has a significant background from processes producing top-quarks, which lead to b-jets in the final state. In order to reduce these backgrounds, we require $N_{b\text{-jets}} = 0$, with b-jets defined as in Section 5.3.2. The $e\mu$ channel requires the maximum of the transverse mass defined with either lepton,

$$m_{\text{T}}^{\ell} = \sqrt{2 p_{\text{T}}^{\ell} \cdot p_{\text{T}}^{\text{miss}} \left(1 - \cos\Delta\phi\right)}\,, \tag{5.6}$$

to be larger than 50 GeV. This reduces DY and multijet contributions, which tend to have lower values of the single-lepton transverse mass m_{T}^{ℓ}. DY in the $ee/\mu\mu$ channel is suppressed by requiring $p_{\text{T,rel}}^{\text{miss,trk}} > 35\,\text{GeV}$ and $f_{\text{recoil}}^{j} < 0.1$, where the definition of f_{recoil} in the presence of a jet is extended to include the jet in the denominator: $\boldsymbol{p}_{\text{T}}^{\ell\ell j} = \boldsymbol{p}_{\text{T}}^{\ell\ell} + \boldsymbol{p}_{\text{T}}^{j}$.

The $Z/\gamma^* \to \tau\tau$ process produces events with a final state similar to that of the signal, including $e\mu$ events. The power to reject $Z/\gamma^* \to \tau\tau$ events with $m_{\ell\ell}$ is reduced because of the neutrinos in the final state. The addition of a jet boosting the dilepton system allows for a better reconstruction of the ditau invariant mass using the approximation that the τ decay products are collinear with the τ in the laboratory frame and that they are the only source of MET [56, 186, 187]. The approximation of the ditau invariant mass is calculated ignoring

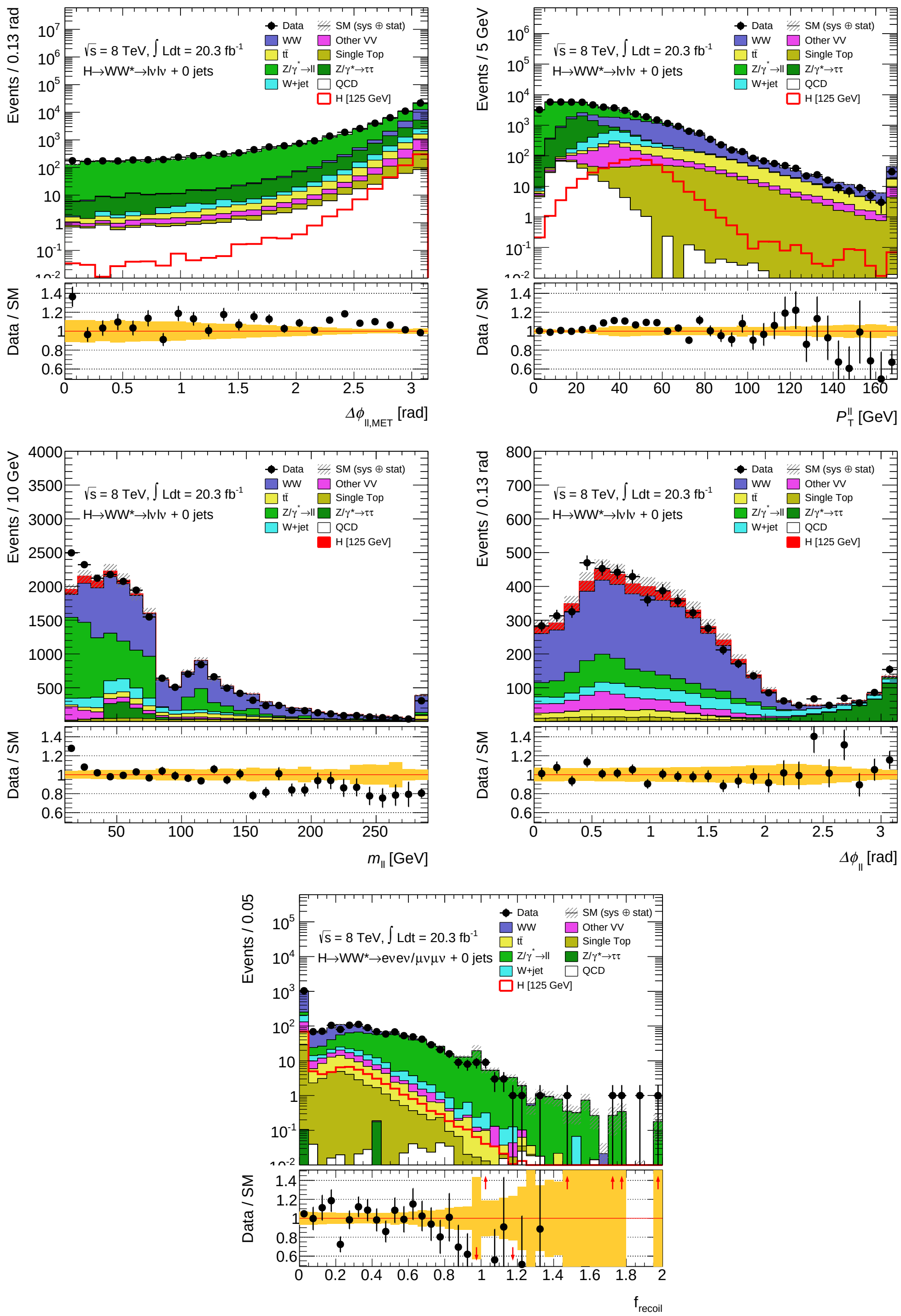

Figure 5.4: Distributions of variables before they are cut on in the 8 TeV $N_{\text{jets}} = 0$ category. The figures with the solid signal histogram have the signal stacked and included in the data to MC ratio; the rest have the signal superimposed to illustrate the shape. The error band, hashed and in the ratio, includes statistical uncertainties from the MC, experimental uncertainties, and theoretical uncertainties on the background and signal acceptance. The last bin contains the overflow.

Cut	Signal	WW	Other VV	$t\bar{t}$	Single Top	$Z \to \ell\ell + \gamma$/jets	$Z \to \tau\tau + \gamma$/jets	W + jets	Multijet	Total Bkg.	Observed	Data/MC
						$e\mu$ Channel						
Jet Veto	322.6 ± 0.9	7113 ± 13	739 ± 8	820 ± 4	407 ± 2	115 ± 15	5567 ± 32	1335 ± 13	237 ± 3	16330 ± 40	16423	1.01 ± 0.01
$\Delta\phi(\boldsymbol{p}_{\mathrm{T}}^{\ell\ell}, \boldsymbol{p}_{\mathrm{T}}^{\mathrm{miss}}) > 1.57$	322.2 ± 0.9	7108 ± 13	736 ± 8	812 ± 4	405 ± 2	114 ± 15	5532 ± 32	1333 ± 13	230 ± 3	16270 ± 40	16339	1.00 ± 0.01
$p_{\mathrm{T}}^{\ell\ell} > 30$	272.8 ± 0.8	5690 ± 11	571 ± 7	730 ± 3	363 ± 2	60 ± 10	783 ± 12	1054 ± 9	28 ± 2	9280 ± 23	9339	1.01 ± 0.01
$m_{\ell\ell} < 55$	232.5 ± 0.7	1670 ± 6	353 ± 6	141 ± 1	79.0 ± 0.8	27 ± 4	350 ± 8	427 ± 6	12 ± 2	3059 ± 14	3411	1.11 ± 0.02
$\Delta\phi_{\ell\ell} < 1.8$	208.9 ± 0.6	1503 ± 6	324 ± 6	132 ± 1	75.0 ± 0.8	19 ± 2	12 ± 2	278 ± 5	9 ± 2	2352 ± 10	2642	1.12 ± 0.02
$0.75 \cdot m_{\mathrm{H}} \leq m_{\mathrm{T}} \leq m_{\mathrm{H}}$	133.6 ± 0.4	660 ± 4	78 ± 3	39.8 ± 0.8	21.3 ± 0.5	4.3 ± 0.9	2.3 ± 0.7	133 ± 3	0.8 ± 0.6	940 ± 6	1129	1.20 ± 0.04
						$ee/\mu\mu$ Channel						
Jet Veto	171.3 ± 0.7	3256 ± 9	358 ± 5	418 ± 2	211 ± 1	31060 ± 230	685 ± 10	504 ± 11	29.2 ± 0.6	36520 ± 230	38040	1.04 ± 0.01
$\Delta\phi(\boldsymbol{p}_{\mathrm{T}}^{\ell\ell}, \boldsymbol{p}_{\mathrm{T}}^{\mathrm{miss}}) > 1.57$	171.1 ± 0.7	3253 ± 9	355 ± 5	416 ± 2	211 ± 1	28520 ± 220	622 ± 10	493 ± 11	25.8 ± 0.6	33890 ± 220	35445	1.05 ± 0.01
$p_{\mathrm{T}}^{\ell\ell} > 30$	160.7 ± 0.6	3009 ± 8	309 ± 5	394 ± 2	201 ± 1	6700 ± 100	21 ± 2	396 ± 7	2.6 ± 0.3	11040 ± 100	11660	1.06 ± 0.01
$m_{\ell\ell} < 55$	146.9 ± 0.6	1256 ± 5	179 ± 4	109 ± 1	64.0 ± 0.8	4843 ± 31	9 ± 1	251 ± 5	2.0 ± 0.3	6713 ± 32	6786	1.01 ± 0.01
$E_{\mathrm{T,rel}}^{\mathrm{miss}} > 40$	121.0 ± 0.5	1097 ± 5	106 ± 3	99 ± 1	58.7 ± 0.7	660 ± 15	0.3 ± 0.2	133 ± 3	0.5 ± 0.2	2156 ± 16	2197	1.02 ± 0.02
$\Delta\phi_{\ell\ell} < 1.8$	117.1 ± 0.5	1068 ± 5	104 ± 3	96 ± 1	57.3 ± 0.7	649 ± 15	0.3 ± 0.2	122 ± 3	0.5 ± 0.2	2097 ± 16	2127	1.01 ± 0.02
$f_{\mathrm{recoil}} < 0.1$	74.8 ± 0.4	786 ± 4	69 ± 2	40.7 ± 0.8	30.9 ± 0.5	91 ± 5	0.1 ± 0.1	78 ± 2	0.0 ± 0.2	1096 ± 8	1108	1.01 ± 0.03
$0.75 \cdot m_{\mathrm{H}} \leq m_{\mathrm{T}} \leq m_{\mathrm{H}}$	58.3 ± 0.3	349 ± 3	31 ± 2	10.8 ± 0.4	8.3 ± 0.3	64 ± 5	0.1 ± 0.1	53 ± 2	-0.1 ± 0.2	517 ± 6	510	0.99 ± 0.05

Table 5.9: Expected and observed event yields for the 8 TeV $e\mu$ and $ee/\mu\mu$ channels for the $N_{\mathrm{jets}} = 0$ category. The NFs in Table 5.28 are applied. See the caption of Table 5.7 for more details on the contents.

Cut	Signal	WW	Other VV	$t\bar{t}$	Single Top	$Z \to \ell\ell + \gamma$/jets	$Z \to \tau\tau + \gamma$/jets	W + jets	Multijet	Total Bkg.	Observed	Data/MC
						$e\mu$ Channel						
$N_{\mathrm{jets}} = 1$	192 ± 1	2754 ± 7	496 ± 7	8413 ± 11	2314 ± 4	66 ± 13	5632 ± 28	663 ± 12	334 ± 2	20670 ± 40	20607	1.00 ± 0.01
b-jet veto	164.9 ± 0.9	2407 ± 7	423 ± 6	1614 ± 5	554 ± 2	56 ± 12	4910 ± 26	535 ± 11	268 ± 2	10767 ± 33	10859	1.01 ± 0.01
Max $m_T^{\ell} > 50$	140.3 ± 0.8	2263 ± 7	366 ± 6	1542 ± 5	530 ± 2	43 ± 11	1983 ± 17	477 ± 7	62.4 ± 1.0	7265 ± 24	7368	1.01 ± 0.01
$Z \to \tau\tau$ veto	119.4 ± 0.7	1667 ± 6	275 ± 5	1106 ± 4	390 ± 2	21 ± 5	688 ± 11	311 ± 6	31.7 ± 0.8	4491 ± 16	4574	1.02 ± 0.02
$m_{\ell\ell} < 55$	100.0 ± 0.6	486 ± 3	139 ± 4	297 ± 2	111 ± 1	6 ± 1	381 ± 8	129 ± 4	18.6 ± 0.6	1569 ± 10	1656	1.06 ± 0.03
$\Delta\phi_{\ell\ell} < 1.8$	87.2 ± 0.5	418 ± 3	119 ± 4	269 ± 2	102 ± 1	5.0 ± 0.9	22 ± 2	88 ± 3	6.1 ± 0.4	1030 ± 6	1129	1.10 ± 0.03
$0.75 \cdot m_{\mathrm{H}} \leq m_{\mathrm{T}} \leq m_{\mathrm{H}}$	48.7 ± 0.4	143 ± 2	42 ± 2	76 ± 1	29.8 ± 0.6	1.1 ± 0.4	2.4 ± 0.7	40 ± 2	0.5 ± 0.2	335 ± 4	407	1.21 ± 0.06
						$ee/\mu\mu$ Channel						
$N_{\mathrm{jets}} = 1$	77.2 ± 0.7	1111 ± 5	192 ± 4	3772 ± 7	999 ± 3	8100 ± 110	279 ± 6	178 ± 7	12.8 ± 0.4	14640 ± 110	15344	1.05 ± 0.01
b-jet veto	66.6 ± 0.6	972 ± 4	163 ± 3	725 ± 3	245 ± 2	6640 ± 100	240 ± 6	137 ± 6	10.2 ± 0.3	9140 ± 100	9897	1.08 ± 0.02
$m_{\ell\ell} < 55$	58.0 ± 0.5	351 ± 3	79 ± 2	226 ± 2	85 ± 1	3420 ± 21	167 ± 5	73 ± 4	7.8 ± 0.3	4409 ± 23	5127	1.16 ± 0.02
$E_{\mathrm{T,rel}}^{\mathrm{miss}} > 35$	42.6 ± 0.4	292 ± 2	49 ± 2	193 ± 2	72.8 ± 0.9	194 ± 8	1.7 ± 0.5	38 ± 2	0.20 ± 0.05	842 ± 9	960	1.14 ± 0.04
$\Delta\phi_{\ell\ell} < 1.8$	38.6 ± 0.4	265 ± 2	44 ± 2	179 ± 2	68.3 ± 0.8	194 ± 8	1.5 ± 0.5	30 ± 2	0.17 ± 0.05	783 ± 9	889	1.14 ± 0.04
$f_{recoil} < 0.10$	23.2 ± 0.3	188 ± 2	30 ± 1	98 ± 1	44.0 ± 0.7	26 ± 3	0.8 ± 0.3	17 ± 1	0.02 ± 0.03	404 ± 4	467	1.16 ± 0.05
$0.75 \cdot m_{\mathrm{H}} \leq m_{\mathrm{T}} \leq m_{\mathrm{H}}$	16.0 ± 0.2	59 ± 1	11.2 ± 0.9	23.1 ± 0.6	10.8 ± 0.3	14 ± 2	0.0 ± 0.0	11.2 ± 1.0	0.00 ± 0.01	129 ± 3	143	1.1 ± 0.1

Table 5.10: Expected and observed event yields for the 8 TeV $e\mu$ and $ee/\mu\mu$ channels for the $N_{\mathrm{jets}} = 1$ category. The NFs in Table 5.28 are applied. See the caption of Table 5.7 for more details on the contents.

the τ rest mass as:

$$m_{\tau\tau} = \frac{m_{\ell\ell}}{\sqrt{x_1 x_2}} \qquad \text{for } x_{1,2} \geq 0 \tag{5.7}$$

$$x_1 = \frac{p^1_x p^2_y - p^1_y p^2_x}{p^1_x p^2_y + E^{\text{miss}}_x p^2_y - p^1_y p^2_x - E^{\text{miss}}_y p^2_x} \tag{5.8}$$

$$x_2 = \frac{p^1_x p^2_y - p^1_y p^2_x}{p^1_x p^2_y - E^{\text{miss}}_x p^1_y - p^1_y p^2_x + E^{\text{miss}}_y p^1_x}\,, \tag{5.9}$$

where $x_{1,2}$ are the fractions of the τ momentum carried by the charged leptons, $p^{1,2}$. The fractions are required to be greater than zero; events failing this approximation, approximately 13 % of $Z/\gamma^* \to \tau\tau$ events, are rejected. This approximation is not used in the $N_{\text{jets}} = 0$ category because roughly 36 % of events fail. A requirement in the $e\mu$ channel of $m_{\tau\tau} < m_Z - 25\,\text{GeV}$ removes a large part of the $Z/\gamma^* \to \tau\tau$ background.

The Higgs topological cuts $m_{\ell\ell}$ and $\Delta\phi_{\ell\ell}$ are the same as in the $N_{\text{jets}} = 0$ category. Figure 5.5 shows max m^{ℓ}_{T}, $m_{\tau\tau}$, $m_{\ell\ell}$, $\Delta\phi_{\ell\ell}$, and f^{j}_{recoil} before they are cut on in the $N_{\text{jets}} = 1$ category. Table 5.10 shows the expected and observed event yields after each requirement Again, generally good agreement between data and MC is observed, with an excess in data where we expect to see the signal.

5.4.4 $N_{\text{jets}} \geq 2$ VBF channel

The $N_{\text{jets}} = 2$ category is divided into VBF and ggF oriented channels. This section covers the VBF selection, primarily driven by a BDT categorization [188, 189]. The BDT is trained with VBF production as signal and the remaining processes, including ggF Higgs boson production, as background. A cut-based cross-check is also performed using some of the BDT inputs, relevant here mostly for distributions of variables and example yields. The VBF topology is characterized by the two forward 'tag' jets (j_1, j_2) with a large rapidity gap between them.

The same ditau mass approximation ($m_{\tau\tau}$) as the $N_{\text{jets}} = 1$ category is used in the $e\mu$ channel to reject $Z/\gamma^* \to \tau\tau$ events with $m_{\tau\tau} < m_Z - 25\,\text{GeV}$. The top-quark background is reduced by requiring $N_{b\text{-jets}} = 0$; though, a significant amount of top-quark events remain, particularly due to b-tagging being limited to the ID acceptance.

Further separation of signal and backgrounds is obtained by using a BDT. The magnitude of the vector sum of transverse momenta, $p^{\text{tot}}_{\text{T}} = |\boldsymbol{p}^{\ell\ell}_{\text{T}} + \boldsymbol{p}^{\text{miss}}_{\text{T}} + \sum_j \boldsymbol{p}^{j}_{\text{T}}|$, is used as an input to the BDT. Additionally, an input to the BDT is the sum of four combinations of lepton–jet invariant masses, $\Sigma m_{\ell j} = m_{\ell 1,j1} + m_{\ell 2,j1} + m_{\ell 1,j2} + m_{\ell 2,j2}$, shown in Fig. 5.6(d), because it has some discrimination against backgrounds, which have different lepton–jet topologies than

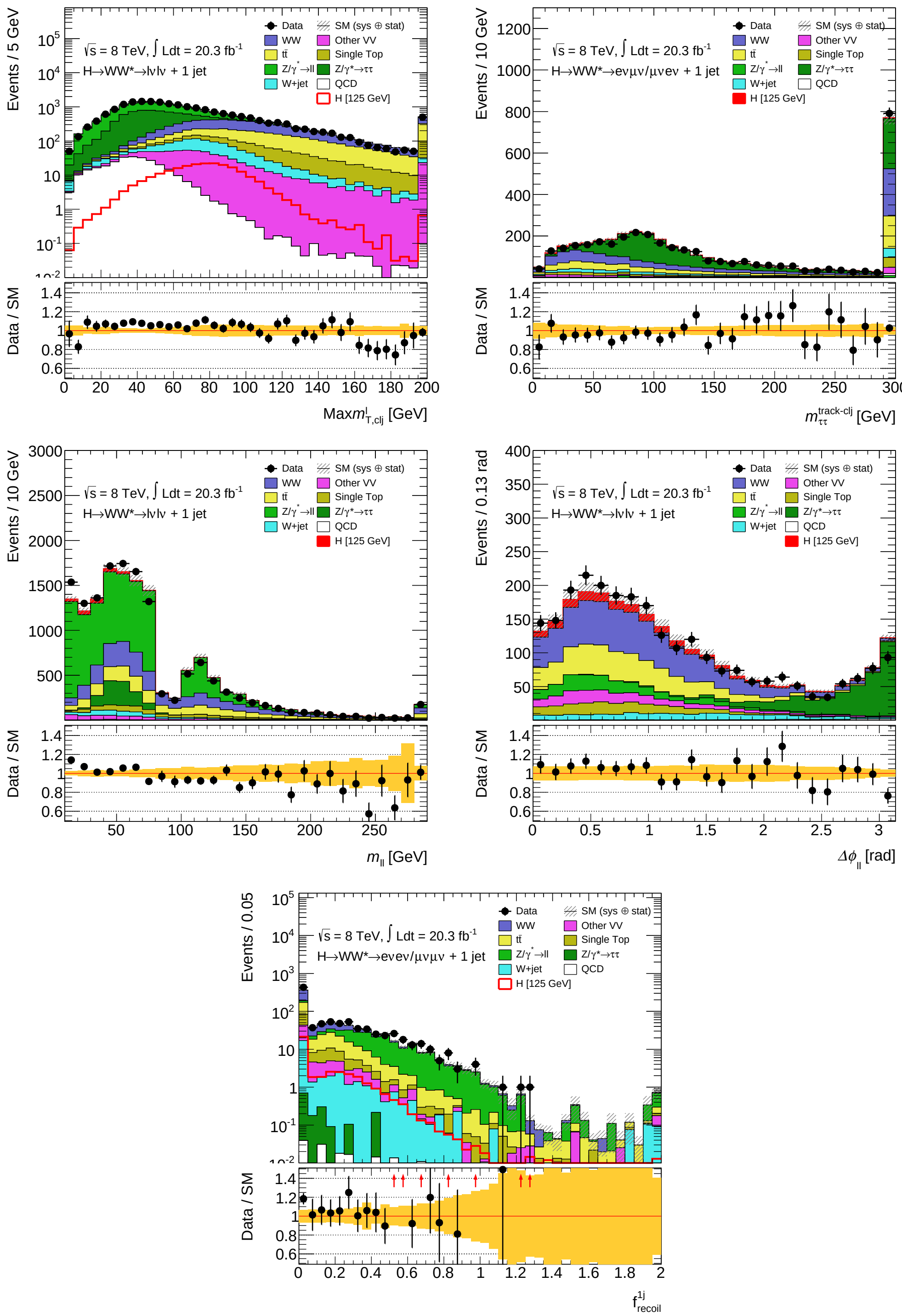

Figure 5.5: Distributions of variables before they are cut on in the 8 TeV $N_{\text{jets}} = 1$ category. The figures with the solid signal histogram have the signal stacked and included in the data to MC ratio; the rest have the signal superimposed to illustrate the shape. The error band, hashed and in the radio, includes statistical uncertainties from the MC, experimental uncertainties, and theoretical uncertainties on the background and signal acceptance. The last bin contains the overflow.

the signal. DY in the $ee/\mu\mu$ channel is further suppressed by requiring $p_{\mathrm{T}}^{\mathrm{miss}} > 40\,\mathrm{GeV}$.

Several inputs to the BDT are designed to take advantage of the forward jet topology of VBF events, including the lack of jets expected in the rapidity gap because the exchanged vector bosons are colorless. Both the dijet invariant mass m_{jj} and rapidity difference Δy_{jj} characterize the forward jet topology and are included in the BDT. Figures 5.6(a) and 5.6(b) show the m_{jj} and Δy_{jj} distributions in the cut-based analysis. The lack of hadronic activity in the central region, rapidity gap, motivates rejecting events with a jet between the forward jets, referred to as a central jet veto (CJV) [190]. The CJV uses jets with $p_{\mathrm{T}} > 20\,\mathrm{GeV}$ and a centrality (C_{j3}) of the third jet is defined:

$$C_{j3} = \frac{\left|\eta_{j3} - \frac{\eta_{j1}+\eta_{j2}}{2}\right|}{\frac{|\eta_{j1}-\eta_{j2}|}{2}}. \tag{5.10}$$

C_{j3} is zero when j_3 is centered between the two tag jets, one when aligned in η with one of the jets, and greater than one when outside of the rapidity gap. Events are required to have $C_{j3} > 1$ in the case of a third jet.

The Higgs boson decay products tend to be central. Using a similarly defined centrality as in Equation 5.10, except with a lepton replacing j_3, both leptons are required to have $C_\ell < 1$ as an outside lepton veto (OLV). The leading lepton centrality from the cut-based analysis is shown in Fig. 5.6(c). The sum of the lepton centralities $\sum C_\ell = C_{\ell 1} + C_{\ell 2}$ is used as an input to the BDT.

Finally, the same Higgs topological variables $m_{\ell\ell}$, $\Delta\phi_{\ell\ell}$, and m_{T} are including in the BDT to take advantage of the decay kinematics. In total, eight distributions are input into the BDT.

The BDT is trained on MC after the preselection, see Section 5.4.1, and additional $m_{\tau\tau}$, C_ℓ, and C_{j3} requirements. The output discriminant (O_{BDT}) lies from -1 to 1, with 1 being signal like. It is binned for the likelihood fit, with the boundaries chosen to maximize expected significance while keeping the bins populated. The binning used has boundaries at $(-1, -0.48, 0.3, 0.78, 1)$, and are labeled 0–3, with bin 0 being mostly background; it is not included in the fit for the VBF channel, but is used for the $N_{\mathrm{jets}} \geq 2$ ggF channel, described in Section 5.4.5.

Tables 5.11 and 5.12 show the expected and observed yields in the 8 TeV VBF analysis. Along with the distributions in Fig. 5.6, generally good agreement between data and MC is observed with an excess in data over the background only expectation.

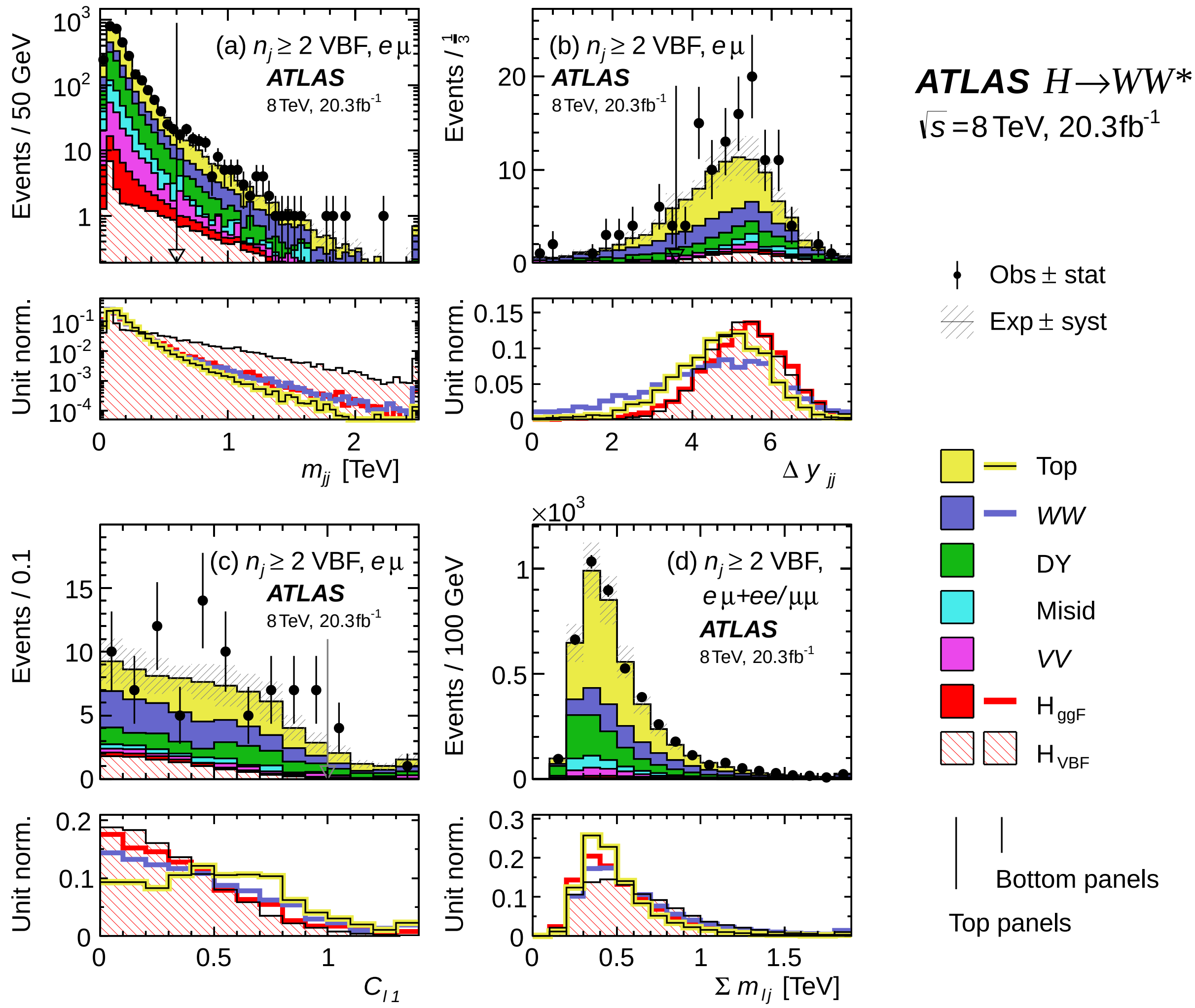

Figure 5.6: Distributions of (a) m_{jj}, (b) Δy_{jj}, (c) $C_{\ell 1}$, and (d) $\Sigma m_{\ell j}$ before they are used in the cut-based analysis (except for $\Sigma m_{\ell j}$ which has no prior selection) [112].

5.4.5 $N_{\text{jets}} \geq 2$ ggF channel

The $N_{\text{jets}} \geq 2$ ggF channel is designed to include more signal in the analysis, which would otherwise be excluded as background by the BDT selection. Only the $e\mu$ final state with the 8 TeV dataset is used, as the rest has negligible signal sensitivity. The selection follows the other ggF categories with the preselection, $m_{\tau\tau} < m_Z - 25$ GeV, and $N_{b\text{-jets}} = 0$ requirements. The channel is forced to be orthogonal to the VBF channel by requiring events to fail at least one of the CJV, OLV, or $O_{\text{BDT}} > -0.48$ requirements. The events are also required to be orthogonal to the cut-based VBF cross-check by failing at least one of $\Delta y_{jj} > 3.6$ and $m_{jj} > 600$ GeV. The final state overlaps with VH production where one of the bosons decays hadronically. The $N_{\text{jets}} \geq 2$ ggF events are made orthogonal to the VH analysis [134] by requiring events to fail at least one of $\Delta y_{jj} \leq 1.2$ and $|m_{jj} - 85| < 15\,\text{GeV}$, where 85 is the average of the Z and W boson masses. The same $m_{\ell\ell}$ and $\Delta\phi_{\ell\ell}$ Higgs boson topological variable requirements are used. Figure 5.7 shows the $m_{\ell\ell}$ distribution before it is cut on, and Table 5.13 lists the expected and observed yields. Generally good agreement between data and MC is observed with an excess in data over the background only expectation.

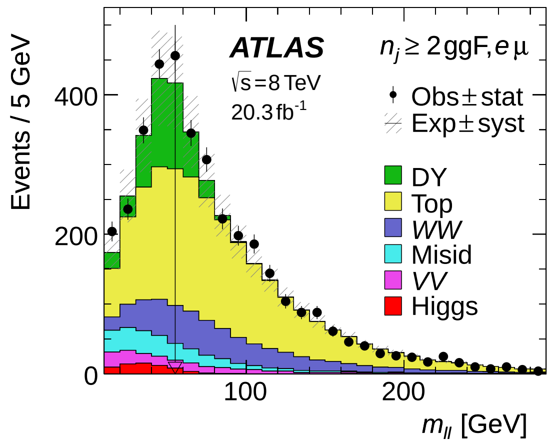

Figure 5.7: Distribution of $m_{\ell\ell}$ in the $N_{\text{jets}} \geq 2$ ggF channel after all selections except $m_{\ell\ell}$ and $\Delta\phi_{\ell\ell}$ [112].

5.4.6 Modifications for 7 TeV dataset

The 7 TeV analysis is kept in line with the 8 TeV analysis where possible, but differs in a few places due to the lower sample size and lower average pile-up.

Only single lepton triggers are used with a p_{T} threshold of 18 GeV for muons and period dependent threshold of 20 or 22 GeV for electrons. Electrons do not use the GSF fit and are identified with only the cut-based Tight++ identification. A tighter isolation requirement on electrons is used to suppress $W+$jets and multijet production. EM jets are used with a tighter $|\text{JVF}| > 0.75$ cut.

The same generators and parton showering are used for the 7 TeV MC, except for WZ and ZZ where POWHEG+PYTHIA6 is used. Pile-up is simulated using PYTHIA6.

The lower pile-up allows for looser requirements. In the $ee/\mu\mu$ channel, the MET requirement is loosened to $E_{\text{T}}^{\text{miss}} > 35\,\text{GeV}$, down from 40 GeV, with no $p_{\text{T}}^{\text{miss}}$ cut. $p_{\text{T}}^{\ell\ell}$ partially compensates this, raised to $p_{\text{T}}^{\ell\ell} > 40\,\text{GeV}$ in $N_{\text{jets}} = 0$ and $p_{\text{T}}^{\ell\ell j} > 35\,\text{GeV}$ (p_{T} of dilepton plus jet system) in $N_{\text{jets}} = 1$. The f_{recoil} cut is loosened to 0.2 and 0.5 in $N_{\text{jets}} = 0$ and $= 1$ respectively. For $N_{\text{jets}} \geq 2$, only the VBF channel is used, with the same BDT, but with bin 2 and 3 merged in the $e\mu$ decay channel, and bins 1–3 merged in the $ee/\mu\mu$ decay channel due to low event yields. Tables 5.14, 5.15, 5.16, and 5.17 show the event yields

Cut	VBF	VH	ggF	WW	$WZ/ZZ/W\gamma$	$t\bar{t}$	Single Top	$Z \to \ell\ell$+jets	EW $Z \to \ell\ell$+jets	$Z \to \tau\tau$+jets	EW $Z \to \tau\tau$+jets	W+jets	QCD	Total Bkg. (+ggf)	Observed	data/MC
$N_{\text{jets}} \geq 2$	32.0 ± 0.2	26 ± 1	85.4 ± 0.3	1422 ± 4	363 ± 6	49775 ± 26	2852 ± 5	49 ± 9	1.4 ± 0.3	3257 ± 21	46 ± 2	885 ± 13	308 ± 2	59040 ± 40	61411	1.04 ± 0.0
b-jet veto	25.5 ± 0.2	16.3 ± 0.8	63.0 ± 0.3	1035 ± 4	260 ± 5	2998 ± 7	363 ± 2	34 ± 9	0.7 ± 0.2	2394 ± 18	28 ± 1	337 ± 8	193 ± 2	7707 ± 23	7815	1.01 ± 0.01
CJV	21.6 ± 0.2	13.5 ± 0.8	50.5 ± 0.2	858 ± 4	216 ± 4	2258 ± 6	300 ± 2	24 ± 6	0.6 ± 0.2	2033 ± 17	23 ± 1	274 ± 8	161 ± 2	6198 ± 21	6310	1.02 ± 0.01
OLV	16.8 ± 0.2	2.5 ± 0.3	15.1 ± 0.1	156 ± 1	44 ± 2	496 ± 3	64.8 ± 0.8	3.6 ± 0.8	0.2 ± 0.1	422 ± 7	8.4 ± 0.7	51 ± 4	33.7 ± 0.7	1295 ± 9	1263	0.98 ± 0.03
$Z \to \tau\tau$ veto	14.5 ± 0.2	1.9 ± 0.3	13.4 ± 0.1	101 ± 1	30 ± 2	339 ± 2	43.5 ± 0.7	2.1 ± 0.7	0.05 ± 0.04	130 ± 4	1.8 ± 0.3	32 ± 3	23.5 ± 0.6	716 ± 6	718	1.00 ± 0.04
$-0.48 < O_{\text{BDT}} < 0.30$	4.20 ± 0.09	0.08 ± 0.05	3.02 ± 0.06	6.0 ± 0.3	2.6 ± 0.5	16.6 ± 0.6	3.1 ± 0.3	0.02 ± 0.02	0.0 ± 0.0	3.9 ± 0.5	0.18 ± 0.09	3.3 ± 0.8	1.8 ± 0.2	40 ± 1	37	0.9 ± 0.1
$0.30 < O_{\text{BDT}} < 0.78$	4.21 ± 0.09	0.02 ± 0.02	1.21 ± 0.04	2.1 ± 0.2	0.8 ± 0.3	1.8 ± 0.1	0.28 ± 0.04	0.0 ± 0.0	0.0 ± 0.0	0.26 ± 0.06	0.4 ± 0.1	0.4 ± 0.3	0.27 ± 0.06	7.4 ± 0.5	14	1.9 ± 0.5
$0.78 < O_{\text{BDT}} < 1.0$	3.12 ± 0.07	0.0 ± 0.0	0.35 ± 0.02	0.54 ± 0.07	0.06 ± 0.06	0.25 ± 0.05	0.07 ± 0.02	0.0 ± 0.0	0.0 ± 0.0	0.06 ± 0.04	0.12 ± 0.09	0.01 ± 0.02	0.0 ± 0.0	1.5 ± 0.1	6	4 ± 2
$0.30 < O_{\text{BDT}} < 1.0$	7.3 ± 0.1	0.02 ± 0.02	1.55 ± 0.04	2.6 ± 0.2	0.8 ± 0.3	2.0 ± 0.1	0.35 ± 0.04	0.0 ± 0.0	0.0 ± 0.0	0.32 ± 0.07	0.5 ± 0.2	0.4 ± 0.3	0.27 ± 0.06	8.8 ± 0.5	20	2.3 ± 0.5

Table 5.11: Expected and observed event yields for the 8 TeV $e\mu$ decay channel for the $N_{\text{jets}} \geq 2$ VBF channel. The NFs in Table 5.28 are applied. See the caption of Table 5.7 for more details on the contents.

Cut	VBF	VH	ggF	WW	$WZ/ZZ/W\gamma$	$t\bar{t}$	Single Top	$Z \to \ell\ell$+jets	EW $Z \to \ell\ell$+jets	$Z \to \tau\tau$+jets	EW $Z \to \tau\tau$+jets	W+jets	QCD	Total Bkg. (+ggf)	Observed	data/MC
$N_{\text{jets}} \geq 2$	20.3 ± 0.2	13.0 ± 0.6	49.6 ± 0.2	392 ± 2	121 ± 3	15086 ± 14	773 ± 3	8330 ± 80	73 ± 2	1234 ± 12	23 ± 1	332 ± 9	36.5 ± 0.6	26450 ± 80	27607	1.04 ± 0.01
b-jet veto	16.1 ± 0.2	7.8 ± 0.5	36.2 ± 0.2	285 ± 2	82 ± 2	882 ± 4	103 ± 1	5840 ± 70	44 ± 1	888 ± 10	14.0 ± 0.9	92 ± 6	22.8 ± 0.5	8290 ± 70	8236	0.99 ± 0.01
$p_{\text{T}}^{\text{miss}} > 40$	14.3 ± 0.2	6.9 ± 0.4	31.1 ± 0.2	265 ± 2	70 ± 2	819 ± 3	95 ± 1	1239 ± 30	9.8 ± 0.7	692 ± 9	11.7 ± 0.8	69 ± 4	11.7 ± 0.3	3313 ± 32	3359	1.01 ± 0.02
CJV	12.1 ± 0.1	5.5 ± 0.4	24.4 ± 0.2	218 ± 2	57 ± 2	619 ± 3	78.3 ± 0.9	952 ± 28	8.0 ± 0.6	566 ± 8	9.5 ± 0.8	53 ± 4	9.3 ± 0.3	2594 ± 30	2648	1.02 ± 0.02
OLV	9.4 ± 0.1	1.0 ± 0.2	7.0 ± 0.1	47.1 ± 0.8	12.9 ± 0.9	157 ± 2	20.0 ± 0.6	226 ± 12	2.3 ± 0.3	116 ± 4	2.9 ± 0.4	8 ± 2	1.9 ± 0.1	601 ± 13	662	1.10 ± 0.05
$Z \to \tau\tau$ veto	7.7 ± 0.1	0.9 ± 0.1	5.95 ± 0.09	40.1 ± 0.8	10.0 ± 0.8	136 ± 1	17.7 ± 0.5	185 ± 11	1.7 ± 0.3	23 ± 2	0.6 ± 0.2	6 ± 1	1.2 ± 0.1	427 ± 11	467	1.09 ± 0.06
$-0.48 < O_{\text{BDT}} < 0.30$	2.17 ± 0.06	0.06 ± 0.04	1.49 ± 0.04	3.5 ± 0.2	0.9 ± 0.2	10.4 ± 0.5	1.8 ± 0.2	25 ± 2	0.4 ± 0.1	1.8 ± 0.3	0.05 ± 0.05	0.8 ± 0.5	0.16 ± 0.04	47 ± 2	53	1.1 ± 0.2
$0.30 < O_{\text{BDT}} < 0.78$	2.48 ± 0.07	0.0 ± 0.0	0.57 ± 0.03	1.1 ± 0.1	0.3 ± 0.2	1.1 ± 0.1	0.23 ± 0.05	4.4 ± 0.6	0.08 ± 0.05	0.28 ± 0.08	0.09 ± 0.05	0.2 ± 0.2	-0.0 ± 0.0	8.5 ± 0.7	14	1.6 ± 0.5
$0.78 < O_{\text{BDT}} < 1.0$	1.74 ± 0.06	0.0 ± 0.0	0.16 ± 0.01	0.26 ± 0.05	0.02 ± 0.02	0.19 ± 0.04	0.04 ± 0.01	0.4 ± 0.1	0.05 ± 0.05	0.01 ± 0.01	0.0 ± 0.0	-0.03 ± 0.02	-0.0 ± 0.0	1.1 ± 0.1	6	6 ± 2
$0.30 < O_{\text{BDT}} < 1.0$	4.21 ± 0.09	0.0 ± 0.0	0.72 ± 0.03	1.4 ± 0.1	0.3 ± 0.2	1.3 ± 0.1	0.27 ± 0.06	4.8 ± 0.6	0.13 ± 0.07	0.29 ± 0.08	0.09 ± 0.05	0.2 ± 0.2	-0.0 ± 0.0	9.6 ± 0.7	20	2.1 ± 0.5

Table 5.12: Expected and observed event yields for the 8 TeV $ee/\mu\mu$ decay channel for the $N_{\text{jets}} \geq 2$ VBF channel. The NFs in Table 5.28 are applied. See the caption of Table 5.7 for more details on the contents.

Cut	Signal	WW	Other VV	$t\bar{t}$	Single Top	$Z \to \ell\ell + \gamma$/jets	$Z \to \tau\tau + \gamma$/jets	W + jets	Multijet	Total Bkg.	Observed	Data/MC
						$e\mu$ Channel						
$N_{\text{jets}} \geq 2$	150 ± 1	1323 ± 4	324 ± 6	49264 ± 27	2814 ± 5	39 ± 11	2514 ± 21	752 ± 12	208 ± 2	57240 ± 40	56759	0.99 ± 0.0
b-jet veto	110.4 ± 0.9	962 ± 4	233 ± 5	2849 ± 6	347 ± 2	28 ± 10	1826 ± 18	277 ± 7	131 ± 2	6652 ± 24	6777	1.02 ± 0.01
$Z \to \tau\tau$ veto	81.7 ± 0.7	610 ± 3	152 ± 4	1898 ± 5	229 ± 2	7 ± 1	478 ± 9	169 ± 6	79 ± 1	3621 ± 13	3826	1.06 ± 0.02
VBF veto	66.6 ± 0.7	592 ± 3	148 ± 4	1871 ± 5	224 ± 2	7 ± 1	470 ± 9	164 ± 5	76 ± 1	3552 ± 13	3736	1.05 ± 0.02
VH veto	57.6 ± 0.6	531 ± 3	132 ± 4	1674 ± 5	198 ± 1	6 ± 1	417 ± 8	142 ± 5	70 ± 1	3170 ± 12	3305	1.04 ± 0.02
$m_{\ell\ell} < 55$	48.5 ± 0.5	158 ± 2	66 ± 3	514 ± 3	58.5 ± 0.8	3.5 ± 0.8	279 ± 7	64 ± 4	59.8 ± 1.0	1202 ± 9	1310	1.09 ± 0.03
$\Delta\phi_{\ell\ell} < 1.8$	44.2 ± 0.4	140 ± 1	60 ± 3	469 ± 3	54.0 ± 0.7	2.5 ± 0.7	130 ± 5	50 ± 4	49.2 ± 0.9	955 ± 7	1017	1.06 ± 0.03
$0.75 \cdot m_{\text{H}} \leq m_{\text{T}} \leq m_{\text{H}}$	17.8 ± 0.3	34.7 ± 0.7	15 ± 1	118 ± 1	12.9 ± 0.4	0.5 ± 0.3	2.7 ± 0.6	15 ± 1	0.6 ± 0.1	200 ± 2	210	1.05 ± 0.07

Table 5.13: Expected and observed event yields for the 8 TeV $e\mu$ decay channel for the $N_{\text{jets}} = 2$ ggF channel. The NFs in Table 5.28 are applied. See the caption of Table 5.7 for more details on the contents.

per requirement in the 7 TeV analysis. The excess in data over background in the 7 TeV is smaller than expected given a Higgs boson; however, the uncertainties are larger, covering this deficit.

5.5 Background estimation

This section describes the methods used to estimate the background processes. The normalization of WW, top-quark processes, $Z/\gamma^* \to \tau\tau$, and other dibosons (VV) are taken from data; for these, the shape and extrapolation of the normalization, is taken from MC. The normalizations of these processes are taken from control regions (CRs), additional background-rich, regions. Only $e\mu$ events are used to normalize backgrounds, except for estimating backgrounds originating from misidentified leptons and DY in the $ee/\mu\mu$ channels. This increases the purity of the CRs used by reducing the DY contamination. In general, the CRs are defined as close to the signal regions (SRs) as possible in order to reduce the theoretical uncertainties on the extrapolation from the CR to the SR. The numbers quoted in this section all pertain to the 8 TeV dataset.

Two quantities discussed in this section are relevant when using CRs. First, normalization factors (NFs) are defined as the scaling needed to match the MC yield to data in the region i:

$$\mathrm{NF}_i = \frac{N_i^{\mathrm{data}} - N_i^{\mathrm{MC,other}}}{N_i^{\mathrm{MC,bkg.}}}\,, \tag{5.11}$$

where $N_i^{\mathrm{MC,other}}$ is the MC prediction for all of the other processes, including the Higgs boson signal, except the background in question $N_i^{\mathrm{MC,bkg.}}$. This represents how far off our predicted yield is, whether from the cross section or from detector effects and poor modeling. The NFs are simultaneously evaluated in the fit, but those listed in Table 5.28 are evaluated sequentially: VV, $Z/\gamma^* \to \tau\tau$, Top, and then WW.

MC is used to model the extrapolation factor α_i of the yields from the CR i to the SR:

$$\alpha_i = \frac{N_{\mathrm{SR}}^{\mathrm{MC,bkg.}}}{N_i^{\mathrm{MC,bkg.}}}\,. \tag{5.12}$$

Theoretical uncertainties are evaluated on these extrapolation factors. These uncertainties are usually smaller than those on the total normalization in the SR by itself. Thus, with a large enough sample in the CR, this method results in a smaller total uncertainty on the predicted background yield.

Table 5.18 summarizes how each background is predicted. The remaining backgrounds not discussed in the following sections, e.g., double parton interaction (DPI) and $Z\gamma$, are

Cut	Signal	WW	$WZ/ZZ/W\gamma$	$t\bar{t}$	Single Top	$Z\to\ell\ell+\gamma$/jets	$Z\to\tau\tau+\gamma$/jets	W+jets	Multijet	Total Bkg.	Observed	Data/Bkg
Jet Veto	46.6 ± 0.3	1132 ± 4	152 ± 3	164 ± 3	71 ± 1	38 ± 5	950 ± 17	288 ± 6	18 ± 1	2812 ± 20	2835	1.01 ± 0.02
$\Delta\phi(\boldsymbol{p}_{\mathrm{T}}^{\ell\ell},\boldsymbol{p}_{\mathrm{T}}^{\mathrm{miss}})>1.57$	46.5 ± 0.3	1128 ± 4	150 ± 3	160 ± 3	70 ± 1	37 ± 5	896 ± 17	289 ± 5	11 ± 1	2740 ± 19	2771	1.01 ± 0.02
$p_{\mathrm{T}}^{\ell\ell}>30$	41.0 ± 0.3	902 ± 3	118 ± 3	145 ± 3	62 ± 1	10 ± 2	123 ± 6	184 ± 4	0.7 ± 0.7	1544 ± 9	1554	1.01 ± 0.03
$m_{\ell\ell}<55$	35.4 ± 0.2	251 ± 2	75 ± 2	26 ± 1	13.2 ± 0.5	4 ± 1	51 ± 4	79 ± 2	0.2 ± 0.7	500 ± 6	486	0.97 ± 0.05
$\Delta\phi_{\ell\ell}<1.8$	32.1 ± 0.2	228 ± 2	69 ± 2	24 ± 1	12.4 ± 0.5	2 ± 1	8 ± 1	57 ± 2	-0.0 ± 0.6	400 ± 4	380	0.95 ± 0.05
$N_{\mathrm{jets}}=1$	21.9 ± 0.2	360 ± 2	84 ± 2	1284 ± 8	326 ± 2	21 ± 3	998 ± 16	31 ± 7	7.4 ± 0.5	3111 ± 20	3140	1.01 ± 0.02
b-jet veto	18.8 ± 0.2	310 ± 2	72 ± 2	236 ± 3	76 ± 1	18 ± 3	856 ± 15	21 ± 6	5.4 ± 0.5	1595 ± 17	1641	1.03 ± 0.03
max $m_{\mathrm{T}}^{\ell}>50$	16.7 ± 0.1	293 ± 2	60 ± 2	226 ± 3	73 ± 1	9 ± 2	317 ± 9	45 ± 5	3.2 ± 0.3	1026 ± 12	1095	1.07 ± 0.03
$m_{\tau\tau}<66$	15.5 ± 0.1	212 ± 2	44 ± 2	161 ± 3	53.1 ± 0.9	4 ± 1	92 ± 5	36 ± 3	1.4 ± 0.3	604 ± 7	660	1.09 ± 0.04
$m_{\ell\ell}<55$	13.3 ± 0.1	60.7 ± 0.8	22 ± 1	41 ± 1	14.7 ± 0.5	1.0 ± 0.5	50 ± 4	15 ± 2	0.9 ± 0.2	205 ± 5	264	1.29 ± 0.08
$\Delta\phi_{\ell\ell}<1.8$	11.7 ± 0.1	52.8 ± 0.7	19 ± 1	37 ± 1	13.5 ± 0.5	1.0 ± 0.5	4.4 ± 1.0	13 ± 2	0.5 ± 0.1	141 ± 3	184	1.3 ± 0.1

Table 5.14: Expected and observed event yields for the 7 TeV $e\mu$ channel for the $N_{\mathrm{jets}}=0$ and $=1$ categories. The NFs in Table 5.28 are applied. See the caption of Table 5.7 for more details on the contents.

Cut	Signal	WW	$WZ/ZZ/W\gamma$	$t\bar{t}$	Single Top	$Z\to\ell\ell+\gamma$/jets	$Z\to\tau\tau+\gamma$/jets	W+jets	QCD	Total Bkg.	Observed	Data/Bkg
Jet Veto	32.1 ± 0.2	612 ± 3	69 ± 2	88 ± 2	40.5 ± 0.8	3640 ± 50	76 ± 5	105 ± 4	4.4 ± 0.7	4630 ± 50	4709	1.02 ± 0.02
$\Delta\phi(\boldsymbol{p}_{\mathrm{T}}^{\ell\ell},\boldsymbol{p}_{\mathrm{T}}^{\mathrm{miss}})>1.57$	32.1 ± 0.2	611 ± 3	68 ± 2	87 ± 2	40.4 ± 0.8	3170 ± 50	67 ± 4	99 ± 4	4.2 ± 0.4	4150 ± 50	4192	1.01 ± 0.02
$p_{\mathrm{T}}^{\ell\ell}>40$	24.3 ± 0.2	473 ± 2	41 ± 1	74 ± 2	34.0 ± 0.8	269 ± 11	0.4 ± 0.3	41 ± 2	0.2 ± 0.1	933 ± 12	907	0.97 ± 0.03
$m_{\ell\ell}<55$	22.8 ± 0.2	193 ± 2	21 ± 1	19.1 ± 0.9	11.0 ± 0.4	181 ± 8	0.0 ± 0.0	27 ± 2	0.2 ± 0.1	452 ± 9	458	1.01 ± 0.05
$\Delta\phi_{\ell\ell}<1.8$	22.2 ± 0.2	189 ± 2	20 ± 1	18.8 ± 0.9	10.9 ± 0.4	175 ± 8	0.0 ± 0.0	25 ± 1	0.2 ± 0.1	438 ± 8	445	1.01 ± 0.05
$f_{\mathrm{recoil}}<0.2$	15.3 ± 0.2	154 ± 1	13.8 ± 0.8	8.4 ± 0.6	6.9 ± 0.3	17 ± 3	0.0 ± 0.0	15 ± 1	0.08 ± 0.09	215 ± 4	214	1.00 ± 0.07
$N_{\mathrm{jets}}=1$	11.7 ± 0.1	168 ± 1	34 ± 1	635 ± 5	156 ± 2	784 ± 20	56 ± 4	35 ± 3	1.3 ± 0.3	1867 ± 21	1901	1.02 ± 0.03
b-jetveto	10.0 ± 0.1	145 ± 1	29 ± 1	117 ± 2	36.4 ± 0.8	654 ± 18	46 ± 4	26 ± 3	1.1 ± 0.3	1054 ± 19	1121	1.06 ± 0.04
$m_{\ell\ell}<55$	8.8 ± 0.1	49.5 ± 0.7	13.8 ± 0.8	36 ± 1	12.7 ± 0.5	311 ± 10	35 ± 3	15 ± 2	0.9 ± 0.2	473 ± 11	503	1.06 ± 0.05
$p_{\mathrm{T}}^{\ell\ell j}>35$	7.8 ± 0.1	46.7 ± 0.7	11.8 ± 0.8	33 ± 1	11.8 ± 0.4	77 ± 6	22 ± 2	9 ± 2	0.4 ± 0.2	212 ± 7	202	0.95 ± 0.07
$\Delta\phi_{\ell\ell}<1.8$	6.66 ± 0.09	40.5 ± 0.6	9.1 ± 0.7	30 ± 1	10.7 ± 0.4	62 ± 5	14 ± 2	5 ± 2	0.2 ± 0.2	172 ± 6	162	0.94 ± 0.08
$f_{\mathrm{recoil}}<0.5$	6.21 ± 0.09	38.8 ± 0.6	8.6 ± 0.6	28 ± 1	9.9 ± 0.4	27 ± 3	13 ± 2	6.1 ± 0.9	-0.00 ± 0.04	131 ± 4	120	0.92 ± 0.09

Table 5.15: Expected and observed event yields for the 7 TeV $ee/\mu\mu$ channel for the $N_{\mathrm{jets}}=0$ and $=1$ categories. The NFs in Table 5.28 are applied. See the caption of Table 5.7 for more details on the contents.

Cut	VBF+VH	ggF	WW	ZW	$W\gamma$	$t\bar{t}$	Single Top	$Z \to \ell\ell$+jets	EW $Z \to \ell\ell$+jets	$Z \to \tau\tau$+jets	EW $Z \to \tau\tau$+jets	W+jets	Total Bkg. (+ggf)	Observed	Data/MC
$N_{\text{jets}} \geq 2$	6.65 ± 0.09	10.6 ± 0.1	143 ± 1	29.8 ± 0.7	24 ± 2	6477 ± 17	358 ± 2	19 ± 2	0.05 ± 0.02	486 ± 9	2.9 ± 0.2	109 ± 6	7670 ± 20	8040 ± 90	1.05 ± 0.01
b-jet veto	4.69 ± 0.07	7.6 ± 0.1	102 ± 1	21.1 ± 0.6	18 ± 1	331 ± 4	40.2 ± 0.8	14 ± 1	0.02 ± 0.02	348 ± 7	1.8 ± 0.1	59 ± 3	948 ± 9	949 ± 31	1.00 ± 0.03
$p_{\text{T}}^{\text{miss}} > 40$	4.69 ± 0.07	7.6 ± 0.1	102 ± 1	21.1 ± 0.6	18 ± 1	331 ± 4	40.2 ± 0.8	14 ± 1	0.02 ± 0.02	348 ± 7	1.8 ± 0.1	59 ± 3	948 ± 9	949 ± 31	1.00 ± 0.03
CJV	4.18 ± 0.06	6.3 ± 0.1	90.8 ± 1.0	18.5 ± 0.6	15 ± 1	260 ± 3	34.2 ± 0.7	12 ± 1	0.02 ± 0.02	297 ± 7	1.6 ± 0.1	56 ± 3	796 ± 9	799 ± 28	1.00 ± 0.04
OLV	2.50 ± 0.04	1.87 ± 0.05	18.3 ± 0.4	3.7 ± 0.2	2.5 ± 0.5	59 ± 2	7.1 ± 0.3	1.4 ± 0.4	0.01 ± 0.01	96 ± 5	0.54 ± 0.07	13 ± 2	204 ± 5	194 ± 14	0.94 ± 0.07
$Z \to \tau\tau$ veto	2.13 ± 0.03	1.63 ± 0.05	11.5 ± 0.3	2.4 ± 0.2	2.0 ± 0.5	31 ± 1	3.9 ± 0.2	0.5 ± 0.2	0	31 ± 3	0.15 ± 0.04	9 ± 1	95 ± 3	100 ± 10	1.0 ± 0.1
$O_{\text{BDT}} > -0.48$	1.48 ± 0.02	0.56 ± 0.03	0.86 ± 0.09	0.20 ± 0.05	0.2 ± 0.1	1.3 ± 0.2	0.21 ± 0.05	0	0	1.3 ± 0.4	0.04 ± 0.02	0.1 ± 0.2	4.9 ± 0.6	6 ± 2	0.9 ± 0.4
$-0.48 < O_{\text{BDT}} 0.3$	0.56 ± 0.01	0.38 ± 0.02	0.58 ± 0.07	0.17 ± 0.05	0.2 ± 0.1	0.9 ± 0.2	0.18 ± 0.04	0	0	1.3 ± 0.4	0.04 ± 0.02	0.1 ± 0.2	4.0 ± 0.5	6 ± 2	1.3 ± 0.6
$O_{\text{BDT}} > 0.3$	0.93 ± 0.02	0.18 ± 0.02	0.28 ± 0.05	0.03 ± 0.03	0	0.3 ± 0.1	0.03 ± 0.02	0	0	0	0	0.02 ± 0.02	0.9 ± 0.1	0	0

Table 5.16: Expected and observed event yields for the 7 TeV $e\mu$ decay channel for the $N_{\text{jets}} \geq 2$ VBF channel. The NFs in Table 5.28 are applied starting at the CJV for $Z/\gamma^* \to \tau\tau$ and OLV for top-quark processes. See the caption of Table 5.7 for more details on the contents.

Cut	VBF+VH	ggF	WW	ZW	$W\gamma$	$t\bar{t}$	Single Top	$Z \to \ell\ell$+jets	EW $Z \to \ell\ell$+jets	$Z \to \tau\tau$+jets	EW $Z \to \tau\tau$+jets	W+jets	Total Bkg.(+ggf)	Data	Data/MC
$N_{\text{jets}} \geq 2$	4.19 ± 0.07	6.2 ± 0.1	39.2 ± 0.7	9.9 ± 0.4	4.7 ± 0.7	1923 ± 9	98 ± 1	427 ± 9	1.8 ± 0.2	177 ± 5	1.5 ± 0.1	25 ± 4	2717 ± 15	2830 ± 50	1.04 ± 0.02
b-jet veto	2.91 ± 0.05	4.31 ± 0.08	27.6 ± 0.5	6.6 ± 0.3	3.6 ± 0.6	101 ± 2	11.2 ± 0.4	296 ± 8	1.1 ± 0.1	122 ± 4	0.79 ± 0.09	7 ± 2	584 ± 10	577 ± 24	0.98 ± 0.04
$p_{\text{T}}^{\text{miss}} > 40$	2.61 ± 0.05	3.70 ± 0.07	25.9 ± 0.5	5.7 ± 0.3	3.4 ± 0.6	95 ± 2	10.5 ± 0.4	71 ± 4	0.24 ± 0.05	101 ± 4	0.69 ± 0.08	4 ± 2	321 ± 6	328 ± 18	1.01 ± 0.06
CJV	2.32 ± 0.05	3.03 ± 0.07	22.8 ± 0.5	5.0 ± 0.3	3.1 ± 0.6	74 ± 2	9.0 ± 0.4	55 ± 4	0.16 ± 0.04	86 ± 4	0.63 ± 0.08	4 ± 1	262 ± 6	261 ± 16	0.99 ± 0.06
OLV	1.37 ± 0.03	0.87 ± 0.04	5.4 ± 0.2	1.0 ± 0.1	0.8 ± 0.3	17.3 ± 0.8	2.3 ± 0.2	11 ± 2	0.03 ± 0.02	23 ± 2	0.17 ± 0.04	0.7 ± 0.6	63 ± 3	56 ± 7	0.9 ± 0.1
$Z \to \tau\tau$ veto	1.12 ± 0.02	0.73 ± 0.03	4.4 ± 0.2	0.8 ± 0.1	0.5 ± 0.2	12.0 ± 0.6	1.5 ± 0.1	8 ± 1	0.03 ± 0.02	6 ± 1	0.03 ± 0.02	0.5 ± 0.5	35 ± 2	39 ± 6	1.1 ± 0.2
$O_{\text{BDT}} > -0.48$	0.82 ± 0.02	0.23 ± 0.02	0.63 ± 0.07	0.07 ± 0.03	0.1 ± 0.1	0.5 ± 0.1	0.10 ± 0.03	2.1 ± 0.7	0	0.7 ± 0.4	0.01 ± 0.01	0.2 ± 0.1	4.6 ± 0.8	3 ± 2	0.6 ± 0.3
$-0.48 < O_{\text{BDT}} < 0.3$	0.29 ± 0.01	0.16 ± 0.02	0.50 ± 0.07	0.06 ± 0.03	0.1 ± 0.1	0.4 ± 0.1	0.08 ± 0.03	1.8 ± 0.6	0	0.7 ± 0.4	0.01 ± 0.01	0.2 ± 0.1	3.9 ± 0.8	1 ± 1	0.2 ± 0.2
$O_{\text{BDT}} > 0.3$	0.53 ± 0.01	0.07 ± 0.01	0.13 ± 0.03	0.0 ± 0.0	0	0.10 ± 0.06	0.01 ± 0.01	0.3 ± 0.2	0	0.08 ± 0.06	0	-0.0 ± 0.0	0.7 ± 0.2	2 ± 1	2 ± 1

Table 5.17: Expected and observed event yields for the 7 TeV $ee/\mu\mu$ decay channel for the $N_{\text{jets}} \geq 2$ VBF channel. The NFs in Table 5.28 are applied starting at the CJV for $Z/\gamma^* \to \tau\tau$ and OLV for top-quark processes. See the caption of Table 5.7 for more details on the contents.

estimated completely from MC.

Category		WW	Top	Misid	VV	Drell–Yan $ee/\mu\mu$	Drell–Yan $\tau\tau$
$N_{\text{jets}} = 0$	$e\mu$	N	N	N/S/E	N	-	N
	$ee/\mu\mu$				-	N/E	
$N_{\text{jets}} = 1$	$e\mu$	N	N	N/S/E	N	-	N
	$ee/\mu\mu$				-	N/E	
$N_{\text{jets}} \geq 2$ ggF	$e\mu$	-	N	N/S/E	-	-	N
$N_{\text{jets}} \geq 2$ VBF	$e\mu$	-	N	N/S/E	-	-	N
	$ee/\mu\mu$					N/E	

Table 5.18: Summary of which background estimations are taken from data, broken into the normalization (N), extrapolation from from CR-to-SR (E), and shape of the distribution (S). An entry indicates data usage, and a dash (-) indicates everything is taken from MC.

5.5.1 Standard Model *WW*

Quark initiated WW production is the dominant background in the $N_{\text{jets}} = 0$ category (64 % of $e\mu$ SR) and in the $N_{\text{jets}} = 1$ category (72 % of $e\mu$ SR). Continuum WW production is an irreducible background, producing the same final state as the signal. An $e\mu$ CR is used in each of these categories to normalize the predicted gluon and quark initiated continuum WW yield in the signal regions.

5.5.1.1 $N_{\text{jets}} \leq 1$ categories

The $N_{\text{jets}} = 0$ WW CR is constructed by starting with events after the $p_{\text{T}}^{\ell\ell} > 30\,\text{GeV}$ requirement, see Table 5.8, leaving out the DY reduction and Higgs boson topological cuts, which are not needed. Then we require $p_{\text{T}}^{\text{sub}} > 15\,\text{GeV}$ for the sub-leading lepton in order to reduce $W + \text{jets}$ contamination and $\Delta\phi_{\ell\ell} < 2.6$ to reduce $Z/\gamma^* \to \tau\tau$ contamination. The region sits next to the SR in $m_{\ell\ell}$, using the range $55 < m_{\ell\ell} < 110\,\text{GeV}$. The upper bound in $m_{\ell\ell}$ is chosen based on the expected signal significance; raising the bound increases the theoretical uncertainty on the extrapolation to the SR, but increases the sample size in the CR. Figure 5.8(a) shows the m_{T} distribution in the $N_{\text{jets}} = 0$ WW CR and Table 5.19 lists the expected and observed yields. The CR is 73 % pure in WW and we observe an NF of 1.22 ± 0.03 (stat.).

The $N_{\text{jets}} = 1$ WW CR is constructed by starting with events after the m_{T}^{ℓ} requirement. Again, $W + \text{jets}$ contamination is reduced by requiring $p_{\text{T}}^{\text{sub}} > 15\,\text{GeV}$ and a $Z/\gamma^* \to \tau\tau$ veto

Region	Signal	WW	Other VV	$t\bar{t}$	Single Top	$Z \to \ell\ell + \gamma$/jets	$Z \to \tau\tau + \gamma$/jets	W + jets	Multijet	Total Bkg.	Observed	Data/MC
0j WW	28.4 ± 0.4	1954 ± 7	97 ± 3	216 ± 2	119 ± 1	9 ± 1	106 ± 4	182 ± 3	2.0 ± 0.5	2685 ± 9	2713	1.01 ± 0.02
0j $Z \to \tau\tau$	22.2 ± 0.3	117 ± 2	33 ± 2	11.5 ± 0.4	5.0 ± 0.3	28 ± 8	4102 ± 28	146 ± 7	93 ± 1	4535 ± 30	4557	1.00 ± 0.02
0j SC VV	2.1 ± 0.4	2.5 ± 0.2	327 ± 6	0.59 ± 0.09	0.47 ± 0.07	19 ± 2	2.7 ± 0.8	174 ± 4	5.5 ± 0.7	531 ± 8	533	1.00 ± 0.05
1j WW	4.2 ± 0.4	1148 ± 5	127 ± 3	834 ± 4	270 ± 2	17 ± 9	81 ± 4	152 ± 3	12.8 ± 0.4	2643 ± 12	2647	1.00 ± 0.02
1j $Z \to \tau\tau$	18.1 ± 0.3	99 ± 1	27 ± 1	56.0 ± 0.9	18.7 ± 0.5	7 ± 3	1225 ± 13	64 ± 4	20.3 ± 0.5	1516 ± 14	1540	1.02 ± 0.03
1j Top	17.0 ± 0.5	244 ± 2	50 ± 2	4642 ± 8	1428 ± 3	6 ± 4	204 ± 6	90 ± 4	12.3 ± 0.4	6676 ± 12	6722	1.01 ± 0.01
1j SC VV	1.9 ± 0.3	1.0 ± 0.1	117 ± 4	1.3 ± 0.1	1.8 ± 0.4	4.7 ± 0.9	0.8 ± 0.4	62 ± 3	3.0 ± 0.2	192 ± 4	194	1.01 ± 0.08
2j Top	4.8 ± 0.5	453 ± 3	101 ± 3	1713 ± 5	213 ± 1	10 ± 6	44 ± 3	112 ± 3	16.9 ± 0.4	2664 ± 10	2664	1.00 ± 0.02
2j $Z \to \tau\tau$	2.5 ± 0.1	10.8 ± 0.4	4.1 ± 0.7	32.4 ± 0.7	3.6 ± 0.3	0.1 ± 0.1	194 ± 6	10 ± 2	8.3 ± 0.6	263 ± 6	266	1.01 ± 0.07

Table 5.19: Expected and observed yields in the control regions of the 8 TeV ggF channels. The data to MC ratio is not identically one because it does not include the signal contribution, while the NF calculation does. The NFs in Table 5.28 are applied. See the caption of Table 5.7 for more details on the contents.

Control regions	Observed	Total Bkg.	Signal	WW	Top	Misid	Other VV	$Z \to \ell\ell$	$Z \to \tau\tau$
CR for top quarks, bin 1	143	142±2	2.1	1.9	130	2.1	0.8	6.3	1.1
CR for top quarks, bin 2–3	14	14.3±0.5	1.8	0.6	11.6	0.2	0.2	0.9	0.2
CR for $Z/\gamma^* \to \tau\tau$	24	20.7±0.9	2.4	0.9	1.2	0.6	0.2	0.8	17

Table 5.20: Expected and observed yields in the 8 TeV VBF control regions. The NFs in Table 5.28 are applied. The uncertainties on the total background are from the MC sample size [112].

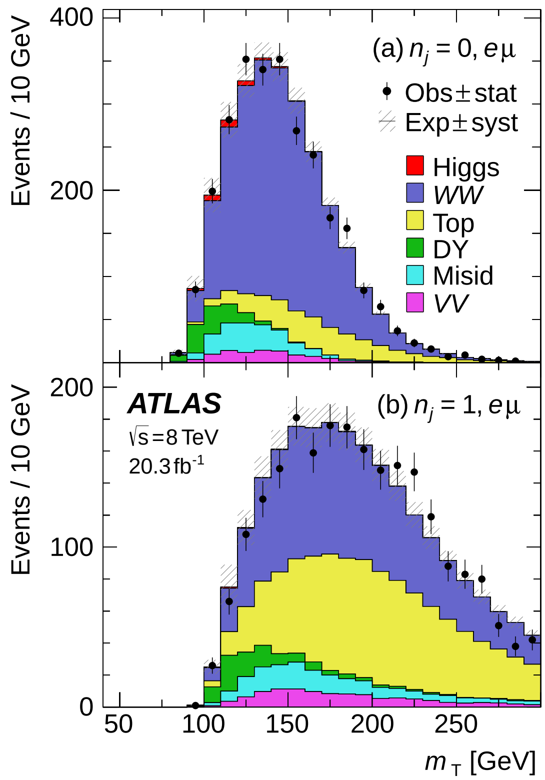

Figure 5.8: WW CR distribution of m_{T} in (a) the $N_{\mathrm{jets}} = 0$ and (b) $N_{\mathrm{jets}} = 1$ categories [112].

is applied with $|m_{\tau\tau} - m_Z| > 15\,\mathrm{GeV}$, which allows for the high $m_{\tau\tau}$ region as compared to the SR. The region uses a lower bound $m_{\ell\ell} > 80\,\mathrm{GeV}$, which further reduces $Z/\gamma^* \to \tau\tau$ contamination at low invariant mass. Figure 5.8(b) shows the m_{T} distribution in the $N_{\mathrm{jets}} = 1$ WW CR and Table 5.19 shows the expected and observed yields. The CR is 43 % pure in WW and we observe an NF of 1.05 ± 0.05 (stat.). The leading contamination comes from top-quark processes, making up 42 % of the region.

Several uncertainties on the extrapolation factor are evaluated. The QCD scale is varied by adjusting the renormalization and factorization scales independently by one-half and two, keeping the ratio of scales between one-half and two [32]. Uncertainties on EW corrections are evaluated by reweighting the MC to the NLO EW calculation [191] and taking the difference with the nominal sample as the uncertainty. PDF uncertainties are evaluated by taking the larger of the difference between the CT10 set and either MSTW2008 or NNPDF2.3 [33] added in quadrature with the CT10 eigenvector errors. The UE/PS uncertainty is evaluated by comparing POWHEG+HERWIG to POWHEG+PYTHIA6. Finally, an uncertainty on the generator used is evaluated by comparing POWHEG+HERWIG to aMC@NLO+HERWIG. The effects of the QCD scale, UE/PS, and generator uncertainties on the WW m_{T} shape are applied as a systematic uncertainty, correlated with the normalization uncertainty, using a linear parametrization between 90 and 170 GeV, which corresponds to a relative change of roughly 20 % at the bounds, depending on the SR. The estimation method and all of the uncertainties are applied to both quark- and gluon-initiated WW. Table 5.21 summarizes the uncertainties on the extrapolation of the WW normalization to the SRs.

Gluon initiated WW makes up 6 %(7 %) of the total WW in the $N_{\text{jets}} = 0(1)$ SRs and 5 %(4 %) in the respective WW CRs. The uncertainty on the total $gg \to WW$ cross section is included to account for possible differences in the fraction of $gg \to WW$ compared to $q\bar{q} \to WW$. Varying the QCD renormalization and factorization scales yields an uncertainty of 26 (33) % in the $N_{\text{jets}} = 0\,(1)$ categories [192], which has a very small impact on the result.

SR category	$N_{\text{jets}} = 0$						$N_{\text{jets}} = 1$					
	Scale	PDF	Gen.	EW	UE/PS	Total	Scale	PDF	Gen.	EW	UE/PS	Total
SR $e\mu$, $10 < m_{\ell\ell} < 30$												
$10 < p_{\text{T}}^{\text{sub}} \leq 15$	0.7	1.0	0.4	1.2	2.2	2.8	3.1	0.6	−3.4	−0.9	−2.4	5.3
$15 < p_{\text{T}}^{\text{sub}} \leq 20$	1.2	0.8	0.9	0.7	1.7	2.5	1.6	0.5	0.7	−1.5	−3.0	3.8
$p_{\text{T}}^{\text{sub}} > 20$	0.7	0.6	3.1	−0.3	−1.9	3.8	1.0	0.6	5.3	−2.8	−3.6	7.1
SR $e\mu$, $30 < m_{\ell\ell} < 55$												
$10 < p_{\text{T}}^{\text{sub}} \leq 15$	0.7	0.8	0.5	0.8	1.5	2.1	3.2	0.5	1.9	−0.9	−2.0	4.3
$15 < p_{\text{T}}^{\text{sub}} \leq 20$	0.8	0.7	1.0	0.5	1.0	1.8	1.5	0.4	2.4	−1.6	−3.0	4.4
$p_{\text{T}}^{\text{sub}} > 20$	0.8	0.7	3.9	−0.4	−2.4	4.7	1.3	0.6	5.6	−2.7	−3.1	7.1
SR SF, $12 < m_{\ell\ell} < 55$												
$p_{\text{T}}^{\text{sub}} > 10$	0.8	1.1	2.4	0.1	−1.2	3.0	0.8	0.9	−3.8	−2.1	−2.3	5.1

Table 5.21: Uncertainties on the WW background extrapolation to the $N_{\text{jets}} = 0$ and $= 1$ SRs from their respective CRs. Relative signs between regions for a given source denote the correlation. Units are in GeV and the uncertainties are relative.

5.5.1.2 VBF and ggF $N_{\text{jets}} \geq 2$ channels

The $q\bar{q} \to WW$ background is estimated purely from MC using SHERPA, separated into diagrams with two QCD vertices and those without QCD vertices, i.e., non-resonant vector boson scattering (VBS) with EW vertices. Uncertainties from the QCD renormalization and factorization scales are evaluated using MADGRAPH [193] and found to be 27 % in the VBF channel and 19 % in the ggF channel. Differences between SHERPA and MADGRAPH are used as a shape uncertainty on the O_{BDT} (8–14 %) and m_{T} (1–7 %) distributions.

5.5.2 Top-quark processes

The processes included in the top-quark background estimate are $t\bar{t}$ (ditop) and Wt, s-channel, and t-channel production of a top-quark in association with another quark (single top). The final state mimics the one we are after when the W bosons decay leptonically, producing good leptons and MET (one misidentified lepton in the case of s-channel and t-channel production), with an additional two b-jets for $t\bar{t}$, or one for single top. The cross section for the production of top-quarks is large at the LHC, roughly a factor of five larger than $q\bar{q} \to WW$, including the leptonic branching fraction. The use of b-tagging, as opposed to b-vetoes in the SRs, allows us to define CRs rich in top-quark processes.

5.5.2.1 Jet veto survival probability for $N_{\text{jets}} = 0$

Most of the top-quark background in the $N_{\text{jets}} = 0$ channel is rejected by the jet veto. Since there are no jets, instead of reversing a b-veto, the 'top-quark veto' is reversed by allowing any number of jets. A CR, shown in Fig. 5.9(a), is defined after the preselection, i.e., before N_{jets} binning, with an additional requirement of $\Delta\phi_{\ell\ell} < 2.8$ to reduce the $Z/\gamma^* \to \tau\tau$ background. The region does include the SR, but the SR makes up only 3 % of the CR. This region is populated by 74 % top-quark processes. The fraction of of top-quark events passing the jet veto, using the jet veto survival probability (JVSP) data-driven estimate, is applied to the CR yield to obtain the estimate in the $N_{\text{jets}} = 0$ category. The ratio of the data-driven estimate to the MC expectation is used as an NF to correct the yield in the SR:

$$\text{NF}_{\text{top,0j}} = \frac{N_{\text{CR}}^{\text{data}} \cdot P_2^{\text{data}}}{N_{\text{CR}}^{\text{MC}} \cdot P_2^{\text{MC}}} \,, \tag{5.13}$$

where N_{CR} is the number of top-quark events (non-top backgrounds subtracted off) and P_2 is the fraction of top-quark events passing the jet veto.

The quantity P_2^{data} is estimated by applying a correction to the MC fraction:

$$P_2^{\text{data}} = P_2^{\text{MC}} \left(\frac{P_1^{\text{btag,data}}}{P_1^{\text{btag,MC}}} \right)^2 \,, \tag{5.14}$$

where P_1 is the single-jet veto survival fraction, and the fraction is squared to account for the two expected jets from $t\bar{t}$. Evaluating P_1^{btag} in a b-tagged region, shown in Fig. 5.9(c), provides a pure top-quark sample, and it is simply the fraction of events without an additional jet. This results in $\text{NF}_{0j}^{\text{top}} = 1.08 \pm 0.02(\text{stat.})$, where the correction $\left(P_1^{\text{btag,data}}/P_1^{\text{btag,MC}}\right)^2 = 1.006$. Theoretical and experimental and systematic uncertainties are propagated to $P_2^{\text{MC}}/\left(P_1^{\text{btag,MC}}\right)^2$ and the extrapolation to the SR ($\alpha_{\text{top},0j}$), resulting in a total systematic uncertainty of 7.6 % on the NF. The systematic uncertainties are summarized in Table 5.22(a).

Unlike other background estimates, the CR described here is not included in the fit. Rather, the NF is applied to the input MC distributions along with the propagated uncertainties.

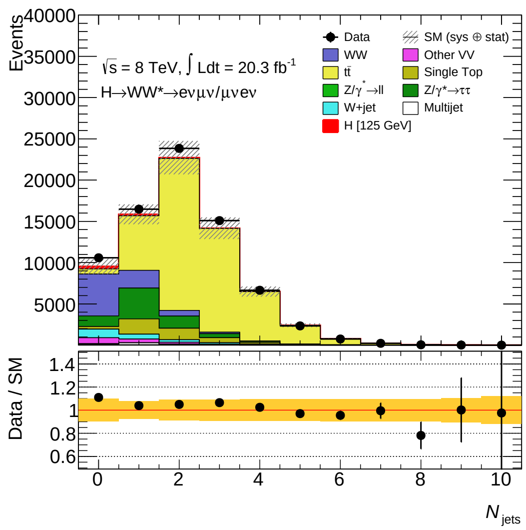

(a)

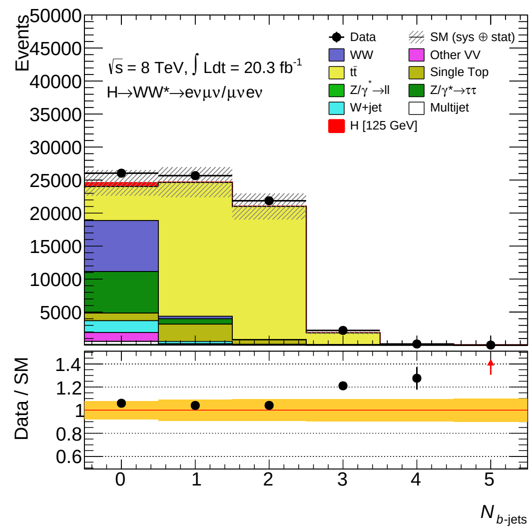

(b)

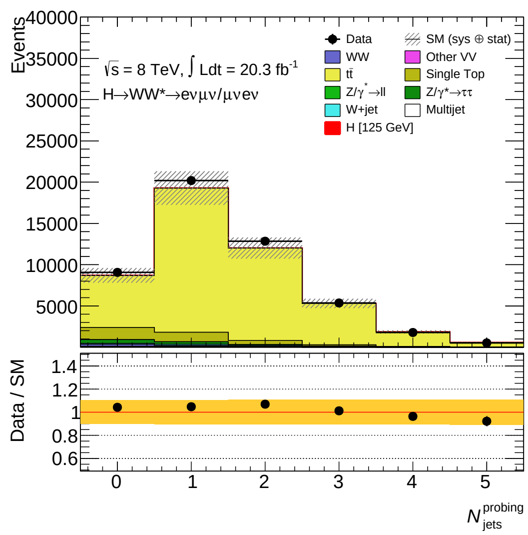

(c)

Figure 5.9: Regions used in the $N_{\text{jets}} = 0$ top-quark background estimate. (a), number of jets in region used to set normalization. (b) , number of b-tagged jets in the previous region. (c), number of additional jets, 'probing' jets, to the b-jet in the b-tagged sample. The NFs, except for WW, in Table 5.28 are applied.

5.5.2.2 Jet b-tagging efficiency extrapolation for $N_{\text{jets}} = 1$

Top-quark events make up a large portion of the expected background in the $N_{\text{jets}} = 1$ category, 36 % in the SR and 42 % in the WW CR, roughly equal to WW itself. Thus, an extrapolation to each from the $N_{\text{jets}} = 1$ top CR is evaluated.

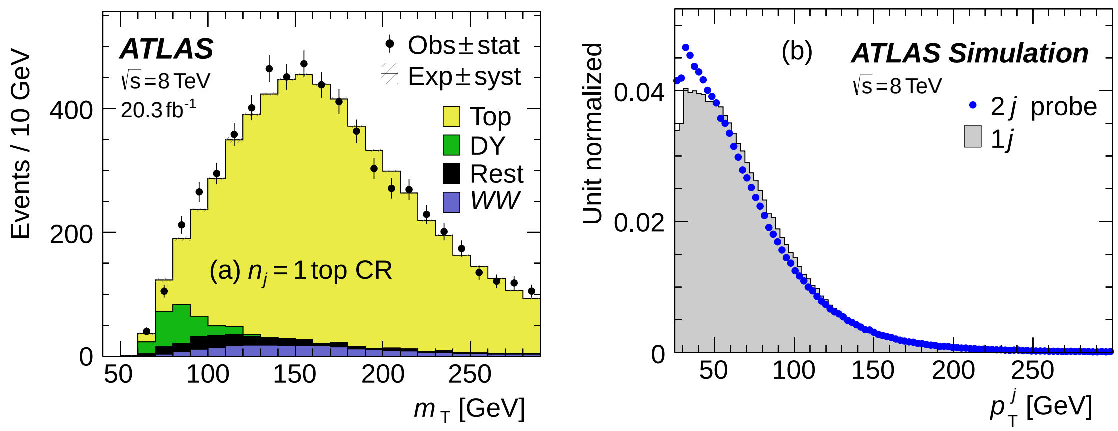

(a) (b)

Figure 5.10: (a), $N_{\text{jets}} = 1$ top-quark CR distribution of m_{T} and (b) jet p_{T} comparison between top-quark ($t\bar{t}$ and Wt) MC with one b-tag for $N_{\text{jets}} = 2$ ($2j$ probe) and $N_{\text{jets}} = 1$ ($1j$) events. For the $N_{\text{jets}} = 2$ events, one jet is randomly chosen to enter the distribution, given the other is b-tagged [112].

The CR is defined after the max m_{T}^{ℓ} veto requirement, see Table 5.8, by reversing the b-veto, except in the $20 < p_{\text{T}}^{\text{jet}} < 25\,\text{GeV}$ range, which is still b-vetoed in order to avoid complications with jet counting. The region is quite pure in top-quark events and well modeled by MC; the m_{T} distribution is shown in Fig. 5.10(a).

Using just the CR, the estimated top-quark background in the SR would be given by:

$$N_{\text{top},1j}^{\text{SR,est.}} = N_{\text{top},1j}^{\text{SR,MC}} \frac{N_{\text{top},1j}^{\text{CR,data}}}{N_{\text{top},1j}^{\text{CR,MC}}} , \tag{5.15}$$

where the latter fraction is the NF calculated in the b-tagged CR. Thus, the extrapolation to the SR is also from b-tagged to b-vetoed events. Equation 5.15 can also be written in terms of the efficiency to b-tag the jet ($\epsilon_{\text{tag}}^{\text{MC},1j}$), which is roughly 73 % due to mistags and other flavor jets being selected:

$$N_{\text{top},1j}^{\text{SR,est.}} = \frac{N_{\text{top},1j}^{\text{CR,data}}}{\epsilon_{\text{tag}}^{\text{MC},1j}} \left(1 - \epsilon_{\text{tag}}^{\text{MC},1j}\right) . \tag{5.16}$$

If we propagate the error on the b-tagging efficiency,

$$\frac{\delta N^{\text{SR,est.}}_{\text{top},1j}}{N^{\text{SR,est.}}_{\text{top},1j}} = \frac{\delta\epsilon^{\text{MC},1j}_{\text{tag}}}{\epsilon^{\text{MC},1j}_{\text{tag}}}\left(\frac{1}{1-\epsilon^{\text{MC},1j}_{\text{tag}}}\right), \tag{5.17}$$

we find that a 5 % error on the efficiency turns into a 25 % error on the top-quark background in the SR. A data-driven method is used to estimate this efficiency, the jet b-tagging efficiency extrapolation (JBEE) method, using $N_{\text{jets}} = 2$ events with $N_{b\text{-jets}} = 1$ and $= 2$, in order to reduce the impact of its uncertainty.

The efficiency to tag an individual jet ($\epsilon^{1j}_{\text{tag}}$) is estimated, using the tag-and-probe method, from the efficiency to tag a jet in a $N_{\text{jets}} = 2$ sample ($\epsilon^{2j}_{\text{tag}}$) along with a correction:

$$\epsilon^{\text{est.},1j}_{\text{tag}} = \epsilon^{\text{data},2j}_{\text{tag}} \cdot \frac{\epsilon^{\text{MC},1j}_{\text{tag}}}{\epsilon^{\text{MC},2j}_{\text{tag}}}, \tag{5.18}$$

where $\epsilon^{\text{MC},1j}_{\text{tag}}/\epsilon^{\text{MC},2j}_{\text{tag}} = 1.079$ with a 1.6 % uncertainty is evaluated in MC and is used to extrapolate the estimated efficiency to tag a jet from the $N_{\text{jets}} = 2$ to $N_{\text{jets}} = 1$ region; Fig. 5.10(b) shows a comparison of the jet p_{T} from MC between the two regions. The efficiency to tag a jet, as derived in a $N_{\text{jets}} = 2$ region, $\epsilon^{\text{data},2j}_{\text{tag}}$ is derived from data:

$$\epsilon^{\text{data},2j}_{\text{tag}} = \frac{N^{2j}_{\text{2-tag}}}{0.5 \cdot N^{2j}_{\text{1-tag}} + N^{2j}_{\text{2-tag}}}, \tag{5.19}$$

where N are the number of events with at least one b-tag (1-tag), and number of events with two b-tags (2-tag), in an $N_{\text{jets}} = 2$ sample with similar selections as the top CR. The factor of one-half accounts for the chance that either jet is b-tagged.

Using this method, the derived NF is 1.06 ± 0.03(stat.) with a systematic uncertainty of 9 %. For the estimation used in the statistical fit, described in Section 5.6.4, the JBEE method is used to estimate the b-tagging efficiency, which is then use to correct the b-vetoed MC estimate in the SR and WW CR by applying the anti-efficiency to the $N_{b\text{-jets}} = 1$ tagged regions respectively—this can be thought of as deriving the $\epsilon^{1j}_{\text{tag}}$ efficiency using the SR or CR selection. Table 5.22(b) summarizes the theoretical systematic uncertainties on the extrapolation of this estimate to the WW CR and SR.

5.5.2.3 $N_{\text{jets}} \geq 2$ VBF channel

The CR used in the VBF channel requires exactly one b-tagged jet in order to be closer to the SR flavor composition than simply reversing the b-veto. This CR also includes $ee/\mu\mu$

Uncertainty source	$P_1^{\text{btag,data}}/P_1^{\text{btag,MC}}$	$\alpha_{\text{top},0j}$	Total
Experimental	4.4	1.2	4.6
Non-top-quark subtraction	2.7	-	2.7
Theoretical	3.9	4.5	4.9
Statistical	2.2	0.7	2.3
Total	6.8	4.7	7.6

(a) $N_{\text{jets}} = 0$

Regions		Scale	PDF	Gen	UE/PS	Tot.
Signal region						
$e\mu$	$(10 < m_{\ell\ell} < 55)$	-1.1	-0.12	-2.4	2.4	3.6
$ee/\mu\mu$	$(12 < m_{\ell\ell} < 55)$	-1.0	-0.12	-2.0	3.0	3.7
WW control region						
$e\mu$	$(m_{\ell\ell} > 80)$	0.6	0.08	2.0	1.8	2.8

(b) $N_{\text{jets}} = 1$

Table 5.22: (a), uncertainties on the top-quark background extrapolation for $N_{\text{jets}} = 0$. (b), uncertainties evaluate on the $N_{\text{jets}} = 1$ top-quark background estimation for the WW CR and SR. Relative signs within a column indicate the correlation between regions [112]. Units are in GeV and the uncertainties are relative.

events since the DY contamination is greatly reduced by the jet requirements. The O_{BDT} distribution of the top-quark backgrounds strongly depends on the MC generator used due to the input jet kinematic variables; thus, each BDT bin is normalized separately to reduce the impact of the modeling uncertainty on the shape. Except, the most sensitive bins, 2 and 3, are merged due to the low expected yield. The m_{jj} and O_{BDT} distributions for the top CR are shown in Fig. 5.11. Uncertainties on the extrapolation to the SR bins are evaluated in the same manner as WW, see Section 5.5.1.1. The modeling uncertainty is the largest source of uncertainty, evaluated by comparing POWHEG+HERWIG, ALPGEN+HERWIG, and MC@NLO[194]+HERWIG. The resulting uncertainty is correlated between bins. Table 5.23 summarizes the NFs and the uncertainties on the extrapolation factors.

5.5.2.4 $N_{\text{jets}} \geq 2$ ggF channel

The ggF $N_{\text{jets}} \geq 2$ channel does not use a b-tagged region to normalize the top-quark background. Rather, the high $m_{\ell\ell} > 80\,\text{GeV}$ region is sufficiently pure (72 %) in top-quark events, see in Fig. 5.7, and avoids extrapolation in b-tagging. The resulting NF is 1.05 ± 0.03 (stat.). Uncertainties on the extrapolation factor are evaluated similarly to

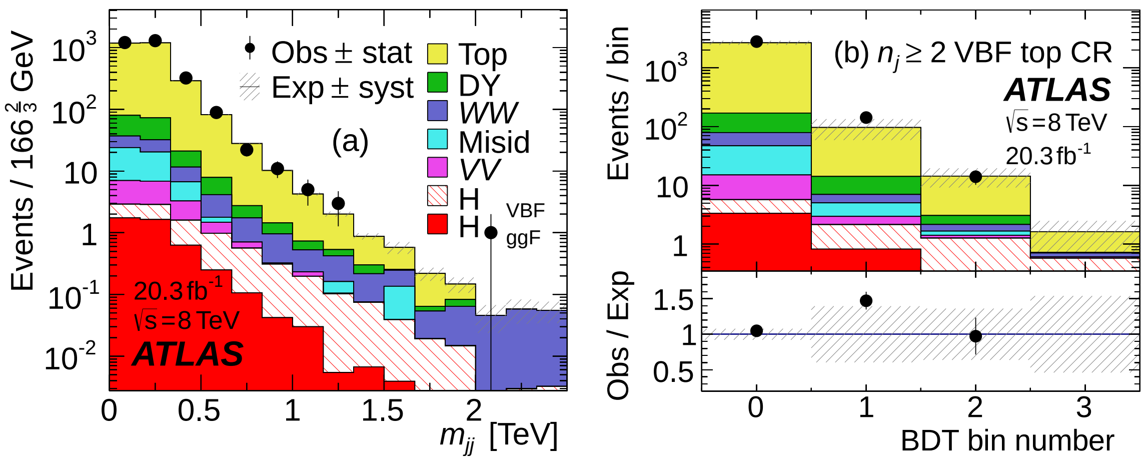

(a) (b)

Figure 5.11: Distributions in the VBF top-quark CR for (a) m_{jj} and (b) O_{BDT} [112].

O_{BDT} bins	$\Delta\alpha/\alpha$	NF Statistical	ΔNF Systematic	ΔNF
Bin 0 (unused)	0.04	1.09	0.02	0.05
Bin 1	0.10	1.58	0.15	0.55
Bin 2	0.12	0.95 {	0.31	0.36
Bin 3	0.21		0.31	0.36

Table 5.23: VBF channel top-quark NFs and extrapolation uncertainties per O_{BDT} bin. The only uncertainty which enters the fit is for the extrapolation [112].

the other channels: the QCD scale uncertainty is 1 %, PDF uncertainty 0.3 %, UE/PS uncertainty 1.2 % from comparing POWHEG+PYTHIA6 with POWHEG+HERWIG, and the generator uncertainty 3.2 % from comparing MC@NLO+HERWIG, ALPGEN+HERWIG, and POWHEG+PYTHIA6.

5.5.3 Z/γ^* + jets

The background estimation for Drell–Yan (DY) is divided by the final state between $ee/\mu\mu$ and $\tau\tau$, because $\tau\tau$ can contribute to the $e\mu$ channel, in which case it is an irreducible background. The $Z/\gamma^* \to \tau\tau$ background is estimated using a simple CR, while more complex methods are used to estimate the DY background in the $ee/\mu\mu$ channels.

The DY background makes up a large portion of $ee/\mu\mu$ events, and enters the signal selection with fake MET. Soft hadronic activity in the events plays a role generating MET and boosting the dilepton system; it is often poorly modeled by the MC. Data-driven methods are used to overcome this.

5.5.3.1 $Z/\gamma^* \to \tau\tau$

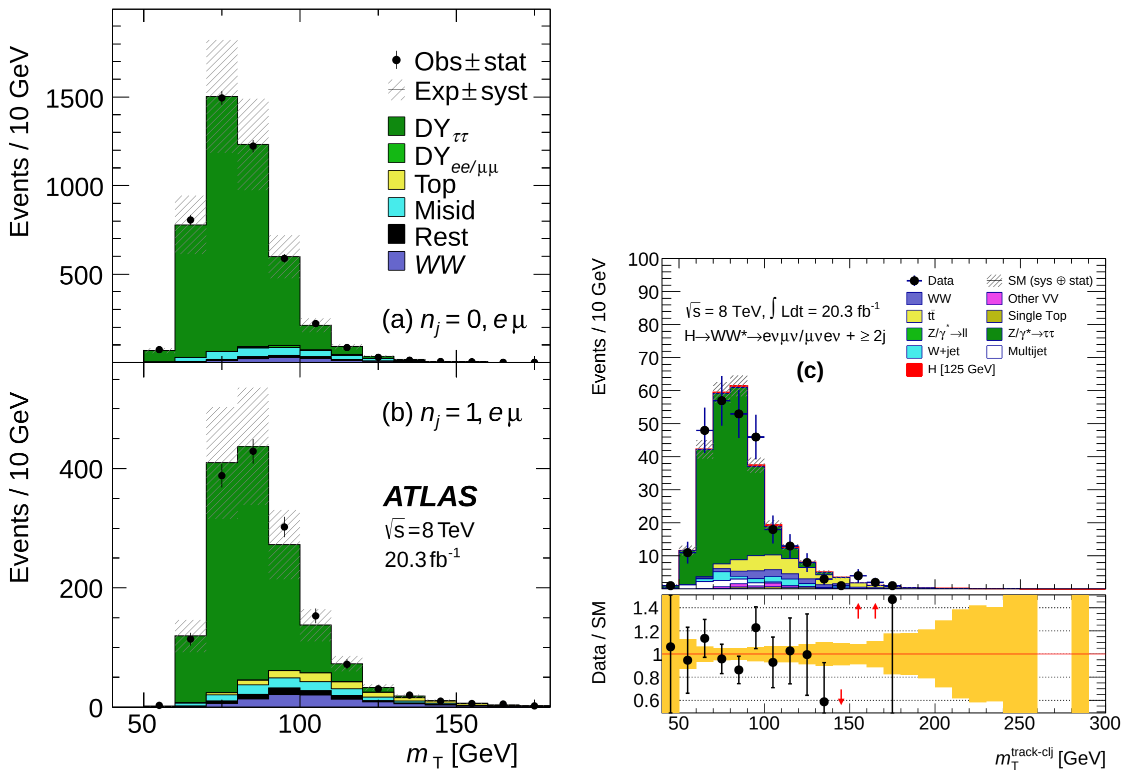

Figure 5.12: $Z/\gamma^* \to \tau\tau$ CR distribution of m_{T} in the ggF (a) $N_{\mathrm{jets}} = 0$, (b) $N_{\mathrm{jets}} = 1$[112], and (c) $N_{\mathrm{jets}} \geq 2$ categories.

In all of the N_{jets} categories, a CR is used to normalize the $Z/\gamma^* \to \tau\tau$ background. We make use of the dilepton invariant mass and reconstructed ditau mass $m_{\tau\tau}$, using the co-linear approximation, to select $Z/\gamma^* \to \tau\tau$ events. $Z/\gamma^* \to \tau\tau$ events fall into the signal region because they create dilepton plus MET final states and play a role in the $e\mu$ channel; they are generally negligible compared to $Z \to ee$ or $Z \to \mu\mu$ events in the SF channel. The NFs derived in the following $Z/\gamma^* \to \tau\tau$ CRs are consistent within statistical uncertainties with unity, see Table 5.28. The systematic uncertainties on the extrapolation factors for the ggF channels are summarized in Table 5.24.

The $Z/\gamma^* \to \tau\tau$ CR in the $N_{\mathrm{jets}} = 0$ category is defined after the jet veto, requiring $\Delta\phi_{\ell\ell} > 2.8$ and $m_{\ell\ell} < 80\,\mathrm{GeV}$ to select $Z/\gamma^* \to \tau\tau$ events which fall below m_Z due to the neutrinos. This region is quite pure in $Z/\gamma^* \to \tau\tau$ at 90 %; the m_{T} distribution is shown in Fig. 5.12(a).

The $p_{\mathrm{T}}^{\ell\ell}$ shape is modeled poorly by the MC (ALPGEN+HERWIG) when no jets are present, i.e, when there is soft hadronic recoil, p_T^Z is poorly modeled. To correct this, a reweighting is derived from a comparison of MC and data in the Z peak using $\mu\mu$ events and applied to the truth $p_{\mathrm{T}}^{\ell\ell}$ spectrum for all $Z \to \ell\ell$ events with zero reconstructed jets. The full weight is used as an uncertainty on the shape on the Z to ee or $\mu\mu$ MC. An uncertainty on the extrapolation from the reweighting is also derived for the $Z/\gamma^* \to \tau\tau$ events, 19 % for the SR and 16 % for the WW CR. These are derived by comparing the nominal weights with those derived from the same Z peak region, but with a $p_{\mathrm{T}}^{\mathrm{miss}} > 20\,\mathrm{GeV}$ requirement, the same used in the $e\mu$ channels.

Events in the $N_{\mathrm{jets}} = 1$ category are boosted enough to make the co-linear mass approximation more efficient. The CR is defined after the m_{T}^{ℓ} requirement, again requiring $m_{\ell\ell} < 80\,\mathrm{GeV}$, but now $m_{\tau\tau} > m_Z - 25\,\mathrm{GeV}$, to select $Z/\gamma^* \to \tau\tau$ events. It has slightly more contamination, being 80 % pure, and the m_{T} distribution is shown in Fig. 5.12(b).

The uncertainty from the modeling of $Z/\gamma^* \to \tau\tau$ in the $N_{\mathrm{jets}} = 0$ and $= 1$ categories is evaluated by comparing ALPGEN+HERWIG and ALPGEN+PYTHIA. QCD scale and PDF uncertainties are also evaluated and summarized in Table 5.24. The QCD scale is evaluated by varying the dynamic scale used in ALPGEN+HERWIG samples with zero, one, and two additional partons. The CTEQ6L1 PDF used in the $Z/\gamma^* \to \ell\ell$ samples is reweighted to the variations needed to evaluated the PDF uncertainties in the same manor as done for the WW background, see Section 5.5.1.1.

Region	Scale	PDF	Gen.	Gen. Stat.	p_{T}^{Z}
Signal regions					
$N_{\mathrm{jets}} = 0$	-1.6	1.4	5.7	15	19
$N_{\mathrm{jets}} = 1$	4.7	1.8	-2.0	7.7	-
$N_{\mathrm{jets}} \geq 2$ ggF	-10.3	1.1	10.4	-	-
WW control regions					
$N_{\mathrm{jets}} = 0$	-5.5	1.0	-8.0	3.2	16
$N_{\mathrm{jets}} = 1$	-7.2	2.1	3.2	3.6	-

Table 5.24: Extrapolation uncertainties on the $Z/\gamma^* \to \tau\tau$ estimate in the ggF channels. The last two uncertainties are from the $p_{\mathrm{T}}^{\ell\ell}$ reweighting (p_{T}^{Z}) and from the large statistical uncertainty (Gen. Stat.) on the MC used to evaluate the modeling uncertainty (Gen.).

Normalization of $Z/\gamma^* \to \tau\tau$ in the VBF $N_{\mathrm{jets}} \geq 2$ VBF channel is done using a CR combining $e\mu$ and $ee/\mu\mu$ events to reduce the statistical uncertainty. Contamination from Z to electrons or muons in the $ee/\mu\mu$ events is small. The CR is defined with $m_{\ell\ell} < 80(75)\,\mathrm{GeV}$ in $e\mu\,(ee/\mu\mu)$ and $|m_{\tau\tau} - m_Z| < 25\,\mathrm{GeV}$. Combining all three O_{BDT} bins, the NF is 0.90 ± 0.30(stat.). QCD, PS, and PDF uncertainties are evaluated, but found to be negligible compared to the large statistical uncertainty, and thus not included.

The CR for the $N_{\mathrm{jets}} \geq 2$ ggF channel is constructed after the b-veto, with the additional requirements of $m_{\ell\ell} < 70\,\text{GeV}$ and $\Delta\phi_{\ell\ell} > 2.8$ to select $Z/\gamma^* \to \tau\tau$ events, shown in Fig. 5.12(c). The VBF region is rejected by requiring the events to fail either the OLV or CJV. The region is 74 % pure.

5.5.3.2 'Pacman' method for $N_{\text{jets}} \leq 1$ $ee/\mu\mu$

The estimate of ee and $\mu\mu$ DY final states uses the f_{recoil} variable to quantify soft hadronic recoil and estimates the efficiency of requirements on this variable with data. The difference in soft hadronic recoil, shown in Fig. 5.13, between processes with real MET, e.g., the signal and processes with neutrinos (non-DY), and those with fake MET (DY), makes f_{recoil} a useful discriminant. The same $p_{\text{T}}^{\ell\ell}$ reweighting described in the previous section is applied to $N_{\text{jets}} = 0$ events.

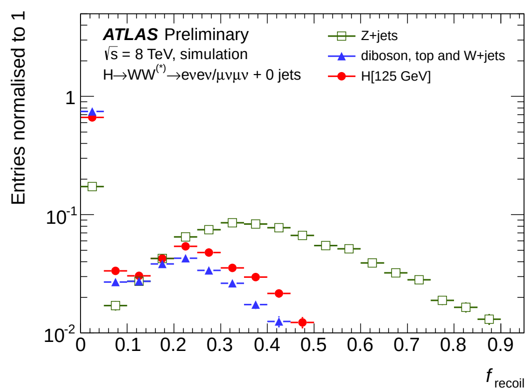

Figure 5.13: f_{recoil} distribution in $N_{\text{jets}} = 0$ signal-like events, from the Moriond CONF note [142], showing the difference between events with real and fake MET.

The efficiency (fraction events passing the f_{recoil} requirement) of DY and non-DY processes are measured in data and used to estimate the amount of DY entering the SR. Events are separated into those which pass and those which fail the f_{recoil} requirement.

The non-DY efficiency ($\epsilon_{\text{non-DY}}$) is derived in an $e\mu$ sample with $ee/\mu\mu$ channel SR requirements, and is used for signal and non-DY processes. These events are almost all non-DY—the region does overlap with the $e\mu$ SR. The DY efficiency (ϵ_{DY}) is derived on the Z-peak, selected with $|m_{\ell\ell} - m_Z| < 15\,\text{GeV}$ in SF events. Since there are non-DY processes in the Z-peak, a third efficiency $\epsilon'_{\text{non-DY}}$ is used, evaluated in the Z-peak, but with $e\mu$ events. Thus, ϵ_{DY} is measured by subtracting off the non-DY contributions, estimated with MC:

$$\epsilon_{\text{DY}} = \frac{N_{\text{data,pass}}^{Z\text{-peak}} - \epsilon'_{\text{non-DY}} \cdot N_{\text{MC,non-DY}}^{Z\text{-peak}}}{N_{\text{data}}^{Z\text{-peak}} - N_{\text{MC,non-DY}}^{Z\text{-peak}}} \,. \tag{5.20}$$

The DY efficiency is then used to estimate the yield in the SR:

$$N_{\mathrm{DY}}^{\mathrm{SR}} = \epsilon_{\mathrm{DY}} \cdot \frac{N_{\mathrm{data,pass}}^{\mathrm{SR}} - \epsilon_{\text{non-DY}} \cdot N_{\mathrm{data}}^{\mathrm{SR}}}{\epsilon_{\mathrm{DY}} - \epsilon_{\text{non-DY}}} . \tag{5.21}$$

where in both equations N is a yield, and pass means the region passing the f_{recoil} requirement. This can be derived from solving for $N_{\mathrm{DY}}^{\mathrm{SR}}$ in:

$$\begin{bmatrix} N_{\mathrm{pass}}^{\mathrm{SR}} \\ N_{\mathrm{pass+fail}}^{\mathrm{SR}} \end{bmatrix} = \begin{bmatrix} 1 & 1 \\ 1/\epsilon_{\mathrm{DY}} & 1/\epsilon_{\text{non-DY}} \end{bmatrix} \cdot \begin{bmatrix} N_{\mathrm{DY}}^{\mathrm{SR}} \\ N_{\text{non-DY}}^{\mathrm{SR}} \end{bmatrix} . \tag{5.22}$$

Uncertainties on $\epsilon_{\text{non-DY}}^{(\prime)}$ for the $e\mu$ to $ee/\mu\mu$ extrapolation are evaluated using MC, with the full difference in efficiencies of $e\mu$ and $ee/\mu\mu$ events in the Z-peak and SR taken as the uncertainties. The difference in f_{recoil} efficiency between signal and non-DY processes is taken as a further uncertainty on the signal. It is 9 % and 7 % in the $N_{\mathrm{jets}} = 0$ and $= 1$ categories respectively. These uncertainties are validated with data and alternate MC samples. The uncertainty on ϵ_{DY} covers the extrapolation from the Z-peak to the SR and is again evaluated using MC. This uncertainty is also validated in data. The efficiencies (ϵ) and their uncertainties are summarized in Table 5.25.

5.5.3.3 $Z/\gamma^* \to \mu\mu/ee$ in VBF

DY in the VBF channel is estimated using an data-driven ABCD method in the $m_{\ell\ell}$ and $E_{\mathrm{T}}^{\mathrm{miss}}$ dimensions, see Fig. 5.14 for an illustration of the regions used. The DY shape is taken from a low $m_{\ell\ell}$ region (B) with the same $m_{\ell\ell}$ requirement as the SR (A), but lower MET requirement. This results in a high purity sample. The normalization is then corrected using the $E_{\mathrm{T}}^{\mathrm{miss}}$ requirement efficiency (C/D) in the Z-peak ($|m_{\ell\ell} - m_Z| < 15\,\mathrm{GeV}$), where region C has the same MET requirement as the SR of $E_{\mathrm{T}}^{\mathrm{miss}} > 45\,\mathrm{GeV}$ and region D the same requirement as B, $25 < E_{\mathrm{T}}^{\mathrm{miss}} < 45\,\mathrm{GeV}$. Resulting in a predicted yield in BDT bin i:

$$N_{\mathrm{DY}}^{\mathrm{SR},i} = N_{\mathrm{DY}}^{\mathrm{B},i} \cdot \frac{N_{\mathrm{DY}}^{\mathrm{C}}}{N_{\mathrm{DY}}^{\mathrm{D}}} \cdot f_{\text{non-closure}} , \tag{5.23}$$

where N are the yields with the expected contamination subtracted and $f_{\text{non-closure}}$ corrects for different $E_{\mathrm{T}}^{\mathrm{miss}}$ efficiencies at low and high $m_{\ell\ell}$, evaluated with MC:

$$f_{\text{non-closure}} = \frac{N_{\mathrm{DY}}^{\mathrm{A}}/N_{\mathrm{DY}}^{\mathrm{B}}}{N_{\mathrm{DY}}^{\mathrm{C}}/N_{\mathrm{DY}}^{\mathrm{D}}} . \tag{5.24}$$

Due to low yield in region B for the last BDT bin, the last two bins are combined.

Efficiency	$N_{\text{jets}} = 0$	$N_{\text{jets}} = 1$
$\epsilon_{\text{non-DY}}$	69 ± 1	64 ± 2
$\epsilon'_{\text{non-DY}}$	68 ± 2	66 ± 3
ϵ_{DY}	14 ± 5	13 ± 4

(a) f_{recoil} requirement efficiencies, in %.

Source	$N_{\text{jets}} = 0$	$N_{\text{jets}} = 1$
Total uncertainty on $\epsilon_{\text{non-DY}}$	1.9	3.2
Statistical	1.8	3.0
$e\mu$ to $ee/\mu\mu$ extrapolation	0.8	1.2
Total uncertainty on $\epsilon'_{\text{non-DY}}$	3.1	4.5
Statistical	1.9	3.9
$e\mu$ to $ee/\mu\mu$ extrapolation	2.5	2.4
Total uncertainty on ϵ_{DY}	38	32
Statistical	9.4	16
Z-peak to low $m_{\ell\ell}$ (SR) extrapolation	32	16
Total uncertainty on SR SR yield estimate	49	45

(b) Systematic uncertainties on f_{recoil} efficiencies, in %.

Table 5.25: Summary tables of (a) the efficiencies extracted for the DY estimate and (b) their respective uncertainties [112].

The (C/D) ratio is 0.43 ± 0.03 and the non-closure factor is 0.83 ± 0.22. Resulting NFs are 1.01 ± 0.15(stat.) for bin 1 and 0.89 ± 0.28(stat.) for combined bins 2 and 3.

The difference between unity and the non-closure, 17 %, is taken as a correlated uncertainty across BDT bins. Uncertainties on the extrapolation of the BDT shape through the MET requirement is evaluated by comparing the deviations of ALPGEN+HERWIG and ALPGEN+PYTHIA6 in each BDT bin in the SR and region B. No $E_{\text{T}}^{\text{miss}}$ dependence on the BDT is observed, and uncertainties of 4, 10, and 60 % are applied in bins 1, 2, and 3 respectively, based on this.

5.5.4 W + jets and multijets

The W + jets and multijets backgrounds, collectively referred to as misid, are estimated in all channels using a data-driven 'fake-factor' applied to a control region of anti-identified leptons, extrapolating the yield to the SR,. Both the shape and normalization are taken from data. These backgrounds enter the signal region when one or two jets are misidentified as good leptons, referred to as fake leptons.

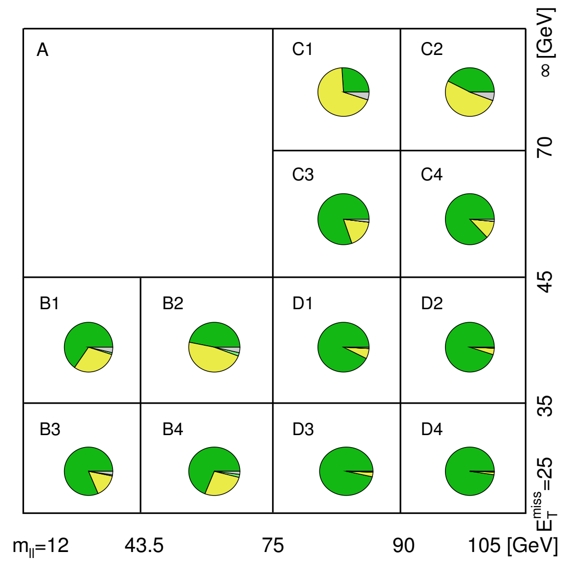

Figure 5.14: The background composition of the ABCD regions used for the DY estimate in the VBF channel. DY is shown in green, top-quark processes in yellow, and other backgrounds in grey. Extra divisions in $m_{\ell\ell}$ and $E_{\mathrm{T}}^{\mathrm{miss}}$ are shown (numbered), which are not used for the estimate.

A sample rich in $W+\mathrm{jets}$ is constructed by requiring one good lepton and another which fails the SR identification, but satisfies a looser selection (referred to as an anti-identified lepton) including looser impact parameter and isolation requirements. Anti-identified electrons differ from the nominal selection by requiring: calorimeter isolation $\Delta R(0.3)/E_{\mathrm{T}} < 0.30$, track isolation $\Delta R(0.3)/E_{\mathrm{T}} < 0.16$, no conversion vertex and B-layer requirements, and failure of the medium and identified electron requirements. Anti-identified muons differ from the nominal selection by requiring: no d_0 requirement; calorimeter isolation of $\Delta R(0.3) < (0.15, 0.25, 0.30)$ for p_{T} between 10–15, 15–20, and >20 GeV; no track isolation, and failure of the identified muon requirements. CRs for the $N_{\mathrm{jets}} = 0$ regions with an anti identified electron and muon are shown in Fig. 5.15.

The fake-factor, or extrapolation factor from anti-identified to identified lepton, is defined as the ratio of all identified leptons over all anti-identified leptons, see Fig. 5.16. It is calculated from jets in events with a Z boson candidate, and includes a correction for expected Z+jets and $W+\mathrm{jets}$ differences in MC (ALPGEN+PYTHIA6). The correction for anti-identified electrons is 0.99 ± 0.20 and 1.00 ± 0.22 for anti-identified muons. The uncertainty is evaluated by comparing the correction factor between ALPGEN+PYTHIA6, ALPGEN+HERWIG, and ALPGEN+PYTHIA8. Non-Z+jets contamination, which produce additional leptons, is estimated with MC, with a 10 % systematic uncertainty. The fake-factor is defined separately for electrons and muons, and is binned in fake-lepton p_{T} and η.

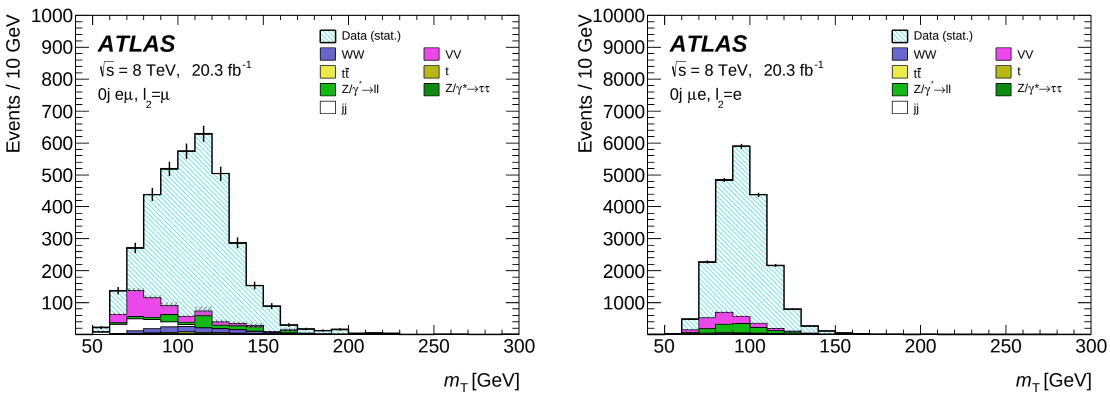

Figure 5.15: Distribution of m_{T} in the $N_{\mathrm{jets}} = 0$ $e\mu$ channel with SR selection for (a) an anti-identified muon and (b) an anti-identified electron. The EW contamination is estimated with MC [112].

A difference in the fake-factor is seen for opposite-charge (OC) and same-charge (SC) lepton pairs, at least in part from Wc production, where the semi-leptonic c-quark decay produces predominantly a lepton of opposite charge to the W-boson. Therefore, the fake-factor is evaluated separately for the two cases, which is important for the $W+$jets estimate used in the VV CR, described in Section 5.5.5. The correction for using Z+jets events to evaluate the fake-factor is quite different for same-charge (SC) events, 1.25 ± 0.31 for anti-identified electrons and 1.40 ± 0.49 for anti-identified muons—the same uncertainty method as for OC events is used. Figure 5.17 shows the fake-factors, OC and SC, and their uncertainties before the correction for using Z+jets events.

Besides the uncertainty on the correction factor, the limited number of events in the Z+jets sample and subtraction of contaminating backgrounds in the sample contribute to the total uncertainty on the fake-factor, summarized in Table 5.26. Since the processes contributing to OC and SC events are not the same, the uncertainty on the correction factor is split into a correlated (across charge) and uncorrelated component. The splitting is based on the estimated fraction of processes overlapping between the regions, namely assuming those contributing to SC events contribute to both, while some contribute predominately to OC events.

The QCD multijet background is similarly estimated by applying, twice, a fake-factor to a CR, now with two anti-identified leptons. The CR with one factor of the extrapolation factor represents the estimate for one identified and one anti-identified lepton, and is used to subtract this small contribution from the $W+$jets estimate, in Equation 5.26. The fake-factor for the multijet background is calculated in a dijet sample constructed by inverting the lepton

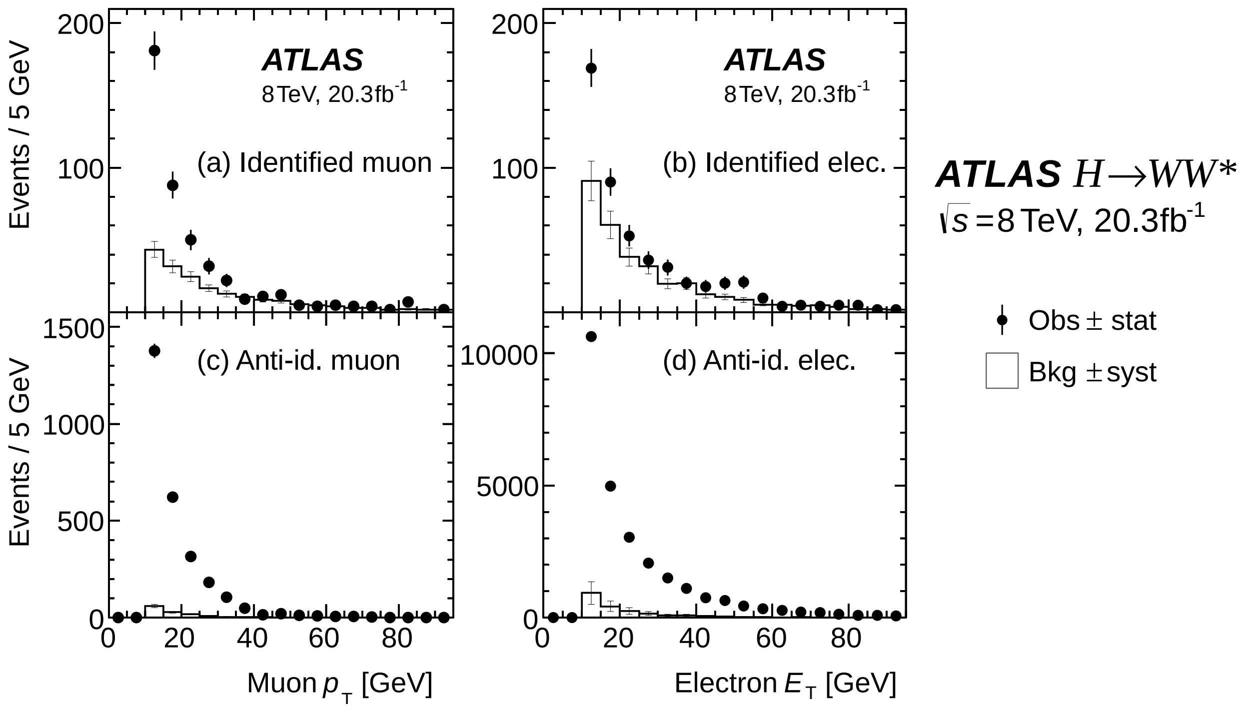

Figure 5.16: Identified and anti-identified (a and c) muon and (b and d) electron p_{T} in the Z+jets sample with non-Z+jets contamination (Bkg.) estimated from MC with a 10 % uncertainty [112].

identification, as before. It is corrected for biases introduced by requiring one of the objects to be identified (f') or anti-identified (f''). The dominant uncertainty on the multijet estimate arises from uncertainties on these corrections, resulting in a total uncertainty between 30–50 % depending on the lepton flavors. The total includes the other uncertainties summarized in Table 5.27, except for the sample dependence, which would account for differences between the dijet and W + jets fake-factors, i.e., if the dijet fake-factor was used for a W + jets estimate.

Finally, the multijet estimate in the SR is calculated by applying the corrected dijet fake-factors, after subtracting off W + jets and other backgrounds, estimated with MC, to the two anti-identified lepton CR:

$$N_{\text{id+id}}^{\text{multijet}} = f'_{\text{dijet}} \cdot f''_{\text{dijet}} \cdot \left(N_{\text{anti-id+anti-id}} - N_{\text{anti-id+anti-id}}^{\text{W+jet,MC}} - N_{\text{anti-id+anti-id}}^{\text{Other bkg.,MC}} \right) . \tag{5.25}$$

The W + jets estimate in the SR is similarly estimated by applying the corrected Z+jets fake-factor to the one anti-identified CR, after subtracting off the multijet and other background

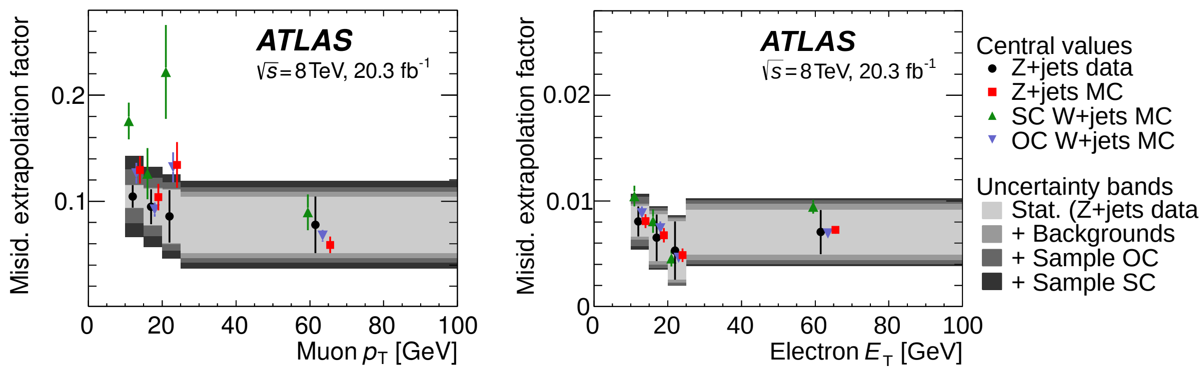

(a) (b)

Figure 5.17: Fake-factors (extrapolation-factors) for (a) mouns and (b) electrons as a function of p_{T} before the correction accounting for use of Z+jets ('Z+jets MC' to 'OC $W+$jets MC') [112].

contamination:

$$N_{\text{id+id}}^{W+\text{jets}} = f_{W+\text{jets}} \cdot \left(N_{\text{id+anti-id}} - N_{\text{id+anti-id}}^{\text{multijet}} - N_{\text{id+anti-id}}^{\text{Other Bkg.,MC}} \right) , \tag{5.26}$$

where $f_{W+\text{jets}}$ is the corrected fake-factor and $N_{\text{id+anti-id}}^{\text{multijet}} = 2 \cdot f''_{\text{dijet}} \cdot N_{\text{anti-id+anti-id}}^{\text{multijet}}$ is taken from Equation 5.25, with a factor of two to account for two objects with the possibility to become the 'identified' one.

5.5.5 Other dibosons: $W\gamma/W\gamma^*/WZ/ZZ$

The $W\gamma$, $W\gamma^*$, WZ, and ZZ processes are referred to as the other dibosons (VV) or non-WW dibosons. They tend to have large theoretical uncertainties and fall into the signal selection through missing, e.g. WZ and ZZ, or misidentified objects, e.g. photon conversions for $W\gamma$. They make up 14 % (12 %) of the $e\mu$ $N_{\text{jets}} = 0\,(1)$ category signal region; though relatively small, the VV processes tend to sit under the signal in m_{T}. In order to reduce the impact of normalization uncertainties in these categories, we take advantage of the fact that these processes, except for ZZ, are charge symmetric and construct a CR with the same selection as the SR except requiring the leptons to have the same charge. The ZZ process is negligible, 1 % of the CRs, so the charge asymmetry can be ignored. Unlike the other CRs, this is only used for the $e\mu$ channels; VV in the $ee/\mu\mu$ channels is estimated purely from MC. This SC CR is rich in the VV processes, at 62 % (61 %) in the $N_{\text{jets}} = 0\,(1)$ SC CRs. Figure 5.18 shows the m_{T} and $p_{\mathrm{T}}^{\text{sub}}$ in the $N_{\text{jets}} = 0$ and $= 1$ SC CRs. $W+$jets and multijet backgrounds are estimated using the data-driven method described in Section 5.5.4. The resulting NFs are 0.92 ± 0.07(stat.) for the $N_{\text{jets}} = 0$ and 0.96 ± 0.12(stat.) for the $N_{\text{jets}} = 1$

SR p_{T} range	Total		Corr. factor					Stat.	Other bkg.
	OC	SC	OC			SC			
			Stat.	Corr.	Uncorr.	Stat.	Corr.		
Electrons									
10–15 GeV	29	32	5	11	15	8	30	18	11
15–20 GeV	44	46	5	11	15	8	30	34	19
20–25 GeV	61	63	5	11	15	8	30	52	25
> 25 GeV	43	45	5	11	15	8	30	30	23
Muons									
10–15 GeV	25	37	8	13	17	14	47	10	3
15–20 GeV	37	46	8	13	17	14	47	18	5
20–25 GeV	37	46	8	13	17	14	47	29	9
> 25 GeV	46	53	8	13	17	14	47	34	21

Table 5.26: Uncertainties (%) on the fake-factor split by anti-identified lepton flavor and p_{T}. The total is broken down into components from the Z+jets correction factor, yield in the sample, and other background contamination [112]. The uncertainty from the correction factor is further split into a statistical term, a systematic uncertainty correlated across charge (opposite-charge (OC) versus same-charge (SC) pairs), and an uncorrelated component.

categories.

QCD scale uncertainties dominate for $W\gamma$ and $W\gamma^*$. The uncertainty for $W\gamma$ is divided into the total cross section (6 %), and uncertainties uncorrelated across jet bins: 9 %, 53 %, and 100 % uncorrelated in the $N_{\text{jets}} = 0, = 1$, and ≥ 2 categories respectively. $W\gamma^*$ has a 7.5 % total cross section uncertainty, and 6.5 %, 30 %, and 26 % uncertainty uncorrelated across the the $N_{\text{jets}} = 0, = 1$, and ≥ 2 categories respectively. Further, for $W\gamma^*$ an m_{T} shape uncertainty from scale variations is evaluated from comparing the nominal MC with MCFM and a SHERPA sample with with ≤ 2 partons. For both $W\gamma$ and $W\gamma^*$, the PDF uncertainty on the acceptance is 3 %. We use a 4 % PDF uncertainty and 5 % QCD scale uncertainty on the total cross section for the WZ and ZZ processes. No uncertainty on the extrapolation from the SC to OC regions is applied because the processes are charge symmetric—verified in the MC used.

Validation regions (VRs) are constructed to check the modeling of $W\gamma$ and $W\gamma^*$. $W\gamma$ events are selected from when the W boson decays leptonically and the photon converts into an e^+e^- pair in the detector, but one of the electrons is lost. These are mitigated by rejecting events with photon conversion vertices. The validation region is constructed by reversing the mitigation, i.e., requiring the electron track to come from a conversion vertex and not have a hit in the B-layer. The rest of the selection is the same as the signal selection, but only events

SR p_{T} range	Total	Sample dependence	Stat.	EW bkg.
Electrons				
10–15 GeV	60	60	2.9	1.9
15–20 GeV	60	60	5.0	1.9
20–25 GeV	60	60	3.9	1.9
> 25 GeV	60	60	3.6	4.2
Muons				
10–15 GeV	40	40	1.1	1.8
15–20 GeV	40	40	0.5	1.8
20–25 GeV	40	40	0.9	1.8
> 25 GeV	40	40	1.6	4.2

Table 5.27: Uncertainties (%), other than the correction factor, on the dijet fake-factor split by anti-identified lepton flavor and p_{T}. The difference between the dijet and $W+\text{jets}$ fake-factors (sample dependence) is not applicable to the multijet estimate. The EW bkg. uncertainty represents contamination from prompt leptons from W/Zs in the event.

selected by the muon trigger are used to avoid the electron trigger selection. This results in a VR which is 83 (87) % $W\gamma$ in the $N_{\text{jets}} = 0\,(1)$ regions. Figures 5.19 (a) and (b), show the m_{T} and electron E_{T} in this region. A further check of photon conversion modeling is performed using $Z \to \mu\mu\gamma$ events, selecting $\mu\mu e$ events with the invariant mass withing 15 GeV of m_Z. This sample is 99 % $Z \to \mu\mu\gamma$ events. We observe a mismodeling of the non-prompt electron rejection and apply an electron p_{T} dependent uncertainty of 25, 18, and 5 % to $W\gamma$ and $Z\gamma$ events in the $10 < p_{\mathrm{T}} \leq 15$, $15 < p_{\mathrm{T}} \leq 20$, and $p_{\mathrm{T}} > 20$ GeV bins respectively.

$W\gamma^*$ events enter the signal region when the W boson decays leptonically and one of the leptons is lost from the γ^* decay into e^+e^- or $\mu^+\mu^-$. A VR is constructed by selecting $e\mu\mu$ events with $p_{\mathrm{T}}^{\text{miss}} > 20$ GeV, the muon pair satisfies $m_{\mu\mu} < 7$ GeV, and both muons are required to pass $\Delta\phi(e,\mu) < 2.8$. Muon pairs consistent with a J/ψ decay are rejected. The leading electron and muon are required to pass the signal selection, and the third muon is allowed to go down $p_{\mathrm{T}} > 3$ GeV. The m_{T} from the leading electron and muon and $m_{\mu\mu}$ are shown in Figs. 5.19 (c) and (d).

5.5.6 Modifications for 7 TeV

Background estimation for the 7 TeV dataset is very similar to those described above. The WW, $Z/\gamma^* \to \tau\tau$, and top-quark control regions are defined the same, and the same extrapolation uncertainties are used. DY estimation in the SF channel also uses the method described in Section 5.5.3.2. The method used for $W+\text{jets}$ is the same, but a multijet sample

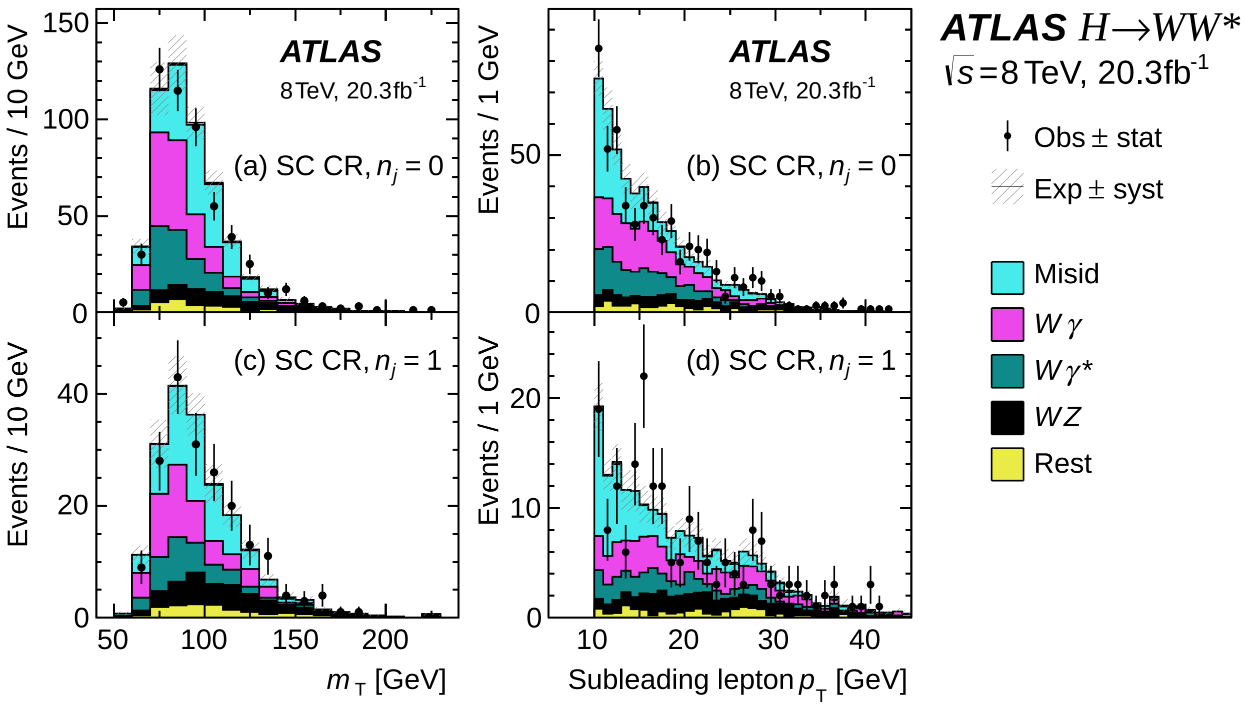

Figure 5.18: Same-charge (SC) CR distributions of (a and c) m_T and (b and d) p_T^{sub} in the $N_{jets} = 0$ and $= 1$ channels [112].

is used to calculate the fake-factor (the dijet fake-factor described in Section 5.5.4). The dominant uncertainty on the fake-factor comes from sample composition uncertainties, 29 % for muons and 36 % for electrons. There are not enough events to make a useful SC CR, so VV is estimated entirely from MC. The VBF channel uses the same methods as the 8 TeV analysis. All of the NFs are summarized in Table 5.28.

5.6 Statistical treatment

A statistical analysis is used to quantify the comparison of the signal and background model with data. A likelihood describing the analysis, including background estimates and uncertainties, is constructed and maximized in order to fit the model to the data and extract results such as the observed signal strength μ_{obs}, i.e., the observed Higgs boson production rate. This likelihood is used in a profile likelihood method to test the signal hypothesis—comparing the expected with the observed. Nuisance parameters (NPs) are profiled, meaning the likelihood is effectively parametrized only by the parameters of interest (POIs). Inputs to the fit are binned histograms of data and estimated backgrounds, as described in Section 5.5, as well as systematic variations of these histograms (some histograms have a single bin). At

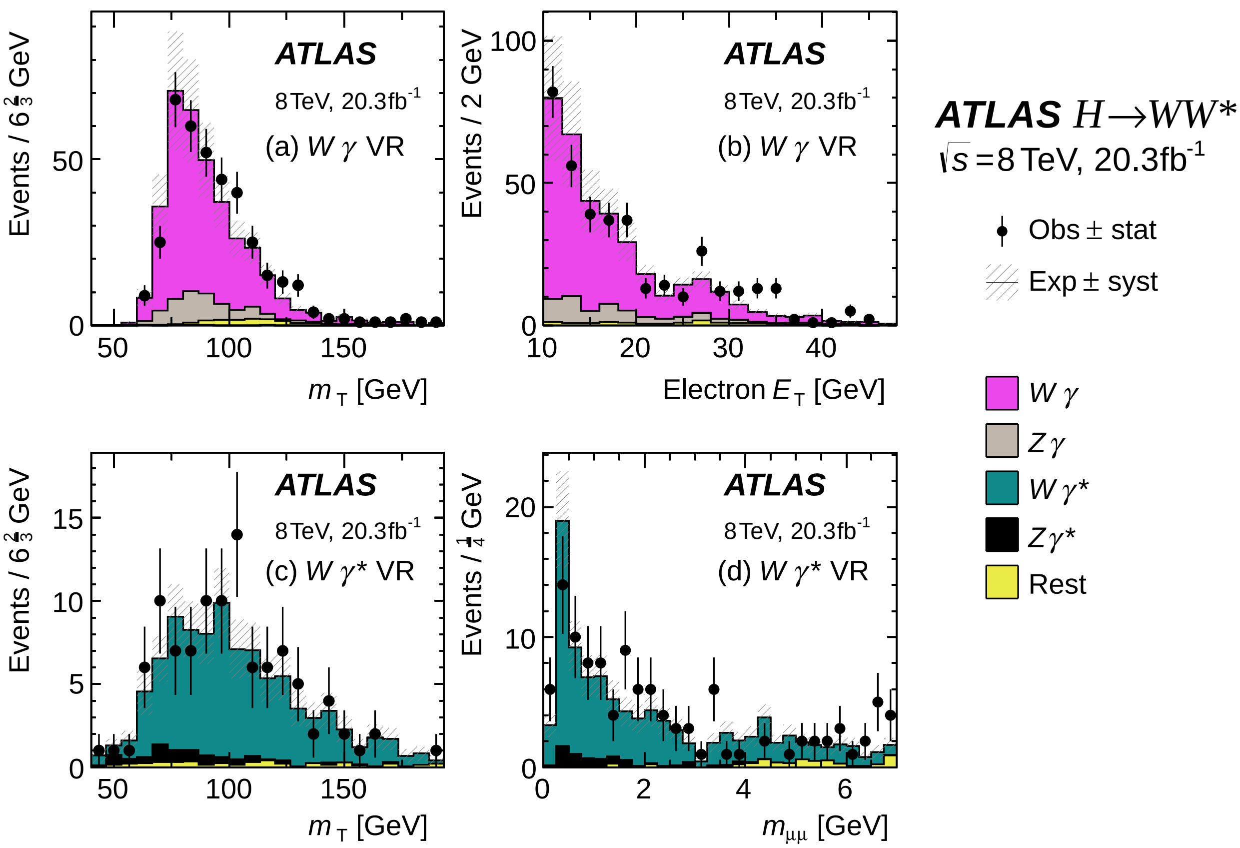

Figure 5.19: (a and b) $W\gamma$ VR m_{T} and electron E_{T} distributions. (c and d) $W\gamma^{*}$ VR m_{T} and $m_{\mu\mu}$ distributions [112].

its simplest, the likelihood would be a Poisson probability of the signal plus background model ($\mu \cdot S + B$), where the signal strength is parametrized with μ, given the observed data yield (N),

$$\mathcal{L}(\mu|N) = P(N|\mu \cdot S + B)\,. \tag{5.27}$$

This can be extended to include the information of a CR designed to normalize the background B, by adding an additional Poisson term and parametrizing the background yield with $\mathcal{N}^{B}$,

$$\mathcal{L}(\mu, \mathcal{N}^{B}|N, N_{\mathrm{CR}}) = P\left(N|\mu \cdot S + \mathcal{N}^{B}B\right) \times P(N_{\mathrm{CR}}|\mathcal{N}^{B}B_{\mathrm{CR}})\,. \tag{5.28}$$

Thus, the normalization of the background is constrained by the additional information of the yield in the CR. The signal strength μ is our POI; it modifies the signal yield, where $\mu = 1$ is the nominal prediction, which in our case will be the SM rate. The symbol $\mathcal{N}$ is a NP—a parameter in the model whose value we are not particularly interested in. We can account for further effects, e.g., the jet energy scale (JES) systematic uncertainty, by introducing another

Category	WW	Top	VV	$Z/\gamma^* \to \tau\tau$
		8 TeV		
$N_{\text{jets}} = 0$	1.22 ± 0.03	1.08 ± 0.02	0.92 ± 0.07	1.00 ± 0.02
$N_{\text{jets}} = 1$	1.05 ± 0.05	1.06 ± 0.03	0.96 ± 0.12	1.05 ± 0.04
$N_{\text{jets}} \geq 2$ ggF	N/A	1.05 ± 0.03	N/A	1.00 ± 0.09
$N_{\text{jets}} \geq 2$ VBF Bin 1	N/A	1.58 ± 0.15	N/A	0.90 ± 0.30
$N_{\text{jets}} \geq 2$ VBF Bin 2-3	N/A	0.95 ± 0.31	N/A	
		7 TeV		
$N_{\text{jets}} = 0$	1.09 ± 0.08	1.12 ± 0.06	N/A	0.89 ± 0.04
$N_{\text{jets}} = 1$	0.98 ± 0.12	0.99 ± 0.04	N/A	1.10 ± 0.09
$N_{\text{jets}} \geq 2$ VBF	N/A	0.82 ± 0.29	N/A	1.52 ± 0.91

Table 5.28: Normalization factors for the various categories in the analysis computed in their respective regions with statistical errors. These are evaluated sequentially: VV, $Z/\gamma^* \to \tau\tau$, Top, and then WW, and do not come from the combined fit.

NP, θ_{JES}, which has some effect on the background normalization such that the background yield is a function $B(\theta_{\text{JES}})$, and introducing a constraint term $\mathcal{M}(\tilde{\theta}_{\text{JES}}|\theta_{\text{JES}})$ representing an auxiliary measurement, where $\tilde{\theta}_{\text{JES}}$ is the nominal value of θ_{JES}. Adding this to the likelihood we obtain

$$\begin{aligned}\mathcal{L}(\mu, \mathcal{N}^B, \theta_{\text{JES}}|N, N_{\text{CR}}) = & P\left(N|\mu \cdot S + \mathcal{N}^B B(\theta_{\text{JES}})\right) \times P(N_{\text{CR}}|\mathcal{N}^B B_{\text{CR}}(\theta_{\text{JES}})) \\ & \times \mathcal{M}(\tilde{\theta}_{\text{JES}}|\theta_{\text{JES}}) \,.\end{aligned} \tag{5.29}$$

The probability density function used for the constraint term varies depending on the NP. Gaussian constraints are frequently used for systematic uncertainties on parameters that can be positive or negative:

$$\mathcal{M}^{\text{Gaussian}}(\tilde{\theta}|\theta) = \frac{1}{\sqrt{2\pi}\sigma} \exp\left(-\frac{(\theta - \tilde{\theta})^2}{2\sigma^2}\right) \,. \tag{5.30}$$

In practice, a normalized Gaussian is used, $\tilde{\theta} = 0$ and $\sigma = 1$, such that an observable B can be represented as $B(\theta) = \tilde{B} \cdot (1 + \sigma_B \theta)$, where σ_B is the uncertainty on B from θ. The latter is the response function $\nu(\theta) = (1 + \sigma_B \theta)$ such that the central value $\tilde{B}$ is separate from the uncertainty parametrized with the θ NP.

Large uncertainties can cause problems if they would shift an expected yield to less than zero (ignoring interference effects). In some cases, a truncated Gaussian is used, restricted to $\nu(\theta) > 0$; however, the log-normal distribution, that of a random variable whose logarithm is normally distributed, is used in most cases because it is naturally restricted to the positive domain for all θ. The log-normal distribution,

$$\mathcal{M}^{\text{log-normal}}(\tilde{\theta}|\theta) = \frac{1}{\sqrt{2\pi}\theta\ln(\kappa)} \exp\left(-\frac{\ln^2(\theta/\tilde{\theta})}{2\ln^2(\kappa)}\right) , \tag{5.31}$$

comes from the Gaussian distribution with $\theta \to \ln(\theta)$, and for convenience $\tilde{\theta} \to \ln(\tilde{\theta})$ and $\sigma \to \ln(\kappa)$, where κ parametrizes the width of the distribution. The response function for a normally distributed θ is $\nu(\theta) = \kappa^{\theta}$. For small uncertainties ϵ, this is approximately $\nu(\theta) \approx (1 + \theta\epsilon)$, for $\kappa = 1 + \epsilon$.

As mentioned before, Poisson distributions are used as the constraint for statistical uncertainties, whether from finite MC events or data yields:

$$\mathcal{M}^{\text{Poisson}}(\tilde{\theta}|\theta\lambda) = \frac{(\theta\lambda)^{\tilde{\theta}} e^{-\theta\lambda}}{\tilde{\theta}!} . \tag{5.32}$$

Here, λ is the expected number of events, typically equal to $\tilde{\theta}$; therefore, $\theta = 1$, not 0, as with Gaussian uncertainties, is the nominal case.

The likelihood above in Equation 5.29 represents the measurement in a single SR; it is extended to include multiple bins and regions by including a product over bins i. We also extend the NP constraints to a product over all NPs. The full likelihood, Equation 5.33, contains observed data yields $\vec{N}$; expected signal $S(\vec{\theta})$ and background $B(\vec{\theta})$ yields, which depend on the NPs as $S(\vec{\theta}) = \tilde{S} \prod_i^{N^\theta} \nu_S(\theta_i)$; normalization factors $\mathcal{N}$, which are unconstrained strength terms modifying the background yields and generally exist per jet bin j; and a Poisson term for MC statistical uncertainties, where M_i is the number of generated events in bin i summed over all processes, γ_i is the nuisance parameter nominally equal to one, and m_i is the expected number of events—see λ in Equation 5.32. The γ NP for MC statistical uncertainty are contained in $S(\vec{\theta})$ and $B(\vec{\theta})$ with a linear response $\nu(\gamma) = \gamma$.

$$\mathcal{L}(\mu, \vec{\theta}|\vec{N}) = \overbrace{\prod_{f}^{\text{flavors}} \prod_{j}^{\text{jet bins}} \prod_{p}^{p_{\mathrm{T}}^{\mathrm{sub}} \text{ bins}} \prod_{m}^{m_{\ell\ell} \text{ bins}} \prod_{t}^{m_{\mathrm{T}} \text{ bins}}}^{\text{Sum over all bins in all SRs shortened to } i} P\Big(N_i|\mu S_i(\vec{\theta}) + \sum_{b}^{N^{\mathrm{Bkgs}}} \mathcal{N}^{b,j} B_i^b(\vec{\theta})\Big) \tag{5.33}$$
$$\times \prod_{c}^{\text{CRs}} P\Big(N_c|\mu S_c(\vec{\theta}) + \mathcal{N}^{b,j} B_c^b(\vec{\theta}) + \sum_{b' \neq b}^{N^{\mathrm{Bkgs}}-1} \mathcal{N}^{b',j} B^{b'}(\vec{\theta})\Big)$$
$$\overbrace{\times \prod_{i=1}^{N^{\theta}} G(\tilde{\theta}_i|\theta_i)}^{\text{Gaussian constraints}} \overbrace{\times P(M_i|\gamma_i m_i)}^{\text{MC stats}}$$

The fit includes many SRs, detailed in Table 5.29, which are input as binned m_{T} and O_{BDT} histograms. For the $N_{\mathrm{jets}} \leq 1$ categories, the binning (shown in Table 5.31) is optimized in each region by setting the boundaries such that each bin has an equal signal yield expectation. Ten m_{T} bins are used for $N_{\mathrm{jets}} = 0$ and six bins for $N_{\mathrm{jets}} = 1$. The m_{T} bin boundaries in GeV for the $N_{\mathrm{jets}} \geq 2$ ggF channel is $(0, 50, 80, 130, \infty)$ for a total of four m_{T} bins. For the VBF channel, the O_{BDT} binning is $(-0.48, 0.3, 0.78, 1)$ for a total of three bins. This makes for a total of 262 SR bins, after accounting for the division by lepton flavor, jet multiplicity, subleading lepton p_{T}, and $m_{\ell\ell}$. CRs are included as single bin regions; the regions and flavors used are listed in Table 5.30. A total of 62 CRs are used in the fit. This includes 8 regions for the $ee/\mu\mu$ DY estimate per jet bin: two flavors, high and low $m_{\ell\ell}$ and pass plus fail, as well as 36 additional b-tagged regions for the top-quark $N_{\mathrm{jets}} = 1$ estimate, which do not include a Poisson term for the expected yields. The regions for the $N_{\mathrm{jets}} = 0$ top-quark background estimate, misid estimate, and VBF DY estimate are not included in the likelihood, but as expectations with systematic uncertainties.

5.6.1 'Pacman' method implementation

The 'Pacman' method to estimate $e\mu$ in the $ee/\mu\mu$ channel, described in Section 5.5.3.2, is included in the likelihood with the regions mentioned above and additional constraint terms. Two Poisson terms incorporate the f_{recoil} pass and fail regions on the Z-peak,

$$P\left(N_{\mathrm{pass}}^{Z\text{-peak}}|\mathcal{N}_{\mathrm{DY}}^{Z\text{-peak}} \epsilon_{\mathrm{DY}} B_{\mathrm{DY}}^{Z\text{-peak}}(\vec{\theta}) + \epsilon'_{\text{non-DY}} B_{\text{non-DY}}^{Z\text{-peak}}(\vec{\theta})\right) \times \tag{5.34}$$
$$P\left(N_{\mathrm{fail}}^{Z\text{-peak}}|\mathcal{N}_{\mathrm{DY}}^{Z\text{-peak}} (1-\epsilon_{\mathrm{DY}}) B_{\mathrm{DY}}^{Z\text{-peak}}(\vec{\theta}) + (1-\epsilon'_{\text{non-DY}}) B_{\text{non-DY}}^{Z\text{-peak}}(\vec{\theta})\right),$$

SR category i				Fit var. $\otimes N^{\rm bins}$
$N_{\rm jets}$, flavor	$\otimes\, m_{\ell\ell}$	$\otimes\, p_{\rm T}^{\rm sub}$	$\otimes\, \ell_2$ Flav.	
$N_{\rm jets} = 0$				
$e\mu$	$\otimes\,[10, 30, 55]$	$\otimes\,[10, 15, 20, \infty)$	$\otimes\,[e, \mu]$	$m_{\rm T} \otimes 10$
$ee/\mu\mu$	$\otimes\,[12, 55]$	$\otimes\,[10, \infty)$		$m_{\rm T} \otimes 6$
$N_{\rm jets} = 1$				
$e\mu$	$\otimes\,[10, 30, 55]$	$\otimes\,[10, 15, 20, \infty)$	$\otimes\,[e, \mu]$	$m_{\rm T} \otimes 10$
$ee/\mu\mu$	$\otimes\,[12, 55]$	$\otimes\,[10, \infty)$		$m_{\rm T} \otimes 6$
$N_{\rm jets} \geq 2$ ggF				
$e\mu$	$\otimes\,[10, 55]$	$\otimes\,[10, \infty)$		$m_{\rm T} \otimes 4$
$N_{\rm jets} \geq$ VBF				
$e\mu$	$\otimes\,[10, 50]$	$\otimes\,[10, \infty)$		$O_{\rm BDT} \otimes 3$
$ee/\mu\mu$	$\otimes\,[12, 50]$	$\otimes\,[10, \infty)$		$O_{\rm BDT} \otimes 3$

Table 5.29: Signal region categories used in the fit that enter the Poisson term on the first line of Equation 5.33. The binning in $m_{\ell\ell}$ and $p_{\rm T}^{\rm sub}$ are denoted by the bin boundaries in GeV [112]. In the fourth column, the number of additional bins in $m_{\rm T}$ and $O_{\rm BDT}$ is indicated, with the $m_{\rm T}$ binning shown in Table 5.31 and BDT bin boundaries being [0.3, 0.78, 1].

where $B_{\text{non-DY}}$ is the sum of backgrounds other than DY and signal. The B yields include the response functions $\nu(\theta)$ and signal strength μ where appropriate. The $\epsilon'_{\text{non-DY}}$ efficiency is constrained in a region with the Z-peak selection but $e\mu$ flavor events,

$$\begin{aligned} &P\left(N_{\rm pass}^{Z\text{-peak},e\mu} | \epsilon'_{\text{non-DY}} B_{\text{non-DY}}^{Z\text{-peak},e\mu}(\vec{\theta})\right) \times \\ &P\left(N_{\rm fail}^{Z\text{-peak},e\mu} | (1-\epsilon'_{\text{non-DY}}) B_{\text{non-DY}}^{Z\text{-peak},e\mu}(\vec{\theta})\right) . \end{aligned} \tag{5.35}$$

Region	WW	VV	Top	DY,$ee/\mu\mu$	DY,$\tau\tau$
$N_{\rm jets} = 0$	$e\mu\rightarrow$Both	$e\mu \rightarrow e\mu$	-	Both$\rightarrow ee/\mu\mu$	$e\mu\rightarrow$Both
$N_{\rm jets} = 1$	$e\mu\rightarrow$Both	$e\mu \rightarrow e\mu$	$e\mu\rightarrow$Both	Both$\rightarrow ee/\mu\mu$	$e\mu\rightarrow$Both
$N_{\rm jets} \geq 2$ VBF	-	-	Both$\rightarrow$Both	-	-
$N_{\rm jets} \geq 2$ ggF	-	-	$e\mu \rightarrow e\mu$	-	$e\mu \rightarrow e\mu$

Table 5.30: CRs included in the fit, along with what flavor sample is used in the CR (left side of arrow) and what flavor the normalization is attached to (right side of arrow).

Signal Region		Bin Boundaries								
$m_{\ell\ell}$	Flav. p_T^{sub}				$N_{jets} = 0$					
< 30	$e\mu$ 10–15	74.5	80.4	85.4	89.9	94.4	98.9	103.9	109.7	118.2
	μe 10–15	76.7	82.5	87.0	91.2	95.2	99.7	104.4	110.1	118.0
	$e\mu$ 15–20	81.6	87.9	92.5	96.6	100.6	104.7	109.2	114.5	122.1
	μe 15–20	80.8	86.7	91.5	95.9	99.8	103.9	108.5	113.8	121.4
	$e\mu > 25$	93.7	100.0	104.6	108.4	112.3	116.1	120.4	125.6	133.7
	$\mu e > 25$	93.1	99.8	104.7	108.7	112.5	116.3	120.5	125.5	133.6
> 30	$e\mu$ 10–15	84.1	90.5	95.1	99.5	103.5	107.9	112.3	117.5	124.7
	μe 10–15	84.9	90.9	95.6	99.9	103.8	107.9	112.3	117.7	125.7
	$e\mu$ 15–20	86.3	92.3	97.0	101.4	105.4	109.4	113.6	118.7	125.8
	μe 15–20	85.0	91.6	96.4	100.5	104.4	108.3	112.5	117.7	125.2
	$e\mu > 25$	93.2	100.2	105.0	109.2	113.0	116.9	121.1	126.4	135.4
	$\mu e > 25$	93.5	100.3	105.2	109.4	113.2	117.0	121.3	126.8	135.8
12–55	$ee/\mu\mu > 10$	95.1	100.0	104.0	107.5	110.8	114.2	117.8	122.1	128.8
	Flav. p_T^{sub}				$N_{jets} = 1$					
< 30	$e\mu$ 10–15	79.0	89.5	98.0	106.8	118.7				
	μe 10–15	79.6	88.7	97.9	106.2	116.0				
	$e\mu$ 15–20	81.6	92.2	101.8	110.2	119.7				
	μe 15–20	81.9	92.2	101.4	110.0	120.2				
	$e\mu > 25$	86.7	97.9	107.0	116.3	127.4				
	$\mu e > 25$	87.4	98.5	107.2	116.5	127.9				
> 30	$e\mu$ 10–15	88.1	98.0	105.9	113.2	123.3				
	μe 10–15	87.0	95.9	105.0	112.0	121.7				
	$e\mu$ 15–20	88.2	97.9	105.8	113.6	123.9				
	μe 15–20	87.4	97.0	105.1	113.7	123.2				
	$e\mu > 25$	92.0	101.5	109.7	118.6	130.2				
	$\mu e > 25$	91.2	101.3	109.6	117.7	129.0				
12–55	$ee/\mu\mu > 10$	96.9	105.2	111.7	118.0	126.7				

Table 5.31: m_T bin boundaries used in the 8 TeV analysis. Units are in GeV. The first bin extends from 0 GeV and the last extends to 500 GeV, where there are no longer any expected events—no events in data are observed above 500 GeV.

Two more Poisson terms handle the f_{recoil} pass and fail regions at low $m_{\ell\ell}$, i.e., the SR,

$$\prod_{i}^{m_{\mathrm{T}}\text{ bins}} P\left(N^{\text{SR}}_{\text{pass},i}|\mathcal{N}^{\text{SR}}_{\text{DY}}\epsilon_{\text{DY}}B^{\text{SR}}_{\text{DY},i}(\vec{\theta}) + \epsilon_{\text{non-DY}}B^{\text{SR}}_{\text{non-DY},i}(\vec{\theta})\right) \times \tag{5.36}$$
$$P\left(N^{\text{SR}}_{\text{fail},i}|\mathcal{N}^{\text{SR}}_{\text{DY}}(1-\epsilon_{\text{DY}})B^{\text{SR}}_{\text{DY},i}(\vec{\theta}) + (1-\epsilon_{\text{non-DY}})B^{\text{SR}}_{\text{non-DY},i}(\vec{\theta})\right) .$$

Again, the non-DY efficiency is constrained in regions with $e\mu$ flavor events, but the same selection as the $ee/\mu\mu$ SR,

$$P\left(N^{\text{SR},e\mu}_{\text{pass}}|\epsilon_{\text{non-DY}}B^{\text{SR},e\mu}_{\text{non-DY}}(\vec{\theta})\right) \times \tag{5.37}$$
$$P\left(N^{\text{SR},e\mu}_{\text{fail}}|(1-\epsilon_{\text{non-DY}})B^{\text{SR},e\mu}_{\text{non-DY}}(\vec{\theta})\right) .$$

Separate DY normalization parameters are used on the Z-peak ($\mathcal{N}^{Z\text{-peak}}_{\text{DY}}$) and in the SR ($\mathcal{N}^{\text{SR}}_{\text{DY}}$).

5.6.2 JBEE method implementation

The b-tagging efficiency correction for the $N_{\text{jets}} = 1$ top-quark background estimate is implemented in the likelihood by including an additional parameter correcting the b-tagging efficiency, which can be thought of as $\mathcal{N}_{b\text{-tag}} = \epsilon^{\text{data},2j}_{\text{tag}}/\epsilon^{\text{MC},2j}_{\text{tag}}$. The two jet regions, two b-tag and one b-tag, for the estimate are included in the likelihood with additional Poisson terms with normalization parameters for each jet, b-tagged or b-vetoed,

$$P\left(N^{2j}_{2\text{-tag}}|\mathcal{N}^{2j}_{\text{top}}\mathcal{N}^{2}_{b\text{-tag}}B^{2j,2\text{-tag}}_{\text{top}} + B^{2j,2\text{-tag}}_{\text{non-top}}\right) \times \tag{5.38}$$
$$P\left(N^{2j}_{1\text{-tag}}|\mathcal{N}^{2j}_{\text{top}}\mathcal{N}_{b\text{-tag}}[B^{2j,1\text{-tag}}_{\text{top}} + 2(1-\mathcal{N}_{b\text{-tag}})B^{2j,2\text{-tag}}_{\text{top}}] + B^{2j,1\text{-tag}}_{\text{non-top}}\right) ,$$

where $\mathcal{N}^{2j}_{\text{top}}$ is the common normalization in the $N_{\text{jets}} = 2$ region only and $\mathcal{N}_{b\text{-tag}}$ is squared. The second Poisson can be derived from plugging in the b-veto normalization parameter

$$\mathcal{N}_{b\text{-veto}} = \frac{(1-\mathcal{N}_{b\text{-tag}}\epsilon^{\text{MC},2j}_{\text{tag}})}{(1-\epsilon^{\text{MC},2j}_{\text{tag}})} \tag{5.39}$$

into the the top-quark yield estimate for the $N_{\text{jets}} = 2$, one b-tag region

$$B^{2j,1\text{-tag,est.}}_{\text{top}} = \mathcal{N}^{2j}_{\text{top}}\mathcal{N}_{b\text{-tag}}\mathcal{N}_{b\text{-veto}}B^{2j,1\text{-tag,MC}}_{\text{top}} , \tag{5.40}$$

and making use of the equivalent Equation 5.19 for MC.

The estimated top-quark yield in the top CR, SR, and WW CR are modified in Equa-

tion 5.33 to include the b-tagging normalizations. Poisson terms for the regions are the following:
for the $N_{\text{jets}} = 1$ top CR

$$P\Big(N_{\text{top CR},1j}|\mu S_{\text{top CR},1j}(\vec{\theta}) + \mathcal{N}^{\text{top},1j}\mathcal{N}_{b\text{-tag}}B^{\text{top}}_{\text{top CR},1j}(\vec{\theta}) + \sum_{b'\neq top}^{N^{\text{Bkgs}}-1}\mathcal{N}^{b',1j}B^{b'}(\vec{\theta})\Big)\,, \tag{5.41}$$

for the $N_{\text{jets}} = 1$ WW CR

$$\begin{aligned} P\Big(N_{WW\text{ CR},1j}|\mu S_{WW\text{ CR},1j}(\vec{\theta}) &+ \mathcal{N}^{WW,1j}B^{WW}_{WW\text{ CR},1j}(\vec{\theta}) \\ &+ \sum_{b'\neq WW||\text{top}}^{N^{\text{Bkgs}}-2}\mathcal{N}^{b',1j}B^{b'}_{WW\text{ CR},1j}(\vec{\theta}) \\ &+ \mathcal{N}^{\text{top},1j}\left[B^{\text{top}}_{WW\text{ CR},1j}(\vec{\theta}) + (1-\mathcal{N}_{b\text{-tag}})B^{\text{top}}_{WW\text{ CR-tag},1j}(\vec{\theta})\right]\Big)\,, \end{aligned} \tag{5.42}$$

and for the $N_{\text{jets}} = 1$ SRs

$$\begin{aligned} P\Big(N_{\text{SR},1j}|\mu S_{\text{SR},1j}(\vec{\theta}) &+ \sum_{b'\neq\text{top}}^{N^{\text{Bkgs}}}\mathcal{N}^{b',1j}B^{b'}_{\text{SR},1j}(\vec{\theta}) \\ &+ \mathcal{N}^{\text{top},1j}\left[B^{\text{top}}_{\text{SR},1j}(\vec{\theta}) + (1-\mathcal{N}_{b\text{-tag}})B^{\text{top}}_{\text{SR-tag},1j}(\vec{\theta})\right]\Big)\,. \end{aligned} \tag{5.43}$$

The SR-tag and CR-tag regions are defined with the same selection, except b-tagged instead of b-vetoed. In this way, the top-quark estimate in the regions is corrected by their respective b-tagged regions and the b-tagging efficiency normalization. If the MC models the efficiency well, i.e., $\mathcal{N}_{b\text{-tag}} = 1$, the unadjusted MC expectations are recovered.

5.6.3 Method and test statistic

A test statistic $\tilde{q}_\mu$ based on a profile likelihood [195] is used to test the null and alternative hypotheses. The profile likelihood is constructed as

$$\lambda(\mu) = \begin{cases} \dfrac{\mathcal{L}\big(\mu, \hat{\hat{\vec{\theta}}}(\mu)\big)}{\mathcal{L}\big(\hat{\mu}, \hat{\vec{\theta}}\big)} & \hat{\mu} \geq 0 \\[2ex] \dfrac{\mathcal{L}\big(\mu, \hat{\hat{\vec{\theta}}}(\mu)\big)}{\mathcal{L}\big(0, \hat{\hat{\vec{\theta}}}(0)\big)} & \hat{\mu} < 0\,. \end{cases} \tag{5.44}$$

The double hats indicate the conditional maximum likelihood estimators (MLEs) given a signal strength of μ, or 0 as noted. The single hats indicate the parameters which maximize the likelihood. Thus $\mathcal{L}\big(\hat{\mu}, \hat{\vec{\theta}}\big)$ is the global maximum of the likelihood and $\mathcal{L}\big(\mu, \hat{\hat{\vec{\theta}}}(\mu)\big)$ the value of the likelihood for a signal strength μ, where the nuisance parameters are allowed to float, i.e., the maximum likelihood for μ. This is the 'profiling' of the nuisance parameters.

The test statistic $\tilde{q}_\mu$ is built from the negative-log likelihood ratio (later written as $-2\ln\Lambda$),

$$\tilde{q}_\mu = \begin{cases} -2\ln\tilde{\lambda}(\mu) & \hat{\mu} \le \mu \\ 0 & \hat{\mu} > \mu \end{cases} = \begin{cases} -2\ln\dfrac{\mathcal{L}\big(\mu, \hat{\hat{\vec{\theta}}}(\mu)\big)}{\mathcal{L}\big(0, \hat{\hat{\vec{\theta}}}(0)\big)} & \hat{\mu} < 0 \\ -2\ln\dfrac{\mathcal{L}\big(\mu, \hat{\hat{\vec{\theta}}}(\mu)\big)}{\mathcal{L}\big(\hat{\mu}, \hat{\vec{\theta}}\big)} & 0 \le \hat{\mu} \le \mu \\ 0 & \hat{\mu} > \mu\,. \end{cases} \tag{5.45}$$

In the case where no signal is observed, we wish to place upper limits on the signal strength μ. This quantifies the probability that the signal plus background model fluctuated down to the observed quantity. Sometimes, we are dealing with an analysis which is not extremely sensitive to the signal model; a modified method is used to avoid excluding the signal hypothesis when we do not expect to have sensitivity. The modified frequentest method known as CL_S [196] is used to compute 95 % confidence level (CL) exclusions, instead of p_μ. For this case, the test statistic is one-sided with the constraint $0 < \hat{\mu} < \mu$. Two p-values are needed: the p-value p_b, probability of observing larger q_μ than observed given the background only hypothesis (larger means less sensitivity to distinguish the signal hypothesis with μ from background only), and p-value p_μ, probability to observe larger q_μ than observed given the signal plus background hypothesis (larger p_μ means data is more compatible with the signal plus background hypothesis). These are computed by integrating probability distributions of the test statistic,

$$p_b = \int_{-\infty}^{\tilde{q}_{\mu,\mathrm{obs}}} f(\tilde{q}_\mu | 0, \hat{\hat{\vec{\theta}}}_0) d\tilde{q}_\mu \tag{5.46}$$

$$p_\mu = \int_{\tilde{q}_{\mu,\mathrm{obs}}}^{\infty} f(\tilde{q}_\mu | \mu, \hat{\hat{\vec{\theta}}}_\mu) d\tilde{q}_\mu\,, \tag{5.47}$$

The distributions can be constructed from toy MC pseudo-data, but computationally quicker asymptotic approximations [195] are used for the evaluation of the probability distributions f.

Upper limits on μ are computed by constructing the CL_S ratio of p-values,

$$CL_S = \frac{p_\mu}{1 - p_b}\,, \tag{5.48}$$

and finding the μ such that $CL_S = 0.05$.

In the case of an excess, we quantify the statistical significance by considering the probability that the background fluctuated up to the observed quantity. The significance of an excess is computed by evaluating the background only p_0, with the constraint $\hat{\mu} > 0$,

$$p_0 = \int_{-\infty}^{\tilde{q}_{0,\mathrm{obs}}} f(\tilde{q}_0 | 0, \hat{\hat{\vec{\theta}}}_0) d\tilde{q}_\mu\,. \tag{5.49}$$

The significance Z_0, in terms of standard deviations, is obtained by inverting the error function

$$Z_0 = \Phi^{-1}(1 - p_0)\,. \tag{5.50}$$

5.6.4 Systematic uncertainties

Systematic uncertainties are divided into theoretical sources, described in Sections 5.2.2.1 and 5.5, and experimental sources, most of which are related to the physics objects, described in Chapter IV.

Flat systematic uncertainties, or those which only affect the normalization of a processes, use a log-normal response function $\nu(\theta) = \kappa^\theta$, where κ is evaluated at 1 standard deviation (s.d.), $\theta = \pm 1$. Systematic uncertainties which also affect the m_T shape, are split into a flat component and a shape which is parametrized with a response function of $\nu(\theta) = 1 + \epsilon\theta$ for each bin. Shape templates are taken at 1 s.d., $\theta = \pm 1$. In both cases, a Gaussian constraint term is used in the likelihood.

Systematic uncertainties are ignored if they are negligible in order to reduce computational time; this is done per region per process. If normalization uncertainties are less than 0.1 % in a region for a given process, or if shape uncertainties are not more than 1 % in a bin, then the uncertainty is ignored in that region for that process. Further, to remove spurious systematic uncertainties, particularly from low sample size or large weighted events migrating in MC, systematic uncertainties in regions which have variations larger than −80 % and 150 % are ignored. Most experimental uncertainties on the shape are ignored as the impact is negligible; changes in the shape are dominated by normalization uncertainties on the individual backgrounds.

Systematic uncertainties can also be full correlated or fully anti-correlated by using the same NP θ or $-\theta$ respectively. This is used, for example, in correlating the m_{T} shape uncertainty and normalization uncertainty on the signal described in Section 5.2.2.1.

Experimental uncertainties mainly arise from the reconstruction and identification of objects, as well as the measurement of their energy and momentum. The uncertainty on the luminosity measurement, 2.8 % for 8 TeV and 1.8 % for 7 TeV [90], and uncertainties on the data-driven misid background estimation are also included in the experimental uncertainties.

Electron and muon uncertainties from reconstruction and identification are described in Sections 4.2 and 4.3 respectively. They are generally well measured, with uncertainties around 2 % or less, see Table 5.32, the largest coming from the isolation requirement, see Tables 4.1 and 4.2. The impact of these uncertainties on the $H \to WW^{(*)} \to \ell\nu\ell\nu$ analysis is very small. An additional uncertainty is applied to electrons reconstructed from converted photons, derived from a $Z\gamma \to \mu\mu e$ validation region. A single NP is used with assigned uncertainties of 25, 18, and 5 % in the $10 < E_{\mathrm{T}} < 15$, $15 < E_{\mathrm{T}} < 20$, and $E_{\mathrm{T}} > 20$ GeV bins. Uncertainties on the lepton trigger efficiencies are less than 1 %.

Source of Uncertainty	Size of the uncertainty
Electron Efficiency	Reconstruction: 0.1–1.0 % depending on E_T and η
	Identification: 0.2–2.7 % depending on E_T and η
Electron Energy Scale	$\sim$ 0.4 % depending on E_T and η (except for crack region)
Electron Energy Resolution	$\sim$ 1 % depending on E_T and η
Muon Efficiency	$<$ 0.46 % depending on p_{T} and η
Muon Energy Scale	$<$ 0.50 % depending on p_{T} and η
Muon Energy Resolution	$<$ 1 % depending on p_{T} and η

Table 5.32: Electron and muon systematic uncertainties.

Uncertainties on the JES are described in Section 4.4 and are a large portion of the experimental uncertainty. They are divided into several independent categories. Also important is the jet energy resolution (JER), which varies from 5–20 % depending on jet p_{T} and η. The JES relative uncertainty ranges from 1–7 % and the uncertainty on the JER varies from 2–40 %, both depending on the jet p_{T} and η. Figure 4.9 shows the uncertainties as a function of p_{T} and η for a subset of the phase-space.

The uncertainty on b-jet identification, described in Section 4.4.1, is split into six components using an eigenvector decomposition, equaling the number of p_{T} bins used in the calibration. JES, JER, and top-quark modeling uncertainties all contribute to the b-tagging uncertainties, more details in Ref. [127]. The uncertainty on b-tagging efficiency in p_{T} bins ranges from 0.01–0.6 % at the smallest to 1.1–7.8 % for the largest variation. Light- or c-jets mistagged as b-jets each have one NP. The uncertainty on light-jet mistagging depends on both p_{T} and η, and ranges from 9–15 % in the central region ($|\eta| < 1.1$), and 9–19 % in the forward region. The uncertainty on c-jets mistagged as b-jets is inclusive in η and ranges from 6–14 % depending on jet p_{T}.

Aside from JES variations, uncertainty on the pile-up modeling is handled by scaling the average interactions per bunch crossing, μ_{pu}, in the MC up and down by 11 %. The impact of the resulting uncertainty is small, around 2 % at most.

The computation of MET makes use of many objects, thus all of the uncertainties on the components, above, are propagated to the MET. That still leaves MET specific uncertainties on the soft term used in the calculation. In order to assess the uncertainties on the soft terms, the longitudinal and perpendicular components, with respect to the hard component of the MET, are smeared and rescaled. The uncertainty is binned by the vector sum of high p_{T} objects and average number of interactions per bunch crossing. For calorimeter-based $E_{\mathrm{T}}^{\mathrm{miss}}$, the mean of the longitudinal component varies by 0.2–0.3 GeV, and the longitudinal and perpendicular resolutions vary by 1–4 %. The left of Fig. 4.12 shows the effect of the soft term scale variation. Similarly for the track-based $p_{\mathrm{T}}^{\mathrm{miss}}$, uncertainties on jets and leptons are propagated to the MET. The balance of tracks in the soft term and the total p_{T} of the hard objects in the event is used to to evaluate the uncertainty. Uncertainties are computed comparing data and MC using $Z \to ee$ and $Z \to \mu\mu$ events, as a function of the vector sum of the p_{T} of hard objects in the events. From this, the variation on the mean of the longitudinal component is in the range 0.3–1.4 GeV, and the variation of the longitudinal and perpendicular resolution is in the range of 1.6–3.3 GeV, the ranges corresponding to the vector sum p_{T} of hard objects below 5 GeV and above 50 GeV respectively.

Table 5.33 summarizes the impacts of the theoretical and experimental uncertainties on the total signal and background yields in the four jet-binned categories. Table 5.34 details the uncertainties per background process, divided into the statistical, experimental systematic, and theoretical systematic uncertainties. Both tables contain post-fit values, see Section 5.7 for the definition of post-fit values.

5.6.5 Combination of channels

All of the channels are combined for the final results: 7 and 8 TeV $e\mu$ and $ee/\mu\mu$ $N_{\mathrm{jets}} \leq 1$; 7 and 8 TeV $e\mu$ and $ee/\mu\mu$ $N_{\mathrm{jets}} \geq 2$ VBF; and 8 TeV $e\mu$ $N_{\mathrm{jets}} \geq 2$ ggF. This involves combining the likelihoods together, and most importantly, implementing a correlation scheme for the NPs and signal strengths. There are 210 NPs and 32 NFs in the combined model. In general, NPs for systematics derived on a particular dataset are correlated within years, i.e., between sub-channels, and uncorrelated between years. For example, b-tagging, electron identification,

	$N_{\text{jets}} = 0$	$N_{\text{jets}} = 1$	$N_{\text{jets}} \geq 2$ ggF	$N_{\text{jets}} \geq 2$ VBF
Uncertainties on Signal				
ggF H, jet veto for $N_{\text{jets}} = 0$, ϵ_0	8.1	14	12	-
ggF H, jet veto for $N_{\text{jets}} = 1$, ϵ_1	-	12	15	-
ggF H, $N_{\text{jets}} \geq 2$ cross section	-	-	-	6.9
ggF H, $N_{\text{jets}} \geq 3$ cross section	-	-	-	3.1
ggF H, total cross section	10	9.1	7.9	2.0
ggF H acceptance model	4.8	4.5	4.2	4.0
VBF H, total cross section	-	0.4	0.8	2.9
VBF H acceptance model	-	0.3	0.6	5.5
$H \to WW^{(*)}$ branch. fraction	4.3	4.3	4.3	4.3
Integrated luminosity	2.8	2.8	2.8	2.8
Jet energy scale & reso.	5.1	2.3	7.1	5.4
$p_{\text{T}}^{\text{miss}}$ scale & resolution	0.6	1.4	0.1	1.2
f_{recoil} efficiency	2.5	2.1	-	-
Trigger efficiency	0.8	0.7	-	0.4
Electron id., iso., reco. eff.	1.4	1.6	1.2	1.0
Muon id., isolation, reco. eff.	1.1	1.6	0.8	0.9
Pile-up model	1.2	0.8	0.8	1.7
Uncertainties on Backgrounds				
WW theoretical model	1.4	1.6	0.7	3.0
Top theoretical model	-	1.2	1.7	3.0
VV theoretical model	-	0.4	1.1	0.5
$Z/\gamma^* \to \tau\tau$ estimate	0.6	0.3	1.6	1.6
$Z/\gamma^* \to \ell\ell$ est. in VBF	-	-	-	4.8
$W +$ jets estimate	1.0	0.8	1.6	1.3
jj estimate	0.1	0.1	1.8	0.9
Integrated luminosity	-	-	0.1	0.4
Jet energy scale & reso.	0.4	0.7	0.9	2.7
$p_{\text{T}}^{\text{miss}}$ scale & resolution	0.1	0.3	0.5	1.6
b-tagging efficiency	-	0.2	0.4	2.0
Light- and c-jet mistag	-	0.2	0.4	2.0
f_{recoil} efficiency	0.5	0.5	-	-
Trigger efficiency	0.3	0.3	0.1	-
Electron id., iso., reco. eff.	0.3	0.3	0.2	0.3
Muon id., isolation, reco. eff.	0.2	0.2	0.3	0.2
Pile-up model	0.4	0.5	0.2	0.8

Table 5.33: Sources of systematic uncertainty on the signal and total background yields in percent for the 8 TeV analysis. Values are post-fit. Dashes indicate the uncertainty is negligible, $< 0.1\,\%$, or not applicable [112].

Sample	Total error	Stat. error	Expt. syst. err.	Theo. syst. err.
$N_{\text{jets}} = 0$				
N_S	16	-	6.7	15
N_B	2.5	1.5	1.2	1.7
N_{WW}	4.2	2.4	2.3	2.6
N_{top}	7.4	2.3	4.2	5.6
N_{misid}	17	-	9.9	14
N_{VV}	9.9	4.8	4.6	7.4
$N_{\tau\tau}$ (DY)	34	1.7	33	7.2
$N_{ee/\mu\mu}$ (DY)	30	14	26	5.5
$N_{\text{jets}} = 1$				
N_S	22	-	5.3	22
N_B	3	1.7	1.4	2.1
N_{WW}	7.7	5.5	2.7	4.6
N_{top}	5	3.4	2.9	2.3
N_{misid}	18	-	11	14
N_{VV}	14	8.9	6.1	8.5
$N_{\tau\tau}$ (DY)	27	3.3	26	6.3
$N_{ee/\mu\mu}$ (DY)	39	27	26	7.4
$N_{\text{jets}} \geq 2$ ggF-enriched				
N_S	23	-	8.6	22
N_B	4.2	1.5	2.2	3.2
N_{WW}	20	-	8.7	18
N_{top}	7.9	2.6	3.4	6.7
N_{misid}	29	-	16	24
N_{VV}	32	-	9.6	31
$N_{\tau\tau}$ (DY)	18	8	13	10
$N_{ee/\mu\mu}$ (DY)	15	-	14	4
$N_{\text{jets}} \geq 2$ VBF-enriched				
N_S	13	-	6.8	12
N_B	9.2	4.7	6.4	4.5
N_{WW}	32	-	14	28
N_{top}	15	9.6	7.6	8.5
N_{misid}	22	-	12	19
N_{VV}	20	-	12	15
$N_{\tau\tau}$ (DY)	40	25	31	2.9
$N_{ee/\mu\mu}$ (DY)	19	11	15	-

Table 5.34: Total post-fit uncertainties on the signal (N_S) and background (N_B) yields for the 8 TeV analysis split by background process and type of uncertainty. Dashes indicate uncertainties which are less than 1 % or not applicable [112].

and some JES systematics are uncorrelated between the 7 TeV and 8 TeV analyses. They are either derived with different methods or sensitive to changes in pile-up. Sources of uncertainty which are statistical in nature are also uncorrelated between sub-channels. For the most part, theoretical uncertainties are correlated everywhere. One example of an exception is the uncertainties on quark initiated WW, between the ggF channels, which use POWHEG, and the VBF channels, using SHERPA. NFs are not correlated outside of their particular sub-channel and dataset. The complete correlation scheme is listed in Appendix C.

The fit model is designed to avoid over-constraining NPs, i.e., avoid a post-fit uncertainty which is smaller than the pre-fit uncertainty on a given θ, which can be measured by scanning the likelihood around $\hat{\theta}$ to find $\hat{\theta} \pm \Delta_\theta$ such that $-2\Delta \ln \mathcal{L} = 1$. Pre- and post-fit refer to before maximizing the likelihood, i.e., all parameters at their nominal input values, and after maximizing the likelihood. By avoiding these constraints, the model relies less on the assumptions of correlations between different regions of phase space. A primary check of the fit results is to compare the pre- and post-fit impacts of NPs on the measured signal strength, checking for constraints and pulls. A pull is a non-zero value of $\hat{\theta}$. The impact of an NP on $\hat{\mu}$ ($\Delta_{\hat{\mu}}$) is calculated by taking the difference between the best-fit $\hat{\mu}(\hat{\theta})$ and at one standard deviation (pre-fit, $\Delta_\theta = \pm 1$), other NPs are allowed to float in the fit while the θ in question is fixed,

$$\Delta_{\hat{\mu}\pm} = \hat{\mu}(\hat{\theta} \pm \Delta_\theta) - \hat{\mu}(\hat{\theta})\,. \tag{5.51}$$

Figure 5.20 shows the top thirty NPs, as ranked by their post-fit impact on $\hat{\mu}$. Most pulls are within 0.5 s.d. and only the WW generator modeling uncertainty is constrained by more than 20 %. This results from the extra WW resolving power in the fit from the high-m_{T} region in the SR. The highest ranked NP is the uncertainty on the total ggF cross section from QCD scale variations.

Another check of the results, is if the central value of the extrapolation from the CRs to the SRs is changing post-fit. Comparing the ratio of post-fit to pre-fit extrapolation factors from the 8 TeV WW CR to the SR, we see no large deviations from the input values. Most extrapolation factors agree to better than 1 %, the largest deviation from unity.

5.7 Results

A summary of the results for the $H \to WW^{(*)} \to \ell\nu\ell\nu$ analysis, described in the previous sections, is presented here. This includes event yields, distributions, and statistical results, such as the observed significance and signal strength. Results are generally presented as 'post-fit', this means that event yields are obtained from the likelihood with NPs at their best fit values; thus, the post-fit results include pulls and constraints on the NPs. For post-fit

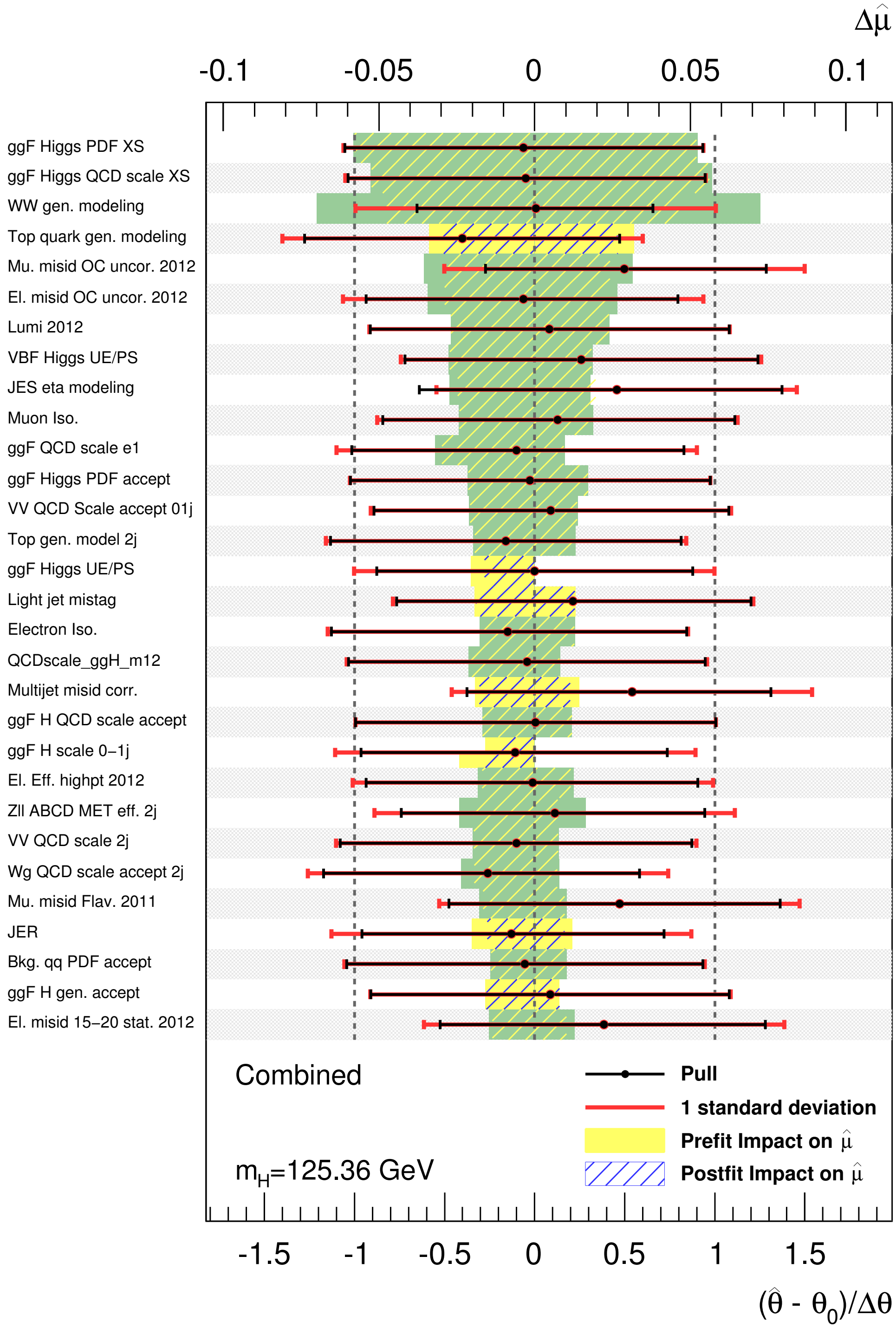

Figure 5.20: Impact of top thirty NPs on $\hat{\mu}$ from a combined fit of the channels, ranked by their post-fit impact, as defined in Equation 5.51. The solid band shows the pre-fit impact on $\hat{\mu}$ and the hashed band the post-fit impact, both use the top axis. A yellow band denotes positive correlation between $\hat{\mu}$ and θ, while a green band denotes an anti-correlation. The black point denotes $\hat{\theta}$ and black bar the post-fit Δ_θ, using the bottom axis; the red bar is ± 1. The degree to which the black bar is smaller than the red bar is how constrained the NP is.

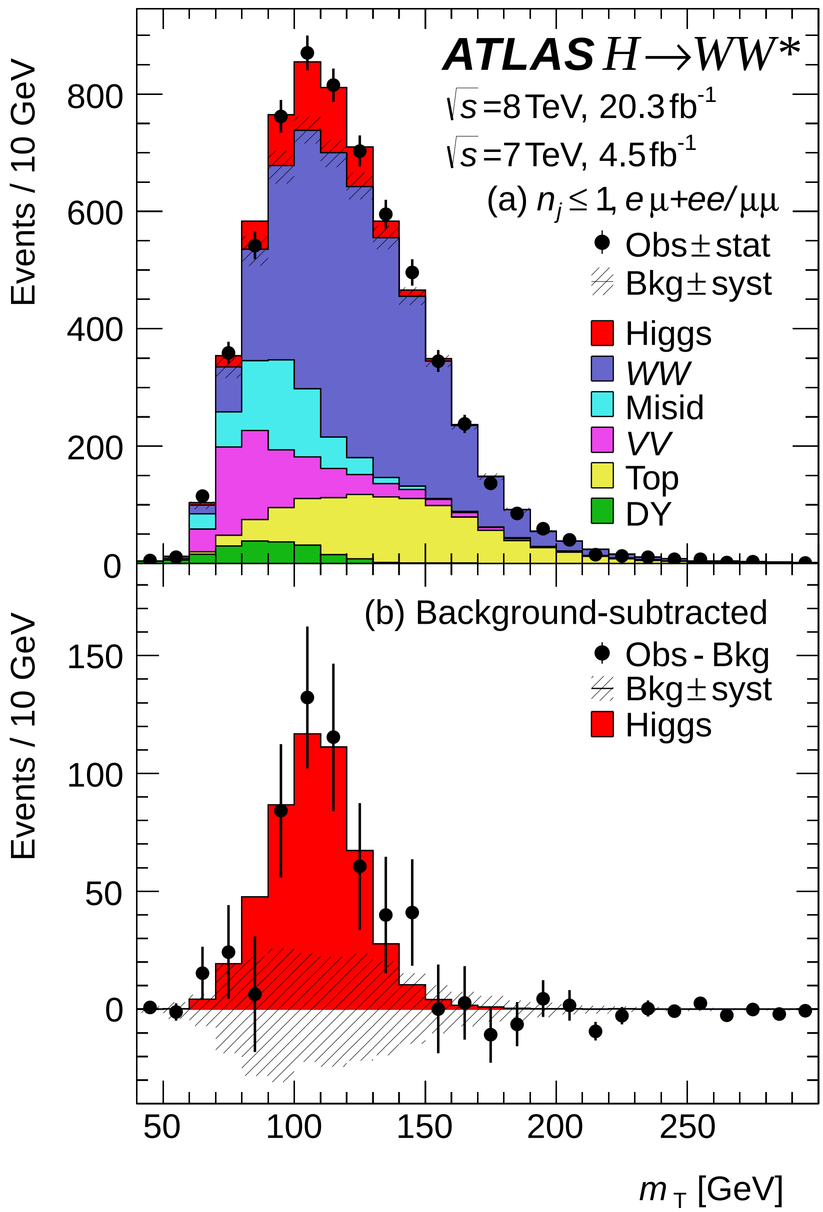

Figure 5.21: Above, post-fit distribution of m_T for the combined $N_{\text{jets}} \leq 1$ signal regions including both 7 and 8 TeV datasets. Below, the background subtracted distribution overlayed with the signal scaled to the observed signal strength of $\mu = 1.09$ [112]. The uncertainty band is partially correlated between bins. It is not taken from the fit (it is a sum of all of the input systematic variations), but is a good representation as there are no large over-constraints in the model.

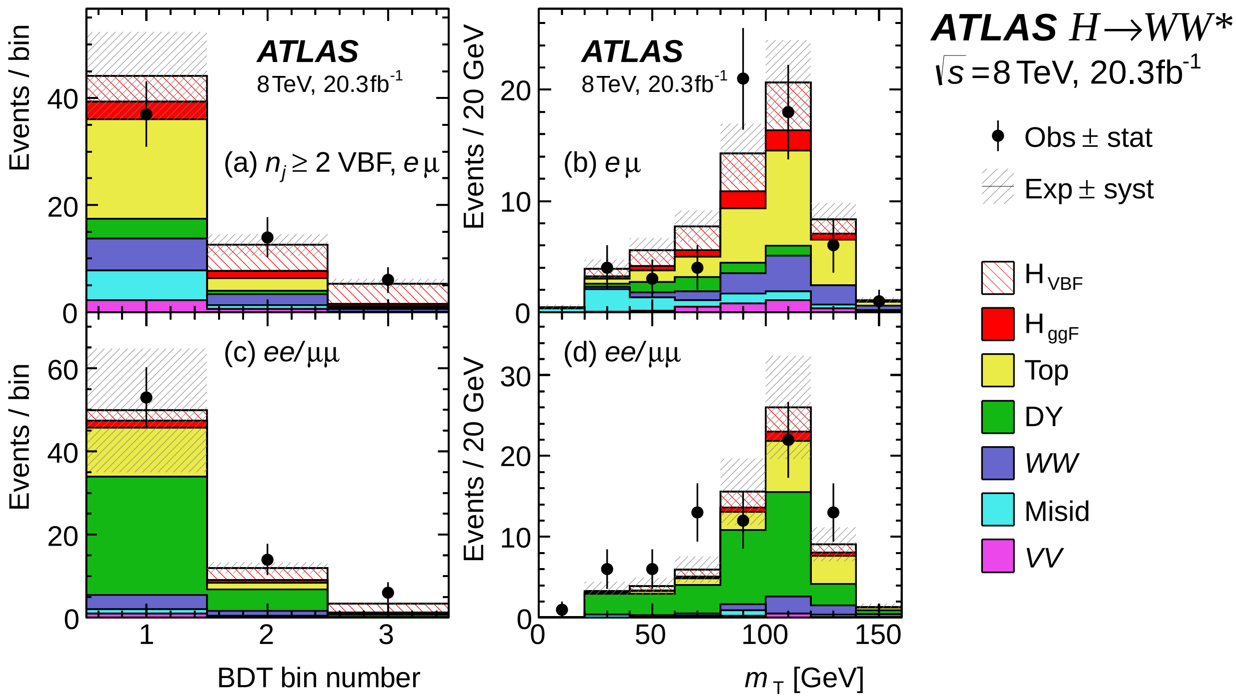

Figure 5.22: Post-fit (a and c) BDT score and (b and d) m_{T} distributions in the $N_{\mathrm{jets}} \geq 2$ 8 TeV VBF channel [112].

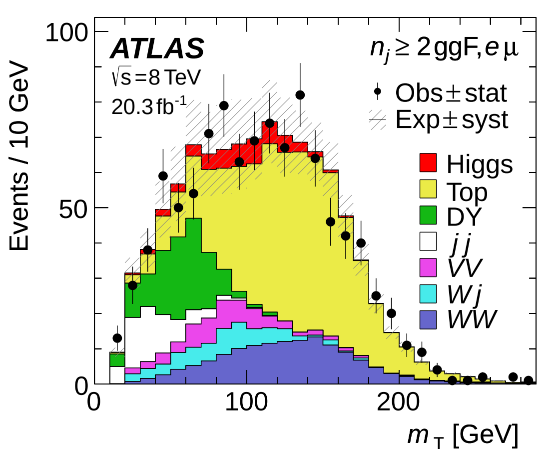

Figure 5.23: Post-fit m_{T} distribution in the $N_{\mathrm{jets}} \geq 2$ ggF channel [112].

distributions, processes are normalized to their respective post-fit yield. Thus the shape of an individual background does not vary for changing NPs—changes in the shape are in any case dominated by changing normalizations of individual processes.

Table 5.35 shows the post-fit event yields in the SRs for the 7 and 8 TeV analyses. Yields are split by process and sub-channel, and the uncertainty includes both statistical and systematic components. Appendix B contains distributions of m_{T} for all of the 8 TeV signal region categories, split by $m_{\ell\ell}$, lepton flavor, and sub-leading lepton p_{T}. Figures 5.21, 5.22, and 5.23 show the m_{T} and O_{BDT} distributions summed over sub-channels for the four main jet categories. A clear excess in data over the expected background is observed. This is also evident in the yields, with a consistent excess across sub-channels; though, we see a smaller excess in the 7 TeV data relative to the SM Higgs boson signal expectation.

This excess is quantified in terms of a p_0, described in Section 5.6.4. Combining all of the channels, the observed local significance Z_0 for $m_H = 125.36\,\mathrm{GeV}$ is 6.1 s.d. with an expected significance of 5.8 s.d. This qualifies as observation of the $H \to WW^{(*)}$ decay mode. The minimum p_0 is found at $m_H = 130\,\mathrm{GeV}$, with the same observed significance of 6.1 s.d. Figure 5.24(a) shows a scan of the combined local significance over the Higgs boson mass hypothesis ranging from $m_H = 110$–$200\,\mathrm{GeV}$. Table 5.36 shows the expected and observed significances split into several categories for $m_H = 125\,\mathrm{GeV}$. The most sensitive category is the 8 TeV $N_{\mathrm{jets}} = 0$ $e\mu$ region.

The excess can also be measured in terms of its size relative to the SM expectation for a Higgs boson, the signal strength μ. The signal strength for $m_H = 125.36\,\mathrm{GeV}$ as measured with the combined channels with the uncertainty shown in three ways is

$$\begin{aligned} \mu &= 1.09^{+0.16}_{-0.15}(\text{stat.})\,^{+0.08}_{-0.07}(\text{expt.})\,^{+0.15}_{-0.12}(\text{theo.}) \pm 0.03(\text{lumi.}) \\ \mu &= 1.09^{+0.16}_{-0.15}(\text{stat.})\,^{+0.17}_{-0.14}(\text{syst.}) \\ \mu &= 1.09^{+0.23}_{-0.21}\,. \end{aligned} \tag{5.52}$$

The result is compatible with the SM expectation within the uncertainties. Table 5.37 shows the expected and observed best fit signal strengths and uncertainties split into several categories for $m_H = 125\,\mathrm{GeV}$. Notably, there is a small observed deficit in the 7 TeV dataset and small excess in the 8 TeV dataset, relative to the SM Higgs boson expectation. Figure 5.24(b) shows a scan of the expected and observed best-fit signal strength ($\hat{\mu}$) as a function of m_H. The observed signal strength crosses unity near 125 GeV, and approaches zero with increasing mass. Its large increase with lower m_H arises mostly from the changing WW^* branching fraction, and is expected as seen in Fig. 5.24(b). Figure 5.24(c) shows contours of the two-dimensional likelihood in the (m_H, μ) plane of the best-fit signal strength

(a) 8 TeV data sample

Channel	Summary				Composition of N_B						
	N_{Obs}	N_B	N_{ggF}	N_{VBF}	N_{WW}	N_{st}	$N_{t\bar{t}}$	$N_{W+\mathrm{jets}}$	N_{jj}	N_{VV}	N_{DY}
$N_{\mathrm{jets}} = 0$	3750	3430±90	300±50	8 ±4	2250±95	112±9	195±15	360±60	16 ±5	420±40	78±21
$e\mu$, $\ell_2 = \mu$	1430	1280±40	129±20	3.0±2.1	830±34	41±3	73±6	149±29	10.1±3.6	167±21	14±2.4
$e\mu$, $\ell_2 = e$	1212	1106±35	97±15	2.5±0.6	686±29	33±3	57±5	128±31	3.8±1.5	184±23	14±2.4
$ee/\mu\mu$	1108	1040±40	77±15	2.4±1.7	740±40	39±3	65±5	82±16	2 ±0.5	68±7	50±21
$N_{\mathrm{jets}} = 1$	1596	1470±40	102±26	17 ±5	630±50	150±10	385±20	108±20	8.2±3.0	143±20	51 ±13
$e\mu$, $\ell_2 = \mu$	621	569±19	45±11	7.4±2	241±20	58±4	147±7	51±11	5.7±2.0	53±10	13.8±3.3
$e\mu$, $\ell_2 = e$	508	475±18	35±9	6.1±1.4	202±17	45±3	119±6	37±9	2.3±0.9	60±10	9.3±2.5
$ee/\mu\mu$	467	427±21	22±6	3.6±1.8	184±15	46±4	119±10	19±4	0.2±0.1	31±4	28 ±12
$N_{\mathrm{jets}} \geq 2$, ggF $e\mu$	1017	960±40	37±11	13 ±1.4	138±28	56±5	480±40	54±25	62±22	56±18	117±21
$N_{\mathrm{jets}} \geq 2$, VBF	130	99 ±9	7.7±2.6	21 ±3	11 ±3.5	5.5±0.7	29 ±5	4.7±1.4	2.8±1.0	4.4±0.9	38 ±7
$e\mu$ bin 1	37	36 ±4	3.3±1.2	4.9±0.5	5.0±1.5	3.0±0.6	15.6±2.6	3.2±1.0	2.3±0.8	2.3±0.7	3.6±1.5
$e\mu$ bin 2	14	6.5±1.3	1.4±0.5	4.9±0.5	1.7±0.7	0.3±0.4	2.0±1.0	0.4±0.1	0.3±0.1	0.7±0.2	0.6±0.2
$e\mu$ bin 3	6	1.2±0.3	0.4±0.3	3.8±0.7	0.3±0.1	0.1±0.0	0.3±0.1	-	-	0.1±0.0	0.2±0.1
$ee/\mu\mu$ bin 1	53	46 ±6	1.7±0.6	2.6±0.3	3.1±1.0	1.7±0.3	10.1±1.6	0.9±0.2	0.2±0.1	1.0±0.3	28 ±5
$ee/\mu\mu$ bin 2	14	8.4±1.8	0.7±0.3	3.0±0.4	0.9±0.3	0.3±0.2	1.2±0.5	0.2±0.1	-	0.3±0.1	5.2±1.7
$ee/\mu\mu$ bin 3	6	1.1±0.4	0.2±0.2	2.1±0.4	0.1±0.1	0.1±0.0	0.2±0.1	-	-	-	0.5±0.3

(b) 7 TeV data sample

$N_{\mathrm{jets}} = 0$	594	575±24	49±8	1.4±0.2	339±24	20.5±2.1	38±4	74±15	1.3±0.6	79±10	23 ±6
$e\mu$, $\ell_2 = \mu$	185	186±8	19±3	0.5±0.0	116±8	7 ±1	14±2	19±5	-	24±3	4.8±1
$e\mu$, $\ell_2 = e$	195	193±12	15±2.4	0.5±0.0	95±7	5.3±0.5	10±1	37±9	1.1±0.5	41±6	4.1±0.9
$ee/\mu\mu$	214	196±11	16±3.1	0.5±0.1	128±10	8 ±1	14±2	18±4	0.2±0.1	14±2	14 ±5
$N_{\mathrm{jets}} = 1$	304	276±15	16 ±4	3.2±0.3	103±15	22±2	58±6	20±4	3.2±1.6	32±8	38 ±6
$e\mu$, $\ell_2 = \mu$	93	75±4	5.7±1.6	1.2±0.1	33±5	7±1	18±2	5±1	-	9±2	2.7±0.4
$e\mu$, $\ell_2 = e$	91	76±5	4.5±1.2	0.9±0.1	28±4	6±1	16±2	10±2	0.7±0.3	14±4	2.3±0.7
$ee/\mu\mu$	120	125±9	5.3±1.6	1.2±0.2	43±6	9±1	24±3	5±1	2.5±1.4	9±2	33 ±6
$N_{\mathrm{jets}} \geq 2$, VBF	9	7.8±1.8	0.9±0.3	2.7±0.3	1.2±0.4	0.3±0.1	1.6±0.8	0.4±0.1	0.1±0.0	0.5±0.2	3.4±1.5
$e\mu$ bin 1	6	3.0±0.9	0.4±0.2	0.6±0.1	0.5±0.2	0.2±0.1	0.9±0.5	0.1±0.0	0.1±0.0	0.3±0.1	0.8±0.6
$e\mu$ bin 2–3	0	0.7±0.2	0.2±0.1	1.1±0.1	0.2±0.1	-	0.3±0.2	-	-	-	-
$ee/\mu\mu$ bins 1–3	3	4.1±1.3	0.3±0.1	1.0±0.1	0.5±0.2	0.1±0.0	0.4±0.3	0.3±0.1	-	0.2±0.1	2.5±1.1

Table 5.35: Post-fit signal region yields for the 7 and 8 TeV analyses with full uncertainties taking into account fit NP values and constraints. The signal yields are scaled to the observed combined signal strength. Values less than 0.1 (0.01) are written as 0.0 (-) [112].

for a given mass hypothesis. The point $(125.36, 1)$ is within the 68 % CL contour, showing compatibility with the SM and the mass measurement from other channels [135]. We also divide the measured signal strength into ggF and VBF production modes by splitting the signal strength parameters in the likelihood,

$$\begin{aligned} \mu_{\text{ggF}} &= 1.02^{+0.19}_{-0.19}(\text{stat.})\,^{+0.22}_{-0.18}(\text{syst.}) = 1.02^{+0.29}_{-0.26} \\ \mu_{\text{VBF}} &= 1.27^{+0.44}_{-0.40}(\text{stat.})\,^{+0.30}_{-0.21}(\text{syst.}) = 1.27^{+0.53}_{-0.45}\,. \end{aligned} \tag{5.53}$$

Gluon fusion involves a quark loop, while VBF directly couples vector bosons to the Higgs boson; thus, the two signal strengths are sensitive to different components of the Higgs boson—this is interpreted more explicitly later. Figure 5.24(d) shows two-dimensional likelihood contours in the μ_{ggF} versus μ_{VBF} plane. The SM expectation is well within one standard deviation of the best-fit point. The $H \to WW^{(*)} \to \ell\nu\ell\nu$ analysis provides the most precise measurement of the signal strengths from a single decay channel. A comparison with other Higgs boson decay channels, which are used as inputs to the ATLAS combined couplings measurement [197], is shown in Fig. 5.25.

Using these split signal strengths, we can test for the presence of VBF production while removing dependence on the branching ratio by using the ratio $\mu_{\text{VBF}}/\mu_{\text{ggF}}$ as the parameter of interest (POI). The difference between the $-2\ln\Lambda$ at the best fit,

$$\frac{\mu_{\text{VBF}}}{\mu_{\text{ggF}}} = 1.26^{+0.61}_{-0.45}(\text{stat.})\,^{+0.50}_{-0.26}(\text{syst.}) = 1.26^{+0.79}_{-0.53}\,, \tag{5.54}$$

and at $\mu_{\text{VBF}}/\mu_{\text{ggF}} = 0$, absence of VBF production, is converted to a significance of VBF production, which is observed to be 3.2 s.d., while the expected significance is 2.7 s.d.. This is evidence for VBF production in $H \to WW^{(*)} \to \ell\nu\ell\nu$. Figure 5.26 shows the $-2\ln\Lambda$ distribution as a function of $\mu_{\text{VBF}}/\mu_{\text{ggF}}$.

We can also interpret the split signal strengths in terms of coupling strengths to fermions and vector bosons relative to their SM expectation, denoted by κ_F and κ_V respectively. This κ-framework is based on the LO diagrams and described in Section 10.2 of Ref. [32]. For example, ggF production is proportional to κ_g^2 and the $H \to WW^{(*)}$ decay is proportional to κ_W^2, thus we have,

$$(\sigma \cdot \text{BR})(gg \to H \to WW^{(*)}) = \sigma_{\text{SM}}(gg \to H) \cdot \text{BR}_{\text{SM}}(H \to WW^{(*)}) \cdot \frac{\kappa_g^2 \kappa_W^2}{\kappa_H^2}\,, \tag{5.55}$$

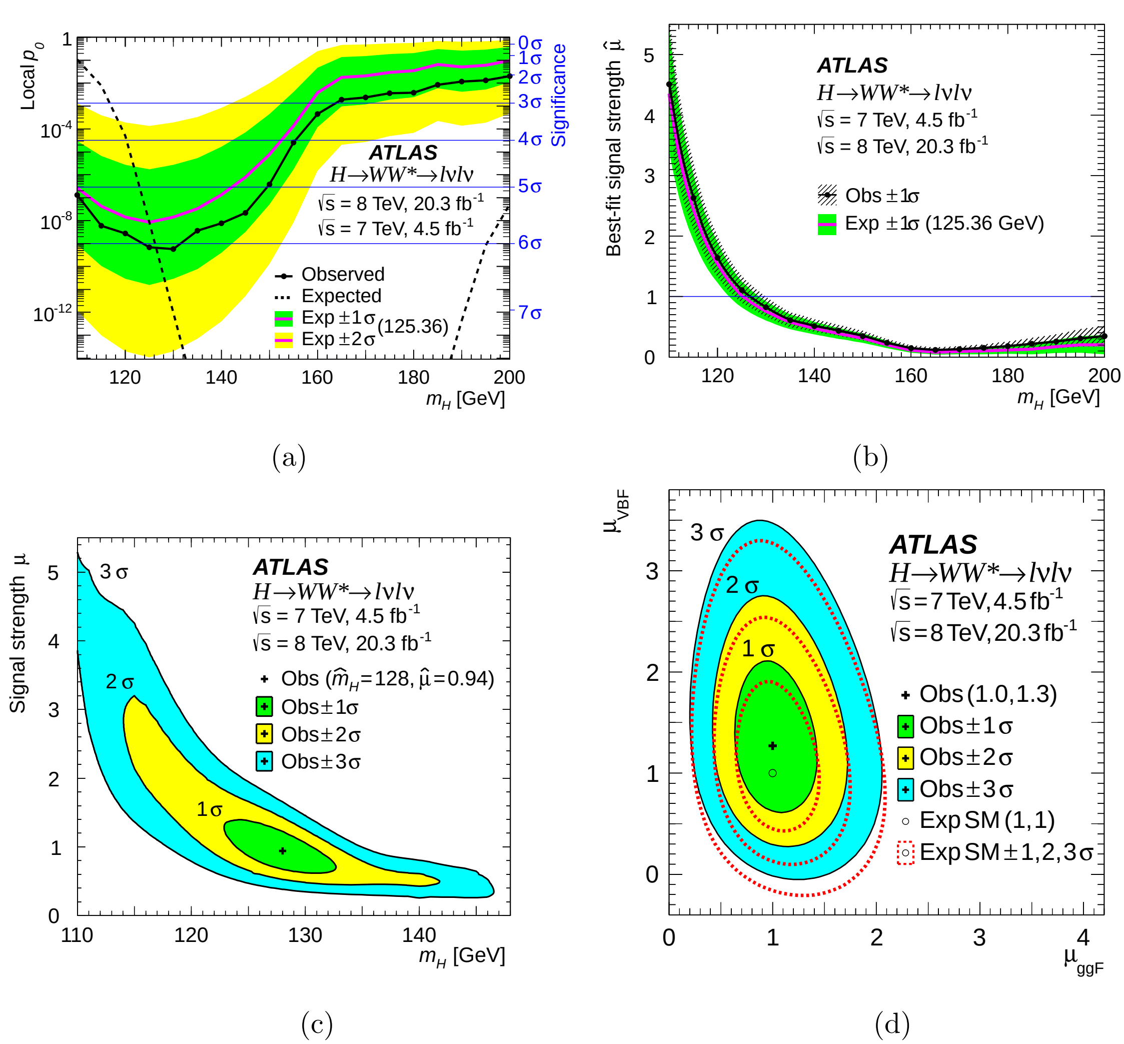

Figure 5.24: Expected and observed statistical results for the combined $H \to WW^{(*)} \to \ell\nu\ell\nu$ analysis as a function of m_H. Green, yellow, and cyan colors represent the 1, 2, and 3 s.d. intervals. In (a) and (b), the solid black curve represents the observed and the purple curve the expected for a Higgs boson with $m_H = 125.36\,\text{GeV}$. (a), significance of data excess over background, with a maximum of 6.1 s.d. observed. (b), best-fit signal strength relative to the SM ($\hat{\mu}$). (c), two-dimensional likelihood contours as a function of signal strength μ and m_H. (d), two-dimensional likelihood contour of μ_{ggF} versus μ_{VBF} [112] .

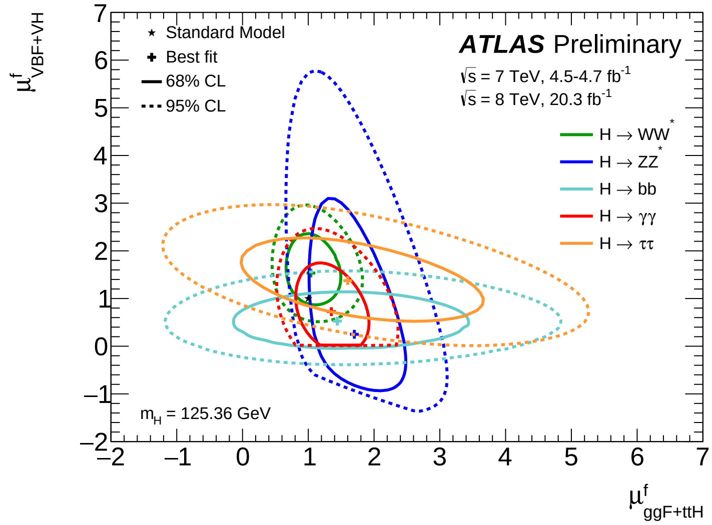

Figure 5.25: Likelihood contours of ggF versus VBF signal strengths for the input decay channels (f) in the ATLAS combined couplings measurement for $m_H = 125.36\,\mathrm{GeV}$ [197].

Year	Category	$e\mu$ Exp.	$e\mu$ Obs.	$ee/\mu\mu$ Exp.	$ee/\mu\mu$ Obs.	$e\mu$+$ee/\mu\mu$ Exp.	$e\mu$+$ee/\mu\mu$ Obs.
2011	$N_{\text{jets}} = 0$	1.37	0.41	0.67	0.54	1.46	0.56
	$N_{\text{jets}} = 1$	0.94	1.59	0.46	−0.03	1.01	1.41
	$N_{\text{jets}} \leq 1$	1.61	1.03	0.81	0.42	1.72	1.04
	$N_{\text{jets}} \geq 2$ VBF	0.40	−0.63	1.11	−0.77	1.17	−0.93
	Comb.	1.96	0.63	0.91	0.08	2.09	0.51
2012	$N_{\text{jets}} = 0$	3.48	4.38	1.71	0.57	3.56	4.18
	$N_{\text{jets}} = 1$	2.43	2.68	0.94	0.26	2.46	2.37
	$N_{\text{jets}} \leq 1$	4.11	4.90	1.66	0.67	4.30	4.68
	$N_{\text{jets}} \geq 2$ ggF	1.21	1.44	–	–	1.21	1.44
	Comb. ggF	4.27	5.00	1.61	0.83	4.44	4.78
	$N_{\text{jets}} \geq 2$ VBF	2.86	3.23	1.55	3.14	3.24	4.11
	Comb.	5.14	5.92	2.28	2.67	5.51	6.30
2011+2012	$N_{\text{jets}} = 0$	3.62	4.24	1.43	0.70	3.70	4.08
	$N_{\text{jets}} = 1$	2.56	2.83	1.02	0.20	2.59	2.49
	$N_{\text{jets}} \leq 1$	4.29	4.84	1.81	0.75	4.47	4.60
	$N_{\text{jets}} \geq 2$ ggF	1.21	1.44	–	–	1.21	1.44
	Comb. ggF	4.45	4.94	1.77	0.93	4.61	4.69
	$N_{\text{jets}} \geq 2$ VBF	3.01	3.02	1.59	2.96	3.38	3.84
	Comb.	5.38	5.76	2.42	2.58	5.75	6.06

Table 5.36: Expected and observed local significances (Z_0's) in standard deviations for the split categories and several combinations of categories for a Higgs boson mass of $m_H = 125.36\,\mathrm{GeV}$.

Year	Category	$e\mu$		$ee/\mu\mu$		$e\mu$+$ee/\mu\mu$	
		Exp.	Obs.	Exp.	Obs.	Exp.	Obs.
2011	$N_{\text{jets}} = 0$	$1^{+0.80}_{-0.69}$	$0.29^{+0.72}_{-0.69}$	$1^{+1.55}_{-1.41}$	$0.81^{+1.53}_{-1.51}$	$1^{+0.72}_{-0.67}$	$0.38^{+0.69}_{-0.66}$
	$N_{\text{jets}} = 1$	$1^{+1.22}_{-1.06}$	$1.91^{+1.48}_{-1.23}$	$1^{+2.40}_{-2.08}$	$-0.03^{+2.18}_{-2.16}$	$1^{+1.12}_{-0.98}$	$1.52^{+1.31}_{-1.09}$
	$N_{\text{jets}} \leq 1$	$1^{+0.65}_{-0.60}$	$0.65^{+0.67}_{-0.64}$	$1^{+1.22}_{-1.20}$	$0.51^{+1.25}_{-1.22}$	$1^{+0.60}_{-0.60}$	$0.61^{+0.63}_{-0.58}$
	$N_{\text{jets}} \geq 2$ VBF	$1^{+1.39}_{-0.95}$	$-0.62^{\dagger}$	$1^{+2.87}_{-2.40}$	$-1.48^{+2.43}_{-2.38}$	$1^{+1.23}_{-0.91}$	$-0.61^{\dagger}$
	Comb.	$1^{+0.58}_{-0.52}$	$0.38^{+0.62}_{-0.60}$	$1^{+1.10}_{-1.08}$	$0.09^{+1.13}_{-1.10}$	$1^{+0.53}_{-0.49}$	$0.28^{+0.56}_{-0.55}$
2012	$N_{\text{jets}} = 0$	$1^{+0.36}_{-0.32}$	$1.38^{+0.44}_{-0.37}$	$1^{+0.79}_{-0.70}$	$0.41^{+0.73}_{-0.73}$	$1^{+0.35}_{-0.31}$	$1.25^{+0.41}_{-0.34}$
	$N_{\text{jets}} = 1$	$1^{+0.53}_{-0.45}$	$1.13^{+0.57}_{-0.46}$	$1^{+1.12}_{-1.00}$	$0.25^{+1.17}_{-1.05}$	$1^{+0.50}_{-0.42}$	$0.96^{+0.51}_{-0.43}$
	$N_{\text{jets}} \leq 1$	$1^{+0.30}_{-0.27}$	$1.27^{+0.34}_{-0.29}$	$1^{+0.62}_{-0.58}$	$0.37^{+0.61}_{-0.57}$	$1^{+0.28}_{-0.25}$	$1.13^{+0.31}_{-0.27}$
	$N_{\text{jets}} \geq 2$ ggF	$1^{+0.96}_{-0.83}$	$1.20^{+1.00}_{-0.83}$	–	–	$1^{+0.96}_{-0.83}$	$1.20^{+1.00}_{-0.83}$
	Comb. ggF	$1^{+0.28}_{-0.25}$	$1.24^{+0.31}_{-0.28}$	$1^{+0.61}_{-0.62}$	$0.48^{+0.64}_{-0.58}$	$1^{+0.27}_{-0.24}$	$1.12^{+0.30}_{-0.26}$
	$N_{\text{jets}} \geq 2$ VBF	$1^{+0.51}_{-0.42}$	$1.11^{+0.51}_{-0.42}$	$1^{+0.91}_{-0.72}$	$2.29^{+1.09}_{-0.88}$	$1^{+0.47}_{-0.38}$	$1.36^{+0.50}_{-0.41}$
	Comb.	$1^{+0.25}_{-0.22}$	$1.20^{+0.27}_{-0.24}$	$1^{+0.51}_{-0.46}$	$1.12^{+0.50}_{-0.44}$	$1^{+0.23}_{-0.21}$	$1.19^{+0.26}_{-0.23}$
2011+2012	$N_{\text{jets}} = 0$	$1^{+0.36}_{-0.32}$	$1.25^{+0.40}_{-0.34}$	$1^{+0.79}_{-0.70}$	$0.46^{+0.68}_{-0.66}$	$1^{+0.35}_{-0.31}$	$1.15^{+0.37}_{-0.32}$
	$N_{\text{jets}} = 1$	$1^{+0.53}_{-0.45}$	$1.16^{+0.56}_{-0.45}$	$1^{+1.12}_{-1.01}$	$0.19^{+1.03}_{-0.97}$	$1^{+0.51}_{-0.42}$	$0.96^{+0.50}_{-0.41}$
	$N_{\text{jets}} \leq 1$	$1^{+0.30}_{-0.27}$	$1.18^{+0.32}_{-0.27}$	$1^{+0.62}_{-0.58}$	$0.39^{+0.55}_{-0.53}$	$1^{+0.28}_{-0.25}$	$1.05^{+0.29}_{-0.25}$
	$N_{\text{jets}} \geq 2$ ggF	$1^{+0.96}_{-0.83}$	$1.20^{+1.00}_{-0.83}$	–	–	$1^{+0.96}_{-0.83}$	$1.20^{+1.00}_{-0.83}$
	Comb. ggF	$1^{+0.28}_{-0.25}$	$1.15^{+0.30}_{-0.26}$	$1^{+0.61}_{-0.62}$	$0.50^{+0.57}_{-0.53}$	$1^{+0.27}_{-0.24}$	$1.04^{+0.28}_{-0.24}$
	$N_{\text{jets}} \geq 2$ VBF	$1^{+0.51}_{-0.42}$	$0.98^{+0.47}_{-0.39}$	$1^{+0.91}_{-0.72}$	$1.98^{+0.97}_{-0.78}$	$1^{+0.47}_{-0.38}$	$1.20^{+0.45}_{-0.38}$
	Comb.	$1^{+0.25}_{-0.22}$	$1.10^{+0.25}_{-0.22}$	$1^{+0.51}_{-0.46}$	$0.99^{+0.45}_{-0.40}$	$1^{+0.23}_{-0.21}$	$1.09^{+0.23}_{-0.21}$

Table 5.37: Expected uncertainty on and observed signal strengths, μ, for the split sub-categories and several combinations of categories for a Higgs boson mass of $m_H = 125.36$ GeV. †Uncertainties are unavailable for these 2011 VBF categories due to improperly converging fits when scanning the likelihood.

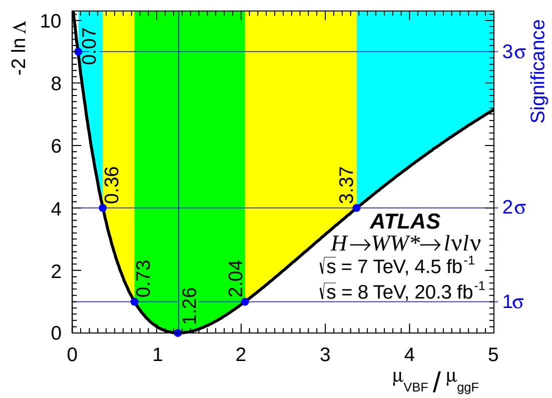

Figure 5.26: Scan of the negative log-likelihood as a function of the ratio of VBF to ggF signal strengths. The value at zero corresponds to the significance of VBF production, observed at 3.2 s.d. [112].

where

$$\kappa_H^2 = \frac{\Gamma_H}{\Gamma_H^{\rm SM}} = \sum_{i\neq H}^{\rm couplings} {\rm BR}_{H\to ii}\cdot\kappa_i^2 \tag{5.56}$$

represents the modification to the total width of the Higgs boson. This parametrization assumes no non-SM decays. If we simplify to common coupling modifiers for fermions and vector bosons, we can parametrize ggF and VBF production as,

$$\begin{aligned} \text{ggF: } \sigma_{\rm SM}(gg\to H)\cdot {\rm BR}_{\rm SM}(H\to WW^{(*)})\cdot \frac{\kappa_F^2\kappa_V^2}{\kappa_H^2(\kappa_F,\kappa_V)} \text{ and} \\ \text{VBF: } \sigma_{\rm SM}(qq\to H)\cdot {\rm BR}_{\rm SM}(H\to WW^{(*)})\cdot \frac{\kappa_V^4}{\kappa_H^2(\kappa_F,\kappa_V)}\,, \end{aligned} \tag{5.57}$$

where $\kappa_H^2(\kappa_F,\kappa_V) = {\rm BR}_{\rm SM}^{H\to ff}\cdot\kappa_F^2 + {\rm BR}_{\rm SM}^{H\to VV}\cdot\kappa_V^2$, $\kappa_F=\kappa_b=\kappa_t=\kappa_\tau=\kappa_g$, and $\kappa_V=\kappa_W=\kappa_Z$. The best fit values are:

$$\begin{aligned} \kappa_F =& 0.93^{+0.24}_{-0.18}(\text{stat.})\,^{+0.21}_{-0.14}(\text{syst.}) = 0.93^{+0.32}_{-0.23} \\ \kappa_V =& 1.04^{+0.07}_{-0.08}(\text{stat.})\,^{+0.07}_{-0.08}(\text{syst.}) = 1.04^{+0.10}_{-0.11}\,, \end{aligned} \tag{5.58}$$

with a correlation between the parameters of $\rho = 0.47$. Figure 5.27(a) shows two-dimensional likelihood contours in the κ_V versus κ_F plane. The relatively large uncertainty on κ_F, even though the ggF channels are the most sensitive, can be understood because $\mu_{\rm ggF}$ becomes independent of κ_F for $\lim_{\kappa_F\to\infty} \kappa_F^2\kappa_V^2/(\kappa_F^2+\kappa_V^2) = \kappa_V^2$.

An SM Higgs boson is considered excluded if the $\mu = 1$ hypothesis is excluded at 95 % CL. Figure 5.27(b) shows the observed and expected exclusion using the CL_S method for Higgs boson masses between $110 \leq m_H \leq 200\,\text{GeV}$. The expected lower bound is 114 GeV, but since there is a clear excess, the observed exclusion for an SM Higgs boson is $132 \leq m_H \leq 200\,\text{GeV}$.

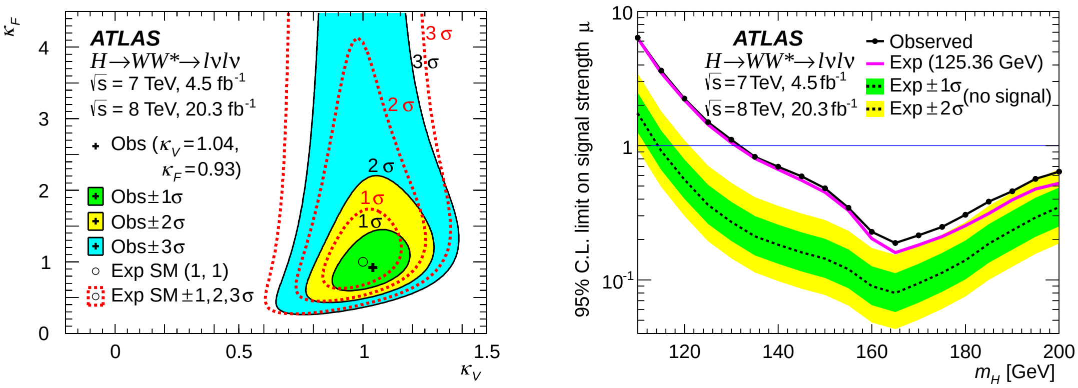

(a) (b)

Figure 5.27: (a), two-dimensional likelihood contour of coupling modifiers κ_V versus κ_F. The best-fit points are denoted with a plus and the SM expectation with a circle. (b), the 95 % CL exclusion limit, with the lower bound observed at 132 GeV. The solid black curve represents the observed and the purple curve the expected for a Higgs boson with $m_H = 125.36\,\text{GeV}$ [112].

The signal strength can be used to evaluate the cross section times branching ratio, $\sigma \cdot \text{BR}_{H\to WW^{(*)}}$ for $m_H = 125.36\,\text{GeV}$. This is done by dividing out the detector acceptance from the number of signal-like events:

$$(\sigma \cdot \text{BR}_{H\to WW^{(*)}}) = \frac{(N_S^{\text{data}})}{\mathcal{A}\cdot\mathcal{C}\cdot\text{BR}_{H\to WW^{(*)}}}\frac{1}{\int L dt}\,. \tag{5.59}$$

Here, $\mathcal{A}$ is the kinematic (e.g., p_{T}) and geometric (e.g., η) acceptance of the detector and $\mathcal{C}$ is the ratio of measured to produced events in the fiducial volume, correcting for the efficiency of the detector. In practice, the central value is simply the predicted cross section multiplied by $\hat{\mu}$. Inclusive cross sections are evaluated in three cases, with the signal strengths evaluated simultaneously,

$$\begin{aligned}
\mu_{\text{ggF}}^{7\,\text{TeV}} &= 0.57^{+0.52}_{-0.51}(\text{stat.})\,^{+0.36}_{-0.34}(\text{syst.})\,^{+0.14}_{-0.004}(\text{sig.})\\
\mu_{\text{ggF}}^{8\,\text{TeV}} &= 1.09^{+0.20}_{-0.20}(\text{stat.})\,^{+0.19}_{-0.17}(\text{syst.})\,^{+0.14}_{-0.009}(\text{sig.})\\
\mu_{\text{VBF}}^{8\,\text{TeV}} &= 1.45^{+0.48}_{-0.44}(\text{stat.})\,^{+0.38}_{-0.24}(\text{syst.})\,^{+0.11}_{-0.06}(\text{sig.})\,,
\end{aligned} \tag{5.60}$$

where (sig.) denotes systematic uncertainties on the total signal yield, i.e., excluding acceptance uncertainties, (QCD scale, PDF, and branching fraction uncertainties), which do not enter the cross section measurement. VH production makes up 0.9 %, which is neglected, and added linearly to the systematic uncertainties. The resulting measured cross sections are

$$\begin{aligned}
\sigma^{7\,\text{TeV}}_{\text{ggF}} \cdot \text{BR}_{H\to WW^{(*)}} &= 2.0^{+1.7}_{-1.7}(\text{stat.})\,^{+1.2}_{-1.1}(\text{syst.}) &&= 2.0^{+2.1}_{-2.0}\,\text{pb} \\
\sigma^{8\,\text{TeV}}_{\text{ggF}} \cdot \text{BR}_{H\to WW^{(*)}} &= 4.6^{+0.9}_{-0.9}(\text{stat.})\,^{+0.8}_{-0.7}(\text{syst.}) &&= 4.6^{+1.2}_{-1.1}\,\text{pb} \\
\sigma^{8\,\text{TeV}}_{\text{VBF}} \cdot \text{BR}_{H\to WW^{(*)}} &= 0.51^{+0.17}_{-0.15}(\text{stat.})\,^{+0.13}_{-0.08}(\text{syst.}) &&= 0.51^{+0.22}_{-0.17}\,\text{pb}\,,
\end{aligned} \tag{5.61}$$

and the predicted values are 3.3 ± 0.4 pb, 4.2 ± 0.5 pb, and 0.35 ± 0.02 pb respectively.

It is also useful to define a fiducial volume and remove the uncertainties associated with the acceptance $\mathcal{A}$. This allows direct comparison in the selected phase-space of measured values with theoretical predictions. The selection used for the fiducial volume is close to the ggF SR selection, and defined with truth level quantities. In particular, the MET is replaced by the dineutrino momentum $p_{\text{T}}^{\nu\nu}$, lepton p_{T} is taken from the generated value summed with all photons in $\Delta R = 0.1$ to account for QED FSR, and jets are defined after PS and hadronization, i.e., as hadrons. The same overlap removal as the detector level results is used on the truth objects. Table 5.38 lists the fiducial selection. Only $e\mu$ 8 TeV data and the $N_{\text{jets}} \leq 1$ category is used for the fiducial measurement. The fiducial cross section σ_{fid} is defined similarly to Equation 5.59, except without the acceptance $\mathcal{A}$ and $\text{BR}_{H\to WW^{(*)}}$,

$$\sigma_{\text{fid}} = \hat{\mu} \cdot (\sigma \cdot \text{BR}_{H\to WW^{(*)}\to e\nu\mu\nu})_{\text{exp.}} \cdot \mathcal{A}\,. \tag{5.62}$$

$N_{\text{jets}} = 0$	$N_{\text{jets}} = 1$
$p_{\text{T}}^{\text{lead}} > 22$, $p_{\text{T}}^{\text{sub}} > 10$	
Opposite charge	
$m_{\ell\ell} > 10$	
$p_{\text{T}}^{\nu\nu} > 20$	
$\Delta\phi(\ell\ell, \nu\nu) > \pi/2$	-
$p_{\text{T}}^{\ell\ell} > 30$	-
-	$m_{\text{T}}^{\ell} > 50$
-	$m_{\tau\tau} < 66$
$m_{\ell\ell} < 55$	
$\Delta\phi_{\ell\ell} < 1.8$	

Table 5.38: Fiducial volume selection, defined with truth level quantities. Mass and momentum units are in GeV.

Correction factors for each jet bin are computed using the signal MC. For simplicity, the fiducial region ignores leptons from τ decays; though, they are present in the reconstructed events. Based on simulation, the fraction of measured signal events in the $N_{\text{jets}} = 0\,(1)$

category is 85 (63) %. The computed correction factors are

$$\begin{aligned} \mathcal{C}_{0j}^{\text{ggF}} &= 0.507 \pm 0.027 \\ \mathcal{C}_{1j}^{\text{ggF}} &= 0.506 \pm 0.022\,. \end{aligned} \tag{5.63}$$

Experimental uncertainties are approximately 5 % and the uncertainty from comparing POWHEG+HERWIG, POWHEG+PYTHIA8, and POWHEG+PYTHIA6 is found to about 2 %, which is ignored. The computed acceptances are

$$\begin{aligned} \mathcal{A}_{0j}^{\text{ggF}} &= 0.206 \pm 0.030 \\ \mathcal{A}_{1j}^{\text{ggF}} &= 0.075 \pm 0.017\,. \end{aligned} \tag{5.64}$$

where the uncertainties are theoretical, with the largest from the effect of the QCD scale on jet multiplicity. The signal strengths used for the fiducial cross section use the $N_{\text{jets}} = 0$ and $= 1$ categories, with the VBF contribution treated as background at the SM expected rate,

$$\begin{aligned} \mu_{0j,e\mu}^{\text{ggF}} &= 1.39^{+0.27}_{-0.27}(\text{stat.})\,^{+0.21}_{-0.19}(\text{syst.})\,^{+0.27}_{-0.17}(\text{sig.}) \\ \mu_{1j,e\mu}^{\text{ggF}} &= 1.14^{+0.42}_{-0.41}(\text{stat.})\,^{+0.27}_{-0.26}(\text{syst.})\,^{+0.42}_{-0.17}(\text{sig.})\,. \end{aligned} \tag{5.65}$$

Here, (sig.) again refers to uncertainties on the signal yield which do not enter the fiducial cross section measurement; additionally, for the fiducial calculation, it includes uncertainties on the jet binning and acceptance uncertainties from event selections. Shape uncertainties on the m_{T} distribution remain in the fit. The resulting 8 TeV fiducial cross sections for $m_H = 125.36$ GeV are

$$\begin{aligned} \sigma_{\text{fid},0j}^{\text{ggF}} &= 27.6^{+5.4}_{-5.3}(\text{stat.})\,^{+4.1}_{-3.9}(\text{syst.}) = 27.6^{+6.8}_{-6.6}\,\text{fb} \\ \sigma_{\text{fid},1j}^{\text{ggF}} &= 8.3^{+3.1}_{-3.0}(\text{stat.})\,^{+2.0}_{-1.9}(\text{syst.}) = 8.3^{+3.7}_{-3.5}\,\text{fb}\,. \end{aligned} \tag{5.66}$$

The predicted values are 19.9 ± 3.3 fb and 7.3 ± 1.8 fb.

CHAPTER VI

Probing the Higgs Boson Width with $H \to WW \to e\nu\mu\nu$

This chapter describes using the $H \to WW \to e\nu\mu\nu$ channel to probe off-shell Higgs boson production, that is the virtual Higgs boson is propagating with $m \neq m_H$. The analysis, and its combination with the $ZZ \to 4\ell$ and $ZZ \to 2\ell 2\nu$ channels, is described in more detail in Ref. [198]. Only the $20.3\,\mathrm{fb}^{-1}$ of data collected at 8 TeV is used. The individual analyses are based on their respective on-shell analyses, see Refs. [199, 200] for the ZZ channels and Chapter V for the WW channel, but optimized for the high-mass region. A similar measurement has also been performed by the CMS collaboration [201]. In brief, a limit on the off-shell signal strength is set using the high mass region, and this is used to set a limit on the Higgs boson decay width.

6.1 Introduction

After the discovery of the Higgs boson, efforts have been focused on measuring the particle's properties. For example, couplings to other particles and its spin and charge parity (CP) properties provide tests for beyond the Standard Model (BSM) physics. Recently, studies [152, 202–204] have shown that the high-mass regions above $2m_V$ in the $H \to WW$ and $H \to ZZ$ channels are sensitive to off-shell Higgs boson production and interference effects. Probing this region provides sensitivity to new physics processes that alter the interactions of the Higgs boson in the high-mass region [205–211]. The measurement of the off-shell Higgs boson signal strength $\mu_{\text{off-shell}}$ can be interpreted as an indirect measurement of the Higgs boson total decay width Γ_H, which is complementary to those from couplings measurements [197, 212] and searches for invisible decays [200, 213]. This is a novel method to probe the Higgs boson total decay width with sensitivity approaching the SM expected width ($\sim 4\,\mathrm{MeV}$), which is well below the roughly $2\,\mathrm{GeV}$ limits from direct measurements [214–216].

6.2 Theory and simulation

The cross section $\sigma^{gg\to H^*\to VV}$ [1] for ggF Higgs production with decays into vector bosons has the form

$$\frac{d\sigma_{gg\to H\to VV}}{dm_{VV}^2} \sim \frac{g_{ggF}^2 g_{H\to VV}^2}{(m_{VV}^2 - m_H^2)^2 + m_H^2\Gamma_H^2}\,, \tag{6.1}$$

where g's are the couplings for ggF production and the decay into vector bosons. In the case of on-shell production $m_{VV}^2 \approx m_H^2$ and in the case of high-mass off-shell production $m_{VV}^2 > m_H^2$. This results in two regimes, which can be expressed in terms of the κ formulation (described in Section 5.7):

$$\mu_{\text{off-shell}}(\hat{s}) \equiv \frac{\sigma_{\text{off-shell}}^{gg\to H^*\to VV}(\hat{s})}{\sigma_{\text{off-shell, SM}}^{gg\to H^*\to VV}(\hat{s})} = \kappa_{g,\text{off-shell}}^2(\hat{s}) \cdot \kappa_{V,\text{off-shell}}^2(\hat{s}) \propto g_{ggF}^2 g_{H\to VV}^2\,, \tag{6.2}$$

$$\mu_{\text{on-shell}} \equiv \frac{\sigma_{\text{on-shell}}^{gg\to H\to VV}}{\sigma_{\text{on-shell, SM}}^{gg\to H\to VV}} = \frac{\kappa_{g,\text{on-shell}}^2 \cdot \kappa_{V,\text{on-shell}}^2}{\Gamma_H/\Gamma_H^{\text{SM}}} \propto \frac{g_{ggF}^2 g_{H\to VV}^2}{\Gamma_H^2}\,, \tag{6.3}$$

where $\hat{s}$ is the energy scale; however, in this analysis $\mu_{\text{off-shell}}$ and $\kappa_{\text{off-shell}}$ are assumed to be independent of $\hat{s}$ in the high-mass region due to the statistically limited sensitivity. The off-shell signal strength is independent of the total Higgs boson decay width. Assuming identical on- and off-shell coupling scale factors, the ratio $\mu_{\text{off-shell}}/\mu_{\text{on-shell}}$ is a measurement of the total Higgs boson decay width. This assumption is important, as new physics often affects the loop in ggF production, which the high-mass region will be more sensitive to. Refs. [205–209] have more details. Since this analysis is currently only sensitive enough to set an upper limit on Γ_H, the requirement that

$$\kappa_{g,\text{on-shell}}^2 \cdot \kappa_{V,\text{on-shell}}^2 \leq \kappa_{g,\text{off-shell}}^2 \cdot \kappa_{V,\text{off-shell}}^2 \tag{6.4}$$

is sufficient. We further assume that any new physics which modifies $\mu_{\text{off-shell}}$ and the off-shell couplings does not change the predicted backgrounds, and that any new physics does not sizably change the kinematics of the off-shell signal, nor introduce sizable unrelated new signals into the SRs [211, 217].

A large negative interference occurs between ggF Higgs boson production, shown in Fig. 6.1(a), and the $gg \to VV$ continuum background, shown in Fig. 6.1(b). The size of the interference is proportional to $\sqrt{\mu_{\text{off-shell}}} = \kappa_{g,\text{off-shell}} \cdot \kappa_{V,\text{off-shell}}$. This makes it impossible to treat the two processes separately. Figure 6.2 shows the differential cross sections as a

[1] The notation $gg \to (H^* \to)VV$ denotes the full signal (S) plus background (B) process including interference (I), $gg \to H^* \to VV$ the Higgs boson signal, and $gg \to VV$ the continuum background. Similar notation is used for VBF production.

function of $m_{4\ell}$ for the signal and background processes for the $gg \to (H^* \to)ZZ$ processes using generator level quantities with the $ZZ \to 4\ell$ event selection, see [198], along with the size of the interference, which is similar in size to the off-shell signal. The distribution for WW processes is very similar to that of ZZ.

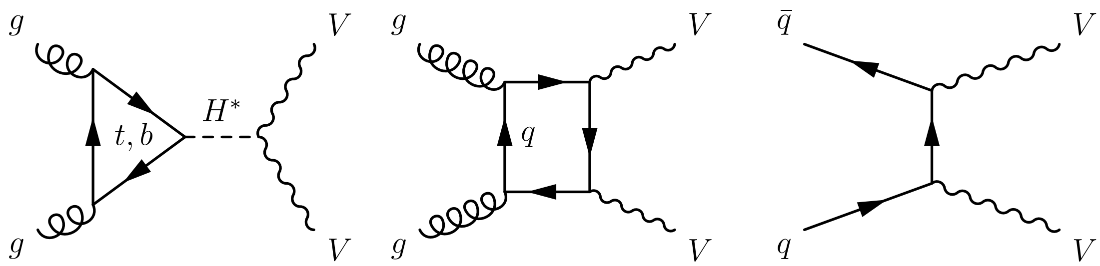

(a) (b) (c)

Figure 6.1: Leading order Feynman diagrams for the (a) ggF signal, (b) continuum $gg \to VV$ background, and (c) $q\bar{q} \to VV$ background.

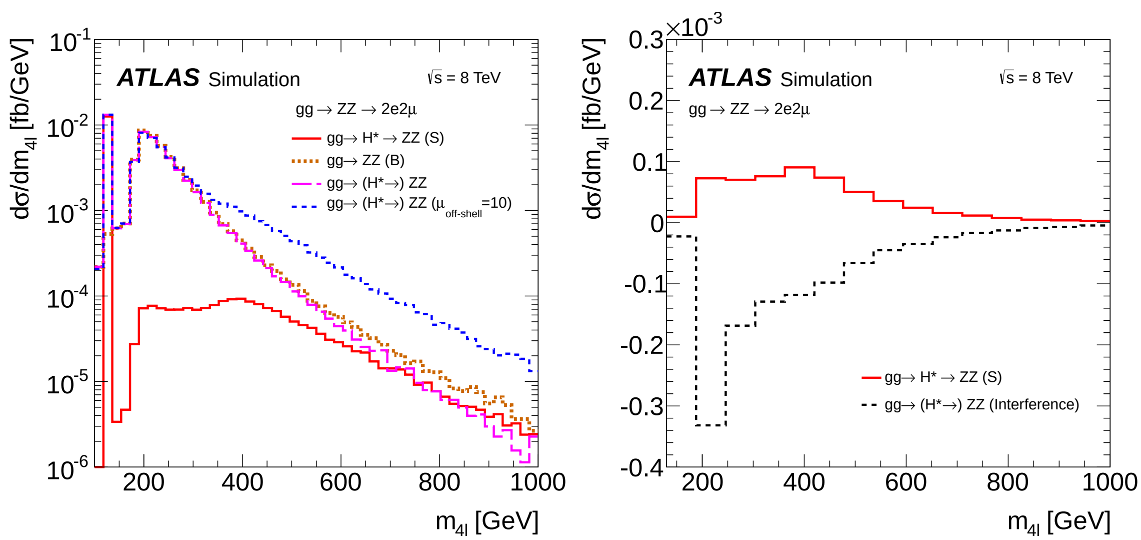

(a) (b)

Figure 6.2: (a) differential cross section of the four-lepton invariant mass $m_{4\ell}$ for the signal (S), background (B), and complete process including interference. The blue dashed line shows the expectation for $\mu_{\text{off-shell}} = 10$. (b) differential cross section of the signal and its interference with the continuum background [198].

All of the background processes, except for $gg \to WW$ are simulated the same as in Section 5.2.2. A Higgs boson mass of $m_H = 125.5\,\text{GeV}$ is assumed for the analysis, the effect due to the small difference with the measured mass of 125.36 GeV [135] is negligible.

6.2.1 $q\bar{q} \to VV$

An NNLO in QCD k-factor [218] is applied to the $q\bar{q} \to WW$ NLO sample (an NNLO calculation also exists for $q\bar{q} \to ZZ$ [219]). It is provided excluding the $gg \to VV$ contribution, which is part of the NNLO $pp \to VV$ calculation, and using a QCD renormalization factor μ_{QCD} to match the $gg \to (H^* \to)VV$ simulation:

$$k_{q\bar{q}}(m_{VV}) \quad = \quad \frac{\sigma^{\mathrm{NNLO}}_{q\bar{q}\to VV}(m_{VV}, \mu_{QCD} = m_{VV}/2) - \sigma^{\mathrm{LO}}_{gg\to VV}(m_{VV}, \mu_{QCD} = m_{VV}/2)}{\sigma^{\mathrm{NLO}}_{q\bar{q}\to VV}(m_{VV}, \mu_{QCD} = m_{VV})}\,. \qquad (6.5)$$

The $q\bar{q} \to VV$ samples are also reweighted with NLO EW corrections for on-shell vector bosons from Refs. [220, 221]. Corrections are applied based on the kinematics of the VV system and initial state quarks, using a method similar to that described in Ref. [222]. Figure 6.3 shows the impact of the reweighting on the $q\bar{q} \to WW$ m_{T} and $m_{\ell\ell}$. The correction decreases the expected cross section in the high-mass region.

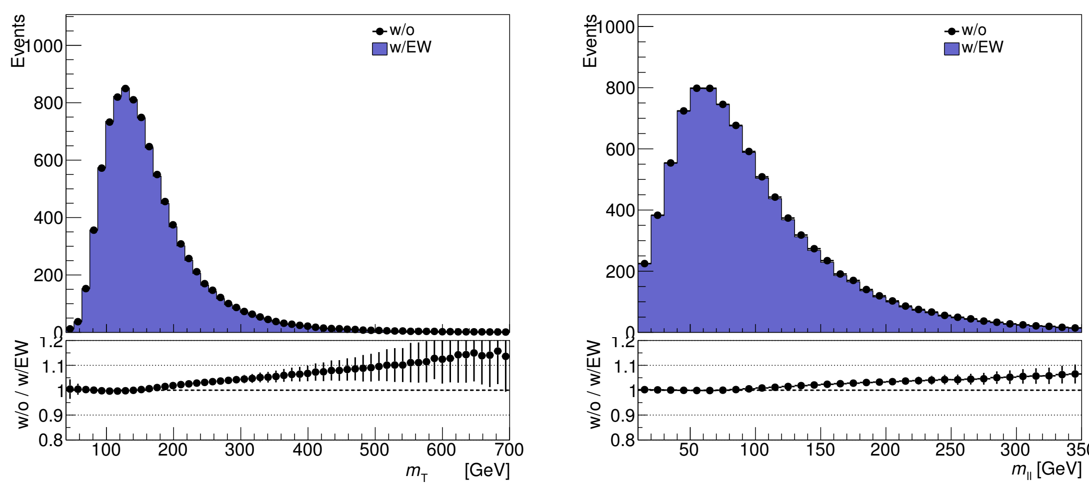

(a) (b)

Figure 6.3: Impact of EW correction on the $q\bar{q} \to WW$ samples for (a) m_{T} and (b) $m_{\ell\ell}$.

6.2.2 $gg \to (H^* \to)VV$

The LO generators GG2VV[169, 202]+PYTHIA8 and MCFM[152, 204]+PYTHIA8, as well as SHERPA+OpenLoops [167, 223, 224], are used to generate the $gg \to H^* \to VV$ and $gg \to VV$ processes including interference effects. The CT10 NNLO PDF set [225] is used, since $gg \to VV$ is part of the NNLO $pp \to VV$ calculation. The QCD renormalization and factorization scales are set to $m_{VV}/2$ [204].

Higher-order QCD and EW corrections are known for the off-shell signal process [226]; however, no higher-order corrections are available for the background process, which are known only to LO. Since it is believed that the background k-factor will be of similar size, the results are presented as a function of the the unknown background k-factor, via its ratio to the signal k-factor,

$$\mathrm{R}^{B}_{H^*} = \frac{k(gg \to VV)}{k(gg \to H^* \to VV)} = \frac{k^{\mathrm{B}}(m_{VV})}{k^{H^*}_{gg}(m_{VV})}\,, \tag{6.6}$$

where $k^{\mathrm{B}}(m_{VV})$ is the unknown background k-factor and $k^{H^*}_{gg}(m_{VV})$ is the k-factor for the gluon initiated signal. No mass dependence is assumed for $\mathrm{R}^{B}_{H^*}$ as $k^{H^*}_{gg}(m_{VV})$ changes by less than 10 % in the relevant phase space. The ratio is scanned from 0.5–2—the signal k-factor itself is close to two. The QCD corrections for the off-shell signal are calculated inclusively in jet multiplicity; therefore, the analysis is performed inclusively in jets, unlike the analysis in Chapter V, and is designed to minimize the impact of the event selection on the jet multiplicity.

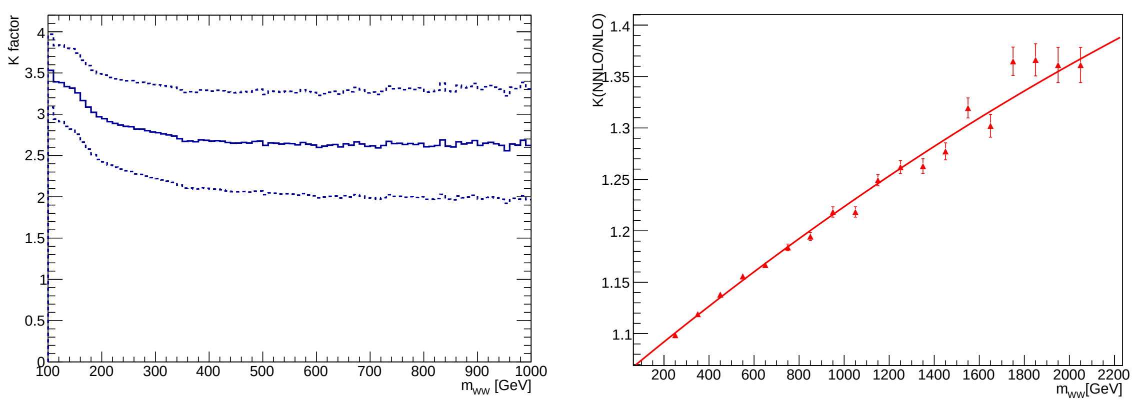

(a) (b)

Figure 6.4: (a) k-factor as a function of m_{WW} for Higgs boson signal production at m_H = 125.5 GeV using the CT10 NNLO PDF. The dotted line represents varying the QCD scales to $m_{WW}/4$ and m_{WW}. (b) NNLO/NLO k-factor for $q\bar{q} \to WW$ as a function of m_{WW}.

The NNLO/LO k-factor $k^{H^*}(m_{VV})$ for the $gg \to H^* \to VV$ (gg includes qg and $q\bar{q}$) signal, including NLO EW corrections, is calculated in Ref. [226] as a function of Higgs boson virtuality m_{VV} using the MSTW2008 PDF set. $k^{H^*}_{gg}(m_{VV})$ and $k^{H^*}(m_{VV})$ differ by about 2 %, but $k^{H^*}_{gg}(m_{VV})$ has much larger uncertainties. Thus, $k^{H^*}(m_{VV})$ is used, ignoring the shift in central value, but taking the difference in uncertainties into account. Corrections are applied to reweight the k-factor to the CT10 PDF used. The total k-factor is shown in Fig. 6.4(a).

The higher-order corrections are studied in the soft-collinear approximation, which is considered suitable for high-mass Higgs boson production [227]. With this approximation, the signal k-factor is found to be reasonable for the $gg \to VV$ background and its interference with signal.

Using the k-factors described, the total $gg \to (H^* \to)VV$ process can be parametrized for an arbitrary $\mu_{\text{off-shell}}$ by using a pure signal, pure background, and full signal plus background plus interference sample:

$$\begin{aligned} \sigma_{gg\to(H^*\to)VV}(\mu_{\text{off-shell}}) = & \, k^{H^*}(m_{VV}) \cdot \mu_{\text{off-shell}} \cdot \sigma^{\text{SM}}_{gg\to H^*\to VV} \\ & + \sqrt{k^{H^*}_{gg}(m_{VV}) \cdot k^{\text{B}}(m_{VV}) \cdot \mu_{\text{off-shell}}} \cdot \sigma^{\text{SM}}_{gg\to VV,\,\text{Interference}} \\ & + k^{\text{B}}(m_{VV}) \cdot \sigma_{gg\to VV,\,\text{Cont}} \end{aligned} \tag{6.7}$$

$$\sigma^{\text{SM}}_{gg\to VV,\ \text{Interference}} = \sigma^{\text{SM}}_{gg\to(H^*\to)VV} - \sigma^{\text{SM}}_{gg\to H^*\to VV} - \sigma_{gg\to VV,\,\text{Cont}}\,. \tag{6.8}$$

Since it is not possible to simulate a standalone interference sample, Equation 6.8 and $\text{R}^{B}_{H^*}$ are used to obtain:

$$\begin{aligned} \sigma_{gg\to(H^*\to)VV}(\mu_{\text{off-shell}}) = & \left(k^{H^*}(m_{VV}) \cdot \mu_{\text{off-shell}} - k^{H^*}_{gg}(m_{VV}) \cdot \sqrt{\text{R}^{B}_{H^*} \cdot \mu_{\text{off-shell}}}\right) \\ & \times \sigma^{\text{SM}}_{gg\to H^*\to VV} \\ & + k^{H^*}_{gg}(m_{VV}) \cdot \sqrt{\text{R}^{B}_{H^*} \cdot \mu_{\text{off-shell}}} \cdot \sigma^{\text{SM}}_{gg\to(H^*\to)VV} \\ & + k^{H^*}_{gg}(m_{VV}) \cdot \left(\text{R}^{B}_{H^*} - \sqrt{\text{R}^{B}_{H^*} \cdot \mu_{\text{off-shell}}}\right) \cdot \sigma_{gg\to VV,\,\text{Cont}}\,. \end{aligned} \tag{6.9}$$

In addition to the k-factor, the p_{T} and rapidity (y) of the VV system are checked against higher-order QCD corrections with SHERPA+OPENLOOPS, which includes the first jet in the matrix element (ME). There is a substantial difference in the p_{T} of the VV system, but small difference in rapidity. To account for this, the LO samples are reweighted to the p_{T} spectrum from SHERPA+OPENLOOPS. Separate functions are derived for the signal, background, and the total calculation because the jet emissions are different. The reweighting affects only the acceptance in the $WW \to e\nu\mu\nu$ channel, the impact is below 1 % for the signal and roughly 5 % for the background.

EW $pp \to VV + 2j$ processes contain both VBF and VH-like events and are simulated using MADGRAPH5[164]+PYTHIA6 [164]. The samples are cross checked with PHANTOM [228]. The QCD factorization and renormalization scales are set to m_W [158]. The VBF-like events include off-shell VBF $H \to VV$ events and t-channel events with a Higgs boson exchanged. VH processes contain an on-shell Higgs boson, and thus are treated separately since the process scales with the on-shell coupling factors. These events are selected by using the generated Higgs boson mass $|m_H^{\text{gen.}} - 125.5| < 1\,\text{GeV}$. Similar to the gluon initiated VV, the EW $pp \to (H^* + 2j \to)VV + 2j$ is parametrized with an arbitrary $\mu_{\text{off-shell}}$:

$$\sigma_{pp\to(H^*+2j\to)VV+2j}(\mu_{\text{off-shell}}) = \mu_{\text{off-shell}} \cdot \sigma^{\text{SM}}_{pp\to(H^*+2j\to)VV+2j} + \sqrt{\mu_{\text{off-shell}}} \cdot \sigma_{pp\to VV+2j,\text{ Interference}} + \sigma_{pp\to VV+2j,\text{Cont}}\,, \tag{6.10}$$

where the samples are defined with the SM sample:

$$\sigma^{\text{SM}}_{pp\to(H^*+2j\to)VV+2j} = \sigma^{\text{SM}}_{pp\to H^*+2j\to VV+2j} + \sigma_{pp\to VV+2j,\text{ Interference}} + \sigma_{pp\to VV+2j,\text{Cont}} \tag{6.11}$$

and a $\mu_{\text{off-shell}} = 10$ MC sample:

$$\sigma^{\kappa_V^4=10}_{pp\to(H^*+2j\to)VV+2j} = 10 \cdot \sigma^{\text{SM}}_{pp\to H^*+2j\to VV+2j} + \sqrt{10} \cdot \sigma_{pp\to VV+2j,\text{ Interference}} + \sigma_{pp\to VV+2j,\text{Cont}}\,. \tag{6.12}$$

The parametrization in terms of generated samples is thus

$$\begin{aligned}\sigma_{pp\to(H^*+2j\to)VV+2j}(\mu_{\text{off-shell}}) = {} & \frac{\mu_{\text{off-shell}} - \sqrt{\mu_{\text{off-shell}}}}{10 - \sqrt{10}} \sigma^{\kappa_V^4=10}_{pp\to(H^*+2j\to)VV+2j} \\ & + \frac{10\sqrt{\mu_{\text{off-shell}}} - \sqrt{10}\mu_{\text{off-shell}}}{10 - \sqrt{10}} \sigma^{\text{SM}}_{pp\to(H^*+2j\to)VV+2j} \\ & + \frac{(\sqrt{\mu_{\text{off-shell}}} - 1) \cdot (\sqrt{\mu_{\text{off-shell}}} - \sqrt{10})}{\sqrt{10}} \sigma_{pp\to VV+2j,\text{Cont}}\,.\end{aligned} \tag{6.13}$$

6.3 $H \to WW \to e\nu\mu\nu$ channel

The analysis of the $WW \to e\nu\mu\nu$ channel closely follows the analysis in Chapter V, but using only $e\mu$ events. This selection ensures orthogonality with the $ZZ \to 2\ell 2\nu$ final state. The same object identification and selection as in Section 5.3 is used. Additionally, the same preselection, see Section 5.4.1, as the ggF initial states is used up to and including a requirement on missing transverse momentum: leading lepton $p_{\text{T}} > 22\,\text{GeV}$, subleading lepton $p_{\text{T}} > 10\,\text{GeV}$, $m_{\ell\ell} > 10\,\text{GeV}$, and $p_{\text{T}}^{\text{miss,track}} > 20\,\text{GeV}$, the magnitude of the missing transverse momentum, with a track-based soft term. The SR and background estimations are revised for the high-mass region used in this analysis. Contrary to the baseline analysis, described in Chapter V, events are not binned by the number of jets. Top-quark events and SM WW production remain the largest expected backgrounds.

6.3.1 Event selection

The neutrinos in the final state do not allow for a kinematic reconstruction of m_{WW}. Thus a transverse mass m_{T}, see Section 5.1, is used as a discriminant. In order to isolate the off-shell Higgs boson production while minimizing the impact of higher-order QCD effects on $gg \to WW$ kinematics, a new variable, R_8, is introduced:

$$\mathrm{R}_8 = \sqrt{m_{\ell\ell}^2 + (0.8 \cdot m_{\mathrm{T}})^2}. \tag{6.14}$$

This variable is found to have a smaller impact on the WW system p_{T} and N_{jets} distributions compared to other discriminants tested, e.g., the lepton p_{T}, to select the off-shell region. One can see in Fig. 6.5(a), that removing the on-shell signal requires $m_{\mathrm{T}} \gtrsim 400\,\mathrm{GeV}$, which would also remove a significant fraction of the off-shell events. Though $m_{\ell\ell}$ and m_{T} are fairly correlated, as seen in Fig. 6.5(b), using an ellipse in this plane recovers some of the off-shell events otherwise lost. Both the coefficient 0.8 and the requirement $\mathrm{R}_8 > 450\,\mathrm{GeV}$ are optimized for off-shell signal sensitivity while also rejecting on-shell Higgs boson events, which have relatively low values of $m_{\ell\ell}$ and m_{T}. Figure 6.5(c) shows the R_8 distribution for on- and off-shell signals compared to the backgrounds. The predicted on-shell signal contamination is $0.04 \pm 0.03(\mathrm{stat.})$ events.

The MV1 algorithm [125], at 85 % efficiency, is used to reject b-jets with $p_{\mathrm{T}} > 20\,\mathrm{GeV}$ and $|\eta| < 2.4$ in order to reject backgrounds containing top quarks. A requirement on the separation between leptons, $\Delta\eta_{\ell\ell} < 1.2$, suppresses quark-initiated WW production relative to gluon-initiated production. The b-jet veto and $\Delta\eta_{\ell\ell}$ requirement are found to have a minimal impact on the WW-system kinematics and jet multiplicity in the $gg \to (H^* \to)WW$ processes. Table 6.4 contains the predicted and observed event yields in the signal region, 90 ± 4 and 82 respectively, showing a small deficit in data. The distribution of the R_8 variable in the signal region is shown in Fig. 6.6(c) for the SM expectation and for a Higgs boson with $\mu_{\text{off-shell}} = 10$. Figure 6.7 shows the generated mass range for ggF and VBF signal events that are selected; they fall above 400 GeV.

6.3.2 Background estimation

The dominant backgrounds arise from processes with real W bosons in the final state. The two backgrounds with the largest expected event yield are top-quark and $q\bar{q} \to WW$ production. Dedicated CRs are constructed to normalize these two backgrounds in the signal region with a simultaneous fit. Uncertainties on the extrapolation from the CRs to the SR are described in Sections 6.3.3.2 and 6.3.3.3.

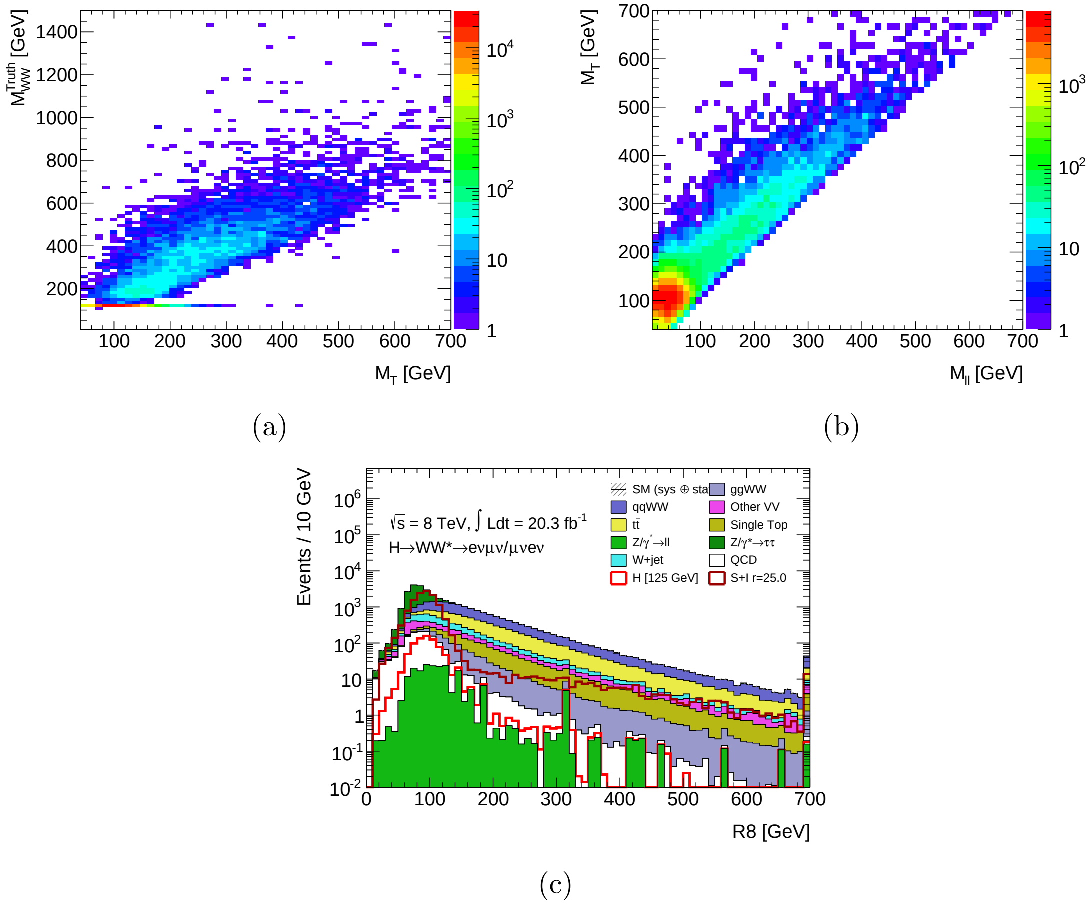

Figure 6.5: (a), m_{T} versus the generated WW system mass for the $gg \rightarrow H^{*} \rightarrow WW$ process. (b), $m_{\ell\ell}$ versus m_{T} for the $gg \rightarrow H^{*} \rightarrow WW$ process. (c), R_8 distribution showing overlays of the on-shell signal only outlined in lighter red and both on- and off-shell signal plus interference with $\mu_{\text{off-shell}} = 25$ outlined in darker red—the on-shell region of the signal plus interference overlay should be ignored as it is also scaled by 25 in this figure.

The top-quark background predictions in the signal and WW SR are both normalized from the same top-quark CR. A sample of top-quark events is obtained by starting from the SR and reversing the b-jet veto by requiring exactly one b-tagged jet. This is closer in phase space to the b-jet-vetoed SR than requiring at least one b-tag and results in a smaller uncertainty. The statistical error on the top-quark background normalization is reduced by expanding the top-quark CR down to $\mathrm{R}_8 > 160\,\mathrm{GeV}$ and dropping the $\Delta\eta_{\ell\ell}$ requirement. The impact of these changes is discussed in Section 6.3.3.3. An event yield of 13498 events is observed in the top-quark CR, see Fig. 6.6(a), resulting in a fit normalization factor of 1.03 ± 0.04, where the uncertainty includes all systematic sources, including extrapolation uncertainties described in Section 6.3.3.3. The top-quark CR is approximately 96 % pure in top-quark events.

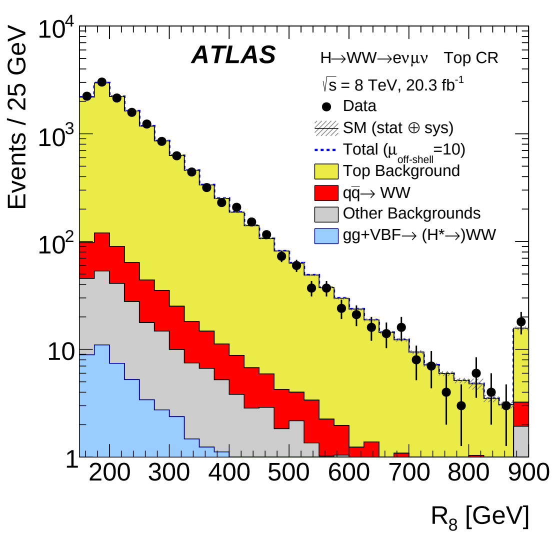

(a)

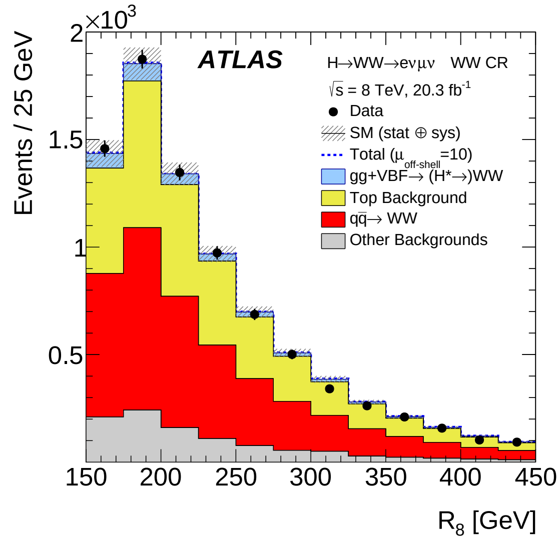

(b)

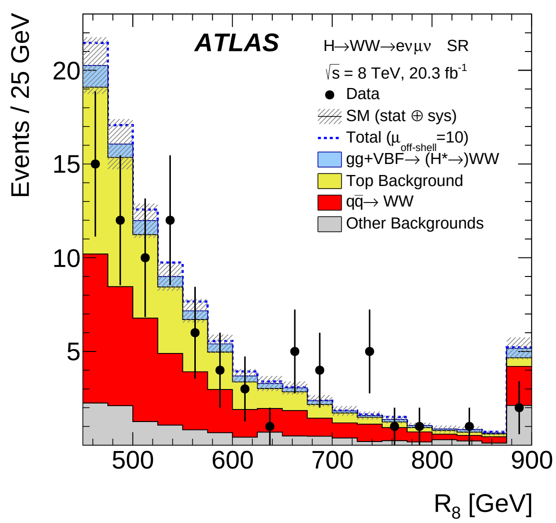

(c)

Figure 6.6: Observed distributions of R_8, constructed from the dilepton invariant mass and transverse mass, see Equation 6.14, in the $WW \to e\nu\mu\nu$ channel for (a) the top control region, (b) WW control region (the CRs start at 160 GeV), and (c) the signal region for R_8 above 450 GeV, compared to the expected contributions from the SM including the Higgs boson (solid fill). The dashed line corresponds to the total expected event yield, including all backgrounds and the Higgs boson with $\mu_{\text{off-shell}} = 10$. The last bin in (a) and (c) includes the overflow. A relative $gg \to WW$ background k-factor of $R^B_{H^*} = 1$ is assumed. The top-quark and WW backgrounds are normalized to data as described in Section 6.3.1. The stacking order follows the legend in each plot.

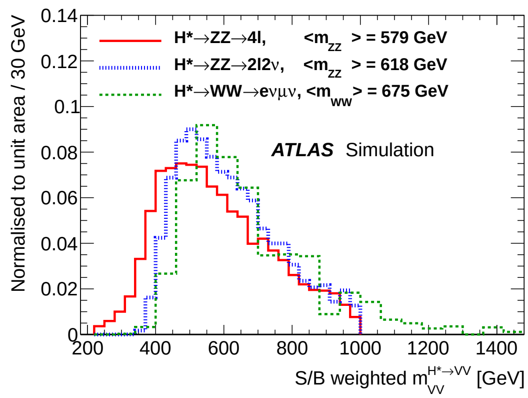

Figure 6.7: Normalized distributions of the selected generated m_{VV} for the ggF and VBF signal processes, weighted by the expected signal-to-background per bin of the final discriminant in each channel—$WW \to e\nu\mu\nu$ uses a single bin, and is thus not affected by the weighting [198].

The $q\bar{q} \to WW$ background is also normalized to data using an additional CR. The region $160 < \mathrm{R}_8 < 450\,\mathrm{GeV}$ without the $\Delta\eta_{\ell\ell}$ requirement is used because it has a large WW contribution with negligible on-shell Higgs boson contamination and is adjacent to the signal region. A b-jet veto is applied to reject part of the substantial top-quark contamination. An event yield of 8007 events is observed in the WW CR, see Fig. 6.6(b), resulting in a fit normalization factor of 1.03 ± 0.11, including all of the uncertainties as above. This CR is approximately 46 % pure in $q\bar{q} \to WW$, while the leading background of top-quark events contributes 39 %. The gluon-initiated WW background is estimated from MC simulation, as discussed in Section 6.2.2.

The remaining background predictions, except for $W+$jets and multijet production, are taken from MC simulation, as described in Section 5.2.2. The predicted fraction of the total background in the signal region arising from $gg \to WW$, $W+$jets, and $W\gamma/W\gamma^*/WZ/ZZ$ events is approximately 4 % each, while for Z+jets it is 2 %. The $W+$jets and multijet backgrounds are estimated with the same data-driven method described in Section 5.5.4.

6.3.3 Systematic uncertainties

All of the experimental uncertainties discussed in Chapter V are also applied in this analysis. The uncertainty on the electron energy scale, followed by the uncertainty on the rate for mistagging light jets as b-jets, and the uncertainty on the JES and JER, are the dominant experimental sources of uncertainty. The remaining experimental sources are significantly smaller than the theoretical uncertainties.

6.3.3.1 $gg \to (H^* \to)WW$

The uncertainty from missing higher order corrections is estimated in Ref. [226]. It amounts to an uncertainty of about 20 % in the high-mass region, which is correlated between processes. The difference in quadrature between uncertainties on k^{H^*} for the signal and $k_{gg}^{H^*}$, which is about 10 %, is applied to the background and interference, with a nuisance parameter uncorrelated with signal.

Reference [227] calculates the cross section of a heavy Higgs boson, including interference with the background, using a soft-collinear approximation. The uncertainty on this is estimated to be 10 %, which amounts to an uncertainty of 30 % on the interference alone. In terms of $\mathrm{R}_{H^*}^{B}$, this is covered by a roughly 60 % variation, and thus the variation of 0.5–2.0 should cover this uncertainty. However, around the expected upper limit on $\mu_{\text{off-shell}}$, there is a large cancellation between the background and interference, leading to a reduced impact of the uncertainties on each. To account for uncertainties on the interference that are not covered by the soft-collinear approximation, the 30 % uncertainty is applied as an extra uncorrelated uncertainty on the interference term.

The PDF uncertainty on the $gg \to (H^* \to)WW$ processes is evaluated using the parametrization $1 \pm 0.0066 \times \sqrt{m_{WW}/\mathrm{GeV} - 10}$ [158]. The uncertainty varies from 10 % in the low-mass region to 20 % in the high-mass region. The PDF acceptance uncertainty on the processes is evaluated in the same way as Section 5.2.2.1, resulting in an uncertainty of 2.3, 3.0, and 3.2 % on the signal, background, and full calculation respectively.

Systematic uncertainties from the p_{T} reweighting are assessed by varying the QCD renormalization and factorization scales in SHERPA. The larger between these scale variations and 50 % of the difference with GG2VV+PYTHIA8 is taken as the systematic uncertainty. PDF uncertainties are found to be negligible.

6.3.3.2 $q\bar{q} \to WW$

Extrapolation uncertainties on the $q\bar{q} \to WW$ process are evaluated using the method described in Section 5.5.1.1. Uncertainties due to missing higher-order corrections are estimated by varying the renormalization and factorization scales independently by factors of one-half and two, keeping the ratio of the scales between one-half and two. Parton shower and matrix-element uncertainties are estimated by comparing POWHEG+PYTHIA8 with POWHEG+HERWIG6 and POWHEG+HERWIG6 with aMC@NLO+HERWIG6, respectively. PDF uncertainties are estimated by taking the largest difference between the nominal PDF CT10 and either the MSTW2008 or the NNPDF2.1 PDF set and adding this in quadrature with the CT10 error eigenvectors. The extrapolation uncertainties from the WW CR to the SR are summarized in Table 6.1.

Region	UE/PS	Gen.	Scale	PDF
Top CR	6.4	2.4	2.4	2.4
WW CR	2.5	2.8	2.3	1.5

Table 6.1: Uncertainties, in percent, on the extrapolation of top-quark processes and $q\bar{q} \to WW$ from their respective CRs to the SR, and from the top-quark CR to the WW CR, from the parton shower and underlying event (UE/PS), from matching the matrix element to the UE/PS model (Gen.), from the QCD renormalization and factorization scale (Scale), and from the PDFs [198].

The EW corrections described in Section 6.2.1 are valid for the LO QCD $qq \to VV$ process with on-shell bosons, which is the case in the high-mass region. For events with high QCD activity, an extra uncertainty is assigned. The QCD activity is assessed using the variable

$$\rho = \left| \sum_{i}^{\text{leptons}} \boldsymbol{p}_{i,\mathrm{T}} + \boldsymbol{E}_{\mathrm{T}}^{\text{miss}} \right| / \left(\sum_{i} \left| \boldsymbol{p}_{i,\mathrm{T}} \right| + \left| \boldsymbol{E}_{\mathrm{T}}^{\text{miss}} \right| \right) , \tag{6.15}$$

from Ref. [222]. No additional uncertainty is applied in the region $\rho < 0.3$, where the NLO simulation used matches LO event kinematics needed for the correction to be applicable. Events with $\rho > 0.3$ are assigned an uncertainty equal to 100 % of the correction, to account for missing mixed QCD-EW corrections. Since the $WW \to e\nu\mu\nu$ channel uses a WW CR, this uncertainty on the EW correction only affects the extrapolation from the CR to the SR.

6.3.3.3 Top-quark processes

Theory uncertainties on extrapolating top-quark processes from the CR to the SR are also evaluated using the same methods as in Section 5.5.2. For the evaluation of the extrapolation uncertainties, the signal region requirements are relaxed in order to increase the sample size; the region is extended down to $\mathrm{R}_8 > 160\,\mathrm{GeV}$ and the $\Delta\eta_{\ell\ell}$ requirement is dropped. The extra uncertainty from this extension is checked in a separate sample with at least one b-tagged jet, again defined so as to reduce the statistical uncertainties, which is simultaneously reweighted in $\Delta\eta_{\ell\ell}$ and R_8 to match the b-vetoed region. With this b-tagged sample, the extra uncertainty from the removal of the $\Delta\eta_{\ell\ell}$ requirement, and from extending the range in R_8, is found to be 3.5 %.

Since the extended SR covers the WW CR, the same systematic uncertainties are valid for the extrapolation from the top-quark CR to the WW CR. These uncertainties, summarized in Table 6.1, are applied to both $t\bar{t}$ and single-top processes, which make up approximately 22 %

of the top background in the signal region. A 20 % uncertainty is assigned to the single-top processes in order to take into account the uncertainty on the relative fraction of top-quark events from the single-top process; the impact on the result is negligible.

6.4 Results

A similar statistical treatment as described in Section 5.6.4 is used to fit the data, using one bin for each region. Table 6.2 shows the expected and observed yields in the SR and two CRs. Additionally, the expected yields with $\mu_{\text{off-shell}} = 20$, which is close to the expected limit from the $WW \to e\nu\mu\nu$ channel, are shown. A small deficit in data is observed, leading to stronger limits than expected. Figure 6.6 shows the R_8 distribution in the SR and two CRs. The $WW \to e\nu\mu\nu$ channel is also combined with the $ZZ \to 4\ell$ and $ZZ \to 2\ell 2\nu$ channels, and additionally with the on-shell $H \to ZZ \to 4\ell$ [199] and $H \to WW^{(*)} \to \ell\nu\ell\nu$ [112] analyses.

Process	SR	WW CR	Top CR
$gg \to H^* \to WW$	1.5 ± 0.4	17 ± 4	3.4 ± 0.9
$gg \to WW$	3.6 ± 1.1	260 ± 60	33 ± 9
$gg \to (H^* \to)WW$	2.4 ± 1.2	240 ± 100	28 ± 12
$gg \to (H^* \to)WW(\mu_{\text{off-shell}} = 20)$	22 ± 10	410 ± 170	64 ± 26
VBF $H^* \to WW$	0.42 ±0.05	1.8 ± 0.12	0.192 ± 0.019
VBF WW	1.63 ± 0.17	37.7 ± 2.5	10.3 ± 1.1
VBF $(H^* \to)WW$	1.07 ± 0.13	34.7 ± 2.3	10.3 ± 1
VBF $(H^* \to)WW(\mu_{\text{off-shell}} = 20)$	5.7 ± 0.6	52.5 ± 3.5	13.1 ± 1.2
$q\bar{q} \to WW$	40 ± 5	3700 ± 400	320 ± 60
Top-quark events	35 ± 4	3070 ± 330	12940 ± 150
Other backgrounds	12.2 ± 1.4	970 ± 140	194 ± 30
Total Expected (SM)	90 ± 4	8000 ± 110	13500 ± 120
Observed	82	8007	13498

Table 6.2: The expected and observed event yields, with statistical and systematic uncertainties combined, in the $WW \to e\nu\mu\nu$ channel corresponding to an integrated luminosity of $20.3\,\text{fb}^{-1}$ at a collision energy of $\sqrt{s} = 8\,\text{TeV}$. The VBF and $gg \to (H^* \to)WW$ processes are reported for both the SM expectation and $\mu_{\text{off-shell}} = 20$. A relative $gg \to WW$ K-factor of $R^B_{H^*} = 1$ is assumed. Uncertainties on the expected total are less than the sum of components due to correlations [198].

Figure 6.8 shows the upper limits on $\mu_{\text{off-shell}}$ from the $WW \to e\nu\mu\nu$ channel, both a scan of the negative log-likelihood and scan of the 95 % CL upper limit on $\mu_{\text{off-shell}}$ as a function of $\mathrm{R}^{B}_{H^*}$ using the CL_s method with alternate hypothesis $\mu_{\text{off-shell}} = 1$. The observed 95 % CL upper limit on $\mu_{\text{off-shell}}$ for $\mathrm{R}^{B}_{H^*} = 1$ is 17.2, while the expected is 21.3. The WW channel's sensitivity is about twice worse than the ZZ channel's, see Table 6.5. Table 6.3 lists the top uncertainties, ranked by the limit including just that uncertainty. The theoretical uncertainties on the $gg \to (H^* \to)VV^*$ processes and the statistical uncertainty from the low SR event yield dominate the sensitivity.

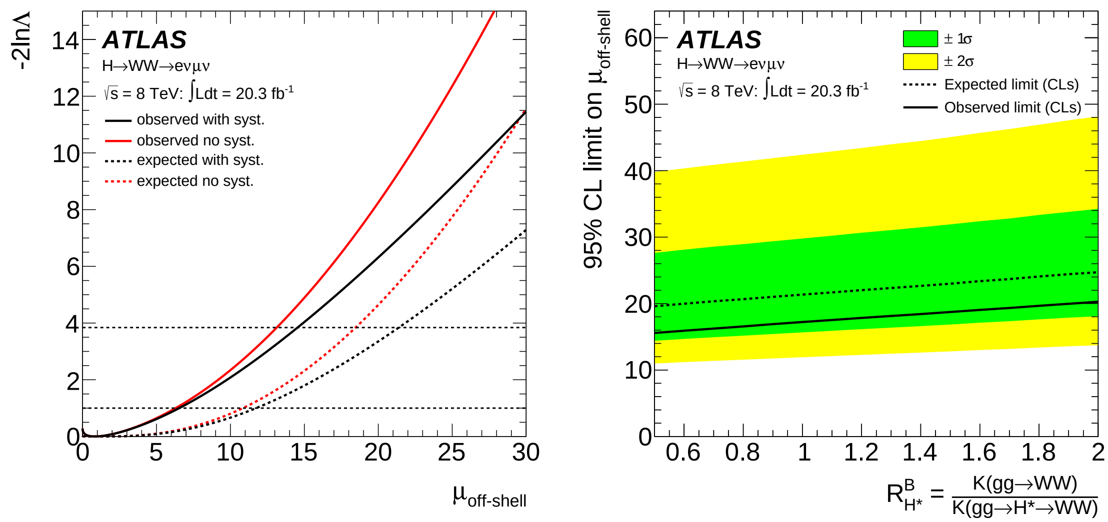

(a) (b)

Figure 6.8: For the $WW \to e\nu\mu\nu$ channel, (a), scan of the negative log-likelihood as a function of $\mu_{\text{off-shell}}$. The red lines represent the the value without systematics, and black with. (b), observed and expected 95 % CL limit on $\mu_{\text{off-shell}}$ as a function of $\mathrm{R}^{B}_{H^*}$ [198].

6.4.1 Combination with ZZ channels

Details on the off-shell analyses using the ZZ channels can be found in Ref. [198]. Figure 6.9 shows the discriminants used in the signal regions of the $ZZ \to 4\ell$ and $ZZ \to 2\ell 2\nu$ channels. Table 6.4 shows the expected and observed yields in the three off-shell channels; also shown, is the expectation for $\mu_{\text{off-shell}} = 10$, which is close to the expected upper limit from the ZZ channels. A small deficit is observed in each of the channels, leading to stricter than expected upper limits on $\mu_{\text{off-shell}}$, shown in Table 6.5.

In order to improve the sensitivity of the analysis, the $WW \to e\nu\mu\nu$, $ZZ \to 4\ell$, and $ZZ \to 2\ell 2\nu$ channels are combined. Two tests are made. An upper limit is placed on $\mu_{\text{off-shell}}$ and instead of using a single parameter of interest (POI) for the ggF and VBF modes, we also fix the VBF rate to the expectation of the SM, with the ggF signal strength as the POI. This signal strength, $\mu^{gg\to H^*\to VV}_{\text{off-shell}}$, can be interpreted as a limit on the off-shell coupling strength

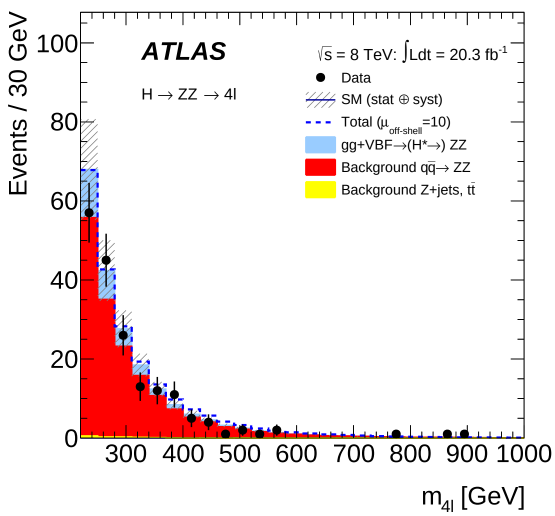

(a) $ZZ \to 4\ell$

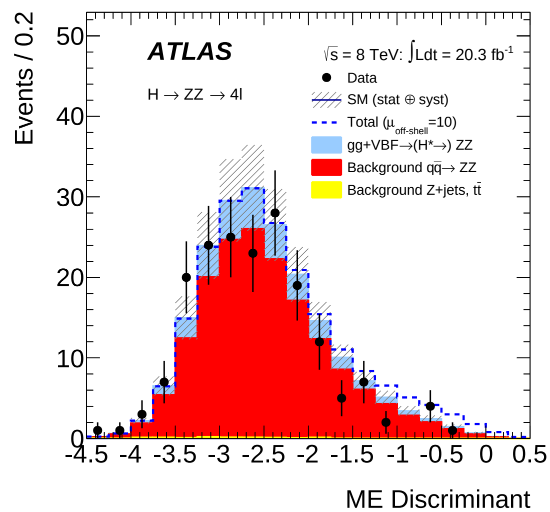

(b) $ZZ \to 4\ell$

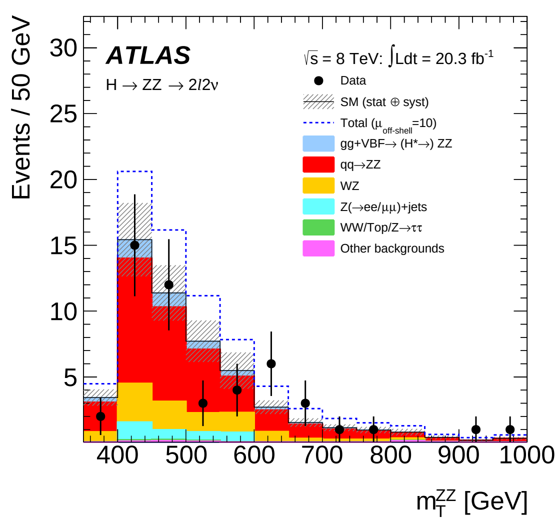

(c) $ZZ \to 2\ell 2\nu$

Figure 6.9: (a), the $m_{4\ell}$ in the range $220 < m_{4\ell} < 1000\,\text{GeV}$ and (b) ME discriminant in the ME-based SR for the $ZZ \to 4\ell$ channel. (c), m_{T}^{ZZ} in the SR of the $ZZ \to 2\ell 2\nu$ channel. The blue dashed lines show the total expected yield for $\mu_{\text{off-shell}} = 10$. A relative $gg \to VV$ K-factor of $R_{H^*}^{B} = 1$ is assumed [198].

Systematic uncertainty	95 % CL limit CL_s
QCD scale for $gg \to WW$	19.6
QCD scale for $gg \to WW$ interference	18.9
PDF for $gg \to (H^* \to)WW$	18.8
Signal region statistics	18.6
Difference between K^{H^*} and $K^{H^*}_{gg}$	18.6
Electron Energy scale	18.6
EW for $qq \to WW$	18.6
B-tagging mis-ID for light jets	18.5
Gen. for $qq \to WW$	18.5
PS/UE for $qq \to WW$	18.5
Jet energy resolution	18.5
All systematic uncertainties	21.3
No systematic uncertainties	18.4

Table 6.3: The expected 95 % CL upper limit on $\mu_{\text{off-shell}}$ in the $WW \to e\nu\mu\nu$ channel. Each row shows limit with just that uncertainty, except the last two, which show the limit with all and no systematic uncertainties. The upper limits are evaluated using the CL_s method, assuming $\mathrm{R}^B_{H^*} = 1$ [198].

$\kappa_{g,\text{off-shell}}$. Table 6.6 shows the observed and expected limits for the two treatments of $\mu^{\text{VBF}}_{\text{off-shell}}$. The impact of systematic uncertainties is shown in Table 6.7; the theory uncertainties on the $gg \to (H^* \to)VV$ processes have the largest impact.

Combining with the on-shell measurements allows us to probe the Higgs width using the ratio of signal strengths: $\mu_{\text{off-shell}}/\mu_{\text{on-shell}} = \Gamma_H/\Gamma_H^{\text{SM}}$. Two scenarios are also tested with this combination. The first uses two signal strengths, one for ggF and one for VBF, and the POI is the ratio $\Gamma_H/\Gamma_H^{\text{SM}}$. We require that $\kappa_{g,\text{on-shell}} = \kappa_{g,\text{on-shell}}$ and the equivalent for VBF.[2] Both κ_g and κ_V coupling factors are profiled for this scenario. The second profiles $\kappa_{V,\text{on-shell}} = \kappa_{V,\text{off-shell}}$, and the POI is $R_{gg} = \mu^{gg\to H^*\to VV}_{\text{off-shell}}/\mu^{gg\to H^*\to VV}_{\text{on-shell}}$, which can be interpreted as the ratio of couplings $\kappa^2_{g,\text{off-shell}}/\kappa^2_{g,\text{on-shell}}$. This also assumes $\Gamma_H/\Gamma_H^{\text{SM}} = 1$. Table 6.8 shows the upper limits on the Higgs boson width and ratio of on- and off-shell ggF couplings; the negative log-likelihood and scan over $\mathrm{R}^B_{H^*}$ are shown in Fig. 6.10. The limit on $\Gamma_H/\Gamma_H^{\text{SM}}$ at $\mathrm{R}^B_{H^*} = 1$ translates to an observed (expected) 95 % CL upper limit on the Higgs boson total width of 22.7 (33.0) MeV.

[2] For the purposes of setting an upper limit, the on-shell coupling factors being less than the off-shell coupling factors is a sufficient requirement.

<table>
<tr><th>Process</th><th>$ZZ \to 4\ell$</th><th>$ZZ \to 2\ell 2\nu$</th><th>$WW \to e\nu\mu\nu$</th></tr>
<tr><td>$gg \to H^* \to VV$ (S)</td><td>1.1 ± 0.3</td><td>3.2 ± 1.0</td><td>1.5 ± 0.4</td></tr>
<tr><td>$gg \to VV$ (B)</td><td>2.8 ± 0.8</td><td>5.3 ± 1.6</td><td>3.6 ± 1.1</td></tr>
<tr><td>$\boldsymbol{gg \to (H^* \to)VV}$</td><td>$\mathbf{2.4 \pm 0.7}$</td><td>$\mathbf{3.9 \pm 1.2}$</td><td>$\mathbf{2.4 \pm 1.2}$</td></tr>
<tr><td>$gg \to (H^* \to)VV$ ($\mu_{\text{off-shell}} = 10$)</td><td>$9.2 \pm 2.5$</td><td>$24.0 \pm 7.3$</td><td>$10 \pm 4$</td></tr>
<tr><td>VBF $H^* \to VV$ (S)</td><td>0.12 ± 0.01</td><td>0.48 ± 0.04</td><td>0.42 ± 0.05</td></tr>
<tr><td>VBF VV (B)</td><td>0.71 ± 0.04</td><td>1.2 ± 0.2</td><td>1.6 ± 0.2</td></tr>
<tr><td>VBF $\boldsymbol{(H^* \to)VV}$</td><td>$\mathbf{0.59 \pm 0.03}$</td><td>$\mathbf{0.7 \pm 0.1}$</td><td>$\mathbf{1.1 \pm 0.1}$</td></tr>
<tr><td>VBF $(H^* \to)VV$ ($\mu_{\text{off-shell}} = 10$)</td><td>$1.17 \pm 0.06$</td><td>$2.9 \pm 0.2$</td><td>$2.8 \pm 0.3$</td></tr>
<tr><td>$q\bar{q} \to ZZ$</td><td>21.3 ± 2.1</td><td>31.5 ± 3.5</td><td rowspan="2">2.0 ± 0.2</td></tr>
<tr><td>$q\bar{q} \to WZ$</td><td>-</td><td>10.6 ± 1.4</td></tr>
<tr><td>$q\bar{q} \to WW$</td><td>-</td><td rowspan="3">0.4 ± 0.2</td><td>40 ± 5</td></tr>
<tr><td>$t\bar{t}$, Wt, and $t\bar{b}/tq\bar{b}$</td><td>-</td><td>35 ± 4</td></tr>
<tr><td>$Z \to \tau\tau$</td><td>-</td><td>1.4 ± 0.2</td></tr>
<tr><td>$Z \to ee, \mu\mu$</td><td>-</td><td>3.5 ± 3.0</td><td>-</td></tr>
<tr><td>Other backgrounds</td><td>-</td><td>0.8 ± 0.2</td><td>8.7 ± 1.3</td></tr>
<tr><td>Total Expected (SM)</td><td>24.4 ± 2.2</td><td>51 ± 6</td><td>90 ± 4</td></tr>
<tr><td>Observed</td><td>18</td><td>48</td><td>82</td></tr>
</table>

Table 6.4: Expected and observed numbers of events in the signal region for all final states in the cut-based approaches. For the $ZZ \to 4\ell$ analysis, a mass range of $400 < m_{4\ell} < 1000$ GeV is used. The other backgrounds in the $ZZ \to 4\ell$ final state include contributions from Z+jets and top-quark processes. For the $ZZ \to 2\ell 2\nu$ analysis, the range $380 < m_{\mathrm{T}}^{ZZ} < 1000$ GeV is considered. For the $WW \to e\nu\mu\nu$ analysis, the region $\mathrm{R}_8 > 450$ GeV is used and background event yields are quoted after the likelihood fit was performed. The expected events for the $gg \to (H^* \to)VV$ and VBF $(H^* \to)VV$ processes (ZZ or WW), including the Higgs boson signal, background and interference, are reported for both the SM predictions (in bold) and $\mu_{\text{off-shell}} = 10$. A relative $gg \to VV$ background K-factor of $\mathrm{R}^B_{H^*}$=1 is assumed. The uncertainties in the number of expected events include the statistical uncertainties from MC samples and systematic uncertainties. The entries with a $-$ are for processes with event yields < 0.1 [198].

$R^B_{H^*}$=	Observed 0.5	Observed **1.0**	Observed 2.0	Median expected 0.5	Median expected **1.0**	Median expected 2.0
$ZZ \to 4\ell$ channel	6.1	**7.3**	10.0	9.1	**10.6**	14.8
$ZZ \to 2\ell 2\nu$ channel	9.9	**11.0**	12.8	9.1	**10.6**	13.6
$WW \to e\nu\mu\nu$ channel	15.6	**17.2**	20.3	19.6	**21.3**	24.7

Table 6.5: The observed and expected 95 % CL upper limits on $\mu_{\text{off-shell}}$ for three values of $R^B_{H^*}$ for the three analysis channels. The bold numbers correspond to the limit assuming $R^B_{H^*} = 1$. The upper limits are evaluated using the CL_s method, with the alternative hypothesis $\mu_{\text{off-shell}} = 1$ [198].

$R^B_{H^*}$=	Observed 0.5	Observed **1.0**	Observed 2.0	Median expected 0.5	Median expected **1.0**	Median expected 2.0	Assumption
$\mu_{\text{off-shell}}$	5.1	**6.2**	8.6	6.7	**8.1**	11.0	$\mu^{gg\to H^*}_{\text{off-shell}}/\mu^{VBF}_{\text{off-shell}}$=1
$\mu^{gg\to H^*\to VV}_{\text{off-shell}}$	5.3	**6.7**	9.8	7.3	**9.1**	13.0	$\mu^{\text{VBF}\ H^*\to VV}_{\text{off-shell}}$=1

Table 6.6: Expected and observed upper limits on $\mu_{\text{off-shell}}$ using the combined off-shell channels with $\mu^{\text{VBF}}_{\text{off-shell}} = \mu^{\text{ggF}}_{\text{off-shell}}$ and upper limit on $\mu^{gg\to H^*\to VV}_{\text{off-shell}}$ with $\mu^{\text{VBF}}_{\text{off-shell}} = 1$. The bold numbers correspond to the limit assuming $R^B_{H^*} = 1$. The upper limits are evaluated using the CL_s method, with the alternative hypothesis $\mu_{\text{off-shell}} = 1$ [198].

Systematic uncertainty	95 % CL lim. CL_s on $\mu_{\text{off-shell}}$
Interference $gg \to (H^* \to)VV$	7.2
QCD scale $k^{H^*}(m_{VV})$ (correlated component)	7.1
PDF $q\bar{q} \to VV$ and $gg \to (H^* \to)VV$	6.7
QCD scale $q\bar{q} \to VV$	6.7
Luminosity	6.6
Drell–Yan background	6.6
QCD scale $k^{H^*}_{gg}(m_{VV})$ (uncorrelated component)	6.5
Remaining systematic uncertainties	6.5
All systematic uncertainties	8.1
No systematic uncertainties	6.5

Table 6.7: The expected 95 % CL upper limit on $\mu_{\text{off-shell}}$ in the combined WW and ZZ off-shell analyses. Each row shows the limit with just that uncertainty, except the last two, which show the limit with all and no systematic uncertainties. The upper limits are evaluated using the CL_s method, assuming $R^B_{H^*}$=1. The ratio of the $gg \to H^*$ and VBF processes is assumed to be as expected in the SM [198].

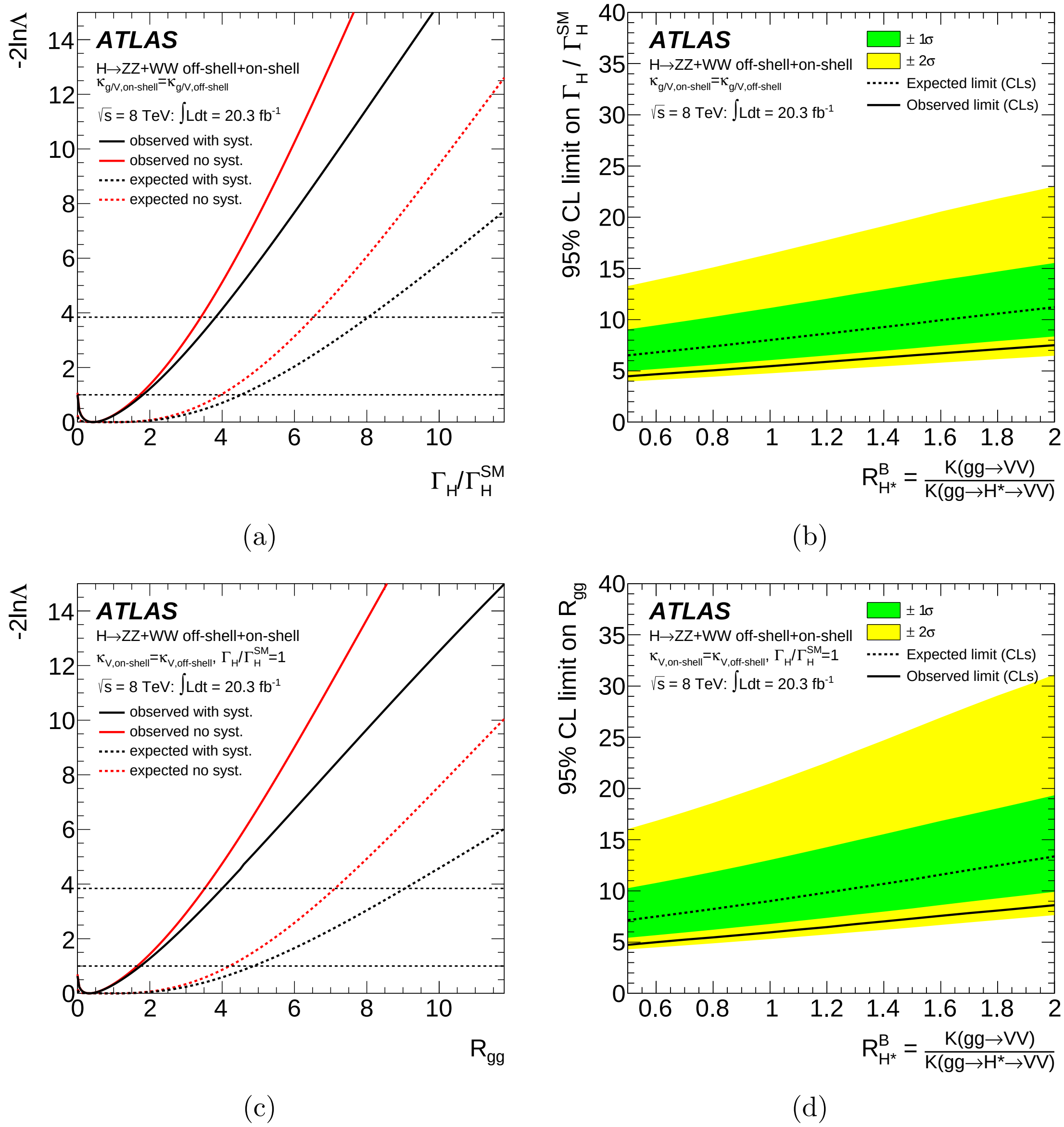

Figure 6.10: From the combined WW and ZZ on- and off-shell analyses, (a) and (b), negative log-likelihood scan and 95 % CL upper limit on $\Gamma_H/\Gamma_H^{\text{SM}}$ respectively. (c) and (d), negative log-likelihood scan and 95 % CL upper limit on R_{gg} respectively [198].

	Observed			Median expected			
$\mathrm{R}^{B}_{H^*}$	0.5	**1.0**	2.0	0.5	**1.0**	2.0	Assumption
$\Gamma_H/\Gamma_H^{\mathrm{SM}}$	4.5	**5.5**	7.5	6.5	**8.0**	11.2	$\kappa_{i,\text{on-shell}} = \kappa_{i,\text{off-shell}}$
$R_{gg} = \kappa^2_{g,\text{off-shell}}/\kappa^2_{g,\text{on-shell}}$	4.7	**6.0**	8.6	7.1	**9.0**	13.4	$\kappa_{V,\text{on-shell}} = \kappa_{V,\text{off-shell}}$, $\Gamma_H/\Gamma_H^{\mathrm{SM}}$=1

Table 6.8: Observed and expected 95% CL upper limits on $\Gamma_H/\Gamma_H^{\mathrm{SM}}$ and R_{gg} for the combined on- and off-shell WW and ZZ analyses [198].

CHAPTER VII

Prospects for the $H \to WW^{(*)} \to \ell\nu\ell\nu$ Analysis at the HL-LHC

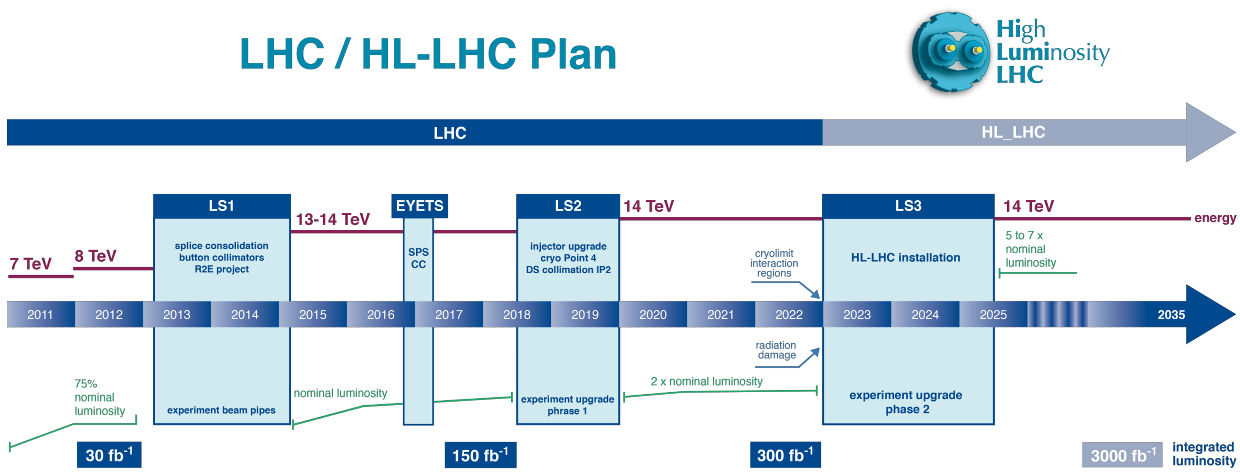

Figure 7.1: Time line for the LHC and HL-LHC [229].

This chapter summarizes projections for the $H \to WW^{(*)} \to \ell\nu\ell\nu$ analysis at the end of the LHC running and for the High Luminosity LHC (HL-LHC) [55], presented as a part of the 2013 European Committee for Future Accelerators (ECFA) Higgs boson projections for ATLAS [230]. The HL-LHC is a proposed upgrade to the LHC in order to run with a higher luminosity, see Table 3.1 for the parameters, such that $3\,\mathrm{ab}^{-1}$ can be collected over a decade, starting in 2025, see Fig. 7.1 for a time line. The important change is a roughly five-fold increase in peak (leveled for the HL-LHC) luminosity over the LHC design, reaching $5 \times 10^{34}\,\mathrm{cm}^{-2}\,\mathrm{s}^{-1}$. Neither the machine nor the experiments are completely defined; the goal of upgrades to the ATLAS detector are to maintain similar performance to the 8 TeV running. Thus, the assumptions that enter these projections are important. Previously, for European

Strategy (ES) studies, the performance was estimated by smearing generator level quantities [231] using the Run I detector with up to $\mu_{\text{pu}} = 69$. Most of the smearing functions have been updated based on full simulation of the Phase-I[1] detector with up to $\mu_{\text{pu}} = 80$ and Phase-II detector with $\mu_{\text{pu}} = 80, 140,$ and 200 [232]. The increase in center-of-mass energy from 8 TeV to 14 TeV increases the cross section of processes, more so for heavy processes. Figure 7.2 shows the ratio of parton luminosities, giving an estimate of the cross section increase. The main concern for the experiments is the high average number of expected inelastic collisions per bunch crossing of $\mu_{\text{pu}} = 140$ for the HL-LHC peak luminosity. These prospects also consider the 300 fb^{-1} to be collected by the LHC by the end of 2022 with $\mu_{\text{pu}} = 50$–60.

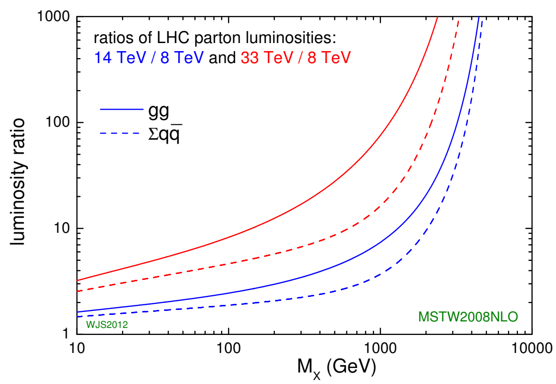

Figure 7.2: Ratio of parton luminosities at the LHC for 8, 14, and 33 TeV [233]. The cross section to produce a resonance or system of mass M_x at higher energies will increase by the parton luminosity ratio.

7.1 Analysis

The $H \to WW^{(*)}$ prospects are based on the Moriond 2013 analysis [142] (referred to as the baseline analysis), which preceded the analysis described in Chapter V. It resulted in an expected significance of 3.7 s.d. and measured signal strength of $\mu = 1.01 \pm 0.31$—this is the baseline to which projections should be compared against.

Only the $e\mu$ $N_{\text{jets}} \leq 1$ and $e\mu$ $N_{\text{jets}} \geq 2$ VBF channels are included in the projections. Prospects for this analysis differ from most of the others in that they are based on fully reconstructed 8 TeV MC, rather than 14 TeV generator level MC. This allows us to use all of the MC available from the 8 TeV analysis and the samples have more generated events. The extrapolation to 14 TeV is performed by reweighting the PDF and emulating performance differences. Table 7.1 summarizes the MC processes used, as well as the 14 TeV cross sections.

[1]Phase-I and II refer to planned upgrades to the detector, see Fig. 7.1

Cross sections at 14 TeV had not yet been computed for all processes, in such cases the scaling from similar processes was applied: $W\gamma$ (2.2), tW (3.7), $t\bar{b}$ (2.2), $tq\bar{b}$ (2.9), and 2.7 for EW diboson processes. The top-quark background is a particular concern at 14 TeV, increasing in cross section by a factor of 4.1, compared to ~ 2.7 for the signal and 2.2 for the quark-initiated WW background. For $W+$jets, the prediction is from a similar data-driven technique [142] as described in Section 5.5.4, with a dijet fake-factor and no explicit separate multijet estimate; it is scaled by 1.81, the inclusive $W+$jets cross section increase from 8 to 14 TeV.

Process	MC generator	$\sigma \cdot \mathcal{B}$ (pb)	σ Ratio 14/8 TeV
	Signal		
ggF $H \to WW^{(*)}$	POWHEG+PYTHIA8	1.2	2.7
VBF $H \to WW^{(*)}$	POWHEG+PYTHIA8	0.10	2.7
VH $H \to WW^{(*)}$	PYTHIA8	0.056	2.3
	Background		
$gg \to WW$	GG2WW3.1.2[234]+HERWIG	0.49	2.3
$gg \to ZZ$	GG2ZZ2.0[177]+HERWIG	0.055	16.5
$q\bar{q} \to WW$ and $qg \to WW$	POWHEG+PYTHIA6	12	2.2
$t\bar{t}$	MC@NLO+HERWIG	978	4.1
Wt, $t\bar{b}$	MC@NLO+HERWIG	96	3.4, 2
$tq\bar{b}$	ACERMC+PYTHIA6	258	2.7
Z/γ^*, inclusive	ALPGEN+HERWIG	29666	2.2
VBS $Z^{(*)} \to \ell\ell + 2j$	SHERPA	3.2	2.7
$Z^{(*)}Z^{(*)} \to 4\ell\,/\,2\ell\,2\nu\,, m_{\ell\ell} \geq 4$ GeV	POWHEG+PYTHIA8	2.6	2.2
VBS $Z^{(*)}Z^{(*)} \to 4\ell\,/\,2\ell\,2\nu + 2j$	SHERPA	0.0054	2.7
$WZ/W\gamma^*$	POWHEG+PYTHIA8	5.0	2.2
VBS $WZ \to 3\ell\nu + 2j$	SHERPA	0.034	2.7
$W\gamma^*, m_{\gamma^*} \leq 7$ GeV	SHERPA	17.6	2.2
$W\gamma$	ALPGEN+HERWIG	705	2.2
VBS $WW \to 2\ell\,2\nu + 2j$	SHERPA	0.107	2.7

Table 7.1: MC generators used to model the signal and background processes. The decays of W and Z bosons are included in the product of the cross section (σ) and branching fraction ($\mathcal{B}$) at 14 TeV. For the VH process, $\sigma \cdot \mathcal{B}$ only includes only leptonic decays. For single top processes, inclusive cross sections are quoted. The last column indicates the scaling of the cross section from 8 to 14 TeV.

The analysis follows a similar object and event selection as used in Ref. [142], which itself is not so different from what is used in Chapter V. Lepton identification and reconstruction is

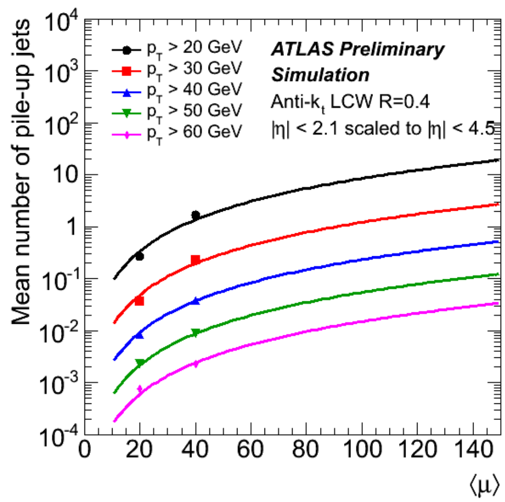

Figure 7.3: Mean pile-up jet multiplicity as a function of μ_{pu} for various jet p_{T} thresholds [231].

kept the same as the baseline analysis, because we expect an upgraded detector and refined techniques to keep current performance—the goal of the upgrades. The key differences are requiring $p_{\text{T}} > 25\,(15)$ GeV for the leading (sub-leading) leptons and using anti-k_{t} $R = 0.4$ jets with $p_{\text{T}} > 30\,(35)$ GeV in the central and forward regions for the $\mu_{\text{pu}} = 50\,(140)$ scenario. A track confirmation of jets, i.e., use of JVF, is applied in the central region [231] to reduce selected pile-up jets, exact requirements are presented in Section 7.2. The jet p_{T} threshold is increased to 45 GeV for the VBF channel in order to mitigate pile-up jets outside of the tracking acceptance. The increase in required jet p_{T} helps mitigate the number of pile-up jets selected, as seen in Fig. 7.3. A jet-corrected $p_{\text{T}}^{\text{miss}}$ is used, as it performs better in the high-pile up environment, compared to the calorimeter based $E_{\text{T}}^{\text{miss}}$ used in the baseline analysis. The top-quark background is reduced by rejecting b-tagged jets with $p_{\text{T}} > 20\,(25)$ GeV for the $\mu_{\text{pu}} = 50\,(140)$ scenario. The MV1 algorithm [125] with an 85 % efficiency working point is used. Table 7.2 summarizes the event selection.

7.2 Performance assumptions

In order to keep the lepton p_{T} thresholds, the use of the dilepton triggers is required, which were not used in the baseline analysis; the loss in triggering efficiency was found to be

Category	$N_{\mathrm{jets}} = 0$	$N_{\mathrm{jets}} = 1$	$N_{\mathrm{jets}} \leq 2$ VBF
Preselection	All N_{jets}: Isolated $e\mu$ pair with opposite charge		
	$p_{\mathrm{T}} > 25$ for the leading lepton ℓ_1		
	$p_{\mathrm{T}}^{\mathrm{sub}} > 15$ for the subleading lepton ℓ_2		
	$m_{\ell\ell} > 10$ for the $e\mu$ sample		
	$p_{\mathrm{T,rel}}^{\mathrm{miss}} > 25$	$p_{\mathrm{T,rel}}^{\mathrm{miss}} > 25$	$p_{\mathrm{T}}^{\mathrm{miss}} > 20$
General selection	-	$N_{b\text{-jets}} = 0$	$N_{b\text{-jets}} = 0$
	$\Delta\phi(\boldsymbol{p}_{\mathrm{T}}^{\ell\ell}, \boldsymbol{p}_{\mathrm{T}}^{\mathrm{miss}}) > \pi/2$	-	$p_{\mathrm{T}}^{\mathrm{tot}} < 20$
	$p_{\mathrm{T}}^{\ell\ell} > 30$	$m_{\tau\tau} < m_Z - 25$	$m_{\tau\tau} < m_Z - 25$
VBF topology	-	-	$\lvert\eta_j\rvert > 2.0$, opposite hemisphere
	-	-	CJV
	-	-	OLV
	-	-	$m_{jj} > 1250$
$H \to WW^{(*)} \to \ell\nu\ell\nu$ decay topology	$m_{\ell\ell} < 50$	$m_{\ell\ell} < 50$	$m_{\ell\ell} < 60$
	$\Delta\phi_{\ell\ell} < 1.8$	$\Delta\phi_{\ell\ell} < 1.8$	$\Delta\phi_{\ell\ell} < 1.8$

Table 7.2: Summary of event selection. Central jet veto (CJV) in this case means no jet with $p_{\mathrm{T}} > 30\,\mathrm{GeV}$ between the tag jets. Outside lepton veto (OLV) in this case means no leptons between the tag jets. A dash (-) indicates no selection. Momentum, mass, and MET quantities are in GeV.

6 %, which is emulated in the analysis.

Reconstructed jets are smeared to match the η-dependent truth-jet-smearing parametrization used for ES studies [231]. Figure 7.4 shows the validation of this, comparing smeared reconstructed jets using a derived smearing, to smeared truth jets. With the raised jet p_{T} thresholds, each event has an average of $\sim 0.3\,(0.8)$ pile-up jets for the $\mu_{\mathrm{pu}} = 50\,(140)$ scenario. Jet vertex fraction (JVF) requirements are used to replicate jet track confirmation. On top of the baseline requirement of $|\mathrm{JVF}| > 0.5$ for jets with $p_{\mathrm{T}} < 50\,\mathrm{GeV}$, jets with $50 < p_{\mathrm{T}} < 80\,\mathrm{GeV}$ are required to have $|\mathrm{JVF}| > 0.1$. This requirement removes about 95 % of the pile-up jets. Additional pile-up jets are inserted into the 8 TeV MC samples according to these rates with their p_{T} and η taken from pile-up jets in a $\mu_{\mathrm{pu}} = 80$ simulated sample, see Fig. 7.5 for the input distributions. Figure 7.6 shows the resulting pile-up jet kinematics in a Higgs boson signal sample, highlighting the large expected pile-up contamination outside of the current tracking acceptance.

For the 85 % efficiency b-tagging working point, pile-up jets were found to be mistagged as b-jets with a probability of 20 % in a $Z \to \ell\ell + \mathrm{jets}$ $\mu_{\mathrm{pu}} = 80$ sample. With the JVF

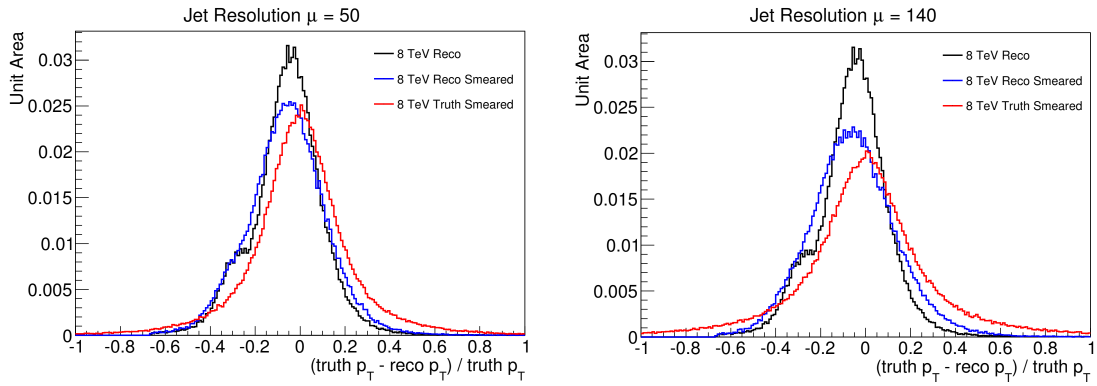

(a) (b)

Figure 7.4: Reconstructed jet p_{T} resolution (black), smeared truth jet p_{T} resolution (red), and smeared reconstructed jet p_{T} resolution (blue) in the $|\eta| < 0.8$ region with an 8 TeV sample for smearing to match (a) $\mu_{\mathrm{pu}} = 50$ and (b) $\mu_{\mathrm{pu}} = 140$ conditions.

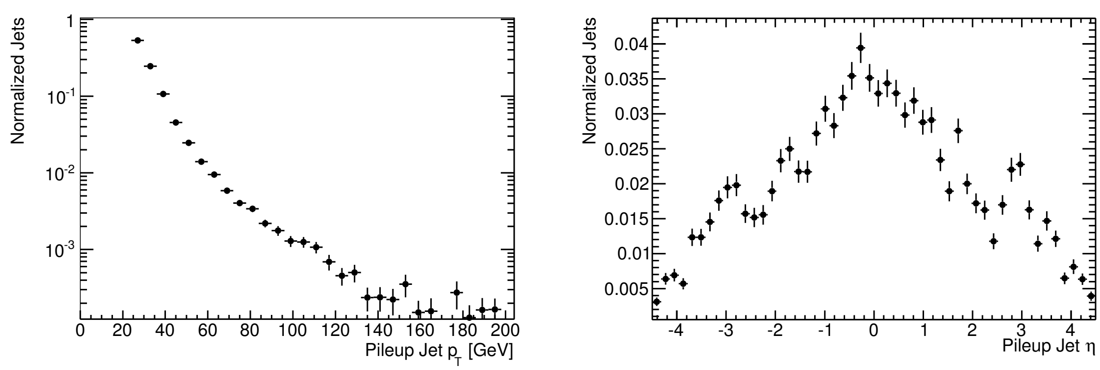

(a) (b)

Figure 7.5: Pile-up jet (a) p_{T} and (b) η as taken from a $Z \to \ell\ell + \mathrm{jets}$ sample with $\mu_{\mathrm{pu}} = 80$ without any JVF requirements.

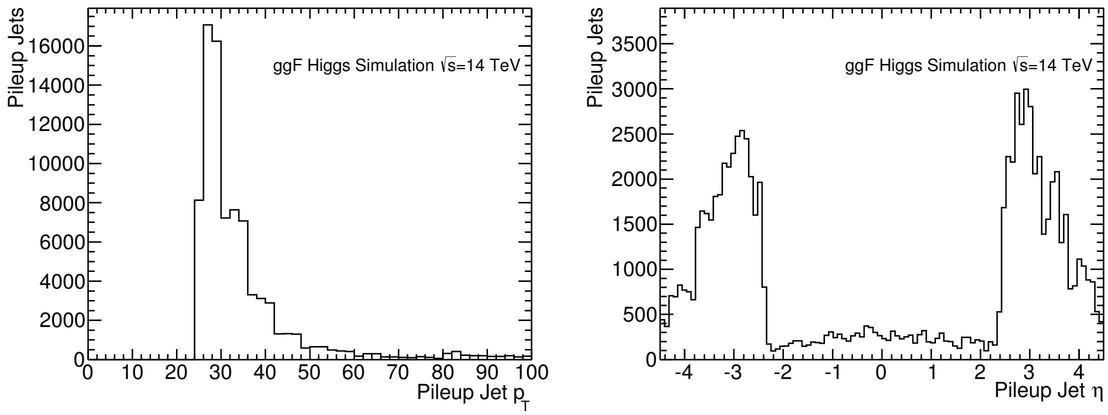

(a) (b)

Figure 7.6: Pile-up jet (a) p_T and (b) η in a $m_H = 125\,\text{GeV}$ Higgs boson signal sample for the $\mu_{\text{pu}} = 140$ scenario after the p_T^{miss} requirements.

requirement, this is reduced to 1 % in the central region.

Jet-corrected p_T^{miss} is used for MET as its mean and resolution were found to be more stable against μ_{pu} than the calorimeter based MET. A resolution smearing, derived in a high pile-up Z boson sample, of 33 MeV per unit of μ_{pu} in the MC is applied to the soft term. Figure 7.7 shows the performance of the smeared p_T^{miss} for the 8 TeV conditions and the two μ_{pu} rates considered.

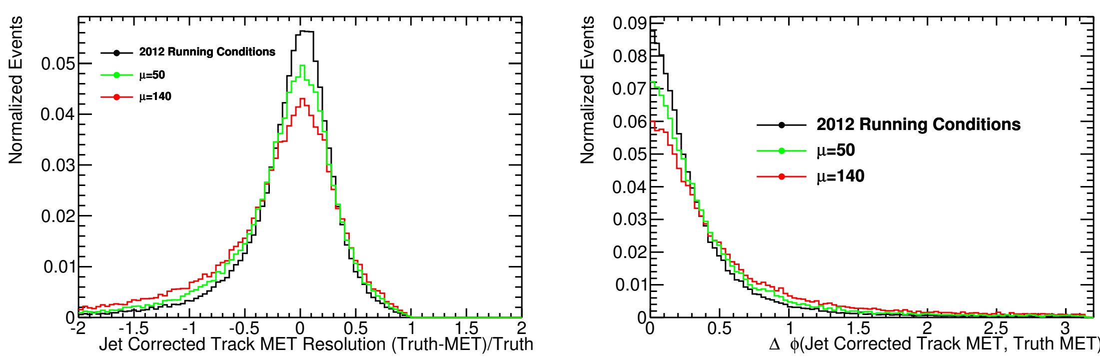

(a) (b)

Figure 7.7: p_T^{miss} (a) energy resolution and (b) ϕ resolution for a ggF Higgs boson signal sample with various running conditions.

7.3 Systematic uncertainties

Two scenarios of signal theoretical uncertainties are tested: using the 8 TeV uncertainties as in Ref. [142], see Table 7.3, and reducing these uncertainties by half. The current uncertainties are a worst case scenario, with no improvement in the calculations, while the reduced uncertainties represent a significant improvement, but still includes the effects of theory uncertainties. This allows us to test the impact of the signal uncertainties, which become more and more dominant with increasing integrated luminosity. The results from combining Higgs analysis channels in Section 7.4 are presented with and without the full 8 TeV theory uncertainties.

	$N_{\text{jets}} = 0$	$N_{\text{jets}} = 1$	$N_{\text{jets}} \geq 2$
ggF QCD scale	17	37	43
ggF QCD acceptance	4	4	4
ggF PDF	8	8	8
ggF UE/PS	3	10	9
ggF Total	19	39	44
VBF QCD scale	1	1	1
VBF QCD acceptance	4	4	4
VBF PDF	3	3	3
VBF UE/PS	3	10	3
VBF Total	6	11	6

Table 7.3: Theoretical uncertainties on the signal (in %) used for the $H \to WW^{(*)} \to \ell\nu\ell\nu$ projections [230].

The dominant experimental systematic uncertainties, such as JES and b-tagging efficiencies, are expected to decrease with the increasing size of the dataset because we will have a better understanding of the detector and reduced statistical uncertainties on data-driven corrections. With the large sample, we will also be able to use more CRs (with large sample sizes) and data-driven estimates. Table 7.4 lists the total systematic uncertainty per background process assumed, as compared to the baseline analysis. Uncertainties on the backgrounds are treated as uncorrelated across jet bins. The significant reduction in VV uncertainties assumes the use of a high sample-size same-charge (SC) CR, as well as possibly promoting the validation regions (VRs) to CRs. Shape uncertainties from the baseline analysis on the WW m_{T} distribution are included at half-size. A 3 % uncertainty on the luminosity is applied.

	$N_{\rm jets}=0$		$N_{\rm jets}=1$		$N_{\rm jets}\geq 2$	
	14 TeV	8 TeV	14 TeV	8 TeV	14 TeV	8 TeV
WW	$1.5 = 1 \oplus 1$	5	$5 = 5 \oplus 1$	6.5	$10 = 9 \oplus 5$	30
VV	2	15	5	20	10	20
$t\bar{t}$	$7 = 5 \oplus 5$	12	$8 = 7 \oplus 5$	23	$10 = 8 \oplus 8$	33
$tW/tb/tqb$	$7 = 5 \oplus 5$	12	$8 = 7 \oplus 5$	23	$10 = 8 \oplus 8$	33
Z+jets	10	15	10	18	10	20
W+jets	20	30	20	30	20	30

Table 7.4: The total systematic uncertainty (in %) for the background processes. The uncertainties on the WW and top-quark backgrounds are broken down into their (theoretical) $\oplus$ (experimental) assumed components. Also shown are the uncertainties used in the baseline 8 TeV analysis [230].

7.4 Results

The results are obtained for two running scenarios: 300 fb^{-1} with $\mu_{\rm pu}=50$ and 3 ab^{-1} with $\mu_{\rm pu}=140$. Tables 7.5 and 7.6 show the expected yields for the 300 fb^{-1} and 3 ab^{-1} scenarios respectively, and with the requirements $0.75\times m_H < m_{\rm T} < m_H$ for $N_{\rm jets}\leq 1$ and $m_{\rm T} < 1.07\times m_H$ for $N_{\rm jets}\geq 2$, which select high signal to background regions. There is a decrease in signal-to-background ratio in the 3 ab^{-1} analysis, compared to 300 fb^{-1}, particularly in the VBF channel, due to the increased pile-up. The $m_{\rm T}$ distributions for the $N_{\rm jets}\leq 1$ categories for both scenarios are shown in Figs. 7.8 and 7.9 and in Fig. 7.10 for the VBF channel—a smoothing algorithm has been applied to each process individually.

$N_{\rm jets}$	$N_{\rm bkg}$	$N_{\rm signal}$	$N_{\rm ggF}$	$N_{\rm VBF}$	N_{WW}	N_{VV}	$N_{t\bar{t}}$	N_t	$N_{\rm Z+jets}$	$N_{\rm W+jets}$
$=0$	34330	4380	4300	80	19000	3500	6000	2600	370	2860
$=1$	21460	1970	1740	230	5760	1800	9360	2850	710	980
≥ 2	101	62	5	57	12	4	60	5	12	8
With $m_{\rm T}$ requirement										
$=0$	14960	2950	2910	40	8800	1390	1880	800	270	1820
$=1$	6305	1030	910	120	1820	710	2520	735	50	470
≥ 2	51	56	4	52	6	1	20	4	12	8

Table 7.5: The signal and background event yields expected at 14 TeV, with $\mu=50$ and 300 fb^{-1}, before and after an $m_{\rm T}$ requirement [230].

Results are obtained with a fit to the $m_{\rm T}$ spectrum, splitting the SRs in $m_{\ell\ell}$ at 30 GeV. Uncertainties due to limited MC sample size are neglected. Table 7.7 summarizes the expected precision on the signal strength for the two luminosity scenarios and two signal

N_{jets}	N_{bkg}	N_{signal}	N_{ggF}	N_{VBF}	N_{WW}	N_{VV}	$N_{t\bar{t}}$	N_t	$N_{\text{Z+jets}}$	$N_{\text{W+jets}}$
$= 0$	366450	41840	40850	990	172950	32000	96600	32150	4150	28600
$= 1$	259610	22375	20050	2325	68810	21570	119560	28110	11200	10360
≥ 2	1825	590	90	500	300	120	745	245	335	80
With m_{T} requirement										
$= 0$	147080	26355	25890	470	77710	13640	26900	9790	810	18230
$= 1$	72010	9540	8660	880	20090	7210	30770	6800	2120	5020
≥ 2	995	503	67	436	110	65	365	40	335	80

Table 7.6: The signal and background event yields expected at 14 TeV, with $\mu = 140$ and $3\,\text{ab}^{-1}$, before and after an m_{T} requirement [230].

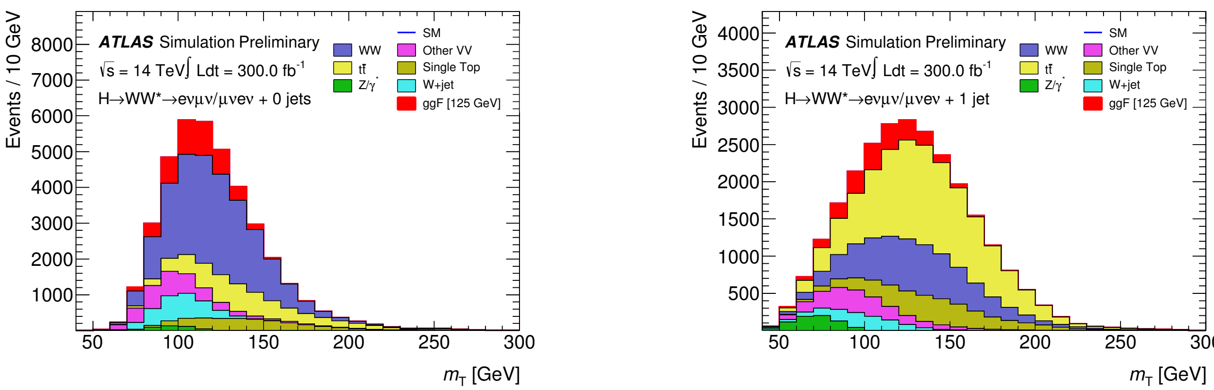

(a) (b)

Figure 7.8: The m_{T} distributions after all the selection cuts, but before the final m_{T} window cut (a) in the $N_{\text{jets}} = 0$ and (b) $N_{\text{jets}} = 1$ final states for $\mu_{\text{pu}} = 50$ with $300\,\text{fb}^{-1}$ of total integrated luminosity [230].

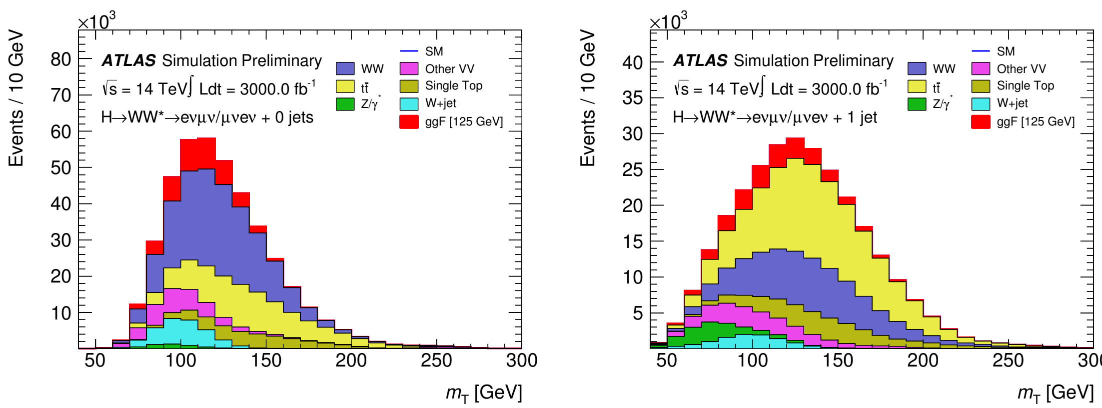

(a) (b)

Figure 7.9: The m_{T} distributions after all the selection cuts, but before the final m_{T} window cut (a) in the $N_{\text{jets}} = 0$ and (b) the $N_{\text{jets}} = 1$ final states for $\mu_{\text{pu}} = 140$ with $3000\,\text{fb}^{-1}$ of total integrated luminosity [230].

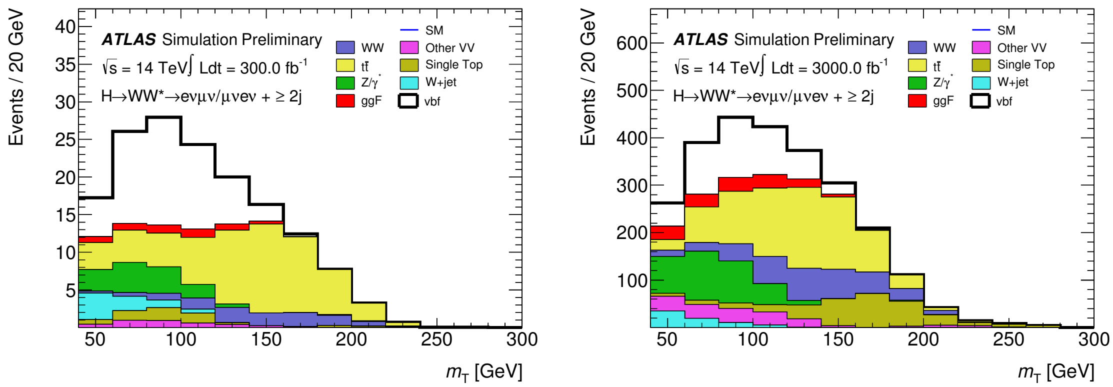

(a) (b)

Figure 7.10: The m_{T} distribution after all the selection cuts, but before the final m_{T} cut in the $N_{\mathrm{jets}} = 2$ final state for (a) $\mu_{\mathrm{pu}} = 50$ with $300\,\mathrm{fb}^{-1}$ of total integrated luminosity and (b) $\mu_{\mathrm{pu}} = 140$ with $3000\,\mathrm{fb}^{-1}$ of total integrated luminosity [230].

theory uncertainty assumptions (full baseline uncertainties and half). A precision of order 10 % on the signal strength is found with the full $3\,\mathrm{ab}^{-1}$, comparable to the other main Higgs boson channels, see Table 7.8. The analysis becomes systematically limited, not improving much between 300 and $3000\,\mathrm{fb}^{-1}$, except for the VBF channel which greatly benefits from the large sample size.

The $H \to WW^{(*)}$ channel is included in an updated combination of Higgs boson prospects [235]. Table 7.8 lists the relative uncertainty on the signal strengths for each channel from the combined fit, also shown in Fig. 7.11. The relative uncertainty on the signal strength per production mode is summarized in Table 7.9. Processes with relative errors less than 20 % are projected to reach discovery level sensitivity, as $Z_0 \approx 1/\Delta\mu$.

The actual outcome will depend on many things, the amount of data collected, theoretical uncertainties, detector performance, existence of the HL-LHC, etc. Much can happen between now and 2035, as evidenced by the 1999 ATLAS performance expectation [39] for $H \to WW^{(*)} \to \ell\nu\ell\nu$ of 4.7 s.d. sensitivity at $m_H = 150\,\mathrm{GeV}$ with $30\,\mathrm{fb}^{-1}$ collected at 14 TeV. Both the center-of-mass energy and branching ratio at $m_H = 150\,\mathrm{GeV}$ would increase the $H \to WW^{(*)}$ channel expected signal yield, yet the Run I analysis has already achieved an expected sensitivity of 5.8 s.d.

Scenario	μ_{ggF}	μ_{VBF}	μ
	8 TeV Signal Theory Unc.		
$300\,\text{fb}^{-1}$	$1^{+0.18}_{-0.15}$	$1^{+0.25}_{-0.22}$	$1^{+0.14}_{-0.13}$
$3000\,\text{fb}^{-1}$	$1^{+0.16}_{-0.14}$	$1^{+0.15}_{-0.15}$	$1^{+0.10}_{-0.09}$
	One-half 8 TeV Signal Theory Unc.		
$300\,\text{fb}^{-1}$	$1^{+0.12}_{-0.11}$	$1^{+0.24}_{-0.21}$	$1^{+0.11}_{-0.10}$
$3000\,\text{fb}^{-1}$	$1^{+0.10}_{-0.09}$	$1^{+0.13}_{-0.12}$	$1^{+0.07}_{-0.07}$

Table 7.7: Projected precision on the signal strength for $H \to WW^{(*)} \to \ell\nu\ell\nu$, and split by production mode, for the $300\,\text{fb}^{-1}$ with $\mu_{\text{pu}} = 50$ and $3000\,\text{fb}^{-1}$ with $\mu_{\text{pu}} = 140$ scenarios. The top section uses the signal theory uncertainties from the baseline analysis, and the bottom uses those uncertainties halved.

$\Delta\mu/\mu$	$300\,\text{fb}^{-1}$		$3000\,\text{fb}^{-1}$	
	All unc.	No theory unc.	All unc.	No theory unc.
$H \to \gamma\gamma$ (comb.)	0.13	0.09	0.09	0.04
(0j)	0.19	0.12	0.16	0.05
(1j)	0.27	0.14	0.23	0.05
(VBF-like)	0.47	0.43	0.22	0.15
(WH-like)	0.48	0.48	0.19	0.17
(ZH-like)	0.85	0.85	0.28	0.27
(ttH-like)	0.38	0.36	0.17	0.12
$H \to ZZ$ (comb.)	0.11	0.07	0.09	0.04
(VH-like)	0.35	0.34	0.13	0.12
(ttH-like)	0.49	0.48	0.20	0.16
(VBF-like)	0.36	0.33	0.21	0.16
(ggF-like)	0.12	0.07	0.11	0.04
$H \to WW$ (comb.)	0.13	0.08	0.11	0.05
(0j)	0.18	0.09	0.16	0.05
(1j)	0.30	0.18	0.26	0.10
(VBF-like)	0.21	0.20	0.15	0.09
$H \to Z\gamma$ (incl.)	0.46	0.44	0.30	0.27
$H \to b\bar{b}$ (comb.)	0.26	0.26	0.14	0.12
(WH-like)	0.57	0.56	0.37	0.36
(ZH-like)	0.29	0.29	0.14	0.13
$H \to \tau\tau$ (VBF-like)	0.21	0.18	0.19	0.15
$H \to \mu\mu$ (comb.)	0.39	0.38	0.16	0.12
(incl.)	0.47	0.45	0.18	0.14
(ttH-like)	0.74	0.72	0.27	0.23

Table 7.8: Relative uncertainty on the signal strength in various decay channels for a SM Higgs boson with $m_H = 125\,\text{GeV}$, with and without current signal theory uncertainties. The uncertainties are slightly different than in Table 7.7 because the theory uncertainties are updated [235].

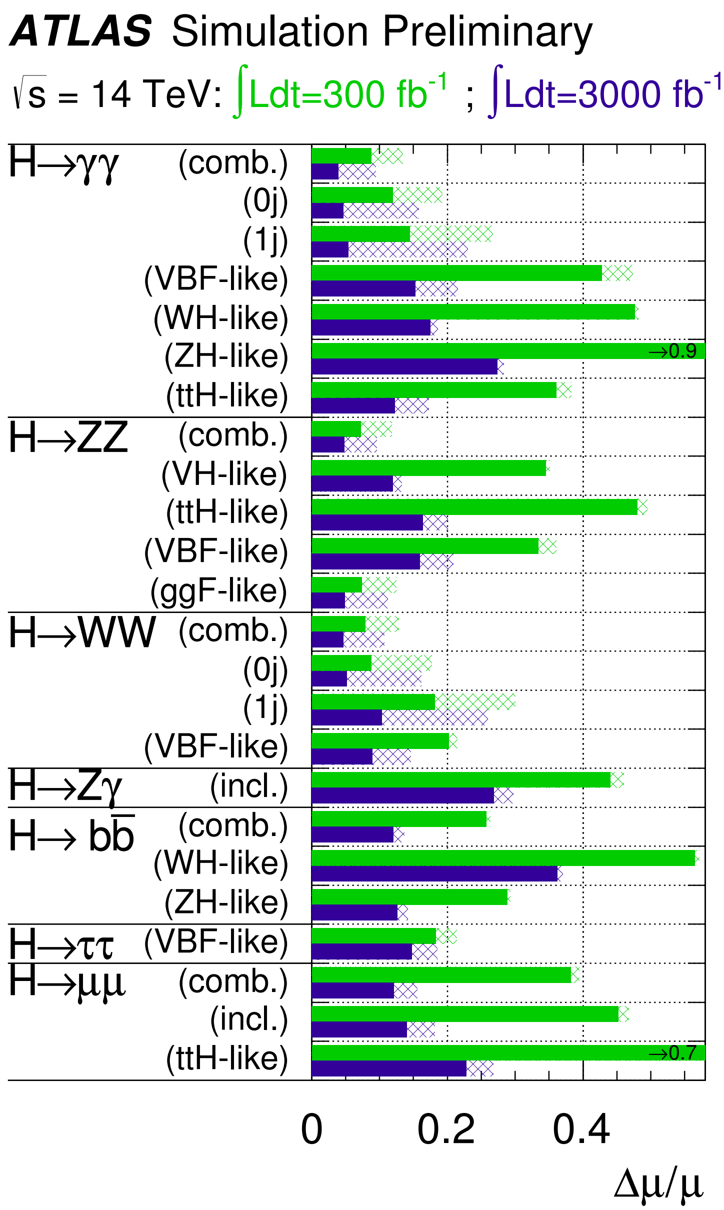

Figure 7.11: Relative uncertainty on the signal strength in various decay channels for a SM Higgs boson with $m_H = 125\,\text{GeV}$. The uncertainties are on the measurement in each channel, not the process. The hashed area indicates the uncertainty due to current signal theory uncertainties [235].

$\Delta\mu/\mu$	$300\,\mathrm{fb}^{-1}$		$3000\,\mathrm{fb}^{-1}$	
	All unc.	No theory unc.	All unc.	No theory unc.
ggF	0.12	0.06	0.11	0.04
VBF	0.18	0.15	0.15	0.09
WH	0.41	0.41	0.18	0.18
$qqZH$	0.80	0.79	0.28	0.27
$ggZH$	3.71	3.62	1.47	1.38
ttH	0.32	0.30	0.16	0.10

Table 7.9: Relative uncertainty on the signal strength for different production modes from a combination of the channels in Fig. 7.11, with and without current signal theory uncertainties [235].

CHAPTER VIII

Conclusion

After the discovery of the Higgs boson, efforts have been focused on measuring its properties. This dissertation has described on- and off-shell analyses of data from the ATLAS detector at the LHC using the $H \to WW^{(*)} \to \ell\nu\ell\nu$ channel. Up to $4.5\,\mathrm{fb}^{-1}$ of data collected at center-of-mass energy 7 TeV and $20.3\,\mathrm{fb}^{-1}$ at 8 TeV are used. Prospects for the on-shell analysis at the HL-LHC have also been presented.

An excess in data over the background only expectation is observed at 6.1 standard deviations, corresponding to a signal rate relative to the expectation for an SM Higgs boson with $m_H = 125.36\,\mathrm{GeV}$ of $\mu = 1.09^{+0.23}_{-0.21}$. The signal strengths for ggF and VBF production are measured to be:

$$\begin{aligned} \mu_{\mathrm{ggF}} &= 1.02^{+0.29}_{-0.26} \\ \mu_{\mathrm{VBF}} &= 1.27^{+0.53}_{-0.45}\,. \end{aligned}$$

With these, the ratio of $\mu_{\mathrm{VBF}}/\mu_{\mathrm{ggF}}$ is used to test for the presence of VBF production, resulting in evidence at the 3.2 standard deviation level. The measured signal strengths are also interpreted as measurements of Higgs boson couplings to fermions and bosons as well as total and fiducial cross section times branching ratios. All of the results are within one standard deviation of the SM expectation. The measurement of a signal strength compatible with the SM indicates that the W boson obtains it's mass through interactions with the Higgs field. This is a firm test of electroweak symmetry breaking (EWSB) in the SM.

Off-shell Higgs boson production is probed in a high-mass region. Assuming a background k-factor equal to that of the Higgs boson signal, an observed (expected) 95 % confidence level (CL) upper limit is set on the off-shell Higgs boson signal strength of 17.2 (21.3). Combining the off- and on-shell measurements of the $H \to WW^{(*)} \to \ell\nu\ell\nu$ and $H \to ZZ$ channels, this is interpreted as an observed (expected) 95 % CL upper limit on the Higgs boson total decay width of 22.7 (33.0) MeV with the assumption that the relevant Higgs boson couplings are independent of the production energy scale.

Prospects for the $H \to WW^{(*)} \to \ell\nu\ell\nu$ channel are computed for $300\,\mathrm{fb}^{-1}$ at the end of the LHC running and $3\,\mathrm{ab}^{-1}$ at the end of the HL-LHC program. With the full $3\,\mathrm{ab}^{-1}$ and current signal theory uncertainties, the analysis is projected to have uncertainties on the signal strength at the level of 10 %, equal in performance to the other main Higgs boson analyses.

At this time, the LHC is preparing to provide pp collisions at 13 TeV. The SM, including the Higgs boson, will be "rediscovered" at 13 TeV, but much of the anticipation for the next run lies in the extended reach for beyond the Standard Model (BSM) searches due to the increased energy available to produce new particles, and eventual increased integrated luminosity. The next couple years will be quite enlightening as to whether anything new will be discovered at the LHC, whether more quickly through direct observation, as for the Higgs boson, or by exploiting large data samples to look for perturbations from SM expectations, e.g., with Higgs boson couplings. Whatever lies ahead, the $H \to WW^{(*)} \to \ell\nu\ell\nu$ analysis will continue to provide more and more precise measurements of the Higgs boson's properties.

APPENDICES

APPENDIX A

MDT Front-end Electronics Drops

During data taking at 7 and 8 TeV, MDT chambers were observed to occasionally drop from data acquisition. Usually, this was resolved by resetting the front-end electronics or chamber service module (CSM). This resulted in dead-time and a loss of acceptance. Understanding the source of drops may lead to preventative solutions. The 2012 data taking period is used to investigate the cause of MDT chamber drops.

It is possible for radiation from the *pp* collisions to pass through the field-programmable gate array (FPGA) in the CSM and flip a bit in the memory—a single-bit upset. Such upsets could lead to the CSM misbehaving and dropping from data acquisition. To investigate this, MDT chamber drop information is correlated with run information, such as luminosity per lumiblock. Several 'hot'[1] chambers are removed from consideration as they have other known issues; the top ten most dropped chambers, Fig. A.1, and similarly for mezzanine cards[2], were removed for the rest of the investigation. Mezzanine card drops are counted per chamber and weighted by the number of cards which were dropped.

To further remove drops from problematic chambers or outside of data taking conditions, chamber drops are ignored if within five minutes of a previous drop, and drops are only counted if during stable beams and the run has at least $1\,\mathrm{pb}^{-1}$. This selects 2089 out of 3082 chamber drops.

Two pieces of evidence indicate some of the drops are from bit upsets. First, there is a trend toward more drops per chamber closer to the beamline in the end-caps, where there is a higher flux, see Fig. A.4. Second, midway through the data taking period, an automatic joint test action group (JTAG) initialization of the MDT chambers at the beginning of runs

[1] Chambers which are outliers in their drop rate.

[2] A mezzanine card performs the basic readout of the MDTs. It contains three Amplifier/Shaper/Discriminator chips, each serving eight tubes, which are routed into a Time-to-Digital Converter. The CSM controls up to 18 mezzanine cards.

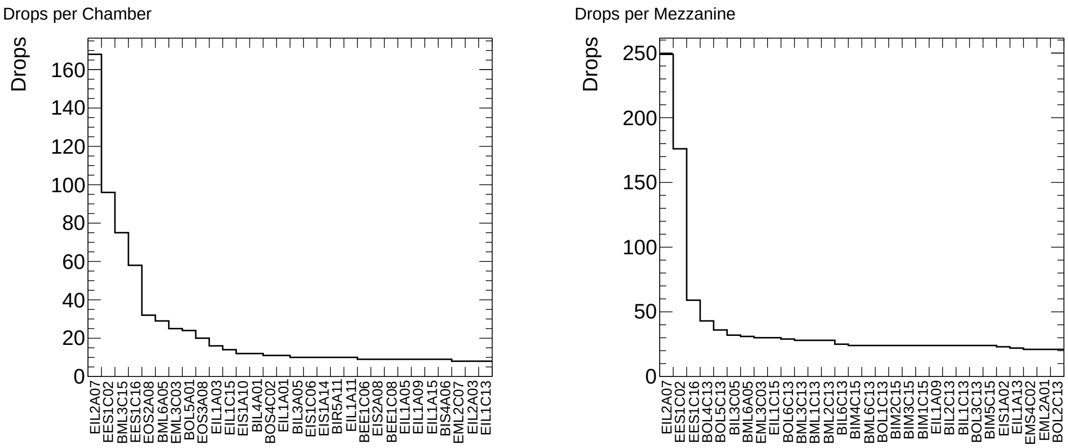

(a) (b)

Figure A.1: (a) MDT chamber drops and (b) mezzanine card drops summed per chamber for the 2012 runs. The labels correspond to chambers, with naming as in Fig. 3.9.

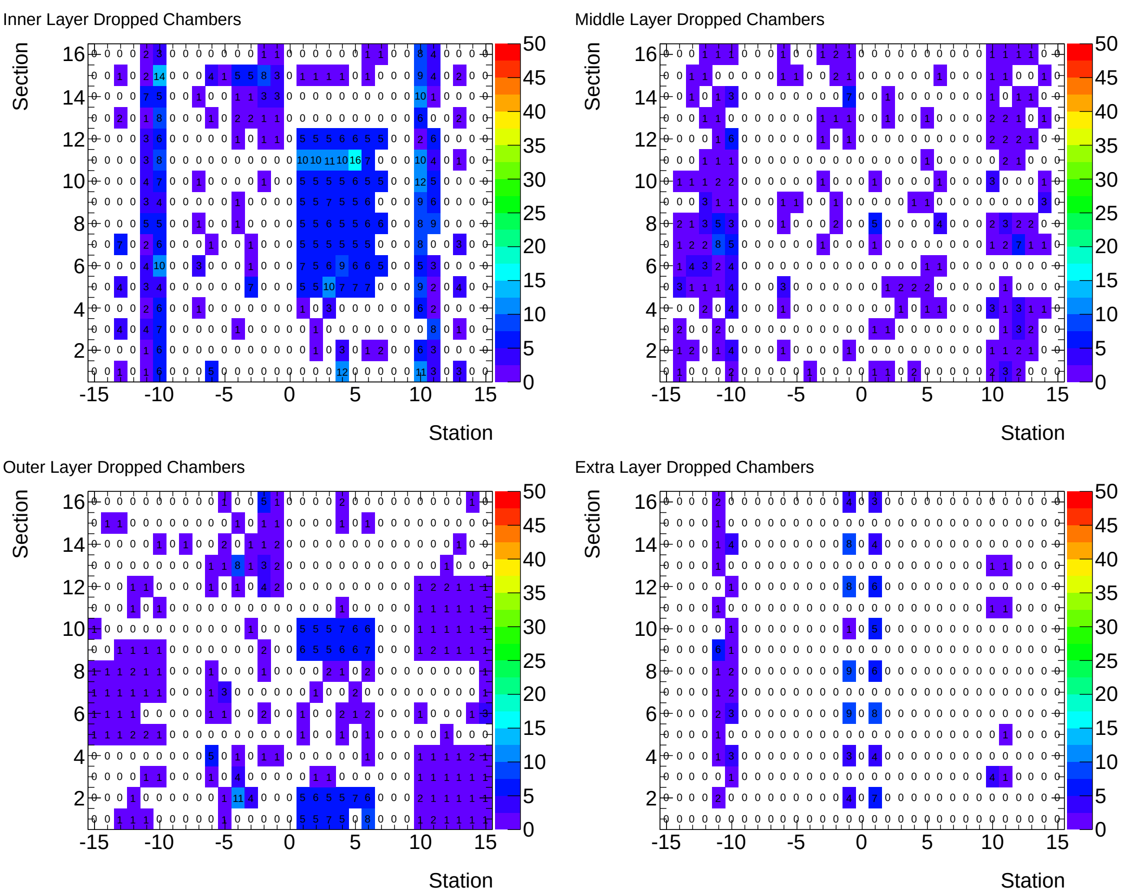

Figure A.2: MDT chamber chamber drops separated into the three layers and 'extra' chambers. End-cap stations are offset by 9 such that they appear outside of the barrel chambers and the A-side corresponds to a positive number. The section corresponds to a position in ϕ and station a position y or z in the barrel and end-caps respectively, see Fig. 3.9.

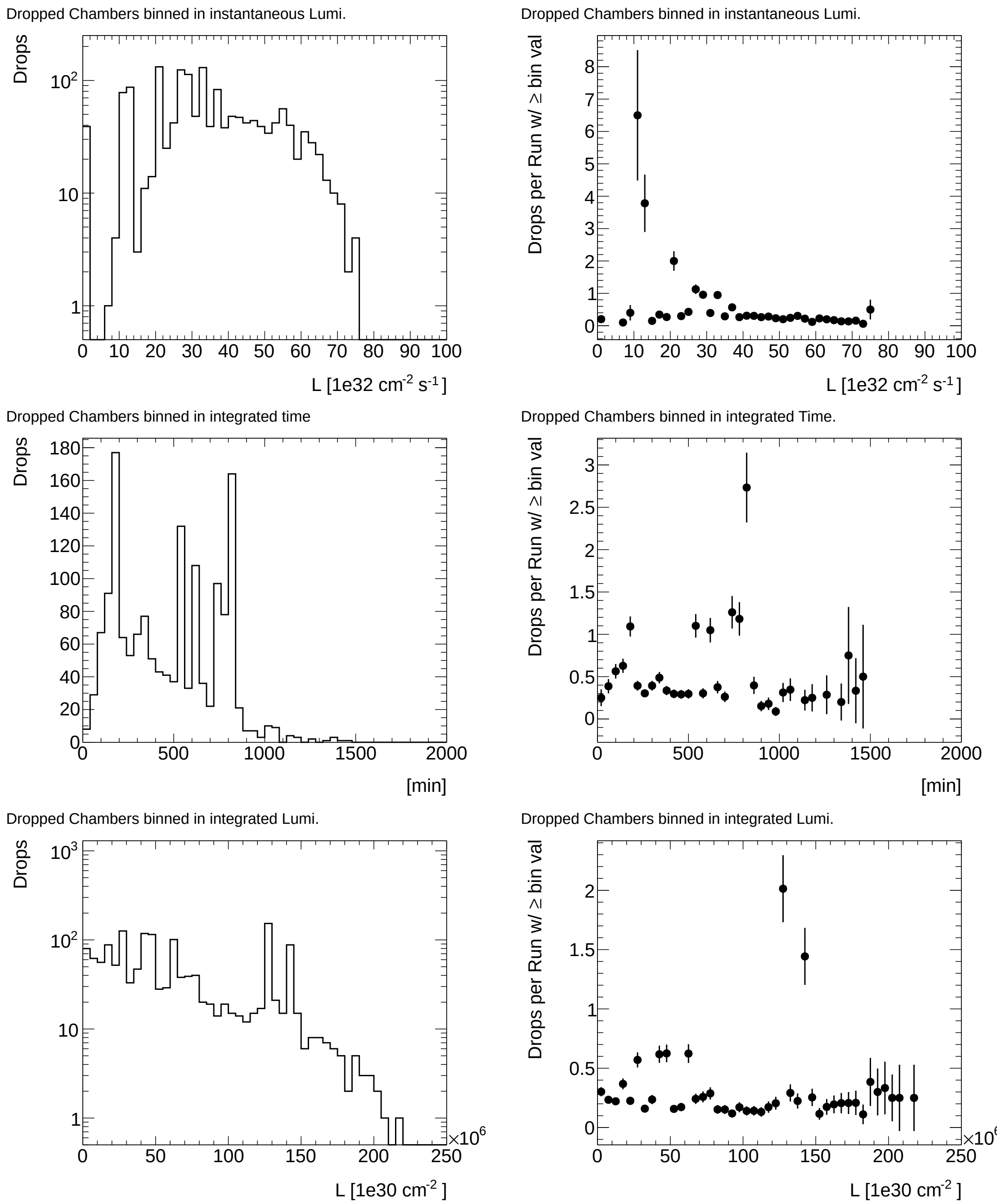

Figure A.3: Left, MDT chamber drops binned in (Top) instantaneous luminosity, (Middle) integrated run time, (Bottom) and integrated luminosity. Right, chamber drops binned in the same variables where each bin is normalized by the number of runs that reached that given luminosity or time.

was implemented which on average resulted in fewer drops per run, see Fig. A.5(a). Such a re-initialization would reset possible bit upsets before they cause a chamber to drop.

Most chambers do not repeatedly drop, see Fig. A.5(b), which could indicate some other fault. We also see that a large number of mezzanine card drops occur immediately after a reported parity error, see Fig. A.5(d).

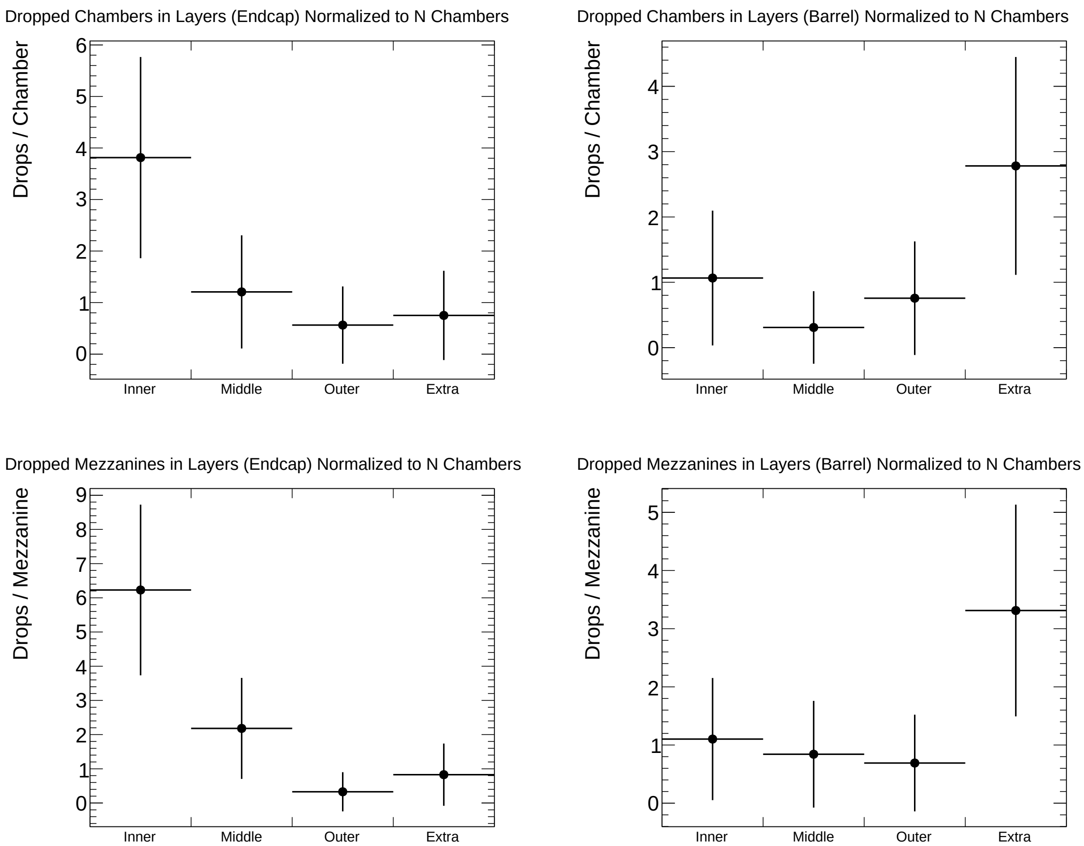

Figure A.4: (Top) MDT chamber drops and (Bottom) mezzanine card drops in the (Left) end-caps and (Right) barrel, normalized by the number of chambers in each category.

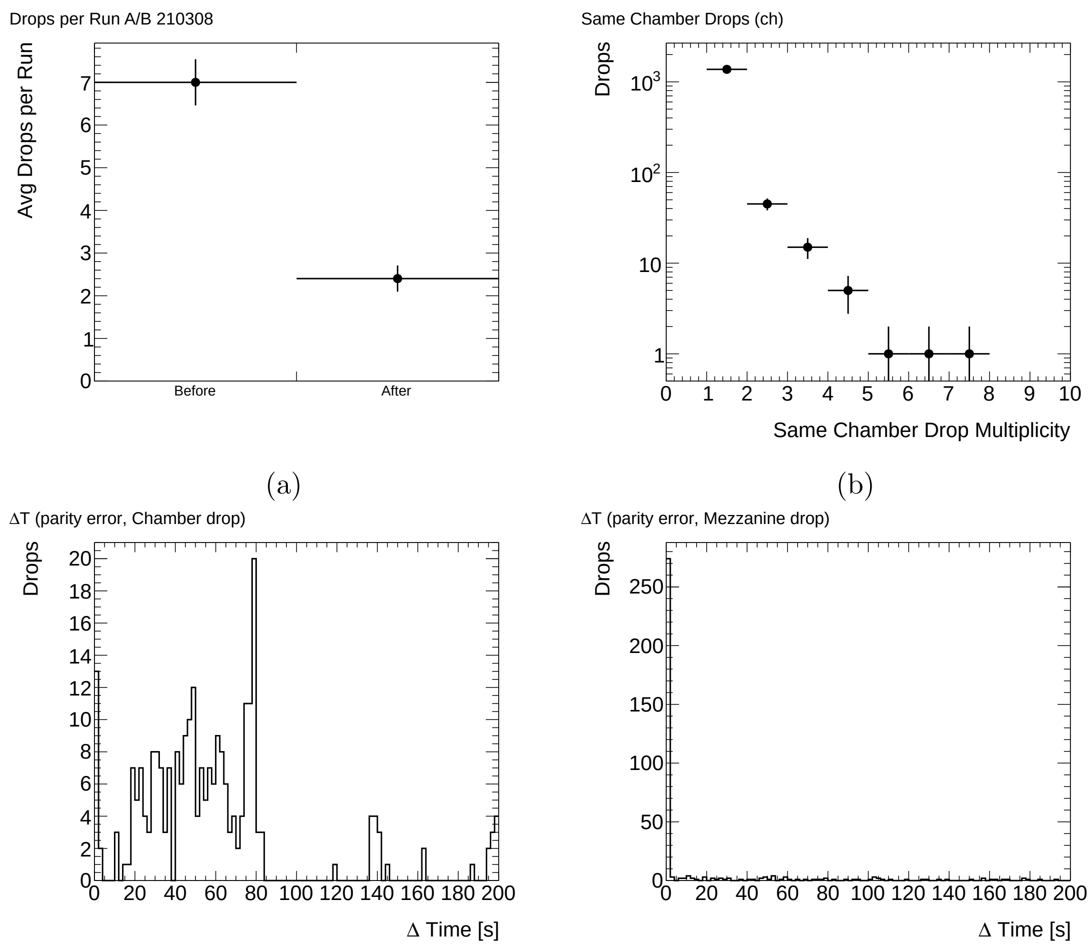

(a) (b) (c) (d)

Figure A.5: (a), average number of drops per run before and after run 210308, where an automatic JTAG initialization was started. (b), number of times a chamber repeatedly drops in the same run, averaged over runs. (c) and (d), time between reported parity errors and MDT chamber and mezzanine card drops.

APPENDIX B

8 TeV Signal Region Categories

This section contains post-fit m_{T} distributions in all of the $N_{\mathrm{jets}} \leq 1$ signal region categories for the 8 TeV analysis in Chapter V. The error bands are a sum of pre-fit uncertainties per process; it includes statistical uncertainties from the MC, experimental uncertainties, and theoretical uncertainties on the background and signal acceptance. See the caption of Fig. 5.2 for details on the figure contents.

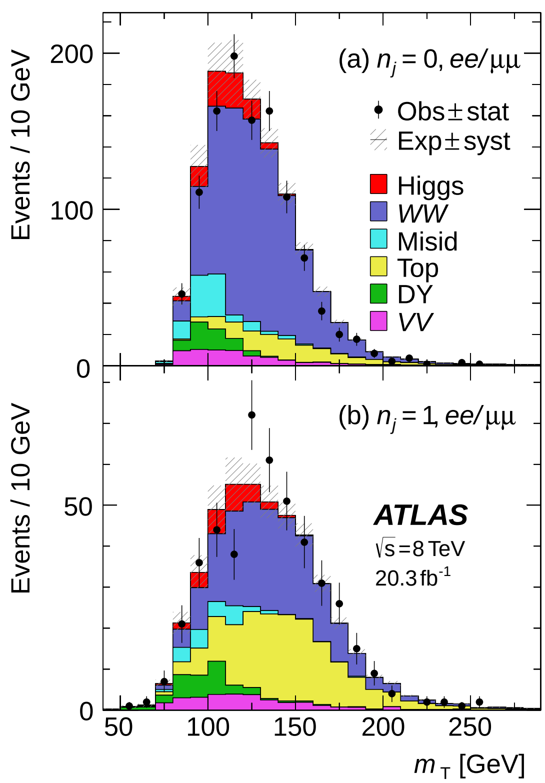

Figure B.1: Distributions of m_{T} for $N_{\mathrm{jets}} = 0$ and $= 1$ events in the $ee/\mu\mu$ channel [112].

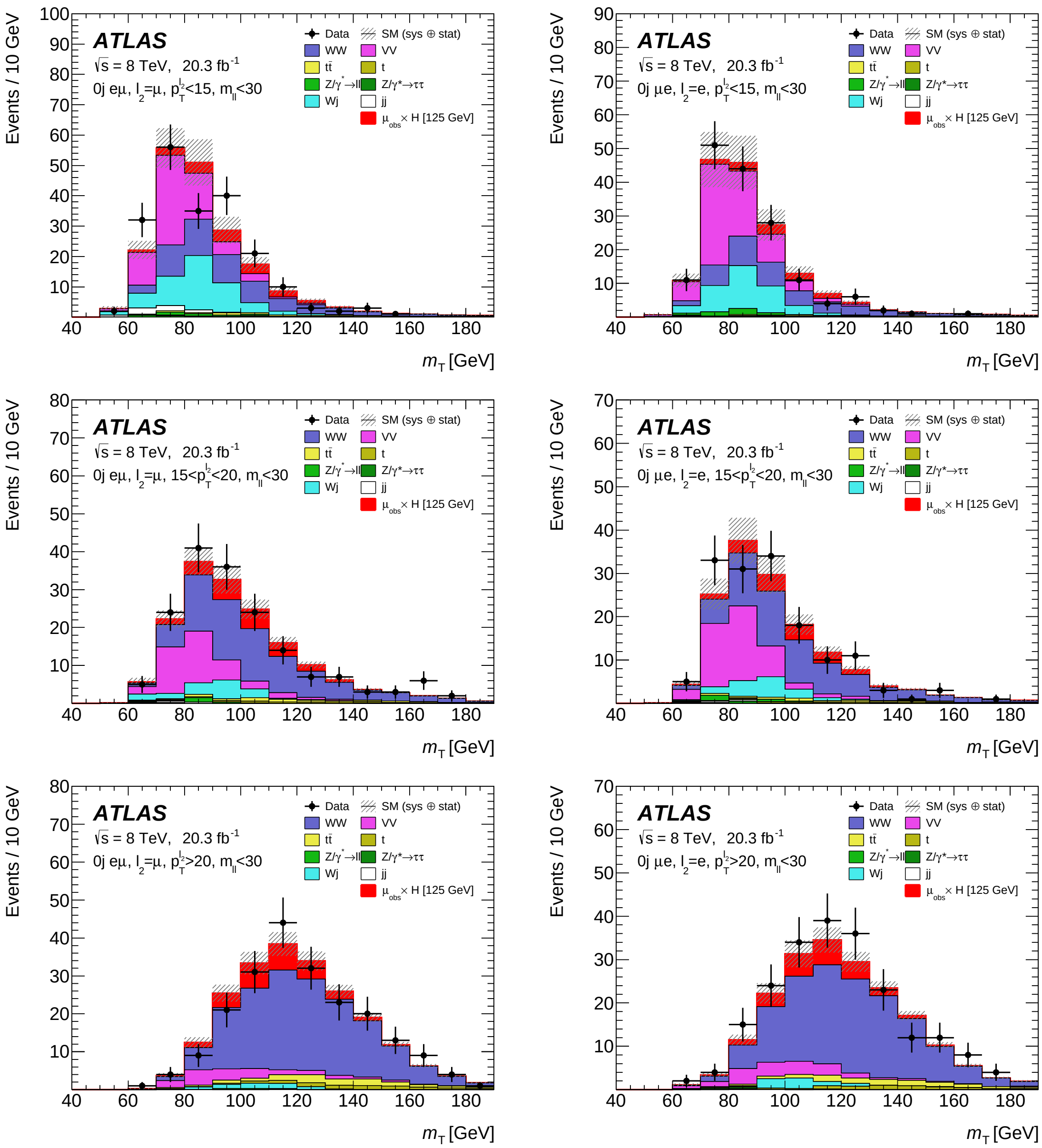

Figure B.2: Distributions of m_{T} for $N_{\mathrm{jets}} = 0$ and $m_{\ell\ell} < 30\,\mathrm{GeV}$ for events with (left) leading electrons and (right) leading muons. The rows correspond to different sub-leading lepton p_{T} selections [112].

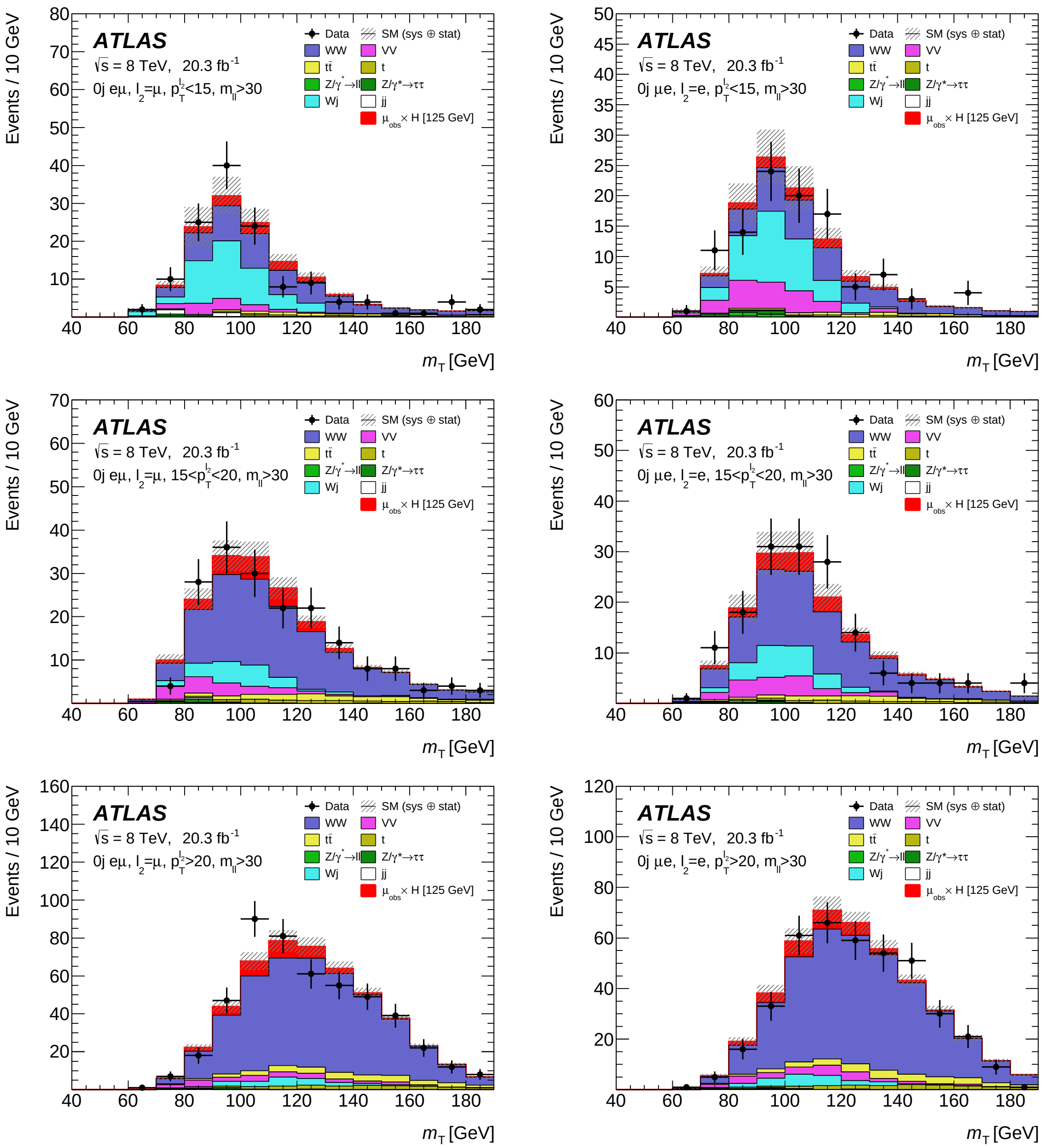

Figure B.3: Distributions of m_{T} for $N_{\mathrm{jets}} = 0$ and $m_{\ell\ell} > 30\,\mathrm{GeV}$ for events with (left) leading electrons and (right) leading muons. The rows correspond to different sub-leading lepton p_{T} selections [112].

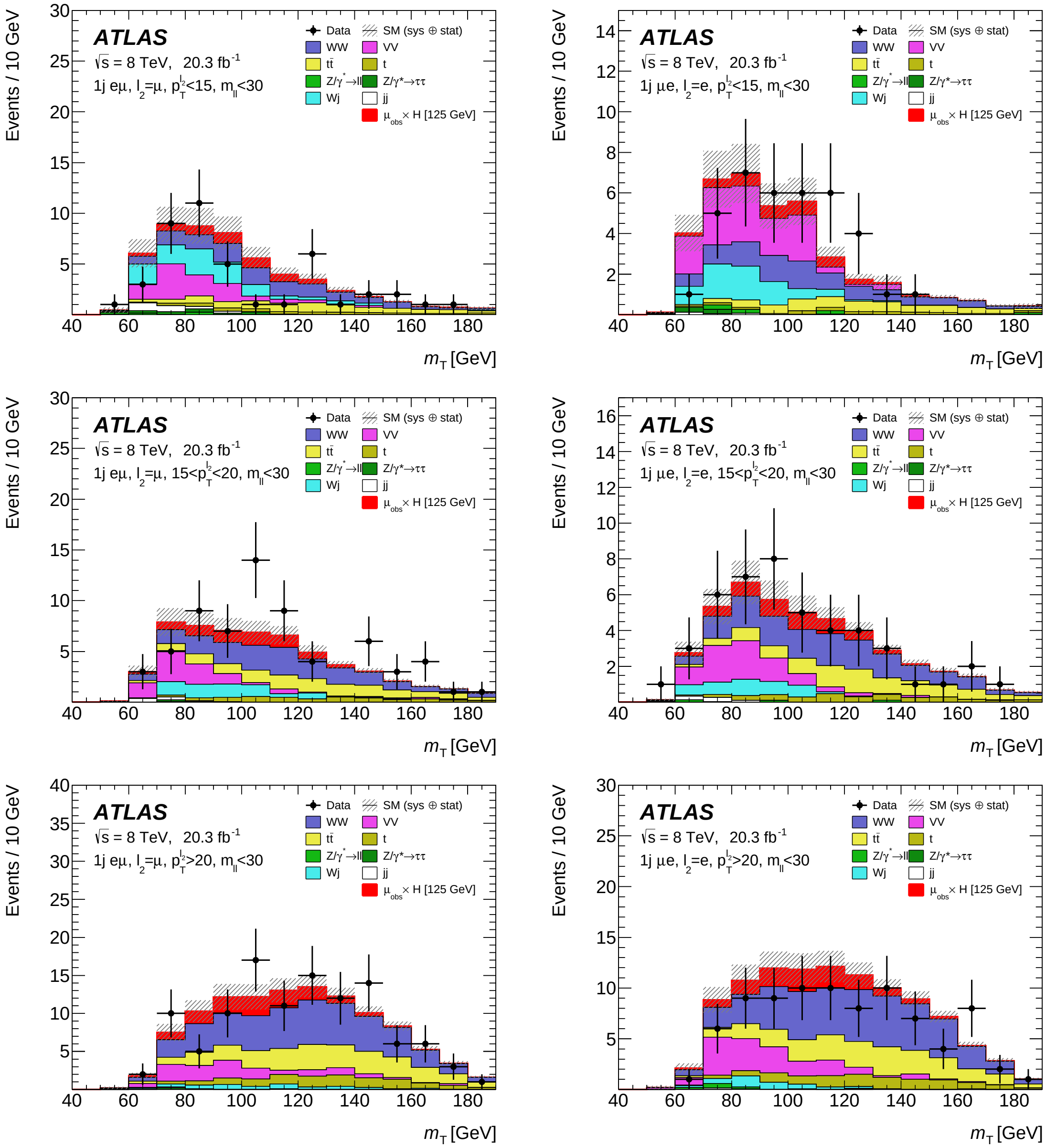

Figure B.4: Distributions of m_{T} for $N_{\text{jets}} = 1$ and $m_{\ell\ell} < 30\,\mathrm{GeV}$ for events with (left) leading electrons and (right) leading muons. The rows correspond to different sub-leading lepton p_{T} selections [112].

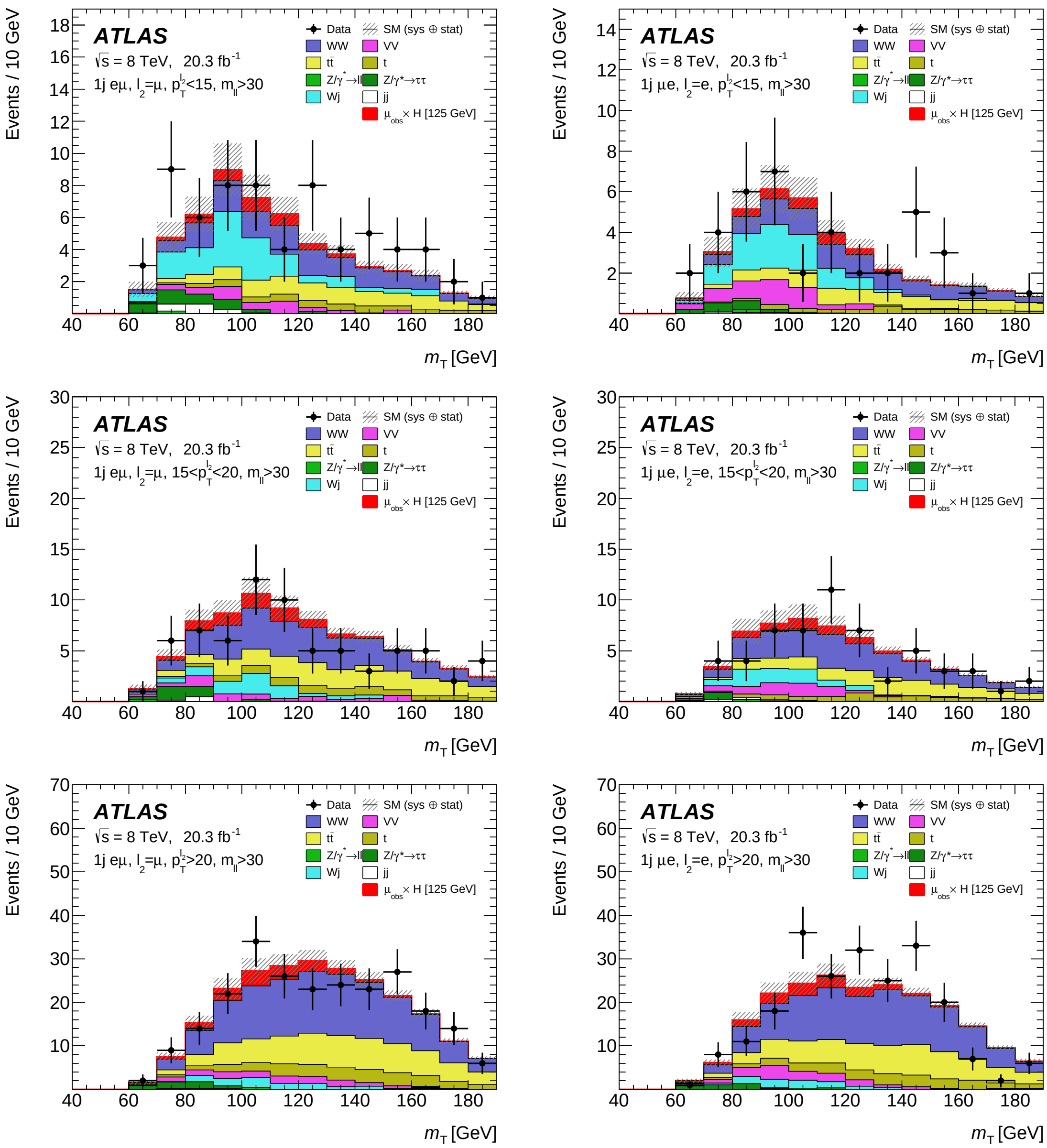

Figure B.5: Distributions of m_{T} for $N_{\mathrm{jets}} = 1$ and $m_{\ell\ell} > 30\,\mathrm{GeV}$ for events with (left) leading electrons and (right) leading muons. The rows correspond to different sub-leading lepton p_{T} selections [112].

APPENDIX C

Nuisance Parameter Correlation Scheme

Table C.1 shows the complete correlation scheme for the combination of channels in the $H \to WW^{(*)} \to \ell\nu\ell\nu$ analysis described in Chapter V. Parameter names are listed as used in the fitting code; those which start with 'scale_' are normalization factors and the remaining majority are nuisance parameters

Table C.1: Correlation scheme of nuisance parameters and normalization factors (scale_*). Nuisance parameters with an 'x' are correlated between channels. NPs without an 'x' are either uncorrelated or do not exist in the channel.

Parameter	ggF 2J	01J 2011	01J 2012	VBF 2011	VBF 2012
ATLAS_BR_VV	x	x	x	x	x
ATLAS_BR_tautau	x	x	x	x	x
ATLAS_BTag_B1EFF_2011		x		x	
ATLAS_BTag_B1EFF_2012	x		x		x
ATLAS_BTag_B2EFF_2011		x		x	
ATLAS_BTag_B2EFF_2012			x		x
ATLAS_BTag_B3EFF_2011		x		x	
ATLAS_BTag_B3EFF_2012	x		x		x
ATLAS_BTag_B4EFF_2011		x		x	
ATLAS_BTag_B4EFF_2012	x		x		x
ATLAS_BTag_B5EFF_2011		x		x	
ATLAS_BTag_B5EFF_2012	x		x		x
ATLAS_BTag_B6EFF_2011		x		x	
ATLAS_BTag_B6EFF_2012	x		x		x
ATLAS_BTag_B7EFF_2011		x		x	
ATLAS_BTag_B8EFF_2011		x		x	
ATLAS_BTag_B9EFF_2011		x		x	
ATLAS_BTag_CEFF_2011		x		x	
ATLAS_BTag_CEFF_2012	x		x		x
ATLAS_BTag_Herwig_LEFF_2012	x		x		x
ATLAS_BTag_LEFF	x	x	x	x	x
ATLAS_BTag_Pythia6_LEFF_2012	x		x		x
ATLAS_BTag_Sherpa_LEFF_2012	x		x		x

Parameter	ggF 2J	01J 2011	01J 2012	VBF 2011	VBF 2012
ATLAS_DPI_XS	x		x		
ATLAS_ELMU_2012_TRIG			x		
ATLAS_EL_2011_TRIG		x		x	
ATLAS_EL_2012_TRIG	x		x		x
ATLAS_EL_EFF_ID_CORRLOW_2011		x		x	
ATLAS_EL_EFF_ID_CORRLOW_2012	x		x		x
ATLAS_EL_EFF_ID_HIGHPT_2011		x		x	
ATLAS_EL_EFF_ID_HIGHPT_2012	x		x		x
ATLAS_EL_EFF_RECOID80010_2011		x		x	
ATLAS_EL_EFF_RECOID80010_2012	x		x		x
ATLAS_EL_EFF_RECOID80015_2011		x		x	
ATLAS_EL_EFF_RECOID80015_2012			x		x
ATLAS_EL_EFF_RECO_CORRLOW_2011		x		x	
ATLAS_EL_EFF_RECO_CORRLOW_2012			x		x
ATLAS_EL_EFF_RECO_CORR_2011		x		x	
ATLAS_EL_EFF_RECO_CORR_2012	x		x		x
ATLAS_EL_ESCALE	x	x	x	x	x
ATLAS_EL_ISO_HWW	x	x	x	x	x
ATLAS_EL_RES	x	x	x	x	x
ATLAS_EW_MODEL_VV_BDT_2j_HWW				x	x
ATLAS_EW_MODEL_VV_HWW		x			
ATLAS_EW_MODEL_Z_HWW_ggf		x			
ATLAS_EW_MODEL_Z_HWW_vbf				x	x
ATLAS_HiggsGGF_UEPS_BDT_2j_HWW				x	x
ATLAS_HiggsVBF_UEPS_BDT_2j_HWW				x	x
ATLAS_Higgs_UEPS	x	x	x		
ATLAS_JER	x	x	x	x	x
ATLAS_JES_1112_Detector1	x	x	x	x	x
ATLAS_JES_1112_Modelling1	x	x	x	x	x
ATLAS_JES_2011_Eta_TotalStat		x		x	
ATLAS_JES_2011_Statistical1		x		x	
ATLAS_JES_2012_Eta_StatMethod	x		x		x
ATLAS_JES_2012_PilePt	x		x		x
ATLAS_JES_2012_PileRho_HWW_GGF	x		x		
ATLAS_JES_2012_PileRho_HWW_VBF					x
ATLAS_JES_CLOSEBY		x			
ATLAS_JES_Eta_Modelling	x	x	x	x	x
ATLAS_JES_FlavComp_HWW_WW		x	x	x	
ATLAS_JES_FlavComp_HWW_other	x	x	x	x	x
ATLAS_JES_FlavComp_HWW_tt		x	x	x	x
ATLAS_JES_FlavResp	x	x	x	x	x
ATLAS_JES_Flavb	x	x	x	x	x
ATLAS_JES_HighPt			x		x
ATLAS_JES_MU	x	x	x	x	x
ATLAS_JES_NPV	x	x	x	x	x
ATLAS_JES_NonClosure_AFII_2012	x		x		x
ATLAS_JES_NonClosure_MC11c		x		x	
ATLAS_LUMI_2011		x		x	
ATLAS_LUMI_2012	x		x		x
ATLAS_MET_RESOSOFT_HWW_2011		x		x	
ATLAS_MET_RESOSOFT_HWW_2012			x		x
ATLAS_MET_SCALESOFT_HWW_2011		x		x	
ATLAS_MET_SCALESOFT_HWW_2012			x		x
ATLAS_MU_2011_TRIG		x		x	

Parameter	ggF 2J	01J 2011	01J 2012	VBF 2011	VBF 2012
ATLAS_MU_2012_TRIG	x		x		x
ATLAS_MU_EFF		x	x	x	x
ATLAS_MU_ESCALE	x	x	x	x	x
ATLAS_MU_ID_RES	x	x	x	x	x
ATLAS_MU_ISO_HWW	x	x	x	x	x
ATLAS_MU_MS_RES	x	x	x	x	x
ATLAS_MU_RESCALE_HWW_2012	x		x		x
ATLAS_PM_EFF_f_recoil_DY0j_lvlv2011		x			
ATLAS_PM_EFF_f_recoil_DY0j_lvlv2012			x		
ATLAS_PM_EFF_f_recoil_DY1j_lvlv2011		x			
ATLAS_PM_EFF_f_recoil_DY1j_lvlv2012			x		
ATLAS_PM_EFF_f_recoil_NDY_SR0j_lvlv2011		x			
ATLAS_PM_EFF_f_recoil_NDY_SR0j_lvlv2012			x		
ATLAS_PM_EFF_f_recoil_NDY_SR1j_lvlv2011		x			
ATLAS_PM_EFF_f_recoil_NDY_SR1j_lvlv2012			x		
ATLAS_PM_EFF_f_recoil_NDY_ZP0j_lvlv2011		x			
ATLAS_PM_EFF_f_recoil_NDY_ZP0j_lvlv2012			x		
ATLAS_PM_EFF_f_recoil_NDY_ZP1j_lvlv2011		x			
ATLAS_PM_EFF_f_recoil_NDY_ZP1j_lvlv2012			x		
ATLAS_PM_f_recoil_DY_SR0j_HWW_lvlv2011		x			
ATLAS_PM_f_recoil_DY_SR0j_HWW_lvlv2012			x		
ATLAS_PM_f_recoil_DY_SR1j_HWW_lvlv2011		x			
ATLAS_PM_f_recoil_DY_SR1j_HWW_lvlv2012			x		
ATLAS_PM_f_recoil_NDY_SR0j_HWW_lvlv2011		x			
ATLAS_PM_f_recoil_NDY_SR0j_HWW_lvlv2012			x		
ATLAS_PM_f_recoil_NDY_SR1j_HWW_lvlv2011		x			
ATLAS_PM_f_recoil_NDY_SR1j_HWW_lvlv2012			x		
ATLAS_PM_f_recoil_NDY_ZP0j_HWW_lvlv2011		x			
ATLAS_PM_f_recoil_NDY_ZP0j_HWW_lvlv2012			x		
ATLAS_PM_f_recoil_NDY_ZP1j_HWW_lvlv2011		x			
ATLAS_PM_f_recoil_NDY_ZP1j_HWW_lvlv2012			x		
ATLAS_PM_theta_SR0j_lvlv2011		x			
ATLAS_PM_theta_SR0j_lvlv2012			x		
ATLAS_PM_theta_SR1j_lvlv2011		x			
ATLAS_PM_theta_SR1j_lvlv2012			x		
ATLAS_PTllRewSyst_HWW		x	x		
ATLAS_QCD_WW_Modelling_BDT_2j_HWW				x	x
ATLAS_QCDscale_VV2in_BDT_2j_HWW				x	x
ATLAS_QCDscale_VV_BDT_2j_HWW				x	x
ATLAS_TOP_ME	x	x	x		
ATLAS_TOP_PDF	x	x	x		
ATLAS_TOP_PS	x	x	x		
ATLAS_TOP_SCALEF_NONTOP_0j_HWW		x	x		
ATLAS_TOP_SCALEF_STATS_0j_HWW_2011		x			
ATLAS_TOP_SCALEF_STATS_0j_HWW_2012			x		
ATLAS_TOP_SCALEF_THEO_0j_HWW		x	x		
ATLAS_TOP_Scale	x	x	x		
ATLAS_TOP_THEO_BDT_2j_HWW				x	x
ATLAS_TRACKMET_RESOPARASOFT_HWW_2011		x			
ATLAS_TRACKMET_RESOPARASOFT_HWW_2012	x		x		x
ATLAS_TRACKMET_RESOPERPSOFT_HWW_2011		x			
ATLAS_TRACKMET_RESOPERPSOFT_HWW_2012	x		x		x
ATLAS_TRACKMET_SCALESOFT_HWW_2011		x			
ATLAS_TRACKMET_SCALESOFT_HWW_2012	x		x		x

Parameter	ggF 2J	01J 2011	01J 2012	VBF 2011	VBF 2012
ATLAS_TopGGF2j_MTSHAPE	x				
ATLAS_VGammaShapeLepPt_HWW	x	x	x		
ATLAS_WW_EWCorr_HWW		x	x		
ATLAS_WW_MTSHAPEMATCHING_HWW		x	x		
ATLAS_WW_MTSHAPEPSUE_HWW		x	x		
ATLAS_WW_MTSHAPESCALE_HWW		x	x		
ATLAS_WW_MTSHAPE_2j_HWW_ggf2j	x				
ATLAS_WgsMTscale		x	x		
ATLAS_ZLEPLEP_ABCD_BDT0_2j_HWW					x
ATLAS_ZLEPLEP_ABCD_BDT1_2j_HWW					x
ATLAS_ZLEPLEP_ABCD_BDT2_2j_HWW					x
ATLAS_ZLEPLEP_ABCD_METEFF_2j_HWW				x	x
ATLAS_ZTAUTAU_BDT0_2j_HWW				x	x
ATLAS_ZTAUTAU_BDT1_2j_HWW				x	x
ATLAS_ZTAUTAU_BDT2_2j_HWW					x
ATLAS_ZTAUTAU_MODELING	x	x	x		
ATLAS_ZTAUTAU_PDF	x	x	x		
ATLAS_ZTAUTAU_PTZREW		x	x		
ATLAS_ZTAUTAU_PYTHIAMCSTAT_CR_0j		x	x		
ATLAS_ZTAUTAU_PYTHIAMCSTAT_CR_1j		x	x		
ATLAS_ZTAUTAU_PYTHIAMCSTAT_SR_0j		x	x		
ATLAS_ZTAUTAU_PYTHIAMCSTAT_SR_1j		x	x		
ATLAS_ZTAUTAU_PYTHIAMCSTAT_SR_2j_HWW_ggf2j	x				
ATLAS_ZTAUTAU_SCALE	x	x	x		
ATLAS_btag21j_extrap_HWW		x	x		
ATLAS_ggH_Matching_ACCEPT	x	x	x		
ATLAS_ggWW_XS_HWW		x	x		
ATLAS_ggfMTPSUE			x		
ATLAS_ggfMTmatching			x		
ATLAS_ggfMTscale			x		
FakeRateCorr_QCD_HWW	x	x	x	x	x
FakeRateOther_QCD_HWW	x	x	x	x	x
FakeRateStat_QCD_HWW	x	x	x	x	x
FakeRate_EL_Corrl_HWW_2012	x		x		x
FakeRate_EL_Flav_HWW_2011		x		x	
FakeRate_EL_Other_HWW_2011		x		x	
FakeRate_EL_Other_HWW_2012	x		x		x
FakeRate_EL_Stat_10_15_HWW_2011		x		x	
FakeRate_EL_Stat_10_15_HWW_2012	x		x		x
FakeRate_EL_Stat_15_20_HWW_2011		x		x	
FakeRate_EL_Stat_15_20_HWW_2012	x		x		x
FakeRate_EL_Stat_20_25_HWW_2011		x		x	
FakeRate_EL_Stat_20_25_HWW_2012	x		x		x
FakeRate_EL_Stat_GT25_HWW_2011		x		x	
FakeRate_EL_Stat_GT25_HWW_2012	x		x		x
FakeRate_EL_Uncorrl_OS_HWW_2012	x		x		x
FakeRate_EL_Uncorrl_SS_HWW_2012			x		
FakeRate_MU_Corrl_HWW_2012	x		x		x
FakeRate_MU_Flav_HWW_2011		x		x	
FakeRate_MU_Other_HWW_2011		x		x	
FakeRate_MU_Other_HWW_2012	x		x		x
FakeRate_MU_Stat_10_15_HWW_2011		x		x	
FakeRate_MU_Stat_10_15_HWW_2012	x		x		x
FakeRate_MU_Stat_15_20_HWW_2011		x		x	

Parameter	ggF 2J	01J 2011	01J 2012	VBF 2011	VBF 2012
FakeRate_MU_Stat_15_20_HWW_2012	x		x		x
FakeRate_MU_Stat_20_25_HWW_2011		x		x	
FakeRate_MU_Stat_20_25_HWW_2012	x		x		x
FakeRate_MU_Stat_GT25_HWW_2011		x		x	
FakeRate_MU_Stat_GT25_HWW_2012	x		x		x
FakeRate_MU_Uncorrl_OS_HWW_2012	x		x		x
FakeRate_MU_Uncorrl_SS_HWW_2012			x		
QCDscale_Bkg_V	x	x	x	x	x
QCDscale_Bkg_VV_ACCEPT_HWW		x	x		
QCDscale_Bkg_VV_HWW	x	x	x	x	x
QCDscale_Bkg_Wg_ACCEPT0j_HWW		x	x		
QCDscale_Bkg_Wg_ACCEPT1j_HWW		x	x		
QCDscale_Bkg_Wgs_ACCEPT0j_HWW		x	x		
QCDscale_Bkg_Wgs_ACCEPT1j_HWW	x	x	x		
QCDscale_Bkg_Wgs_ACCEPT2j_HWW	x	x	x	x	x
QCDscale_Higgs_ggH	x	x	x		
QCDscale_Higgs_ggH_ACCEPT	x	x	x		
QCDscale_Higgs_ggH_e1	x	x	x		
QCDscale_Higgs_qqH	x	x	x	x	x
QCDscale_Higgs_qqH_ACCEPT	x	x	x	x	x
QCDscale_VH	x	x	x		
QCDscale_VV_ACCEPT_2j_ggf2j	x				
QCDscale_Wg_ACCEPT2j_HWW	x	x	x	x	x
QCDscale_ZLEPLEP_ABCD_2j_HWW					x
QCDscale_ggH_m12				x	x
QCDscale_ggH_m23				x	x
QCDscale_ggH_ptH_m01	x	x	x		
SigXsecOverSM_HWW	x	x	x	x	x
VBF_Higgs_MODEL_BDT_2j_HWW				x	x
mu_BR_WW	x	x	x	x	x
mu_BR_tautau	x	x	x	x	x
mu_XS7_ggF		x		x	
mu_XS7_vbf		x		x	
mu_XS7_wh		x		x	
mu_XS7_zh		x		x	
mu_XS8_ggF	x		x		x
mu_XS8_vbf	x		x		x
mu_XS8_wh	x		x		x
mu_XS8_zh	x		x		x
pdf_Higgs_ggH	x	x	x	x	x
pdf_Higgs_ggH_ACCEPT		x	x		
pdf_Higgs_qqH	x	x	x	x	x
pdf_Wg_ACCEPT_HWW	x	x	x	x	x
pdf_Wgs_ACCEPT_HWW	x	x	x	x	x
pdf_gg	x	x	x	x	x
pdf_gg_ACCEPT	x	x	x	x	x
pdf_qq	x	x	x	x	x
pdf_qq_ACCEPT		x	x	x	x
scale_ATLAS_norm_SF_Diboson0j_lvlv2012			x		
scale_ATLAS_norm_SF_Diboson1j_lvlv2012			x		
scale_ATLAS_norm_SF_SF_MUSR_DY0j_lvlv2011		x			
scale_ATLAS_norm_SF_SF_MUSR_DY0j_lvlv2012			x		
scale_ATLAS_norm_SF_SF_MUSR_DY1j_lvlv2011		x			
scale_ATLAS_norm_SF_SF_MUSR_DY1j_lvlv2012			x		

Parameter	ggF 2J	01J 2011	01J 2012	VBF 2011	VBF 2012
scale_ATLAS_norm_SF_SF_MU_DY0j_lvlv2011		x			
scale_ATLAS_norm_SF_SF_MU_DY0j_lvlv2012			x		
scale_ATLAS_norm_SF_SF_MU_DY1j_lvlv2011		x			
scale_ATLAS_norm_SF_SF_MU_DY1j_lvlv2012			x		
scale_ATLAS_norm_SF_Top1j_lvlv2011		x			
scale_ATLAS_norm_SF_Top1j_lvlv2012			x		
scale_ATLAS_norm_SF_Top2j_ggf2j_lvlv2012	x				
scale_ATLAS_norm_SF_TopPF2j_lvlv2011		x			
scale_ATLAS_norm_SF_TopPF2j_lvlv2012			x		
scale_ATLAS_norm_SF_Top_0_2j_vbf2011				x	
scale_ATLAS_norm_SF_Top_0_2j_vbf2012					x
scale_ATLAS_norm_SF_Top_1_2j_vbf2012					x
scale_ATLAS_norm_SF_WW0j_lvlv2011		x			
scale_ATLAS_norm_SF_WW0j_lvlv2012			x		
scale_ATLAS_norm_SF_WW1j_lvlv2011		x			
scale_ATLAS_norm_SF_WW1j_lvlv2012			x		
scale_ATLAS_norm_SF_Zleplep0_2j_vbf2011				x	
scale_ATLAS_norm_SF_Zleplep0_2j_vbf2012					x
scale_ATLAS_norm_SF_Zleplep1_2j_vbf2012					x
scale_ATLAS_norm_SF_Ztautau0j_lvlv2011		x			
scale_ATLAS_norm_SF_Ztautau0j_lvlv2012			x		
scale_ATLAS_norm_SF_Ztautau1j_lvlv2011		x			
scale_ATLAS_norm_SF_Ztautau1j_lvlv2012			x		
scale_ATLAS_norm_SF_Ztautau2j_ggf2j_lvlv2012	x				
scale_ATLAS_norm_SF_btag_lvlv2011		x			
scale_ATLAS_norm_SF_btag_lvlv2012			x		

APPENDIX D

Full Nuisance Parameter Ranking and Pulls

Figure D.1 shows the full nuisance parameter ranking, including the top thirty which are shown in Section 5.6.5. All nuisance parameter pulls are within one standard deviation of the nominal value.

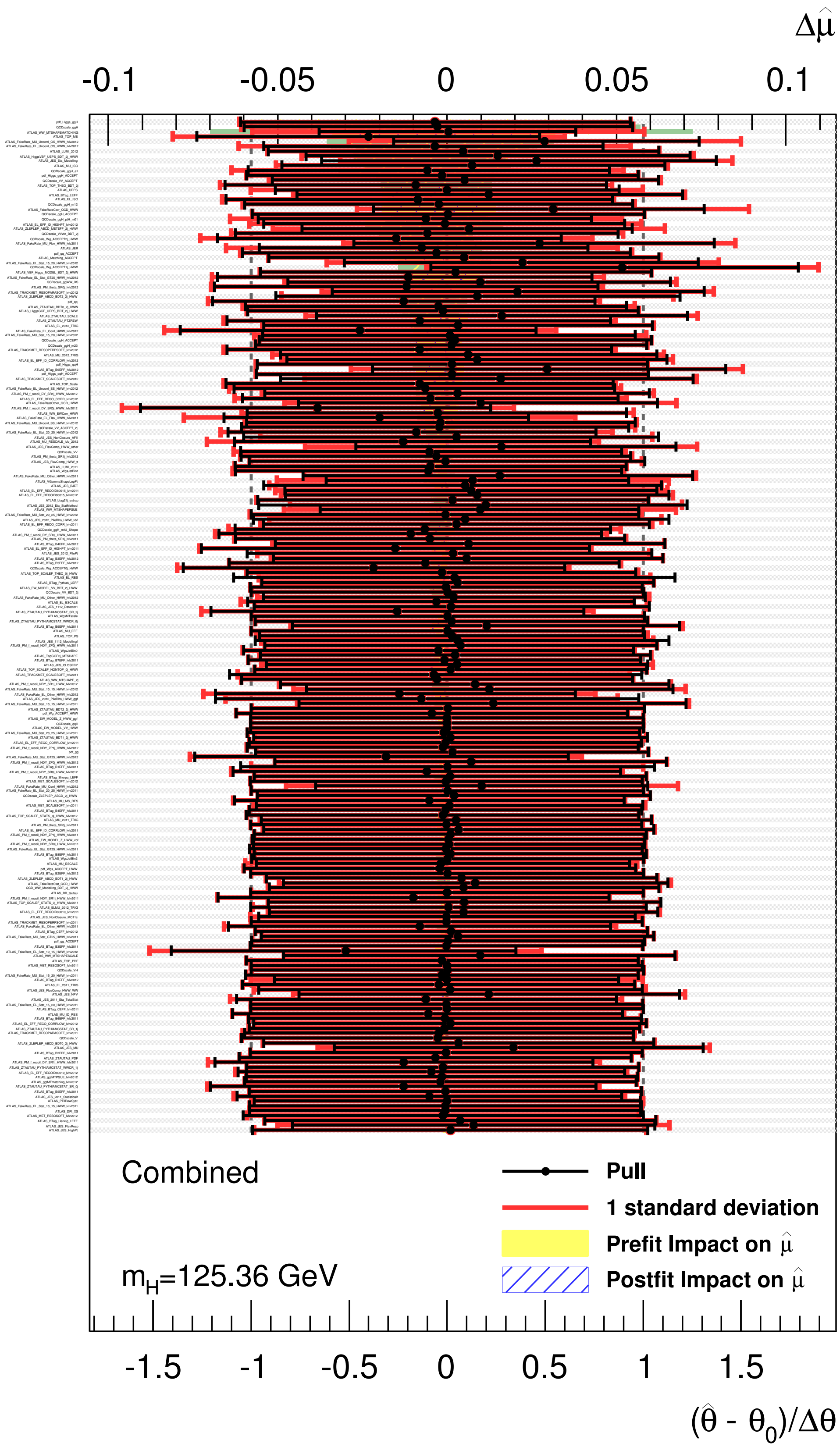

Figure D.1: Impact of all NPs. See Figure 5.20 for the description.

BIBLIOGRAPHY

BIBLIOGRAPHY

[1] ATLAS Collaboration, G. Aad et al., *Observation of a new particle in the search for the Standard Model Higgs boson with the ATLAS detector at the LHC*, Phys. Lett. B **716** (2012) 1–29, `arXiv:1207.7214 [hep-ex]`.

[2] CMS Collaboration, S. Chatrchyan et al., *Observation of a new boson at a mass of 125 GeV with the CMS experiment at the LHC*, Phys. Lett. B **716** (2012) 30–61, `arXiv:1207.7235 [hep-ex]`.

[3] D. Griffiths, *Introduction to Elementary Particles*. Wiley-VCH, Weinheim Germany, 2 ed., 2008.

[4] M. Srednicki, *Quantum Field Theory*. Cambridge University Press, Cambridge, 2007.

[5] M. Peskin and D. Schroeder, *An Introduction to Quantum Field Theory*. Perseus Publishing, Cambridge, Massachusetts, 1995.

[6] G. L. Kane, *Modern Elementary Particle Physics: The Fundamental Particles and Forces?* Perseus Publishing, Cambridge, Massachusetts, 1993.

[7] Glashow, S.L., *Partial Symmetries of Weak Interactions*, Nucl. Phys. **22** (1961) 579–588.

[8] S. Weinberg, *A Model of Leptons*, Phys. Rev. Lett. **19** (1967) 1264–1266.

[9] A. Salam, *Weak and Electromagnetic Interactions*, Proceedings of the Nobel Symposium **C680519** (1968) 367–377.

[10] G. 't Hooft and M. Veltman, *Regularization and Renormalization of Gauge Fields*, Nucl. Phys. B **44** (1972) 189–213.

[11] M. Gell-Mann, *A schematic model of baryons and mesons*, Phys. Lett. **8** no. 3, (1964) 214 – 215.

[12] G. Zweig, *An SU_3 model for strong interaction symmetry and its breaking; Version 1*, Tech. Rep. CERN-TH-401, CERN, Geneva, Jan, 1964.

[13] H. Fritzsch, M. Gell-Mann, and H. Leutwyler, *Advantages of the color octet gluon picture*, Phys. Lett. B **47** no. 4, (1973) 365 – 368.

[14] D. J. Gross and F. Wilczek, *Asymptotically Free Gauge Theories. I*, Phys. Rev. D **8** (1973) 3633–3652.

[15] H. D. Politzer, *Reliable Perturbative Results for Strong Interactions?*, Phys. Rev. Lett. **30** (1973) 1346–1349.

[16] T. Aoyama, M. Hayakawa, T. Kinoshita, and M. Nio, *Revised value of the eighth-order QED contribution to the anomalous magnetic moment of the electron*, Phys. Rev. D **77** (2008) 053012, arXiv:0712.2607 [hep-ph].

[17] Olive, K.A. et al., *2014 Review of Particle Physics*, Chin. Phys. C **38** (2014) 090001.

[18] E. Noether, *Invariante Variationsprobleme*, Nachrichten von der königlichen Gesellschaft der Wissenschaften zu Göttingen, Mathematisch-Physikalische Klasse (1918) 235–257.

[19] A. Pich, *The Standard Model of electroweak interactions*, arXiv:0705.4264 [hep-ph].

[20] F. Englert and R. Brout, *Broken Symmetry and the Mass of Gauge Vector Mesons*, Phys. Rev. Lett. **13** (1964) 321–323.

[21] P. W. Higgs, *Broken symmetries, massless particles and gauge fields*, Phys. Lett. **12** (1964) 132–133.

[22] P. W. Higgs, *Broken Symmetries and the Masses of Gauge Bosons*, Phys. Rev. Lett. **13** (1964) 508–509.

[23] G. Guralnik, C. Hagen, and T. Kibble, *Global Conservation Laws and Massless Particles*, Phys. Rev. Lett. **13** (1964) 585–587.

[24] P. W. Higgs, *Spontaneous Symmetry Breakdown without Massless Bosons*, Phys. Rev. **145** (1966) 1156–1163.

[25] T. Kibble, *Symmetry breaking in non-Abelian gauge theories*, Phys. Rev. **155** (1967) 1554–1561.

[26] A. Djouadi, *The anatomy of electro-weak symmetry breaking. I: The Higgs boson in the standard model*, Phys. Rep. **457** (2008) 1–216, arXiv:hep-ph/0503172 [hep-ph].

[27] The ALEPH, DELPHI, L3, OPAL Collaborations, the LEP Electroweak Working Group, *Electroweak Measurements in Electron-Positron Collisions at W-Boson-Pair Energies at LEP*, Phys. Rep. **532** (2013) 119, arXiv:1302.3415 [hep-ex].

[28] Tevatron New Physics Higgs Working Group, CDF, D0 Collaboration, *Updated Combination of CDF and D0 Searches for Standard Model Higgs Boson Production with up to 10.0 fb^{-1} of Data*, arXiv:1207.0449 [hep-ex].

[29] CDF, D0 Collaboration, *Evidence for a particle produced in association with weak bosons and decaying to a bottom-antibottom quark pair in Higgs boson searches at the Tevatron*, Phys. Rev. Lett. **109** (2012) 071804, arXiv:1207.6436 [hep-ex].

[30] ATLAS, CMS Collaboration, *Combined Measurement of the Higgs Boson Mass in pp Collisions at $\sqrt{s} = 7$ and 8 TeV with the ATLAS and CMS Experiments*, Phys. Rev. Lett. **114** (2015) 191803, arXiv:1503.07589 [hep-ex].

[31] LHC Higgs Cross Section Working Group, 2014. https://twiki.cern.ch/twiki/bin/view/LHCPhysics/LHCHXSWG.

[32] LHC Higgs Cross Section Working Group, S. Heinemeyer, C. Mariotti, G. Passarino, and R. Tanaka (Eds.), *Handbook of LHC Higgs Cross Sections: 3. Higgs Properties*, arXiv:1307.1347 [hep-ph].

[33] R. D. Ball, V. Bertone, S. Carrazza, et al., *Parton distributions with LHC data*, Nucl. Phys. B **867** (2013) 244 – 289.

[34] LHC Study Group Collaboration, T. S. Pettersson and P. Lefvre, *The Large Hadron Collider: conceptual design*, Tech. Rep. CERN-AC-95-05 LHC, CERN, Geneva, Oct, 1995.

[35] L. Evans and P. Bryant, *LHC Machine*, J. Instrum. **3** (2008) S08001.

[36] T. Linnecar, M. E. Angoletta, L. Arnaudon, et al., *Hardware and Initial Beam Commissioning of the LHC RF Systems*, Tech. Rep. LHC-PROJECT-Report-1172, CERN-LHC-PROJECT-Report-1172, CERN, Geneva, Oct, 2008.

[37] ATLAS Collaboration, *The ATLAS Experiment at the CERN Large Hadron Collider*, J. Instrum. **3** (2008) S08003.

[38] ATLAS Collaboration, *ATLAS detector and physics performance: Technical Design Report, 1*, Tech. Rep. ATLAS-TDR-14, CERN-LHCC-99-014, Geneva, 1999.

[39] ATLAS Collaboration, *ATLAS detector and physics performance: Technical Design Report, 2*, Tech. Rep. ATLAS-TDR-15, CERN-LHCC-99-015, Geneva, 1999.

[40] CERN, *LEP design report.* No. CERN-LEP-84-01. CERN, Geneva, 1984. Copies shelved as reports in LEP, PS and SPS libraries.

[41] ALICE Collaboration, *The ALICE experiment at the CERN LHC*, J. Instrum. **3** (2008) S08002.

[42] CMS Collaboration, *The CMS experiment at the CERN LHC. The Compact Muon Solenoid experiment*, J. Instrum. **3** (2008) S08004. 361 p. Also published by CERN Geneva in 2010.

[43] LHCb Collaboration, *The LHCb Detector at the LHC*, J. Instrum. **3** (2008) S08005.

[44] TOTEM Collaboration, *Total cross-section, elastic scattering and diffraction dissociation at the Large Hadron Collider at CERN: TOTEM Technical Design Report*, Tech. Rep. CERN-LHCC-2004-002, TOTEM-TDR-001, Geneva, 2004.

[45] MoEDAL Collaboration, *Technical Design Report of the MoEDAL Experiment*, Tech. Rep. CERN-LHCC-2009-006, MoEDAL-TDR-001, CERN, Geneva, Jun, 2009.

[46] LHCf Collaboration, *LHCf experiment: Technical Design Report*, Tech. Rep. LHCF-TDR-001, CERN-LHCC-2006-004, Geneva, 2006.

[47] CERN, *ECFA-CERN Workshop on Large Hadron Collider in the LEP Tunnel*. CERN, Geneva, 1984.

[48] O. S. Brning, P. Collier, P. Lebrun, et al., *LHC Design Report*. CERN, Geneva, 2004.

[49] CERN, *LHC to restart in 2009*, 2008. `http://press.web.cern.ch/press-releases/2008/12/lhc-restart-2009`.

[50] CERN, *The CERN accelerator complex*, 2013. `https://cds.cern.ch/record/1621894`.

[51] CERN, *Chamonix 2012 Workshop on LHC Performance*. CERN, Geneva, 2012.

[52] ATLAS Collaboration, *ATLAS Data Summary*, 2015. `https://atlas.web.cern.ch/Atlas/GROUPS/DATAPREPARATION/DataSummary`.

[53] F. Zimmerman, *LHC: The Machine*, Presented at SLAC Summer Institute 2012, 2012.

[54] P. Baudrenghien and T. Mastoridis, *Longitudinal emittance blowup in the large hadron collider*, Nucl. Instrum. Meth. Phys. Res. A **726** no. 0, (2013) 181 – 190.

[55] G. Apollinari, O. Brning, and L. Rossi, *High Luminosity LHC Project Description* , Tech. Rep. CERN-ACC-2014-0321, CERN, Geneva, Dec, 2014. `http://cds.cern.ch/record/1974419`.

[56] ATLAS Collaboration, *Expected Performance of the ATLAS Experiment - Detector, Trigger and Physics*, `arXiv:0901.0512 [hep-ex]`.

[57] ATLAS Collaboration, *ATLAS inner detector: Technical Design Report, 1*. CERN, Geneva, 1997.

[58] ATLAS Collaboration, *ATLAS inner detector: Technical Design Report, 2*. CERN, Geneva, 1997.

[59] ATLAS Collaboration, *The ATLAS Inner Detector commissioning and calibration*, Eur. Phys. J. C **70** (2010) 787–821, `arXiv:1004.5293`.

[60] ATLAS Collaboration, *Readiness of the ATLAS liquid argon calorimeter for LHC collisions*, Eur. Phys. J. C **70** (2010) 723–753, `arXiv:0912.2642`.

[61] E. Abat, J. Abdallah, T. Addy, et al., *Study of energy response and resolution of the ATLAS barrel calorimeter to hadrons of energies from 20 to 350 GeV*, Nucl. Instrum. Meth. Phys. Res. A **621** no. 13, (2010) 134 – 150.

[62] B. Aubert, J. Ballansat, A. Bazan, et al., *Performance of the ATLAS electromagnetic calorimeter end-cap module 0*, Nucl. Instrum. Meth. Phys. Res. A **500** (2003) 178 – 201.

[63] J. P. Archambault, A. Artamonov, M. Cadabeschi, et al., *Performance of the ATLAS liquid argon forward calorimeter in beam tests*, J. Instrum. **8** (2013) P05006. `http://stacks.iop.org/1748-0221/8/i=05/a=P05006`.

[64] ATLAS Collaboration, *Muon Momentum Resolution in First Pass Reconstruction of pp Collision Data Recorded by ATLAS in 2010*, Tech. Rep. ATLAS-CONF-2011-046, CERN, Geneva, Mar, 2011. `https://cds.cern.ch/record/1338575`.

[65] ATLAS Collaboration, *Studies of the performance of the ATLAS detector using cosmic-ray muons*, Eur. Phys. J. C **71** (2011) 1593, `arXiv:1011.6665`.

[66] ATLAS Collaboration, *Performance of the ATLAS Detector using First Collision Data*, J. High Energy Phys. **1009** (2010) 056, `arXiv:1005.5254 [hep-ex]`.

[67] D. Parchet, "Def. axes detecteur, machine, genie cevil." Technical drawing, December, 1998. `http://atlas.web.cern.ch/Atlas/GROUPS/INNER_DETECTOR/TDR/dev/Appendix/imported/`. AT130133PL.

[68] M. Shochet, L. Tompkins, V. Cavaliere, et al., *Fast TracKer (FTK) Technical Design Report*, Tech. Rep. CERN-LHCC-2013-007, ATLAS-TDR-021, CERN, Geneva, Jun, 2013.

[69] J. Pequenao, *Computer generated image of the ATLAS inner detector*, Mar, 2008. `https://cds.cern.ch/record/1095926`.

[70] ATLAS Collaboration, *ATLAS pixel detector: Technical Design Report*, Tech. Rep. ATLAS-TDR-11, CERN-LHCC-98-013, Geneva, 1998.

[71] ATLAS Collaboration, *ATLAS pixel detector electronics and sensors*, J. Instrum. **3** (2008) P07007.

[72] ATLAS Collaboration, *The barrel modules of the ATLAS semiconductor tracker*, Nucl. Instrum. Meth. Phys. Res. A **568** no. 2, (2006) 642 – 671.

[73] ATLAS Collaboration, *The ATLAS semiconductor tracker end-cap module*, Nucl. Instrum. Meth. Phys. Res. A **575** no. 3, (2007) 353 – 389.

[74] ATLAS Collaboration, *The silicon microstrip sensors of the ATLAS semiconductor tracker*, Nucl. Instrum. Meth. Phys. Res. A **578** no. 1, (2007) 98 – 118.

[75] The ATLAS TRT Collaboration, *The ATLAS TRT Barrel Detector*, J. Instrum. **3** (2008) P02014.

[76] The ATLAS TRT Collaboration, *The ATLAS TRT end-cap detectors*, J. Instrum. **3** (2008) P10003.

[77] J. Pequenao, *Computer Generated image of the ATLAS calorimeter*, Mar, 2008. https://cds.cern.ch/record/1095927.

[78] ATLAS Collaboration, *ATLAS calorimeter performance: Technical Design Report*. CERN, Geneva, 1996.

[79] ATLAS Collaboration, *ATLAS liquid-argon calorimeter: Technical Design Report*. CERN, Geneva, 1996.

[80] H. Wilkens and the ATLAS LArg Collaboration, *The ATLAS Liquid Argon calorimeter: An overview*, JPCS **160** (2009) 012043.

[81] ATLAS Collaboration, *ATLAS tile calorimeter: Technical Design Report*. CERN, Geneva, 1996.

[82] ATLAS Collaboration, *Electron performance measurements with the ATLAS detector using the 2010 LHC proton-proton collision data*, Eur. Phys. J. C **72** (2012) 1–46.

[83] ATLAS Collaboration, *ATLAS muon spectrometer: Technical Design Report*. CERN, Geneva, 1997. distribution.

[84] ATLAS Collaboration, *Commissioning of the ATLAS Muon Spectrometer with cosmic rays*, Eur. Phys. J. C **70** (2010) 875–916, arXiv:1006.4384 [physics.ins-det].

[85] ATLAS Collaboration, *Measurement of the muon reconstruction performance of the ATLAS detector using 2011 and 2012 LHC proton-proton collision data*, Eur. Phys. J. C **74** (2014) 3130, arXiv:1407.3935 [hep-ex].

[86] ATLAS Collaboration, *ATLAS central solenoid: Technical Design Report*. No. ATLAS-TDR-9, CERN-LHCC-97-021. CERN, Geneva, 1997.

[87] ATLAS Collaboration, J. P. Badiou, J. Beltramelli, J. M. Baze, and J. Belorgey, *ATLAS barrel toroid: Technical Design Report*. CERN, Geneva, 1997.

[88] ATLAS Collaboration, *ATLAS end-cap toroids: Technical Design Report*. CERN, Geneva, 1997.

[89] B. Muratori, *Luminosity and luminous region calculations for the LHC*, Tech. Rep. LHC-PROJECT-NOTE-301, CERN, Geneva, Sep, 2002.

[90] ATLAS Collaboration, *Improved luminosity determination in pp collisions at* $\sqrt{s} = 7$ TeV *using the ATLAS detector at the LHC*, Eur. Phys. J. C **73** (2013).

[91] ATLAS Collaboration, *Total Integrated Luminosity and Data Quality in 2011 and 2012*, September, 2013. https://twiki.cern.ch/twiki/bin/view/AtlasPublic/LuminosityPublicResults.

[92] ATLAS Collaboration, "Number of interactions per crossing." https://twiki.cern.ch/twiki/bin/view/AtlasPublic/LuminosityPublicResults.

[93] ATLAS Collaboration, *Trigger Operation Public Results*, February, 2013. https://twiki.cern.ch/twiki/bin/view/AtlasPublic/TriggerOperationPublicResults.

[94] ATLAS Collaboration, *ATLAS level-1 trigger: Technical Design Report*. CERN, Geneva, 1998.

[95] ATLAS Collaboration, P. Jenni, M. Nessi, M. Nordberg, and K. Smith, *ATLAS high-level trigger, data-acquisition and controls: Technical Design Report*. CERN, Geneva, 2003.

[96] A. Sfyrla, *ATLAS triggering on SUSY in 2012*, Tech. Rep. ATL-DAQ-PROC-2013-001, CERN, Geneva, Jan, 2013.

[97] ATLAS Collaboration, *Performance of the ATLAS Electron and Photon Trigger in p-p Collisions at* $\sqrt{s} = 7\,\mathrm{TeV}$ *in 2011*, Tech. Rep. ATLAS-CONF-2012-048, CERN, Geneva, May, 2012.

[98] ATLAS Collaboration, G. Aad et al., *Performance of the ATLAS muon trigger in pp collisions at* $\sqrt{s} = 8$ *TeV*, arXiv:1408.3179 [hep-ex].

[99] J. Pequenao and P. Schaffner, *An computer generated image representing how ATLAS detects particles*, Jan, 2013. https://cds.cern.ch/record/1505342.

[100] ATLAS Collaboration, *Performance of the ATLAS Silicon Pattern Recognition Algorithm in Data and Simulation at* $\sqrt{s} = 7$ *TeV*, Tech. Rep. ATLAS-CONF-2010-072, CERN, Geneva, Jul, 2010.

[101] ATLAS Collaboration, *Performance of the ATLAS Inner Detector Track and Vertex Reconstruction in the High Pile-Up LHC Environment*, Tech. Rep. ATLAS-CONF-2012-042, CERN, Geneva, Mar, 2012.

[102] T. Cornelissen, M. Elsing, S. Fleischmann, et al., *Concepts, Design and Implementation of the ATLAS New Tracking (NEWT)*, Tech. Rep. ATL-SOFT-PUB-2007-007, ATL-COM-SOFT-2007-002, CERN, Geneva, Mar, 2007.

[103] K. Hamano, A. Morley, and A. Salzburger, *Track Reconstruction Performance and Efficiency Estimation using different ID geometry samples*, Tech. Rep. ATL-COM-PHYS-2012-1541, CERN, Geneva, Oct, 2012. plots for a poster at HCP.

[104] ATLAS Collaboration, *Performance of primary vertex reconstruction in proton-proton collisions at* $\sqrt{s}$ *=7 TeV in the ATLAS experiment*, Tech. Rep. ATLAS-CONF-2010-069, CERN, Geneva, Jul, 2010.

[105] S. Pagan Griso, K. Prokofiev, A. Andreazza, et al., *Vertex reconstruction plots: Collision performance plots for approval*, Tech. Rep. ATL-COM-PHYS-2012-474, CERN, Geneva, Apr, 2012.

[106] W. Lampl, S. Laplace, D. Lelas, et al., *Calorimeter Clustering Algorithms: Description and Performance*, Tech. Rep. ATL-LARG-PUB-2008-002, ATL-COM-LARG-2008-003, 2008.

[107] ATLAS Collaboration, *Electron efficiency measurements with the ATLAS detector using the 2012 LHC proton-proton collision data*, Tech. Rep. ATLAS-CONF-2014-032, 2014.

[108] ATLAS Collaboration, *Electron and photon energy calibration with the ATLAS detector using LHC Run 1 data*, Eur. Phys. J. C **74** (2014) 3071, `arXiv:1407.5063 [hep-ex]`.

[109] ATLAS Collaboration, *Improved electron reconstruction in ATLAS using the Gaussian Sum Filter-based model for bremsstrahlung*, Tech. Rep. ATLAS-CONF-2012-047, CERN, Geneva, May, 2012.

[110] ATLAS Collaboration, *Expected electron performance in the ATLAS experiment*, Tech. Rep. ATL-PHYS-PUB-2011-006, CERN, Geneva, Apr, 2011.

[111] ATLAS Collaboration, *Electron reconstruction and identification efficiency measurements with the ATLAS detector using the 2011 LHC proton-proton collision data*, Eur. Phys. J. C **74** (2014) 2941, `arXiv:1404.2240 [hep-ex]`.

[112] ATLAS Collaboration, G. Aad et al., *Observation and measurement of Higgs boson decays to WW^* with the ATLAS detector*, `arXiv:1412.2641 [hep-ex]`.

[113] S. Hassani, L. Chevalier, E. Lanon, et al., *A muon identification and combined reconstruction procedure for the ATLAS detector at the LHC using the (MUONBOY, STACO, MuTag) reconstruction packages*, Nucl. Instrum. Meth. Phys. Res. A **572** (2007) 77 – 79. Frontier Detectors for Frontier Physics Proceedings of the 10th Pisa Meeting on Advanced Detectors.

[114] T. Lagouri, D. Adams, K. A. Assamagan, et al., *A Muon Identification and Combined Reconstruction Procedure for the ATLAS Detector at the LHC at CERN*, Tech. Rep. ATL-CONF-2003-011, Oct, 2003.

[115] S. Catani, Y. L. Dokshitzer, M. H. Seymour, and B. R. Webber, *Longitudinally-invariant $k_\perp$-clustering algorithms for hadron-hadron collisions*, Nucl. Phys. B **406** no. CERN-TH-6775-93, LU-TP-93-2, (1993) 187–224. 38 p.

[116] S. D. Ellis and D. E. Soper, *Successive combination jet algorithm for hadron collisions*, Phys. Rev. D **48** (1993) 3160–3166, `arXiv:hep-ph/9305266 [hep-ph]`.

[117] Y. L. Dokshitzer, G. Leder, S. Moretti, and B. Webber, *Better jet clustering algorithms*, J. High Energy Phys. **9708** (1997) 001, `arXiv:hep-ph/9707323 [hep-ph]`.

[118] M. Wobisch and T. Wengler, *Hadronization corrections to jet cross-sections in deep inelastic scattering*, `arXiv:hep-ph/9907280 [hep-ph]`.

[119] M. Cacciari, G. P. Salam, and G. Soyez, *The anti-k_t jet clustering algorithm*, J. High Energy Phys. **2008** (2008) 063.

[120] ATLAS Collaboration, *Jet energy measurement and its systematic uncertainty in proton-proton collisions at $\sqrt{s} = 7\,\mathrm{TeV}$ with the ATLAS detector*, Eur. Phys. J. C **75** (2015).

[121] ATLAS Collaboration, *Jet energy measurement with the ATLAS detector in proton-proton collisions at* $\sqrt{s} = 7\,\text{TeV}$, Eur. Phys. J. C **73** (2013).

[122] ATLAS Collaboration, *Pile-up corrections for jets from proton-proton collisions at* $\sqrt{s} = 7$ TeV *in ATLAS in 2011*, Tech. Rep. ATLAS-CONF-2012-064, CERN, Geneva, Jul, 2012.

[123] ATLAS Collaboration, *Pile-up subtraction and suppression for jets in ATLAS*, Tech. Rep. ATLAS-CONF-2013-083, CERN, Geneva, Aug, 2013.

[124] ATLAS Collaboration, *JES Uncertainties*, May, 2013. `https://twiki.cern.ch/twiki/bin/view/AtlasPublic/JetEtmissApproved2013JESUncertainty`.

[125] ATLAS Collaboration, *Calibration of the performance of b-tagging for c and light-flavour jets in the 2012 ATLAS data*, Tech. Rep. ATLAS-CONF-2014-046, CERN, Geneva, Jul, 2014.

[126] ATLAS Collaboration, *Commissioning of the ATLAS high-performance b-tagging algorithms in the 7 TeV collision data*, Tech. Rep. ATLAS-CONF-2011-102, CERN, Geneva, Jul, 2011.

[127] ATLAS Collaboration, *Calibration of b-tagging using dileptonic top pair events in a combinatorial likelihood approach with the ATLAS experiment*, Tech. Rep. ATLAS-CONF-2014-004, CERN, Geneva, Feb, 2014.

[128] ATLAS Collaboration, *Performance of Missing Transverse Momentum Reconstruction in ATLAS studied in Proton-Proton Collisions recorded in 2012 at 8 TeV*, Tech. Rep. ATLAS-CONF-2013-082, CERN, Geneva, Aug, 2013.

[129] ATLAS Collaboration, G. Aad et al., *Performance of Missing Transverse Momentum Reconstruction in Proton-Proton Collisions at 7 TeV with ATLAS*, Eur. Phys. J. C **72** (2012) 1844, `arXiv:1108.5602 [hep-ex]`.

[130] T. Sjstrand, S. Mrenna, and P. Skands, *A brief introduction to PYTHIA 8.1*, Comput. Phys. Commun. **178** (2008) 852 – 867.

[131] ATLAS Collaboration, *The ATLAS Simulation Infrastructure*, Eur. Phys. J. C **70** (2010) 823–874. 53 p, `arXiv:1005.4568`.

[132] S. Agostinelli, J. Allison, K. Amako, et al., *Geant4a simulation toolkit*, Nucl. Instrum. Meth. Phys. Res. A **506** (2003) 250 – 303.

[133] ATLAS Collaboration, M. Beckingham, M. Duehrssen, E. Schmidt, et al., *The simulation principle and performance of the ATLAS fast calorimeter simulation FastCaloSim*, Tech. Rep. ATL-PHYS-PUB-2010-013, CERN, Geneva, Oct, 2010.

[134] ATLAS Collaboration, *Study of the Higgs boson decaying to* WW^* *produced in association with a weak boson with the ATLAS detector at the LHC*, Tech. Rep. ATLAS-CONF-2015-005, CERN, Geneva, Mar, 2015.

[135] ATLAS Collaboration, *Measurement of the Higgs boson mass from the $H \to \gamma\gamma$ and $H \to ZZ^* \to 4\ell$ channels in pp collisions at center-of-mass energies of 7 and 8 TeV with the ATLAS detector*, Phys. Rev. D **90** (2014) 052004.

[136] ATLAS Collaboration, *Determination of spin and parity of the Higgs boson in the $WW^* \to e\nu\mu\nu$ decay channel with the ATLAS detector*, arXiv:1503.03643 [hep-ex].

[137] ATLAS Collaboration, *Higgs Boson Searches using the $H \to WW^{(*)} \to \ell\nu\ell\nu$ Decay Mode with the ATLAS Detector at 7 TeV*, Tech. Rep. ATLAS-CONF-2011-005, CERN, Geneva, Feb, 2011.

[138] ATLAS Collaboration, *Search for the Higgs boson in the $H \to$ WW(*) $\to \ell_\nu \ell_\nu$ decay channel in pp collisions at $\sqrt{s} = 7$ TeV with the ATLAS detector*, Phys. Rev. Lett. **108** (2012) 111802, arXiv:1112.2577 [hep-ex].

[139] ATLAS Collaboration, *Search for the Standard Model Higgs boson in the $H \to$ WW(*) $\to \ell\nu\ell\nu$ decay mode with 4.7 /fb of ATLAS data at $\sqrt{s} = 7$ TeV*, Phys. Lett. B **716** (2012) 62–81, arXiv:1206.0756 [hep-ex].

[140] ATLAS Collaboration, *Observation of an Excess of Events in the Search for the Standard Model Higgs Boson in the $H \to WW^{(*)} \to \ell\nu\ell\nu$ Channel with the ATLAS Detector*, Tech. Rep. ATLAS-CONF-2012-098, CERN, Geneva, Jul, 2012.

[141] ATLAS Collaboration, *Update of the $H \to WW^{(*)} \to e\nu\mu\nu$ Analysis with 13 fb^{-1} of $\sqrt{s} = 8$ TeV Data Collected with the ATLAS Detector*, Tech. Rep. ATLAS-CONF-2012-158, CERN, Geneva, Nov, 2012.

[142] ATLAS Collaboration, *Measurements of the properties of the Higgs-like boson in the $WW^{(*)} \to \ell\nu\ell\nu$ decay channel with the ATLAS detector using 25 fb^{-1} of proton-proton collision data*, Tech. Rep. ATLAS-CONF-2013-030, CERN, Geneva, Mar, 2013.

[143] S. Alioli, P. Nason, C. Oleari, and E. Re, *A general framework for implementing NLO calculations in shower Monte Carlo programs: the POWHEG BOX*, J. High Energy Phys. **1006** (2010) 043, arXiv:1002.2581 [hep-ph].

[144] A. Bredenstein, A. Denner, S. Dittmaier, and M. M. Weber, *Precise predictions for the Higgs-boson decay $H \to WW/ZZ \to 4$ leptons*, Phys. Rev. D **74** (2006) 013004.

[145] A. Djouadi, J. Kalinowski, and M. Spira, *HDECAY: A Program for Higgs boson decays in the standard model and its supersymmetric extension*, Comput. Phys. Commun. **108** (1998) 56–74, arXiv:hep-ph/9704448 [hep-ph].

[146] C. Anastasiou and K. Melnikov, *Higgs boson production at hadron colliders in NNLO QCD*, Nucl. Phys. B **646** (2002) 220 – 256.

[147] M. Spira, A. Djouadi, D. Graudenz, and R. Zerwas, *Higgs boson production at the LHC*, Nucl. Phys. B **453** (1995) 17 – 82.

[148] S. Catani, D. de Florian, M. Grazzini, and P. Nason, *Soft-gluon resummation for Higgs boson production at hadron colliders*, J. High Energy Phys. **2003** (2003) 028.

[149] U. Aglietti, R. Bonciani, G. Degrassi, and A. Vicini, *Master integrals for the two-loop light fermion contributions to and*, Phys. Lett. B **600** (2004) 57 – 64.

[150] G. Degrassi and F. Maltoni, *Two-loop electroweak corrections to Higgs production at hadron colliders*, Phys. Lett. B **600** (2004) 255 – 260.

[151] D. de Florian and M. Grazzini, *Higgs production at the LHC: Updated cross sections at*, Phys. Lett. B **718** (2012) 117 – 120.

[152] J. M. Campbell, R. K. Ellis, and C. Williams, *Bounding the Higgs width at the LHC: Complementary results from $H \to WW$*, Phys. Rev. D **89** (2014) 053011, arXiv:1312.1628 [hep-ph].

[153] G. Bozzi, S. Catani, D. de Florian, and M. Grazzini, *Transverse-momentum resummation and the spectrum of the Higgs boson at the LHC*, Nucl. Phys. B **737** (2006) 73–120, arXiv:hep-ph/0508068 [hep-ph].

[154] D. de Florian, G. Ferrera, M. Grazzini, and D. Tommasini, *Transverse-momentum resummation: Higgs boson production at the Tevatron and the LHC*, J. High Energy Phys. **1111** (2011) 064, arXiv:1109.2109 [hep-ph].

[155] D. de Florian, G. Ferrera, M. Grazzini, and D. Tommasini, *Higgs boson production at the LHC: transverse momentum resummation effects in the H , H WW ll and H ZZ 4l decay modes*, J. High Energy Phys. **2012** (2012).

[156] M. Grazzini and H. Sargsyan, *Heavy-quark mass effects in Higgs boson production at the LHC*, J. High Energy Phys. **2013** (2013).

[157] K. Hamilton, P. Nason, and G. Zanderighi, *MINLO: multi-scale improved NLO*, J. High Energy Phys. **2012** (2012).

[158] LHC Higgs Cross Section Working Group, S. Dittmaier, C. Mariotti, G. Passarino, and R. Tanaka (Eds.), *Handbook of LHC Higgs Cross Sections: 2. Differential Distributions*, arXiv:1201.3084 [hep-ph].

[159] J. Butterworth, G. Dissertori, S. Dittmaier, et al., *Les Houches 2013: Physics at TeV Colliders: Standard Model Working Group Report*, arXiv:1405.1067 [hep-ph].

[160] I. W. Stewart and F. J. Tackmann, *Theory uncertainties for Higgs mass and other searches using jet bins*, Phys. Rev. D **85** (2012) 034011.

[161] A. Banfi, G. Salam, and G. Zanderighi, *NLL+NNLO predictions for jet-veto efficiencies in Higgs-boson and Drell-Yan production*, J. High Energy Phys. **2012** (2012).

[162] A. Martin, W. Stirling, R. Thorne, and G. Watt, *Parton distributions for the LHC*, Eur. Phys. J. C **63** (2009) 189–285.

[163] H.-L. Lai, M. Guzzi, J. Huston, et al., *New parton distributions for collider physics*, Phys. Rev. D **82** (2010) 074024.

[164] J. Alwall et al., *The automated computation of tree-level and next-to-leading order differential cross sections, and their matching to parton shower simulations*, J. High Energy Phys. **07** (2014) 079, `arXiv:1405.0301 [hep-ph]`. optimised by the authors for the production of VBF $(H^* \to)VV$.

[165] P. Bolzoni, F. Maltoni, S.-O. Moch, and M. Zaro, *Higgs Boson Production via Vector-Boson Fusion at Next-to-Next-to-Leading Order in QCD*, Phys. Rev. Lett. **105** (2010) 011801.

[166] M. Ciccolini, D. A., and D. S., *Electroweak and QCD corrections to Higgs production via vector-boson fusion at the CERN LHC*, Phys. Rev. D **77** (2008) 013002.

[167] Gleisberg, T. and Höche, Stefan. and Krauss, F. and Schönherr, M. and Schumann, S. and others, *Event generation with SHERPA 1.1*, J. High Energy Phys. **0902** (2009) 007, `arXiv:0811.4622 [hep-ph]`.

[168] M. L. Mangano, M. Moretti, F. Piccinini, R. Pittau, and A. D. Polosa, *ALPGEN, a generator for hard multiparton processes in hadronic collisions*, J. High Energy Phys. **0307** (2003) 001, `arXiv:hep-ph/0206293 [hep-ph]`.

[169] N. Kauer, *Interference effects for $H \to WW/ZZ \to \ell\bar{\nu}_\ell\bar{\ell}\nu_\ell$ searches in gluon fusion at the LHC*, J. High Energy Phys. **1312** (2013) 082, `arXiv:1310.7011 [hep-ph]`.

[170] B. P. Kersevan and E. Richter-Was, *The Monte Carlo event generator AcerMC versions 2.0 to 3.8 with interfaces to PYTHIA 6.4, HERWIG 6.5 and ARIADNE 4.1*, Comput. Phys. Commun. **184** (2013) 919 – 985.

[171] Sjöstrand, Torbjorn and Mrenna, Stephen and Skands, Peter Z., *PYTHIA 6.4 Physics and Manual*, J. High Energy Phys. **0605** (2006) 026, `arXiv:hep-ph/0603175`.

[172] G. Corcella, I. Knowles, G. Marchesini, et al., *HERWIG 6: An Event generator for hadron emission reactions with interfering gluons (including supersymmetric processes)*, J. High Energy Phys. **0101** (2001) 010, `arXiv:hep-ph/0011363 [hep-ph]`.

[173] J. Butterworth, J. Forshaw, and M. Seymour, *Multiparton interactions in photoproduction at HERA*, Zeitschrift fr Physik C: Particles and Fields **72** (1996) 637–646.

[174] J. Pumplin, D. R. Stump, J. Huston, et al., *New Generation of Parton Distributions with Uncertainties from Global QCD Analysis*, J. High Energy Phys. **2002** (2002) 012.

[175] A. Sherstnev and R. Thorne, *Parton distributions for LO generators*, Eur. Phys. J. C **55** (2008) 553–575.

[176] J. Campbell, R. Ellis, and C. Williams, *Vector boson pair production at the LHC*, J. High Energy Phys. **2011** (2011).

[177] T. Binoth, N. Kauer, and P. Mertsch, *Gluon-induced QCD corrections to $pp \to ZZ \to \ell\bar{\ell}\ell'\bar{\ell}'$*, arXiv:0807.0024 [hep-ph].

[178] M. Czakon and A. Mitov, *Top++: A program for the calculation of the top-pair cross-section at hadron colliders*, Comput. Phys. Commun. **185** (2014) 2930 – 2938.

[179] N. Kidonakis, *Next-to-next-to-leading logarithm resummation for s-channel single top quark production*, Phys. Rev. D **81** (2010) 054028.

[180] N. Kidonakis, *Next-to-next-to-leading-order collinear and soft gluon corrections for t-channel single top quark production*, Phys. Rev. D **83** (2011) 091503.

[181] N. Kidonakis, *Two-loop soft anomalous dimensions for single top quark associated production with a W^- or H^-*, Phys. Rev. D **82** (2010) 054018.

[182] S. Catani and M. Grazzini, *Next-to-Next-to-Leading-Order Subtraction Formalism in Hadron Collisions and its Application to Higgs-Boson Production at the Large Hadron Collider*, Phys. Rev. Lett. **98** (2007) 222002.

[183] S. Catani, L. Cieri, G. Ferrera, D. de Florian, and M. Grazzini, *Vector Boson Production at Hadron Colliders: A Fully Exclusive QCD Calculation at Next-to-Next-to-Leading Order*, Phys. Rev. Lett. **103** (2009) 082001.

[184] ATLAS Collaboration, *Measurement of hard double-parton interactions in $W(\to \ell\nu)+$ 2-jet events at $\sqrt{s} = 7$ TeV with the ATLAS detector*, New J. Phys **15** (2013) 033038.

[185] B. Blok, Y. Dokshitzer, L. Frankfurt, and M. Strikman, *Perturbative QCD correlations in multi-parton collisions*, Eur. Phys. J. C **74** (2014).

[186] R. Ellis, I. Hinchliffe, M. Soldate, and J. V. D. Bij, *Higgs decay to $\pi^+\pi^-$: A possible signature of intermediate mass Higgs bosons at high energy hadron colliders*, Nucl. Phys. B **297** (1988) 221 – 243.

[187] T. Plehn, D. Rainwater, and D. Zeppenfield, *Method for identifying $H \to \tau\tau \to e^{\pm}\mu^{\mp}\not{p}_T$ at the CERN LHC*, Phys. Rev. D **61** (2000) 093005.

[188] Y. Freund and R. E. Schapire, *A Decision-Theoretic Generalization of On-Line Learning and an Application to Boosting*, J. Comput. Syst. Sci. **55** (1997) 119 – 139.

[189] J. H. Friedman, *Stochastic gradient boosting*, Comput. Stat. Data Anal. **38** (2002) 367 – 378. Nonlinear Methods and Data Mining.

[190] V. Barger, R. Phillips, and D. Zeppenfeld, *Minijet veto: a tool for the heavy Higgs search at the LHC*, Phys. Lett. B **346** (1995) 106 – 114.

[191] A. Bierweiler, T. Kasprzik, and J. Khn, *Vector-boson pair production at the LHC to $\mathcal{O}(\alpha^3)$ accuracy*, J. High Energy Phys. **2013** (2013).

[192] T. Melia, K. Melnikov, R. Rntsch, M. Schulze, and G. Zanderighi, *Gluon fusion contribution to W^+W^-+ jet production*, J. High Energy Phys. **2012** (2012).

[193] J. Alwall et al., *MadGraph/MadEvent v4: The New Web Generation*, J. High Energy Phys. **0709** (2007) 028.

[194] Frixione, Stefano and Webber, Bryan R., *Matching NLO QCD computations and parton shower simulations*, J. High Energy Phys. **0206** (2002) 029, `arXiv:hep-ph/0204244 [hep-ph]`.

[195] G. Cowan, K. Cranmer, E. Gross, and O. Vitells, *Asymptotic formulae for likelihood-based tests of new physics*, Eur. Phys. J. C **71** (2011).

[196] A. L. Read, *Presentation of search results: the CL s technique*, J. Phys. G **28** (2002) 2693.

[197] ATLAS Collaboration, *Measurements of the Higgs boson production and decay rates and coupling strengths using pp collision data at* $\sqrt{s}$ *= 7 and 8* TeV *in the ATLAS experiment*, Tech. Rep. ATLAS-CONF-2015-007, CERN, Geneva, Mar, 2015.

[198] ATLAS Collaboration, *Determination of the off-shell Higgs boson signal strength in the high-mass* ZZ *and* WW *final states with the ATLAS detector*, `arXiv:1503.01060 [hep-ex]`.

[199] ATLAS Collaboration, *Measurements of Higgs boson production and couplings in the four-lepton channel in pp collisions at center-of-mass energies of 7 and 8 TeV with the ATLAS detector*, Phys. Rev. D **91** (2015) 012006, `arXiv:1408.5191 [hep-ex]`.

[200] ATLAS Collaboration, *Search for Invisible Decays of a Higgs Boson Produced in Association with a Z Boson in ATLAS*, Phys. Rev. Lett. **112** (2014) 201802, `arXiv:1402.3244 [hep-ex]`.

[201] CMS Collaboration, *Constraints on the Higgs boson width from off-shell production and decay to* Z*-boson pairs*, Phys. Lett. B **736** (2014) 64, `arXiv:1405.3455 [hep-ex]`.

[202] N. Kauer and G. Passarino, *Inadequacy of zero-width approximation for a light Higgs boson signal*, `arXiv:1206.4803 [hep-ph]`.

[203] F. Caola and K. Melnikov, *Constraining the Higgs boson width with ZZ production at the LHC*, Phys. Rev. D **88** (2013) 054024, `arXiv:1307.4935 [hep-ph]`.

[204] J. M. Campbell, R. K. Ellis, and C. Williams, *Bounding the Higgs width at the LHC using full analytic results for* $gg \to e^- e^+ \mu^- \mu^+$, J. High Energy Phys. **04** (2014) 060, `arXiv:1311.3589 [hep-ph]`.

[205] C. Englert and M. Spannowsky, *Limitations and Opportunities of Off-Shell Coupling Measurements*, Phys. Rev. D **90** (2014) 053003, `arXiv:1405.0285 [hep-ph]`.

[206] G. Cacciapaglia, A. Deandrea, G. D. La Rochelle, and J.-B. Flament, *Higgs couplings: disentangling New Physics with off-shell measurements*, Phys. Rev. Lett. **113** (2014) 201802, `arXiv:1406.1757 [hep-ph]`.

[207] A. Azatov, C. Grojean, A. Paul, and E. Salvioni, *Taming the off-shell Higgs boson*, J. Exp. Theor. Phys. **147 (3)** (2015), arXiv:1406.6338 [hep-ph].

[208] M. Ghezzi, G. Passarino, and S. Uccirati, *Bounding the Higgs Width Using Effective Field Theory*, PoS LL2014 **072** (2014), arXiv:1405.1925 [hep-ph].

[209] M. Buschmann et al., *Mass Effects in the Higgs-Gluon Coupling: Boosted vs Off-Shell Production*, arXiv:1410.5806 [hep-ph].

[210] J. S. Gainer, J. Lykken, K. T. Matchev, S. Mrenna, and M. Park, *Beyond Geolocating: Constraining Higher Dimensional Operators in $H \to 4\ell$ with Off-Shell Production and More*, arXiv:1403.4951 [hep-ph].

[211] C. Englert, Y. Soreq, and M. Spannowsky, *Off-Shell Higgs Coupling Measurements in BSM scenarios*, arXiv:1410.5440 [hep-ph].

[212] CMS Collaboration, *Precise determination of the mass of the Higgs boson and tests of compatibility of its couplings with the standard model predictions using proton collisions at 7 and 8 TeV*, arXiv:1412.8662 [hep-ex].

[213] CMS Collaboration, *Search for invisible decays of Higgs bosons in the vector boson fusion and associated ZH production modes*, Eur. Phys. J. C **74** (2014) 2980, arXiv:1404.1344 [hep-ex].

[214] ATLAS Collaboration, *Measurement of the Higgs boson mass from the $H \to \gamma\gamma$ and $H \to ZZ^* \to 4\ell$ channels with the ATLAS detector using 25 fb^{-1} of pp collision data*, Phys. Rev. D **90** (2014) 052004, arXiv:1406.3827 [hep-ex].

[215] CMS Collaboration, V. Khachatryan et al., *Observation of the diphoton decay of the Higgs boson and measurement of its properties*, Eur. Phys. J. C **74** (2014) 3076, arXiv:1407.0558 [hep-ex].

[216] CMS Collaboration, S. Chatrchyan et al., *Measurement of the properties of a Higgs boson in the four-lepton final state*, Phys. Rev. D **89** (2014) 092007, arXiv:1312.5353 [hep-ex].

[217] H. E. Logan, *Hiding a Higgs width enhancement from off-shell $gg(\to h^*) \to ZZ$ measurements*, arXiv:1412.7577 [hep-ph].

[218] T. Gehrmann et al., *W^+W^- production at hadron colliders in NNLO QCD*, Phys. Rev. Lett. **113** (2014) 212001, arXiv:1408.5243 [hep-ph]. Extended by the authors to provide NNLO/NLO K-factors as a function of m_{WW}.

[219] F. Cascioli et al., *ZZ production at hadron colliders in NNLO QCD*, Phys. Lett. B **735** (2014) 311, arXiv:1405.2219 [hep-ph]. Extended by the authors to provide NNLO/NLO K-factors as a function of m_{ZZ}.

[220] A. Bierweiler, T. Kasprzik, and J. H. Kühn, *Vector-boson pair production at the LHC to $\mathcal{O}(\alpha^3)$ accuracy*, J. High Energy Phys. **12** (2013) 071, arXiv:1305.5402 [hep-ph].

[221] J. Baglio, L. D. Ninh, and M. M. Weber, *Massive gauge boson pair production at the LHC: a next-to-leading order story*, Phys. Rev. D **88** (2013) 113005, arXiv:1307.4331.

[222] S. Gieseke, T. Kasprzik, and J. H. Kühn, *Vector-boson pair production and electroweak corrections in HERWIG++*, Eur. Phys. J. C **74** (2014) 2988, arXiv:1401.3964 [hep-ph].

[223] F. Cascioli et al., *Precise Higgs-background predictions: merging NLO QCD and squared quark-loop corrections to four-lepton + 0,1 jet production*, J. High Energy Phys. **01** (2014) 046, arXiv:1309.0500 [hep-ph].

[224] F. Cascioli, P. Maierhöfer, and S. Pozzorini, *Scattering Amplitudes with Open Loops*, Phys. Rev. Lett. **108** (2012) 111601, arXiv:1111.5206 [hep-ph].

[225] J. Gao et al., *The CT10 NNLO Global Analysis of QCD*, Phys. Rev. D **89** (2014) 033009, arXiv:1302.6246 [hep-ph].

[226] G. Passarino, *Higgs CAT*, Eur. Phys. J. C **74** (2014) 2866, arXiv:1312.2397 [hep-ph].

[227] M. Bonvini, F. Caola, S. Forte, K. Melnikov, and G. Ridolfi, *Signal-background interference effects for $gg \to H \to W^+W^-$ beyond leading order*, Phys. Rev. D **88** (2013) 034032, arXiv:1304.3053 [hep-ph].

[228] A. Ballestrero, A. Belhouari, G. Bevilacqua, V. Kashkan, and E. Maina, *PHANTOM: A Monte Carlo event generator for six parton final states at high energy colliders*, Comput. Phys. Commun. **180** (2009) 401–417, arXiv:0801.3359 [hep-ph]. Extended by the authors to include the production of the VBF $H^* \to VV$ signal process.

[229] H. L. D. Study, "LHC / HL-LHC Plan." http://hilumilhc.web.cern.ch/about/hl-lhc-project. Updated 2015-03-03.

[230] ATLAS Collaboration, *Projections for measurements of Higgs boson cross sections, branching ratios and coupling parameters with the ATLAS detector at a HL-LHC*, Tech. Rep. ATL-PHYS-PUB-2013-014, CERN, Geneva, Oct, 2013.

[231] ATLAS Collaboration, *Performance assumptions for an upgraded ATLAS detector at a High-Luminosity LHC*, Tech. Rep. ATL-PHYS-PUB-2013-004, CERN, Geneva, Mar, 2013.

[232] ATLAS Collaboration, *Performance assumptions based on full simulation for an upgraded ATLAS detector at a High-Luminosity LHC*, Tech. Rep. ATL-PHYS-PUB-2013-009, CERN, Geneva, Sep, 2013.

[233] W. Stirling, "8, 14, 33 TeV LHC Luminosity Ratios." http://www.hep.ph.ic.ac.uk/~wstirlin/plots/plots.html. Private Communication.

[234] T. Binoth, M. Ciccolini, N. Kauer, and M. Kramer, *Gluon-induced W-boson pair production at the LHC*, J. High Energy Phys. **0612** (2006) 046, arXiv:hep-ph/0611170 [hep-ph].

[235] ATLAS Collaboration, *Projections for measurements of Higgs boson signal strengths and coupling parameters with the ATLAS detector at a HL-LHC*, Tech. Rep. ATL-PHYS-PUB-2014-016, CERN, Geneva, Oct, 2014.